

Safe in their hands?

Britain's restructuring of research funding and the budget announced last week are welcome. But a cloud still hangs over basic biomedical science.

Every country with any interest in biomedical science and its applications wants to boost 'translational research': the work required to shift biological insights discovered in laboratories towards their application in the clinic. Britain is no exception, and given its scientific and industrial strengths, it is well placed to do so, as part of a drive to deliver the greatest economic return from its scientific investment.

The 2008–09 budget announced last week was fully consistent with this general goal. With a tough review of government spending yet to be completed, Tony Blair's government has nevertheless committed to a growth in science funds of 2.7% above inflation, with increased incentives for industrial innovation.

But beneath the surface, all is not well for Britain's future commitment to basic biomedical research. To consider the money first, the allocated funds have to pay for the new initiatives to boost translational research. But they also have to cover other government commitments, including more realistic compensation to universities for the costs of all government-funded research. These will make substantial claims on the budget of the Medical Research Council (MRC), so the basic biomedical research that it has long supported seems bound to take a hit.

Basic science is vulnerable for another reason: changing organization. Last year, the government announced the removal of funds from the National Health Service trusts that currently control them so the money could be more transparently and rigorously deployed as a dedicated research budget under the auspices of a new National Institute for Health Research (NIHR), working alongside the MRC. Above these bodies sits the Office for Strategic Coordination of Health Research, chaired by John Bell, professor of medicine at the University of Oxford.

This is all to the good. But here too there are devils in the detail. The NIHR will not materialize until 2009 at the earliest, a year later than originally envisaged. There are major negotiations ahead about who has what responsibility for enhancing translational and clinical research and developing the necessary infrastructures. Translational

research is, after all, very different from basic research in terms of its organizational and regulatory requirements and associated costs.

There is no doubt about Bell's belief in basic research. But this top-level development requires healthy cooperation between the various parties involved. It also requires strong leadership at the MRC to protect the interests of basic research. But the MRC's chief executive, Colin Blakemore, and the Department of Health research director, Sally Davies, are reportedly not communicating on such matters. Furthermore, the MRC has been somewhat marginalized in developing bids to the Treasury in the spending review. And its clout is further reduced by the fact that Blakemore's term as MRC chief executive will come to an end later this year, with no replacement in sight.

The MRC faces other challenges, too. Last October saw its appointment of a chair, John Chisholm, who has a strong track record in privatizing defence research laboratories. He has recently sent signals that have left MRC researchers dumbfounded. To judge by recent statements, he views biomedical research as being applied research by definition, and sees fundamental research to be all but irrelevant. A review of MRC governance that he commissioned, to be considered by the MRC's council this week, leaves open the possibility that the representation of basic science on that governing body will be weakened. And it is anybody's guess whether Blakemore's successor will be a sufficiently forceful champion of fundamental research among the various fiefdoms competing for leverage and budgets within the new structures.

In short, despite a seemingly strong environment for Britain's basic biomedical research, an unfortunate combination of issues leaves it looking vulnerable. Translation is one critical route to the biomedical future, but equally important for the MRC are the people responsible for fundamental discoveries, including some with little idea about applying their knowledge outside their labs. Unless Britain's new biomedical hierarchy demonstrably commits itself to such people, it risks losing not only some excellent scientists, but also its ability to retain and attract those very industries on which the country's science-based economic strategy depends. ■

Mutant mice galore

A new consortium will fulfil a genomics dream — provided it gets the support it deserves.

The purpose of sequencing the mouse genome was to further the career of *Mus musculus* as the biologist's favourite model of human disease. The task was completed in 2002, a year after the human genome. To exploit the new knowledge, a catalogue of mutant mice had to be created in the service of biomedical science.

The outstanding questions were just how many genes needed to be individually mutated in mice, and how to set about it.

Some five years later, genetic technologies have developed so fast that the questions have virtually answered themselves. The community at large, in the form of the newly created International Mouse Knockout Consortium, has now declared that each and every one of the 20,000 or so genes in the mouse genome will be systematically targeted and mutated in embryonic stem cells. And all this is only the beginning.

The consortium is now taking requests from the community for genes to be targeted, with the gaps to be filled in later. Soon, if all

goes according to plan, anyone will be able to order an off-the-shelf mutant mouse to test any biological hypotheses or develop any disease model.

The consortium formally launched itself earlier this month with the signing of a cooperation agreement between three funding agencies that together are committing several hundred thousand dollars to the cause over the next five years or so: the European Commission, the US National Institutes of Health and Genome Canada. The signing took place during a two-day meeting organized by the European Commission at a lakeside chateau in Genval, a village just outside Brussels, where delegates from around the world were able to discuss the implementation of the ambitious plan and to dream about the next steps.

The practicalities don't depend only on money. Databases are needed so that the consortium can efficiently share information and avoid duplication. The most important mutants need to be 'phenotyped', or characterized, to record the physiological effects caused by the lack of a gene. This means expanding and standardizing the activities of the 'mouse clinics' that have sprung up, mostly in Europe, to support previous research programmes. The question of how much phenotyping needs to be done during this phase, and on how

many of the chosen mutants, still remains to be resolved.

Grandiose as these plans are, they are but one major step towards the vision of offering an even fuller service to biologists. For example, most of the embryonic stem-cell mutants currently available are 'null' knockouts — the targeted gene simply doesn't function. But, at a greater cost, it is now possible to make 'null-first conditional-ready' mutants. In these, the gene is knocked out by default but can be re-established and knocked out at will in particular tissues at particular times. This flexibility is much more valuable to researchers.

This technology cannot currently be applied to all genes, but it is developing fast. A fuller service would require that more extensive phenotyping be done on each of the mutants. Moreover, a further database is required to document the differences between mouse and human gene function, to ensure a deeper understanding of mouse models of human disease. The full service will be costly.

This vision represents the fulfilment of mouse genome sequencing. Support for that project needs to be followed through: the mouse has already led to excellent insights into many human diseases, and the continuation of this approach will deliver many more. Budgets have tightened, but funding agencies that stay the course can be assured of ample returns on their investment. ■

Cut the climate antics

A long run of congressional theatre should close.

Last week, Al Gore made a triumphant return to Washington, testifying in the US Congress for the first time since his film, *An Inconvenient Truth*, turned the man who was almost president into an Oscar-winning environmental saint. He is now reckoned by almost everybody to have been right all along, and his star turn could mark the moment when Congress gives up arguing about whether climate change is real, and starts arguing about how to handle it.

The affair was suitably raucous, with a burst of camera shutters punctuating the former vice-president's every gesture and scribbling journalists packed in so tight they had to keep their elbows in front of them. Looking solid but progressive in a blue-checked shirt and blue tie, Gore called on Congress to be bold on climate change. "There is a sense of hope in this country that this Congress will rise to the occasion," he said. "We do not have time to play around with this."

Gore also made specific recommendations for action, suggesting changes that are probably too bold for any sitting politician but that may expand the outer bounds of what is considered feasible. They included freezing emissions levels immediately, then reducing them by 90% by 2050; a carbon tax and a cap-and-trade scheme; bans on incandescent light bulbs and new coal plants that cannot be made to capture and store carbon; corporate disclosure of carbon emissions; and tougher mileage standards for cars.

The leading Republicans in the committees where he spoke kept up their increasingly surreal insistence that climate change isn't happening. Joe Barton of Texas in the House of Representatives and James Inhofe of Oklahoma in the Senate not only presented increasingly threadbare arguments against climate change, but seemed to be trying

to take the lustre off the occasion by extensively negotiating how much time they would get to speak.

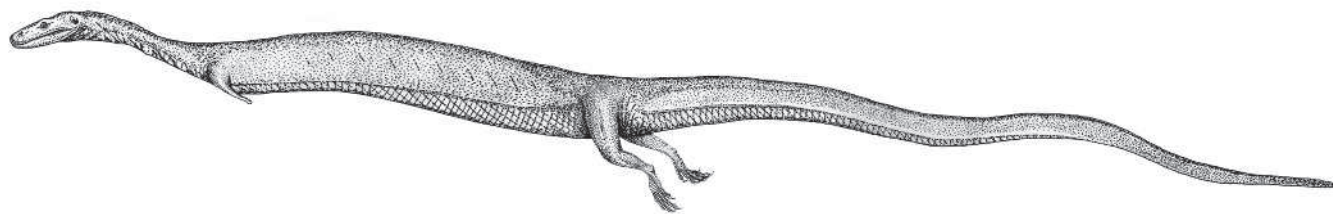
Inhofe was so determined to get his share of the time that he wanted Gore to respond to all his questions in writing only. He was overruled by Barbara Boxer, the Democrat senator from California who now runs what used to be Inhofe's committee in the Senate and clearly relishes it — at one point she brandished her gavel at him triumphantly. Gore responded to their questions with scientific lectures, deep sighs and offers of one-to-one tutoring in climate science.

More productively, most Republicans asked Gore substantive questions about policy approaches, notably on the challenge of convincing China and India to act, and on the possibility of a renaissance for nuclear power (Gore is wary of it, being an ardent fan of distributed micro-generation). Some Republicans seemed willing to make it their issue too. Republican stalwart Senator John Warner of Virginia said: "I am prepared to fight with you on this." In the House, Bob Inglis of South Carolina framed it as a Christian issue and said that efforts should be made to cut down emissions even without China and India because "you teach your children to do the right thing, even if no one is looking".

In the metro system beneath the Capitol complex, Boxer said that Gore was pleased with the Republican response. As she chatted with reporters, Gore dashed to an adjoining carriage. As the doors threatened to close on him, a Capitol worker reached out and held the door for him. Boxer watched in astonishment. "I've never seen them do that for anyone before," she said.

It was all good theatre, but the high jinks of the climate-change sceptics already seem outdated, and many in their own party are starting to ignore them with the serene expression seen on the faces of parents when their children throw a temper tantrum in public. This is the duty of all sensible politicians as they move forward on climate-change policy. The naysayers should be indulged no longer. ■

RESEARCH HIGHLIGHTS



A. PALCI

Hissing link?

J. Vertebr. Paleontol. **27**, 1–7 (2007)

The complex history of how snakes lost their limbs to evolution may become clearer, thanks to a fossil found in Slovenia.

Snakes evolved from four-limbed lizards, but

the details of how this happened are unclear. Alessandro Palci of the University of Modena, Italy, and Michael Caldwell of the University of Alberta in Edmonton, Canada, describe the first fossil of a lizard that shows limb reduction. Dubbed *Adriosaurus microbrachis* (pictured), the marine lizard lived about 95 million years

ago. The fossil has greatly reduced forelimbs, a diminished supporting skeletal girdle and an elongated neck, as seen today in snakes including pythons and boas.

But researchers cannot conclude that snakes evolved directly from such lizards without other fossils to fill the evolutionary gaps.

CHEMICAL BIOLOGY

Turn up the genes

Angew. Chem. Int. Edn doi:10.1002/anie.200604485 (2007)

It's relatively easy for biologists to switch off genes to study their functions, but harder to turn genes' expression up. Researchers in the United States have synthesized a molecule that can penetrate living cells and do this.

The molecule consists of a peptoid — similar to a peptide — bound to a protein that activates gene expression, and a compound called ImPy7 that binds DNA. It increased by more than threefold the expression of 45 genes with multiple binding sites for ImPy7.

Thomas Kodadek and his colleagues at the University of Texas Southwestern Medical Center in Dallas put the molecule together after screening 50,000 peptoids to identify those that could both bind the gene-activating protein and cross the cell membrane.

CELL BIOLOGY

Old before their time

Proc. Natl Acad. Sci. USA **104**, 4949–4954; 4955–4960 (2007)

The mutant protein responsible for Hutchinson–Gilford progeria syndrome, which causes premature ageing, may hold up the cell cycle, two groups have shown.

Teams led by Francis Collins of the National Human Genome Research Institute in Bethesda, Maryland, and by Robert Goldman of Northwestern University in Chicago, Illinois, studied cells that were making the mutant form of lamin A, which normally acts as scaffolding for the cell nucleus. They found abnormalities in various processes, such as chromosome segregation, assembly of the nuclear membrane and cell division. Similar defects occur in a fraction

of normal human cells, backing the idea that this anomalous protein contributes to the normal ageing process.

NANOTECHNOLOGY

Jitter balls

Nano Lett. doi:10.1021/nl070210a (2007)

Movies of molecules jittering about on a metal surface may inform how future electronic devices are built, says a team led by Ellen Williams of the University of Maryland.

Researchers hoping to build devices in which single molecules serve as wires need first to understand how a device's performance may be affected by changes in the position of the wires or of their contact points. Thermal energy causes fluctuations on these scales.

Using a scanning tunnelling microscope, Williams and her colleagues imaged the motion of carbon C_{60} molecules lined up around the edge of plateaus of silver atoms (C_{60} molecules appear as bright lines in the image below). The researchers characterized

the fluctuations, measuring how frequently the C_{60} molecules and silver atoms moved apart.

PHYSIOLOGY

Tiny heartbreaker

Science doi:10.1126/science.1139089 (2007)

A small RNA molecule regulates some forms of stress-induced heart damage, a new study has shown.

Eric Olson and his colleagues at the University of Texas Southwestern Medical Center in Dallas created mice that lacked a microRNA molecule called miR-208. The mutant mice seemed normal at birth, but when subjected to conditions that stress the heart, sustained less stress-induced cardiac damage (such as excessive heart growth) than normal mice.

miR-208 is highly conserved among mammals, suggesting that its function may also be conserved. Blocking the action of miR-208 may provide a future means of preventing heart damage.

CLIMATE SCIENCE

Sea change

Geophys. Res. Lett. doi:10.1029/2006GL028605 (2007)

Rising concentrations of carbon dioxide in the atmosphere will increase the acidity of the world's oceans by roughly the same amount, regardless of how much global temperatures go up, say Long Cao of the University of Illinois in Urbana and his colleagues.

The oceans' ability to absorb CO_2 is thought to help offset climate change. But, through making the oceans more acidic, it may also change the ocean chemistry to a point that affects marine life. For example, corals and other calcifying marine species may be unable to form shells and skeletons.

AM. CHEM. SOC.

The researchers used an Earth system model to estimate changes in ocean pH for climates that show different temperature responses to CO₂. Whether this climate 'sensitivity' was small or large, surface ocean pH dropped by around 0.5 units relative to a pre-industrial value of 8.17 by 2500. This occurred under a scenario in which CO₂ levels were stabilized at 1,000 parts per million.

NEUROBIOLOGY

Three-seeing mice

Science **315**, 1723–1725 (2007)

Mice endowed with a human eye pigment gain the ability to see extra colours, report Gerald Jacobs from the University of California in Santa Barbara and his colleagues. The pigment allows mice to see longer-wavelength light than their two natural photopigments can detect.

The fact that the mouse's brain is plastic enough to process information from the foreign photopigment suggests that a simple mutation creating an additional light-detecting protein could have given rise to tri-colour vision in some primates. They are unique among mammals in having more than two photopigments.

The team had previously shown that human pigments expressed in mouse retinas create electrical signals in response to light, but have only now completed the behavioural trials that prove the extra pigment enhances a mouse's ability to distinguish colours.

ASTROPHYSICS

A star is spawned

Astrophys. J. **657**, 884–896 (2007)

Might light from a massive star trigger the birth of smaller stars in its neighbourhood? Hsu-Tai Lee and Wen-Ping Chen of the National Central University, Taiwan, say yes.

The team analysed loose groupings of stars known as OB associations. In such systems, the smaller B-type stars are arranged in order of decreasing age between a massive O-type star and nearby clumps of molecular gas.

This odd geometry can be explained if photons from the O star progressively eat their way through the gas cloud, ionizing and compressing it. The denser patches of gas fall in on themselves gravitationally, forming new stars and exposing the next stretch of cloud.

GENETICS

When two fuse with one

Hum. Genet. **121**, 179–185 (2007)

Researchers have discovered a pair of twins who are identical through their mother's side,

but share only half the genes inherited from their father.

The twins result from the combination of two sperm cells with a single egg — a previously unknown way for twins to come about, says the team that made the finding. The twins are also chimaeras, meaning that their cells are not genetically uniform. Each sperm has contributed genes to each child.

There are two routes by which this might have happened. Either the egg cell divided, without separating, and each cell was then fertilized with a single sperm. The genetically mixed embryo then later split. Or, two sperm



D. PHILLIPS/SPL

cells fused with a single egg, creating a cell with three sets of chromosomes which later split into two embryos having a normal complement of chromosomes.

Vivienne Souter of the Banner Good Samaritan Medical Center in Phoenix, Arizona, and her colleagues investigated the twins' genetic make-up because one was born with ambiguous genitalia.

PALAEONTOLOGY

Dinosaurs' digs

Proc. R. Soc. B doi:10.1098/rspb.2006.0443 (2007)

The jumbled remains of an adult dinosaur found together with two juveniles in an underground den provide what experts say is the first evidence that dinosaurs burrowed. It also supports the idea that dinosaur parents cared for their young.

David Varricchio of Montana State University in Bozeman and his colleagues found the fossils in what looks to be a custom-built hole in southern Montana. The 2-metre-long burrow seems to have been filled with mud during a flood, burying its occupants.

The team has named the beast *Oryctodromeus cubicularis*. The skeletons show that, when fully grown, the animal was about 2.1 metres long with a broad snout and powerful shoulders well adapted for digging.

JOURNAL CLUB

Philippe Grangier
Institut d'Optique, Palaiseau,
France

A physicist hopes that cool techniques could show up quantum effects in 'big' systems.

When I was a postdoc in Bell Labs during the 1980s, many of the ideas stimulating our work in quantum optics came from researchers developing sensors for gravitational waves.

Gravitational waves propagate as distortions in space, and a passing wave is expected to have a subtle influence on the oscillation of a heavy bar, or to change by a fraction the separation of two mirrors.

To minimize the uncertainty in measurements of such effects, researchers developed new concepts for manipulating the quantum fluctuations that affect parameters such as an oscillator's position.

Concepts they invented, such as 'quantum non-demolition measurements' and 'squeezed states', have since been demonstrated (sometimes with my help), but with light beams rather than massive objects.

Detecting quantum effects in 'big' systems has remained an elusive goal, despite experiments moving to smaller masses and higher oscillation frequencies to make the quantum noise larger. The stumbling block has been heat — thermal excitations overwhelm the well-hidden quantum noise.

Here, recent work suggests a way forward. Three papers published last autumn (S. Gigan *et al. Nature* **444**, 67–70; O. Arcizet *et al. Nature* **444**, 71–74; D. Kleckner & D. Bouwmeester *Nature* **444**, 75–78; 2006) each show that the techniques used to measure a micromirror's motion can cool the mirror at the same time, pushing its temperature close to absolute zero.

Such cold micromirrors could well become the first 'heavy-weight' quantum-mechanical objects — and the techniques developed in quantum optics may eventually feed back into the gravitational-wave detectors that got us started.

NEWS

Cancer patients opt for unapproved drug

An experimental cancer drug shrinks tumours in rats with no apparent side effects. The scientists behind the study plan to do a clinical trial in humans, but it could take years to complete. Meanwhile, dying patients begin taking the unapproved drug and collect their results on the web. Both groups desperately want to save lives: but which is the right route to follow?

This scenario has been playing out in recent weeks for a compound called dichloroacetate (DCA). It taps into long-running issues about whether terminally ill patients should be able to get access to drugs that have not yet had formal approval. Researchers fear that those taking the drug could suffer unanticipated side effects; patients argue they don't have the luxury of waiting for clinical trials to find out.

In January this year, Evangelos Michelakis at the University of Alberta in Edmonton, Canada, and his colleagues reported that DCA has seemingly remarkable anticancer properties (S. Bonnet *et al. Cancer Cell* **11**, 37–51; 2007). DCA is a small molecule that blocks an enzyme in mitochondria — the energy-production centres in cells — causing more glucose to be metabolized in the mitochondria rather than by a different pathway in the cytoplasm. The compound has been in clinical trials for years as a treatment for certain mitochondrial diseases, but it has not yet been approved.

Mitochondria also control cell suicide, and Michelakis wondered whether cancer cells were suppressing these cellular structures to prevent the cells from dying — and so thought DCA might reactivate them. When his team gave DCA to rats that were growing human lung tumours, the tumours stopped growing within a week, and three months later were half the size of those in untreated animals. Other experimental drugs have had similar effects. But DCA stands out because it seems to leave healthy cells untouched, has been relatively safe in human trials, can be taken by mouth and easily penetrates tissues. “If there were a magic bullet,” wrote *Newsweek* about the discovery, “it might be something like dichloroacetate.”

Because DCA has been around for years, its structure can't be patented and Michelakis found that pharmaceutical companies weren't

interested in developing the drug. So he is raising money and hopes to start his own small clinical trial within the next few months.

In the meantime Jim Tassano, who owns a pest-control and marketing company in Sonora, California, came across DCA when researching alternative cancer therapies to help his dying ballroom-dance instructor. He wanted something that was effective, safe and that he could lay his hands on: DCA fit the bill. He ordered some from chemical supply companies, teamed up with a chemist friend and they worked out a way to synthesize the compound themselves. “I couldn't walk away from it,” Tassano says. “It could do so much good for so many people.”

Tassano set up two websites. The first of these (thedcasite.com) hosts information on DCA and a patient chatroom. On the second (buydca.com) Tassano is selling his home-made DCA — labelled for veterinary use, as drugs sold for human use in the United States

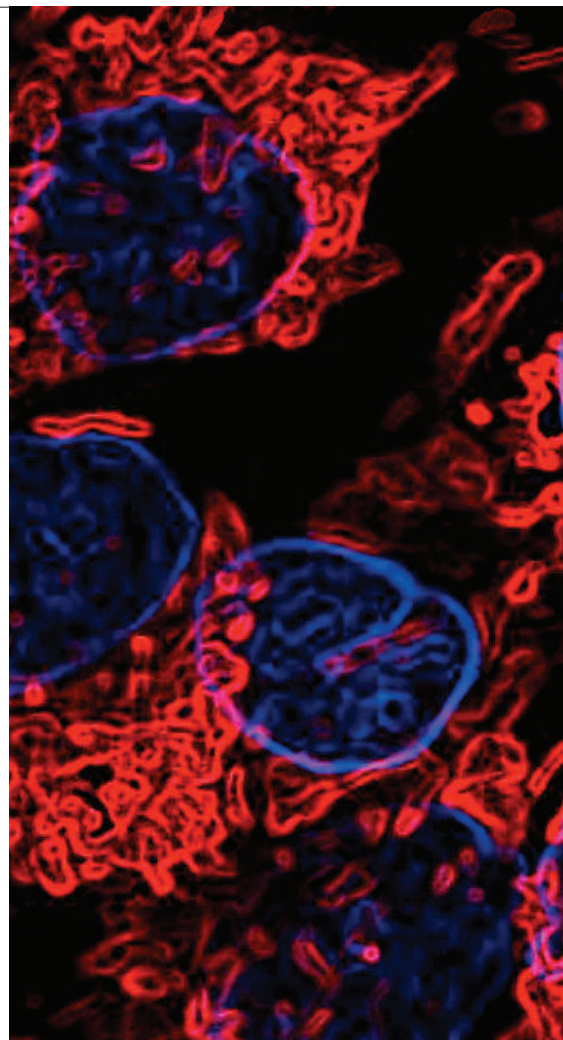
must have approval from the Food and Drug Administration (FDA). Tassano says he is sure patients are buying the drug to use on themselves, and reckons that a couple of hundred of people from around the world have bought from the

site. Many patients taking DCA — acquired from Tassano, chemical companies or other sources — are reporting their progress on thedcasite.com.

Some of these patients plan to set up a database on Tassano's website to collect DCA results in a more organized way. They want people to submit information including the type of cancer they suffer, medical history and the dose they are taking, says Susan Hirasawa in Seattle, Washington, who suffers from late-stage breast cancer and is one of the organizers. The idea is to provide information for others who want to take DCA, she says, but “it's not a real clinical trial”.

Michelakis and other researchers are worried by the development. Although DCA seems safe overall, they point to a clinical trial that was stopped early because those taking the drug developed damage to their peripheral nerves (P. Kaufmann *et al. Neurology* **66**, 324–330; 2006). Without a control group, they point out, it will be impossible to tell whether any improvement in the patients' condition is

“It's destroying efforts to do this right. Any way you look at this, it's a negative development.”

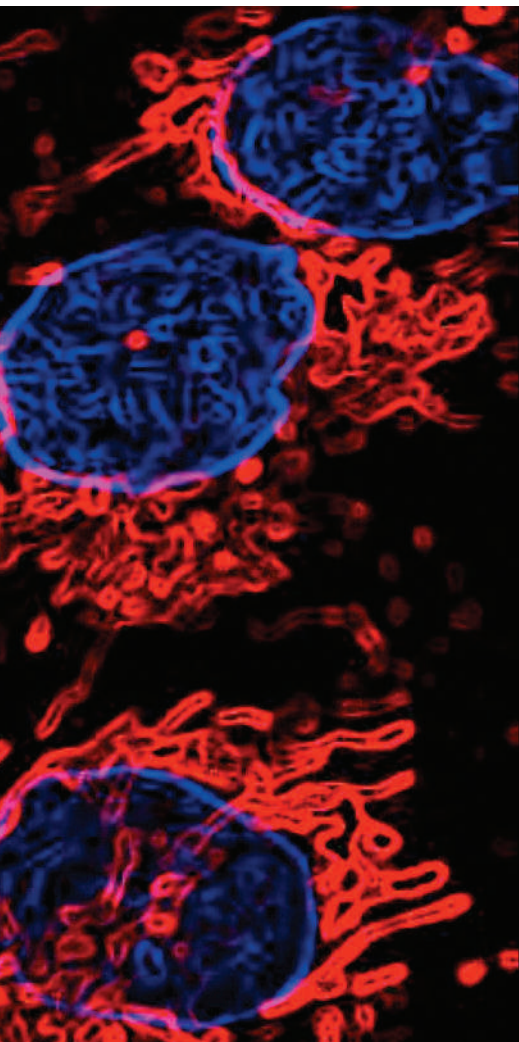


caused by the drug. Patients could also be taking DCA that is not of pharmaceutical grade and might contain harmful impurities.

Michelakis says the patients could end up undermining efforts to do a controlled clinical trial if, for example, some develop harmful side effects and the drug earns a bad reputation. “It's destroying efforts to do this right,” he says. “Any way you look at this, it's a negative development.” An FDA spokesperson told *Nature* that the agency is looking into the matter.

The battle between dying patients who want immediate access to unapproved drugs and doctors who urge trials and caution is a perennial one. Some patients argue that they cannot wait for trials and should have the right to take unapproved drugs, regardless of the risks.

But there are arguments against this. An estimated 95% of cancer drugs that enter clinical trials do not get approval, many because they are ineffective or unsafe, so patients risk shortening their life or making their last days more uncomfortable. “They say what do I have to lose? The truth of the matter is, you have the



E. MICHELAKIS

Reactivating mitochondria seems to trigger cancer cells to commit suicide.

rest of your life to lose," says George Annas, an expert in bioethics at Boston University School of Public Health.

And if patients can access DCA — or other unapproved drugs — there is no incentive for them to enter a clinical trial. So in terms of public health, ethicists argue, more people will be helped if access to unapproved drugs is restricted and proper trials performed.

Peter Jacobsen, an expert in ethics, health and law at the University of Michigan in Ann Arbor, doubts whether any good can come of the patients' efforts. They are so desperate to see results, he says, that there is no way they can report unbiased results and no mechanism to ensure the reports are accurate. "I don't trust the data," he says. "It's hard enough to rely on them in clinical trials, let alone this."

Helen Pearson

BANGALORE

A biotechnology company in Bangalore has launched a project to build a genetic, genealogical and medical database of India's 69,000-strong Parsi community. Parsis are thought to be particularly genetically homogenous, so researchers hope to use the data to identify genes involved in disease and develop new treatments and diagnostics — in a similar way to a national genetic database already set up in Iceland.

Fleeing persecution by invading Arabs, the Parsis arrived in India from Persia 1,200 years ago, around the same time that a few hundred Vikings arrived in Iceland. They speak a unique Indian dialect and their religion forbids marriage outside the community, so they have remained relatively inbred.

"I realized four years ago that I was sitting on a goldmine or a powder keg," says Viloo Morawala Patell, a Parsi and molecular biologist who founded the biotech company Avesthagen in 1998. Patell says she refers to a powder keg because of the fear that Parsis will soon become extinct because of inbreeding (the population has shrunk to its present size from a high of 115,000 in 1941). But like Iceland, the project could also present a commercial opportunity. In 1999, Iceland's government licensed the genetic information from the national database to deCODE Genetics, a biomedical company that hopes to develop new cures and diagnostic kits.

Hoping to do the same for the Parsis, Patell launched the 1.25-billion-rupee (US\$30-million) project on 21 March.

She plans to create a database that holds genetic data, together with genealogical and medical histories, of at least 50,000 Parsis in five years and eventually of the entire community. Parsis already keep extensive genealogical data, says Patell, and it should be possible to reconstruct their medical records from clinics and hospitals in Mumbai, where more than 90% of Parsis live. The company's genomics and bioinformatics facilities have been upgraded so they can sequence selected markers in



The Parsi community has a unique gene pool.

the participants' DNA.

Avesthagen will provide the initial capital and plans to raise the rest from prosperous sections of the Parsi community and other sources. Patell declines to name potential sources, although Avesthagen already has several international collaborations, including with the French company bioMérieux for the development of diagnostic chips, US company Sequenom for the validation of genetic markers for cancers, and European drug giants AstraZeneca and Novartis.

Patell says that she has been discussing the project with prominent members of the Parsi community for four years, making the case that the information gained will directly benefit the health of the dwindling population. A council

of eminent Parsi figures will manage the project, deciding on matters such as who will own the database and who can access the data.

Vasanth Muthuswamy, deputy chief of the Indian Council of Medical Research (ICMR), says that the government has no problem with the commercialization of the community's genetic information as long as the ICMR's biobanking guidelines are followed. Among other things, these require informed consent and

data confidentiality — issues that overshadowed Iceland's plans to establish a database for the health sector. "After Iceland, this has become a global issue," Muthuswamy told *Nature*. "We have to see what kind of agreement the Parsi community signs with Avesthagen."

Patell says that the genome analysis will focus on genetic defects common in Parsis, such as a deficiency of G6PD (glucose-6-phosphate dehydrogenase) — an enzyme that triggers the sudden destruction of red blood cells. Reduced fertility, ovarian disease, Parkinson's, Alzheimer's and breast cancer are other likely areas of study.

But not everyone is convinced that the project will work. Studies suggest that there has been some mixing of Parsi genes with those of other Indians. "It is a bit of a gamble," says Indraneel Mittra, director of the Bhopal Memorial Hospital and Research Centre in India. "My feeling is that the Parsis are not as pure as Icelanders, and in any case I do not know how fruitful the Icelandic study has been."

K. S. Jayaraman



HOT TOPIC: HOMEOPATHY
Should alternative therapies be the subject of science degrees? Join the debate.
<http://tinyurl.com/3as3ea>

I. MUKHERJEE/AFP/GETTY

ROBOT NEWS

Star car

John Jostins, designer of *Star Wars* icon R2-D2, has created a hydrogen-powered car. Called the Microcab, it will presumably be slightly faster than the trundling droid.

SCORECARD



Bill Gates's credentials

The world's richest college dropout will finally claim his degree from Harvard — albeit an honorary one — when he speaks at the university's commencement ceremony in June.



Cell biologists' aches

Repetitive strain injury in the biology lab could be a thing of the past with the advent of the Shake 'N Plate, an ergonomic invention that reduces the strain caused by endless hours of bacterial culture plating.

ZOO NEWS

The calamari's off

Researchers in New Zealand are considering microwaving the largest squid ever caught... but not so they can eat it. They hope the treatment would help to thaw the 490-kilogram frozen specimen without it rotting so that they can study it.

Born survivor

Knut, the world's new favourite bear (pictured), has shrugged off a bizarre request by animal activists that he should be killed because keepers at Berlin Zoo raised him by hand — an action that was apparently a "gross violation" of animal-protection laws.

Sources: Times Higher Education Supplement, Network World, Joint Genome Institute, Bloomberg.com, Yahoo news

M. SCHREIBER/AP



Chinese network to start trials of spinal surgery

Earlier this month, around 60 of China's top orthopaedic surgeons and neurosurgeons met at a military hospital in the southwest provincial capital, Kunming. Over three days of discussion and joint operations on two monkeys, the surgeons reached a consensus on how and where incisions should be made to transplant materials in spinal-cord treatment. "It's hard to get a bunch of prima-donna surgeons to agree," says Wise Young, a neuroscientist studying spinal-cord injuries at Rutgers University in Piscataway, New Jersey. "We need to have them roll up their sleeves and do it."

Young, originally from Hong Kong, is preparing a network of surgeons to address a big problem in China: maverick doctors, pushed by growing medical tourism, are increasingly transplanting cells or drugs into injured spines despite having only anecdotal support for their effectiveness. There is also little rigorous follow-up of the patients, so although many procedures are done, the field does not advance. But Chinese local and national governments are increasingly requiring doctors to use clinically proven procedures. "People are starting to demand data," says Young.

Young's network — called China SCINet and based in Hong Kong — aims to provide those data. Its first major trial will test a combination therapy of lithium and stem cells. Starting in 2008, the team will transplant umbilical-cord stem cells to around 400 patients. Half of the patients will also receive lithium, which stimulates the growth of neurons, in the same oral doses as those prescribed for manic depression (L.-W. Yick, K.-F. So, P. T. Cheung and W. Wu *J. Neurotrauma* **21**, 932–943; 2004). The idea is that the stem cells will provide a 'bridge' at the injury site, which new axons can grow on. Twenty centres in the network are already doing an observational study on the patients who will be in the trial, to get a baseline from which to judge improvement from the therapy.

Young also hopes to involve industry. He is negotiating with pharmaceutical companies to provide a third element to add to the mix — drugs known to block the chemicals that inhibit growth of neurons.

Young says that he has two main reasons to work in China. The number of patients living with spinal-cord injuries has increased over

the past decade, which Young attributes to the growth of the automobile market and better care, which keeps patients alive longer. China now has more of these patients than any other country. In addition, it is fast and cheap to run trials there. Large numbers of patients gather in relatively few hospitals, making recruitment easy. "You can get hundreds, or even thousands, of patients at a single centre," says Young. And the cost of surgery and after-care is about US\$20,000 per patient in China — about a fifth of that in the United States.

The combination therapy in the trial will be preceded by preliminary studies on lithium and umbilical-cord transplants separately, the first of which will begin next month. Together, the trials will cost just US\$12 million.

The 2008 trial will be the first controlled study for spinal-cord injury in a country where doctors have increasingly been transplanting all kinds of cells. The most famous example is Hongyun Huang from Chaoyang Hospital in Beijing, who has performed hundreds of procedures in China after working with Young as a postdoctoral student at Rutgers (see *Nature* **437**, 810–811; 2005 and **440**, 850–851; 2006).

These studies tend to claim that the treatments are effective, often on the basis of patient testimony, without peer review or any rigorous follow-up. Huang is now carrying out

"It's hard to get a bunch of prima-donna surgeons to agree."



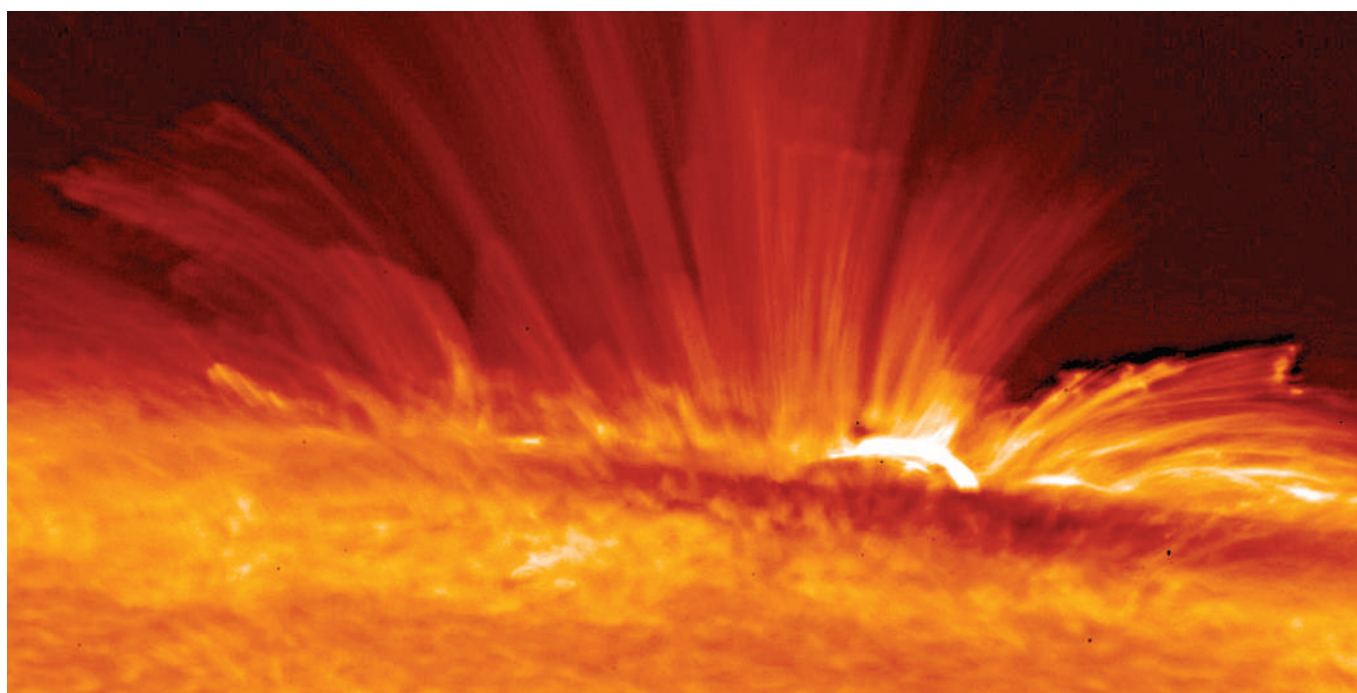
Spinal tap: some techniques lack solid data.

D. RIESS/THE IMAGEBANK/GETTY


AMERICAN CHEMICAL SOCIETY

Get diary reports from the meeting on our newsblog.
<http://blogs.nature.com/news>

H. JAXA/NASA



SNAPSHOT

The best images of the Sun yet obtained are now streaming in — and they are both illuminating and baffling for scientists.

The Hinode spacecraft, an international mission led by the Japanese space agency JAXA, was launched in September 2006, and is now circling Earth in an orbit that gives it a good view of the Sun. The latest data to be sent back from its three main instruments show our star as a dynamic, turbulent, mysterious hothouse of magnetic activity.

Researchers have long been puzzled by the observation

that the Sun's corona — the atmosphere of gas that extends out from the Sun at a temperature of millions of degrees Celsius — is about 100 times hotter than its surface. One possible explanation is that magnetic fields projecting from the Sun twist about in the turbulent environment until they eventually snap, releasing energy as heat. The data being returned by Hinode's X-Ray Telescope add weight to this theory.

"We can see the corona structures twisting and shearing," says Leon Golub of the Harvard-Smithsonian Center

for Astrophysics in Cambridge, Massachusetts. "There are things that look exactly as predicted," he says.

But some of the observations are proving more confusing. Astrophysicists have been stunned by a video image of a magnetic arc collapsing in on itself. "We are used to seeing magnetic fields emerging outwards," says Golub. But this one went in the other direction. "Nobody can explain how this happens," Golub says.

Golub expects that this, too, may be related to the corona's high temperature, but says

that as yet there is no theory to predict this kind of activity.

"Processes that we see on the Sun are not intuitive and not easily explained," says Alan Title of the Lockheed Martin Advanced Technology Center in Palo Alto, California. Title works on Hinode's third instrument, the Solar Optical Telescope.

And Hinode is likely to provide yet more surprises. "Almost every day we see data coming down and we don't know what they mean," says Golub. ■

▶ To see the video, go to www.nature.com/news/2007/070319/full/070319-11.html

trials with fetal Schwann cells, fetal olfactory cells and a combination of the two, which he says have a strong scientific basis. But his critics remain sceptical. Huang has "had a thousand or so chances so far to acquire scientific data", says James Guest, a neuroscientist with the Miami Project, a huge spinal-cord-injury research centre at the University of Miami in Florida, referring to the number of patients Huang has treated.

Guest says he hopes that Young's network will "standardize spinal-cord injury care within China", adding that "a success of this venture could do a lot to establish China as a credible place to do multicentre trials".

Young's reputation, including his work with one of the first successful treatments for spinal-cord injury, methylprednisolone, should set the project in good stead. "There is no doubt that he can run a clinical trial," says John Steeves, director of the International Collaboration On Repair Discoveries at the University of British Columbia in Vancouver.

But there are concerns that the procedure and follow-up must be high level and consistent across the trial. "Having a lot of patients does not necessarily mean you can test them all in a controlled, valid manner," says Steeves. And Guest worries whether a cultural aversion to admitting problems might hamper data

sharing: "Will the adverse events really be disclosed?" he asks. Some spinal-cord clinicians also suggest that more animal data should be collected for lithium and umbilical cells before moving to humans.

Young says he knows that the difficulty will now be in the trial's execution. But he argues that even establishing a network in a country where harsh competition makes researchers and doctors hesitant to collaborate is a huge achievement: "They used to say, 'no way, I'm not letting Dr so-and-so come into my hospital'. But now they are pooling resources and setting up joint teams." ■

David Cyranoski

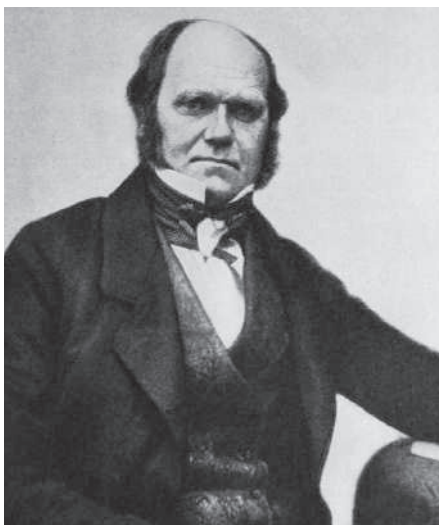
Darwin and the 20-year publication gap

BETTMANN/CORBIS

Did Darwin delay publishing his theory of evolution by natural selection because he feared an outcry from the establishment? This has been a popular belief, and has been stoked by the fact that although Darwin began formulating the theory in 1837, he did not publish *On the Origin of Species* until 1859.

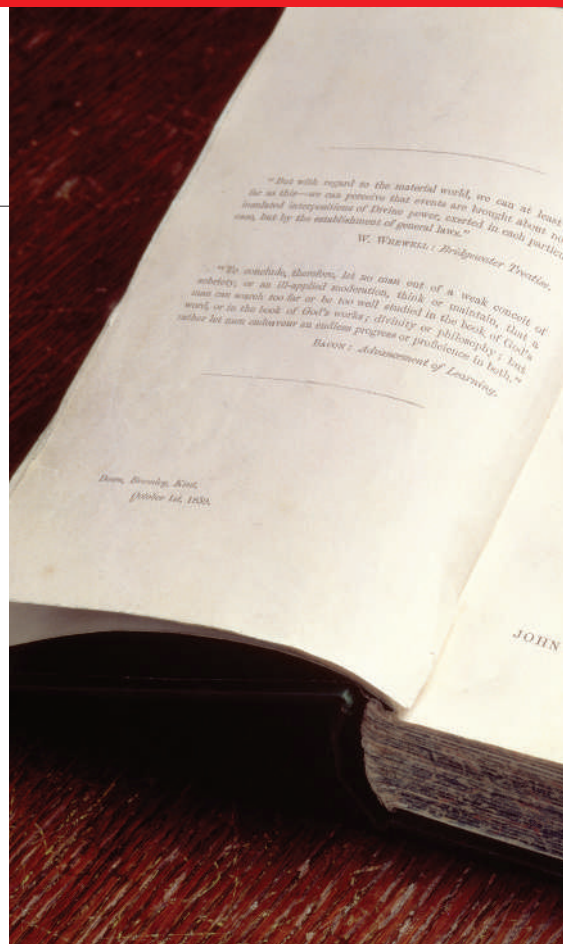
Now John van Wyhe, a science historian at the University of Cambridge, UK, says that after a painstaking trawl through the letters, notes and books written by, to or about Darwin, he can rule out the idea once and for all. But van Wyhe's work has irritated several prominent historians, who argue that he has gone too far in downplaying ideas about Darwin's reluctance to publish. "Portraying Darwin as having no feelings or reactions to the outside world warps the biographical picture," says David Kohn, editor of the Darwin Digital Library of Evolution.

Darwin scholars have long pondered over the time it took to publish *Origin of Species*. According to van Wyhe, the idea that Darwin delayed because he was scared to publish a theory that so obviously contradicted religious beliefs about creation has dominated both popular and scholarly accounts of the man for decades.



But in a study published this week in *Notes and Records of the Royal Society* (doi:10.1098/rsnr.2006.0171; 2007), van Wyhe concludes that there is no direct evidence for the idea, and that it is simply a myth that has passed down the generations without question.

To carry out his study, Van Wyhe searched for the word "delay" in primary and secondary



sources covering the period in which Darwin was working on *Origin of Species*. He says Darwin and those who knew him never unambiguously referred to a delay in publishing, or gave any explanation for the 20-year 'gap'. Indeed, in all the texts on Darwin, he says, the earliest reference to a delay appears in the 1940s. Only in a 1948 popular book, *Darwin: Before and*

Q&A

A vision for Italy's role in space

Giovanni Bignami, former scientific director of the Italian Space Agency (ASI) and former chair of the European Space Agency's (ESA's) space science advisory committee, was last week nominated as the ASI's next president. *Nature* asks him about his plans at the ASI, Europe's prospects in space and the art of Galileo Galilei.

What are Italy's main achievements in space?

The most recent success was the 1996–2002 Italian–Dutch BeppoSax mission dedicated to γ -ray bursts. A new γ -ray mission, AGILE, will be launched soon.

And its weaknesses?

New missions have been delayed, and new concepts crushed, by poor administration hindering the flow of contracts to industry and the scientific community.

What are your plans at the ASI?

We need to have a longer vision. Italy hasn't flown a space mission for more than a decade. I want to bring the ASI back to flying satellite missions, both in science and in a variety of applications.

How can Italy live up to its legacy in space?

Besides hard work and efficiency, this will require balancing a profound European commitment with exploiting the resources

of our scientific community in conjunction with industry.

European space research is funded by national agencies such as the ASI, directly and through ESA. Is this mix an obstacle to Europe's competitiveness in space?

On the contrary, this is a gift to European nations. Out of the national programmes comes the greater breadth of the European programmes. United we stand, divided we fall.

In its 'Cosmic Vision 2015–2025', ESA has proposed a set of priorities for European space research. Which of

the proposed missions do you consider most important?

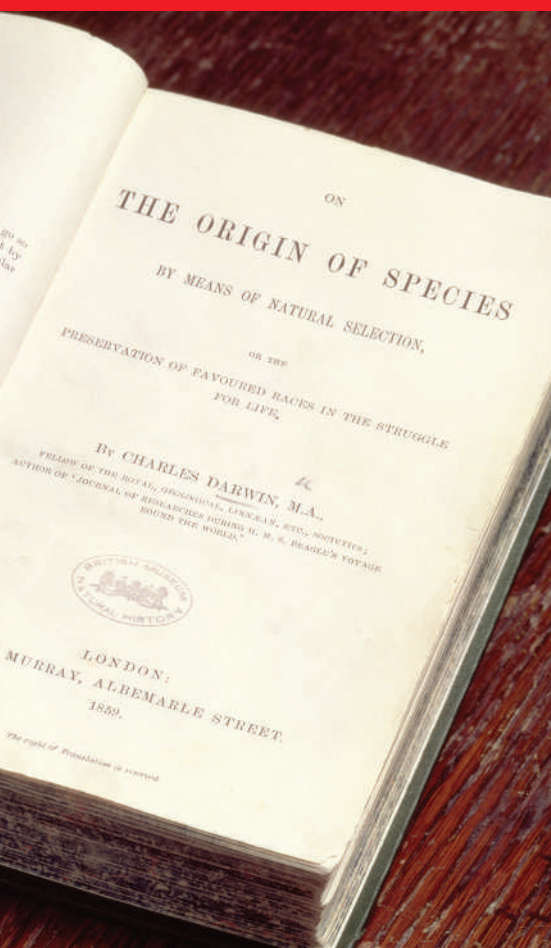
It is most important that Europe now has a vision for its future in space science, from planets to the origin of the Universe. I do not have a scientific preference. That decision will be taken by Europe's scientists. A call for proposals has already hit the streets.

Should Europe join the new 'race to the Moon'?

Cum grano salis [with a grain of salt].

What about Mars?

I am a firm supporter of Aurora, ESA's planetary exploration programme.



After, in which Robert Clark describes how Darwin was made ill by “an uncertainty that he allowed to haunt him for twenty years”, do you see all the elements of the modern story, says van Wyhe.

The historian further argues that in letters to friends, family and colleagues, Darwin continually communicated his belief that species

It has been thought that Charles Darwin (left) delayed publication of his theory of evolution because of concerns over the public's reaction to it.

could change, and that this is inconsistent with the notion that he was keeping his heretical ideas secret during this period. He even paid copiers on at least two occasions to produce early drafts of his species theory.

By documenting exactly what he was doing during the ‘gap years’, van Wyhe makes the case that Darwin just didn’t get down to writing *Origin of Species* until he had completed other work in hand, including an eight-year study of barnacles. He was determined to build a formidable mass of documentation supporting his theory and to solve major stumbling blocks, such as that posed by non-reproductive castes of social insects. This, together with a busy personal life but poor health, filled the years. In other words, Darwin did not postpone publication; he just didn’t publish until he was ready. “In my view, this settles the question once and for all,” says van Wyhe.

Janet Browne, a science historian at Harvard University in Cambridge, Massachusetts, reckons that van Wyhe’s study is a valuable piece of work. “It may not shake the world, but it’s an important point to make,” she says.

But several Darwin scholars are not convinced. Kohn and others agree that the way in



HOW THE GREEKS COULD HEAR PLAYS FROM THE BACK ROW

An ancient theatre filters out background noise.

www.nature.com/news

which cultural and social pressures influenced Darwin’s decisions may have been overplayed, particularly in the public arena, with less attention being paid to the involved process of scientific discovery. But the consensus in the field is likely to remain that a multitude of factors underpinned Darwin’s delay.

Kohn points out that searching for explicit references to a “delay” is a simplistic approach to the problem, and that other factors should be considered. For example, Darwin often criticized religion in his notebooks, which suggests that he would have been aware of the probable implications of his theory for religion. It is hard to see how the absence of specific references to

a delay rules out any influence of cultural and societal factors on Darwin’s decisions, agrees David Quammen, author of *The Reluctant Mr Darwin*.

Kohn also points out that in Darwin’s later publication *The Descent of Man*, which applied the theory of evolution to humans, Darwin specifically states in the opening lines that he delayed publishing this tome until he was convinced that the climate was right. It seems likely, therefore, that he would have been aware of the controversy his theories would cause from the outset, and probably avoided discussing humans in *Origin of Species* for this reason.

Lucy Odling-Smee



Bignami: wants Italy to return to flying satellite missions.

Its immediate aim is the robotic exploration of Mars. This is a great opportunity for Europe. Aurora also considers manned missions to Mars, albeit in the distant future.

Space exploration requires strong industrial partners.

Is the balance in Europe between commercial interests and basic research needs in order?

All space missions are being designed, built and flown by industry. European industry needs political support to meet the challenge that is coming from all over the world, in the fields of launchers, satellite production and ground infrastructure. Basic research and commercial interests both represent challenges that can spur European industry to take a leading role in space.

Should Europe reach out for Russia as a partner in space?

Russia is already a partner. Imagine a world where Russia joins ESA. This might look difficult now, but it is potentially very interesting.

And NASA?

Since Italy’s very first steps in space more than 40 years ago, it has been collaborating with NASA. I received my space education in the United States, and I will certainly try to increase the quality of the ASI’s collaboration with NASA.

Which key questions do you think space scientists will answer in the next two decades?

Three things spring to mind: the nature and origin of dark matter, the observation of gravitational waves from the Big Bang, and discovering a new ‘Earth’. All of them require bold, innovative space technologies, which are already at work in precursor missions such as ESA’s Gaia, Planck, Herschel and LISA Pathfinder and the NASA/ESA

James Webb Space Telescope. Finding a new Earth, possibly with evidence for life on it, will require the development of new technologies, such as space infrared interferometry.

Galileo Galilei has written some very worldly poems, the longest of which you have translated into English. What has the great scientist achieved in art?

Galileo’s achievements in science were born of his post-Renaissance artistic education. He was a skilled draftsman, musician, and of course had a way with words. The Italian novelist Italo Calvino considered him the greatest writer in Italian literature. I remain fascinated by Galileo’s genius.

Interview by Quirin Schiermeier.

Congress requests bubble-fusion reports

The US Congress has asked Purdue University for reports of its inquiries into allegations against nuclear engineer Rusi Taleyarkhan.

The request is one of the first actions from the House subcommittee on Investigations and Oversight, which was re-established in January 2007 when the Democrats took control of the US House of Representatives after twelve years of Republican majority. The move suggests that Congress is preparing to take a more active role in investigating the way that publicly funded research is policed.

Taleyarkhan has published several controversial papers claiming that he can trigger the energy-releasing process of fusion by passing ultrasound through deuterated liquids — a phenomenon known as bubble fusion.

In February, Purdue issued a statement saying that Taleyarkhan had been cleared of internal allegations of research misconduct. But critics have questioned how the finding was reached, and asked why the university's administration failed to say whether the fraud allegations it had received were considered (see *Nature* **445**, 690–691; 2007).

Now, Representative Brad Miller (Democrat, North Carolina), the chairman of the oversight subcommittee, is seeking clarification. In a letter sent to Purdue's president Martin Jischke last week, Miller asked that two copies of the university's internal inquiry reports on the allegations be delivered to the subcommittee by 30 March. He says that Congress expects universities that receive federal funds to investigate when questions are raised about the integrity of research. "It was about whether they were policing the research correctly," he told *Nature*.

Purdue, which is based in West Lafayette, Indiana, has held two inquiries into Taleyarkhan's research. The first, which followed a report on questions about Taleyarkhan's work in *Nature* (see doi:10.1038/news060306-1; 2006), was announced by the university's provost Sally Mason in March 2006, and finished in June 2006. Its findings were kept confidential, but the subcommittee believes that it recommended a full-scale investigation

into Taleyarkhan that never took place. A second inquiry cleared Taleyarkhan in February this year, but it is unclear why the two inquiries reached different conclusions. A congressional staff member who is familiar with the subcommittee's interest says that it would be a concern if the university had found procedural reasons to restrict the allegations or evidence that were available to an inquiry. "The university intends to comply fully with the committee's request.

In doing so, we must attend to certain legal obligations under our own policy," Purdue has said in a statement.

"It is very rare for Congress to intervene in such matters," says Mark Frankel, director of the Scientific Freedom, Responsibility and Law Program at the American Association for the Advancement of Science in Washington DC. Between 1981 and 1995, when it was disbanded by the Republicans, the subcommittee has taken an interest in cases of alleged or actual research misconduct. These

included the highly publicized and controversial hearings on allegations against Thereza Imanishi-Kari, a biologist working at Massachusetts Institute of Technology in Cambridge with the Nobel laureate David Baltimore in the late 1980s. Imanishi-Kari was later exonerated. Since then, Congress has mostly deferred to the agencies that fund research to oversee institutional processes. Frankel is not persuaded that Congress now needs to take a more active approach. Miller emphasizes that the current focus is on learning more about how Purdue handled the allegations rather than assessing the research itself.

Taleyarkhan's research has been funded by the State of Indiana, the Department of Energy through Oak Ridge National Laboratory in Tennessee, where he previously worked, and the Defense Advanced Research Projects Agency (DARPA). The inspector-general of the Office of Naval Research, which administers some DARPA grants, is conducting an inquiry into allegations against bubble-fusion research concurrent with the congressional probe. ■

Eugenie Samuel Reich

See Correspondence, page 492.



Congress has intervened in Purdue's inquiries about Rusi Taleyarkhan.

L. FRENEY/US DEPT ENERGY

FDA proposes tighter rules on conflicts of interest

After a flurry of criticism for perceived conflicts of interest, the US Food and Drug Administration (FDA) is planning to significantly tighten the rules that govern when financial conflicts should exclude experts from serving on its external advisory committees. The committees are important because the agency nearly always follows their advice on approving drugs and devices and on emerging safety issues.

In its draft policy released on 21 March, the FDA said that individuals will generally be excluded from participating on advisory committees if they have financial interests exceeding \$50,000 in the issue being discussed. Experts with financial interests of less than \$50,000 might be allowed to participate in discussions without voting, the agency said. The draft proposal is open for public comment until 21 May.

Flu study faces shake-up over industry funding

Japan's health ministry is expected to remove two researchers from its eight-member study group on influenza, because their research in other areas was partly funded by a Japanese distributor of the flu drug Tamiflu.

The study of some 10,000 children will investigate the possible side effects of Tamiflu (oseltamivir) as part of its remit.

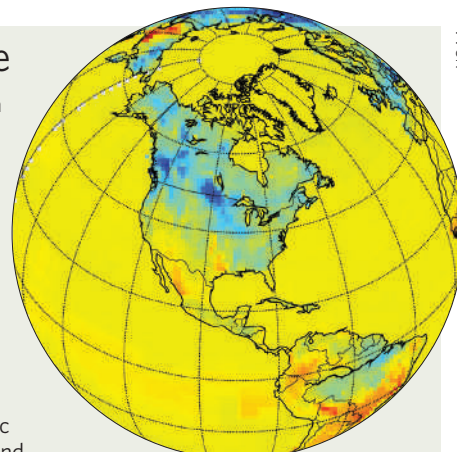
The health ministry last week warned doctors not to give Tamiflu to teenagers, after a number of new reports linked the drug to psychiatric effects such as suicidal tendencies among the age group (see *Nature* doi:10.1038/446358a; 2007). Swiss drug firm Roche, which makes Tamiflu, says that no such causal link has been established, and the World Health Organization says Tamiflu remains the drug of choice for treating people infected with the bird flu virus H5N1.

Shunpei Yokota of Yokohama City University, the study group's leader, and Tsuneo Morishima of Okayama

On the track of carbon dioxide

It's still pretty raw, but an online tool to track carbon dioxide emissions is being set up by the US government. The new CarbonTracker website (<http://carbontracker.noaa.gov>) is meant to provide a public-friendly view of greenhouse-gas emissions from various sources around the world. The snapshot on the right shows CO₂ uptake for a week in July 2005 — dark blue represents the strongest CO₂ sinks.

So far, though, the data are sparse. Only 60 carbon monitoring sites worldwide are included, with 20 of them in the United States. Project scientists at the National Oceanic and Atmospheric Administration say they hope to add further sites and eventually develop CarbonTracker into a resource for policy-makers and scientists.



NOAA

University have received some ¥12 million (US\$100,000) between them from Tokyo-based Chugai Pharmaceutical, which distributes products for Roche. Health minister Hakuo Yanagisawa told a parliamentary committee on 23 March that the researchers ought to be excluded from the flu study.

UK league table revisits problems caused by drugs

Alcohol and tobacco are better than heroin but worse than cannabis, according to a UK ranking of the dangers of recreational drugs (D. Nutt *et al. Lancet* 369, 1047–1053; 2007).

The new system is an attempt to provide a scientific — if still simplistic — way to compare the social and health tolls taken by recreational drugs. Current British drug laws are shaped by political prejudice as much as by the actual threats posed by the substances, says team member David Nutt of the University of Bristol.

His team asked experts — including psychiatrists specializing in addiction, the police, forensic experts and doctors — to give up to 20 drugs a score in nine subcategories within the larger categories of physical harm, dependence and social harm.

The result? Heroin and cocaine were ranked as the most dangerous, reflecting their status as class A drugs — the most harmful tier of Britain's three-category system. But ecstasy, another class A drug, finished eighteenth in their list — below commercial solvents and anabolic steroids.

Budget gives Canadian science a cash injection

Canada's science infrastructure got a boost last week with the release of the country's budget plan for 2007.

The two main science granting agencies — the Natural Sciences and Engineering Research Council and the Canadian

Institutes of Health Research — will each get an extra Can\$37 million (US\$32 million), raising their combined budgets to roughly Can\$1.4 billion. A further Can\$510 million is allocated to modernize the research infrastructure at universities and other research institutions. And Genome Canada will receive an extra Can\$100 million for grants and regional genome centres.

Another winner, to the tune of Can\$50 million, is the Perimeter Institute for Theoretical Physics in Waterloo, Ontario. Seven other targeted institutes, including some focusing on neurology and sustainable energy, will share an extra Can\$105 million.

SpaceX rocket burns up after missing orbit

The privately financed Falcon 1 launch vehicle reached an altitude of 300 kilometres last week before developing problems and burning up on re-entry into Earth's atmosphere. But space-industry experts say the test should be considered a success.

Falcon 1 was developed by the California-based company SpaceX as a rapid way of getting satellites into orbit. Space launches usually take months of planning, but industry observers say Falcon 1 should be turned around quickly because SpaceX has used a simple design that the firm says will eventually be operated by as few as 15 staff.

SpaceX is investigating why the Falcon 1 vehicle developed a rolling motion during the flight, which caused its engines to shut down, about 6 minutes after launching from the Marshall Islands on 20 March. The company is still aiming for another launch later this year to put a US Department of Defense satellite into orbit.

Correction

Our News in Brief story 'Upstart forum created for German conferences' (*Nature* 446, 360; 2007) contained an incorrect reference to an earlier story on the topic. The correct reference is *Nature* 433, 446 (2005).



The Japanese government wants to investigate the possible side effects of flu drug Tamiflu.

BUSINESS

Biofuels bandwagon hits a rut

As politicians propose higher biofuel targets, soaring maize prices in the United States are putting new investment in ethanol production on hold. **Lucy Odling-Smee** reports.

The scramble by investors in the United States to get into biofuels has caused a surge in production of the nation's main biofuel — corn-based ethanol — and pushed up the price of corn (maize). Theoretical concerns about competing demands for fuel and food are now economic reality.

Livestock farmers who use corn for animal feed are feeling the pinch of prices that have doubled since last year. And ethanol investors are waiting to see whether farmers can increase corn production in the coming season and pull costs back down.

"The question is, how quickly can both economic systems adjust?" asks Steve Bantz, a senior engineer with the clean-vehicles programme at the Union of Concerned Scientists (UCS), a liberal advocacy group in Washington DC.

The soaring price of corn is arguably unsurprising, given that ethanol-production capacity has nearly quadrupled since 2000, to 21 billion litres (5.6 billion gallons). It is expected to double again in the near future if plans for new processing plants and the expansion of existing ones are followed through. The US ethanol industry is already expected to use up 20% of the country's corn crop this year, compared with 5% or less before 2000.

The ethanol boom stems from converging economic and political forces. The price of oil has been relatively high in recent years, and energy security and independence have emerged as a political issue. As part of a push for greater independence, a law enacted by Congress in 2005 requires 28 billion litres (7.5 billion gallons) of the nation's fuel to come from ethanol and biodiesel by 2012. On 4 January, five Democratic senators introduced the Biofuels Security Act of 2007, which would raise this to 227 billion litres.

A 51-cent tax credit currently goes to buyers for every gallon of ethanol they mix with petrol. The industry is also protected from foreign competition by a hefty export tariff of 54 cents per gallon on imported ethanol.

Renewable-energy analysts say, however, that the most important driver of the surge in ethanol production has been its use as a substitute for methyl-*t*-butyl ether (MTBE) — an additive used to make petrol meet emissions requirements. Scores of states have recently



The high price of maize is starting to hit livestock farmers.

banned MTBE after reports that it poses a health risk. Phasing it out has left a 7.5-billion-litre hole for ethanol to fill.

All these factors have lured investors, including major agribusinesses such as Archer Daniels Midland (ADM), based in Decatur, Illinois, and Cargill, headquartered in Minneapolis, Minnesota. ADM alone accounts for one-fifth of US ethanol production — and the company has plans to expand that by more than 25%. More than 100 other companies, many privately held, have also come on board.

However, for companies that haven't yet put their money on ethanol, investments that looked rosy several years ago are beginning to lose their shine. Corn prices that stand at \$162 per tonne (\$4.10 a bushel), up from \$79 last year, aren't the only deterrent: costs of building materials are rising, and qualified engineers and technicians are scarce.

"The bloom is off the rose," says Ben Lieberman, a policy analyst at the Heritage Foundation, a conservative think tank in Washington DC.

Brian Jennings, executive vice-president of an ethanol-advocacy group, the American Coalition for Ethanol, in Sioux Falls, South Dakota, says that in the past two months he has been contacted by a dozen companies that have decided not to take their projects forward because of market conditions.

Ethanol-advocacy groups are confident that the market for corn will recalibrate, however, with farmers turning to other feed for their livestock, and planting corn on land not used for the crop before. "US farmers will probably plant one of the largest corn crops on record this year," predicts Jennings.

This prospect makes environmentalists worry that the biofuels industry will stress not only the food economy but also the environment. Using more marginal land could mean more fertilizers, more irrigation and more pesticides, says Bantz. The real problem, he adds, is the rate at which the ethanol industry has taken off — before a proper analysis to quantify the advantages and disadvantages, in terms of energy obtained and emissions released, of biofuels made from different starting materials.

Bantz and others contend that, for ethanol to become a serious player in helping the United States reduce its reliance on petrol, a slower pace may be crucial — in part to allow technological developments such as genetically modified corn that gives a higher ethanol yield or the scaling up of ethanol production from non-food sources such as switchgrass or sawdust.

According to Barbara Bramble of the Washington-based National Wildlife Federation, the United States may have something to learn from Europe. There, she says, the industry is developing slowly enough to allow appropriate adjustments in land use and technology to be made.

"US farmers will probably plant one of the largest corn crops on record this year."
— Brian Jennings



The hard copy

Researchers have found certain stem-cell studies notoriously difficult to replicate. **Erika Check** finds out why, and whether it is slowing down the field.

Eight years ago, a team of scientists based in Canada and Italy published an astonishing paper in *Science*. They started with mouse neural stem cells — cells destined to give rise to brain tissue. At the time, scientific dogma held that cells such as these, which are already moving towards one destiny, cannot switch paths and generate other types of cell.

The *Science* paper challenged that view. The team transplanted the stem cells into mice whose bone marrow had been wiped out. Lo and behold, a miraculous transformation seemed to occur: the stem cells changed their fate and gave rise to the haematopoietic cells that normally reside in bone marrow and generate blood and immune cells. The paper was provocatively titled ‘Turning brain into blood’¹. It was part of a wave of studies reporting a fate-switching phenomenon that some termed ‘transdifferentiation’, and that offered a possible way to grow replacement tissues without destroying embryos for stem cells.

It took a separate group of scientists more than two and a half years of painstaking work to show that the *Science* paper wasn’t as exciting as it had first seemed. This group tried to replicate the findings by transplanting neural stem cells into each of 128 mice whose bone marrow had also been killed. But after exhaustive analysis, they never saw these stem cells

generate haematopoietic cells. They concluded that the cells may rarely switch fates, but that this occurs only because of genetic changes that accumulate after long periods growing in a Petri dish². The authors of the *Science* paper disputed this conclusion, and there is still no consensus on whether this phenomenon can ever be useful in medical practice.

Reputation at stake

The brain-to-blood debate highlights a more pervasive problem in the adult stem-cell field: that many teams struggle to reproduce others’ seemingly promising results. Replication is a crucial and arduous part of the scientific process³, and it is one that has been especially problematic in this area because of restrictions surrounding the use of stem cells, inexperienced researchers and technical difficulties. Many scientists feel that these problems have slowed progress and harmed the field’s reputation. “Overall damage to the field has been enormous,” says stem-cell biologist Naohiro Terada of the University of Florida in Gainesville. “If we keep producing hype, no one will trust stem-cell researchers.”

The issue of replication was most recently thrust into the spotlight because of renewed attention on a 2002 *Nature* paper⁴ by Catherine Verfaillie of the University of Minnesota, Minneapolis, and her colleagues. After

culturing mouse bone-marrow cells for months, the researchers reported that they could extract an exceptional population of cells they termed multipotent adult progenitor cells, or MAPCs.

When they injected these cells into developing mouse embryos, and studied the chimaeric baby mice that were born from them, the MAPCs seemed to contribute to all the major cell types of the body, including brain, heart, bone marrow, skin, blood and lung. This and other experiments raised the possibility that MAPCs could be used therapeutically in organ regeneration and repair. The finding created a buzz, because no other adult stem cell had been found to generate such a variety of different cell types — a range almost equivalent to that produced by embryonic stem cells.

Verfaillie’s work has since proven exceedingly difficult to replicate, although some groups have reproduced certain parts. Earlier this year, after spending several years learning to work with MAPCs, Scott Dylla, a former postdoctoral fellow in the lab of Stanford University biologist Irving Weissman, was able to use MAPCs to make blood-forming haematopoietic stem cells in mice⁵. But although many groups have tried, none has managed to repeat the key aspect of Verfaillie’s paper — injecting MAPCs into an embryo to create all the major cell types of the body. “I have not seen any convincing data showing that anyone has repeated

the chimaera experiment, so I don't think this part of it is true," says Rudolf Jaenisch of the Whitehead Institute in Cambridge, Massachusetts, whose lab tried and failed to reproduce the work.

Restricted access

Stuart Orkin of Harvard Medical School in Boston, Massachusetts, requested MAPCs from Verfaillie's lab a few months after her paper was published. He found clauses in the material transfer agreement — the contract that governs use of shared research material — saying that users could not disclose information about the cells to others not working on the project. "We couldn't accept that," says Orkin. More broadly, researchers sometimes have difficulty laying their hands on stem-cell lines and methods because of competition between labs and because these cells could prove commercially valuable and so access to them can be restricted.

Those labs that could negotiate licences for MAPCs ran up against another problem: the cells themselves are very tricky to work with. Two labs told *Nature* that they couldn't keep the MAPCs alive long enough to study them, and so abandoned attempts to replicate Verfaillie's work. Both labs followed Verfaillie's published and unpublished instructions closely.

A large part of the problem is that methodology on how to handle the cells keeps evolving, says Paul Simmons at the University of Texas Health Science Center in Houston and one of those who tried in vain to repeat the work. "There's been a series of moving goal-posts as far as the conditions for replication are concerned," he says. For instance, it has now become clear from Verfaillie's later work that MAPCs grow better in low-oxygen conditions, and that they are best taken from very young mice.

"Methodology is everything, and the devil is in the details," says Simmons, who is also president of the International Society for Stem Cell Research. "There's a real need to have methodologies out there that include all the protocol details." But scientists say they feel forced to skimp on their methods sections so they can cram as much data as possible into high-profile journals with severe page limits. And Verfaillie says that the improvements in culture conditions were discussed at meetings and published.

The circumstances surrounding Verfaillie's paper became even murkier last month when questions about duplicated figures used in her *Nature* paper and another published in

*Experimental Hematology*⁶ prompted the University of Minnesota to convene an inquiry into her study. The inquiry found that some of her procedures were flawed.

Verfaillie has said that the duplicated figures were an honest mistake. And other scientists have not suggested that she committed fraud — on the contrary, Verfaillie, now at the Catholic University of Leuven, Belgium, enjoys a reputation as a meticulous researcher. Verfaillie says that the *Nature* paper discussed several possible explanations for the chimaera results and that its conclusions still stand. But



Researchers have struggled to replicate parts of Catherine Verfaillie's work on mouse embryos.



she admits that the duplication errors in her published work may have contributed to confusion in the field: "We have made mistakes for which I take responsibility, and we have done everything possible to alert the scientific community regarding these mistakes," Verfaillie wrote in an e-mail to *Nature*. The confusion looks set to continue: last week, new questions were raised about duplicated images in other work from Verfaillie's lab.

Lack of experience

Technical problems have scuppered many attempts to replicate stem-cell experiments. The best way to isolate and handle fiddly stem-cell lines is only just being worked out, and by their very nature, stem cells constantly divide and change, making it demanding to extract or maintain precisely the same population of cells in culture.

In 2001, a team led by biologist Diane Krause of Yale University in New Haven, Connecticut, published a high-profile paper in *Cell* claiming that a single bone-marrow cell could give rise to multiple cell types, from gut to lung to skin⁷. But the following year, a second group disagreed, saying they could not obtain such a range of cell types from a bone-marrow cell⁸.

Krause says that although some groups have

replicated aspects of her work, others have not, and that it is important to her to understand why. Probably the main reason is that different labs have used different experimental techniques, she says, so they may have isolated slightly different starting populations of bone-marrow stem cells.

The same year, two groups showed that results such as Krause's might be explained by cell fusion, in which stem cells that seem to adopt new fates were actually merging with other cells^{9,10}. The fusion experiments helped to discredit the idea of transdifferentiation, which has now become a taboo word among most serious stem-cell researchers. Krause says she is performing experiments to clarify how much cell fusion contributed to her results.

Inexperience is another problem in the stem-cell field, which attracts new researchers with its white-hot reputation. This has been a particular issue with the transdifferentiation studies, says cell biologist Sean Morrison of the University of Michigan, Ann Arbor. Some may make honest mistakes because they are new to the studies. Others may be sloppy. "In some cases people have a get-rich-quick mentality and are more interested in publishing high-profile papers than in getting the answers right," he says.

Does any of this really matter? Similar problems crop up in many young fields, in which scientists can struggle to reproduce initially exciting data. Inevitably, some results fall by the wayside if they cannot be repeated.

But the adult stem-cell field is under particular scrutiny because of its medical promise and its potential to bypass embryonic stem-cell research. It takes tremendous time and resources to see whether an experiment can be repeated. The difficulties with replication might partly explain why there is no consensus on the properties of most adult stem-cell lines, or which lines are most medically promising.

"If your research depends critically on the veracity of an observation, it's incumbent upon you to reproduce it — if it's not a solid observation, it becomes a roadblock," Simmons says. Add up enough of these roadblocks, and it is easy to see how a field can get bogged down chasing spurious leads, instead of forging ahead in new directions. ■

"Methodology is everything, and the devil is in the details."
— Paul Simmons

1. Bjornson, C. R. R. *et al. Science* **283**, 534–537 (1999).
2. Morshead, C. M. *et al. Nature Med.* **8**, 268–273 (2002).
3. Giles, J. *Nature* **442**, 344–347 (2006).
4. Jiang, Y. *et al. Nature* **418**, 41–49 (2002).
5. Serafini, M. *et al. J. Exp. Med.* **204**, 129–139 (2007).
6. Jiang, Y. *et al. Exp. Hematol.* **30**, 896–904 (2002).
7. Krause, D. S. *et al. Cell* **105**, 369–377 (2001).
8. Wagers, A. J. *et al. Science* **297**, 2256–2259 (2002).
9. Terada, N. *et al. Nature* **416**, 542–545 (2002).
10. Ying, Q.-L. *et al. Nature* **416**, 545–548 (2002).

A LEAP OF FAITH

How much can geometry and mathematics reveal about paintings? How far should hidden meanings be trusted in art? **Jo Marchant** investigates the latest, and possibly most controversial, interpretation of a Renaissance masterpiece.

The scene is eerily still. In the distance, a half-naked figure is being whipped, watched over by an impassive ruler. In the foreground stand three expressionless men, more richly dressed, apparently unaware of the violence behind them and even of each other. The scene is vivid and lifelike, yet it has a dream-like quality. Nobody speaks. Nobody catches anyone else's eye. No wonder this painting has been described as the pictorial equivalent of silence.

This is *The Flagellation*, painted by Piero della Francesca in fifteenth-century Italy and reproduced in full on the cover of this issue. An accomplished mathematician, Piero is known for his stunning use of perspective (just look at the tiled floor), which has helped make this painting one of the most famous masterpieces of the Renaissance. But that is not its only fascination.

Piero planned his paintings down to the last detail, and this meticulously executed scene contains several mysteries, particularly the identities of the three men on the right. Countless attempts have been made to name them. "The interpretation of *The Flagellation* is one of those *causes célèbres*, like *The Last Supper*," says Martin Kemp, an art historian at Oxford University, UK, who has written on Piero's paintings. "It's in that league as a magnet for theories."

A leading historian of science now believes he has historical evidence that can identify all the mysterious figures at a stroke. David King, director of the Institute for the History of Science in Frankfurt, Germany, says that his interpretation reveals new mathematical features that push our understanding of Piero's geometrical



vision beyond anything thought to have been achieved at the time.

The consensus on the painting is that it is Christ being flagellated, perhaps along with the Church, or the Byzantine Empire, which fell to the Ottoman Turks in 1453. The ruler sitting on the throne of Pontius Pilate and watching over the punishment seems to be the fifteenth-century Byzantine emperor Ioannis VIII, identified by his characteristic red hat. The man in the turban with his back to us has been identified as either King Herod or the Ottoman sultan, Mehmet II. But the identity and purpose of the figures on the right has been the subject of wild speculation.

There is no documentary evidence on who commissioned the painting, why, or even when (though historians think it was late in Piero's career, around 1460). The painter left just one tantalizing clue: according to a report in 1839, an integral frame, now lost, bore the painting's original title, *Convenerunt in unum*, or "They came together in one."

Controversially, King's smoking gun is not a manuscript but a scientific instrument, and its meaning is buried deep within a mind-boggling code. If he is right, the painting can be seen as one of the most ingenious hidden messages of all time. Although some scholars cautiously welcome his ideas, art historians are notably less impressed. King pushes his theory to its limits,

and his bullish claims have angered some.

King thinks the reluctance to accept his work results from a culture clash between mathematical expertise and art history. Kemp, who has a scientific background, acknowledges that when it comes to studying painters such as Piero, art historians could do with a better understanding of mathematics. "The maths isn't that hard," he says. "If you can do Euclid you can do Piero."

Art historians counter that King has been too quick to disregard criteria they have developed to guide legitimate enquiry into such enigmatic artworks. "It's not a case of keeping outsiders out," Kemp agrees. "David King is a major historian of scientific instruments. It is a question of how far his huge expertise is transferable without a good deal of caution."

Material evidence

King's interest in this story began with a fifteenth-century astrolabe made in Vienna. Now superseded by modern instruments, astrolabes were used by Renaissance astronomers for time-telling, navigation and predicting the movements of the heavens. This particular astrolabe is modest, just 11.5 centimetres across,

These enigmatic figures in Piero della Francesca's *The Flagellation* have puzzled art historians for some time.

SOPRINTENDENZA PATR. STORICO, ART. ETNOANTROPOL. MARCHE

but it has an unusual inscription on the back (see opposite).

Roughly translated, the inscription says “Under the protection of the divine Bessarion, said to come from the axis, I arise as the work of Johannes in Rome in 1462.” (The inscription is reproduced at larger size in the graphic overleaf.) The couplet suggests that the astrolabe was a gift from Johannes Regiomontanus, a young astronomer and instrument-maker, to his mentor Bessarion. The gift is dated to 1462, roughly the time that Piero painted *The Flagellation*.

Master and pupil

Johannes (Ioannis) Bessarion was a Greek cardinal who famously switched churches to become a cardinal in Rome, following failed attempts to unify the Eastern and Western Churches in 1439. In Rome, Bessarion campaigned for a crusade to fight off the advancing Ottoman Turks, and when Constantinople, the centre of the Eastern Church, fell to the Turks in 1453, the cardinal was devastated.

A learned scholar, Bessarion brought hundreds of Greek manuscripts to Italy to be translated into Latin, helping to kick-start the Renaissance there. Bessarion met Regiomontanus in Vienna in 1460, and persuaded the youth to come to Rome as his student. King believes that Bessarion at the time had in his possession a famous Byzantine astrolabe made in 1062 with a Greek inscription, which King has also studied, and that Bessarion showed it to Regiomontanus while in Vienna. Before leaving for Rome, Regiomontanus made Bessarion another astrolabe as a gift, inscribed with a personal message.

Flaws in the inscribed couplet have intrigued King for years. The metre is almost — but not quite — perfect. The letters are oddly spaced, with some squeezed together and others stretched apart. And the name ‘Ioannis’ is split over two lines. Regiomontanus was a renowned poet and instrument-maker — so why would he have let pass such imperfections in a gift to his beloved mentor?

These and other loose ends have caused some scholars to brand the astrolabe a fake. King has since described 22 other astrolabes from fifteenth-century Vienna, which he believes validate this one (although not all his critics are convinced).



Berthold Holzschuh deciphered hidden meanings in the inscription on the back of a fifteenth-century astrolabe (below).



None of these other astrolabes has an inscription, however. Early in 2005, King asked a mature student, Berthold Holzschuh, to study the inscription for a seminar at the Frankfurt institute. A wood-construction engineer, Holzschuh is fluent in Greek and Latin, and has a long-standing interest in astrolabes.

He turned up at the seminar beaming. He had spotted names and meanings hidden within the inscription, which explained why the couplet was so oddly arranged.

A date referring to the original Byzantine astrolabe, 1062, can be found in the lower right of the inscription, using the IO from IOANNIS, perhaps explaining why Regiomontanus split that word. Reading down the left-hand side, Holzschuh noticed the phrase SVB CD ANNIS — ‘at 400 years’ — which would refer to the anniversary of the Byzantine astrolabe. And reordering the words in the inscription produced the message: “Under the protection of

Bessarion, I arise in Rome in 1462 as a work of Johannes explaining the rotation of the universe,” which is reminiscent of the Greek inscription on the Byzantine astrolabe.

It is the sort of puzzle that Bessarion would have appreciated, says King, and that the brilliant Regiomontanus was perfectly placed to devise. The mystery of the imperfect couplet thus apparently solved, King and Holzschuh wrote a paper on the topic. But when King went to Holzschuh with the finished manuscript, the engineer had another surprise for him.

In researching Bessarion, Holzschuh discovered that the cardinal had been proposed as the bearded figure in *The Flagellation*, and he found that several more names identified in the inscription also appear in interpretations of the picture. He made an enlarged photocopy of the inscription, the same width as the painting, and laid it underneath (see graphic overleaf). Names in the poem started to line up with the appropriate figures. Could it provide a key to the painting?

King has since extended Holzschuh’s findings into a 300-page book intended for publication this year. He looked for clusters of letters suggesting names that would have been important to Bessarion, and found they fell into eight vertical groupings across the inscription: “We tried other combinations but they didn’t work.” King concluded that the eight vertical groupings correspond to the eight figures in the painting.

Cryptic crossword

For the figures on the left, King finds clusters of letters suggesting Latin names that roughly agree with previously proposed identities. For the man on the throne, King picks out references to Ioannis VIII and Herod, as well as the word SEDES, meaning throne, and suggesting Pontius Pilate. For the man being whipped, he identifies references to Christ and the Church, and for the turbaned figure, names suggesting the Ottoman sultan and Herod again.

For the two figures whipping Christ, King associates the man on the right with Herod, Pontius Pilate and Caesar. But for the man on the left, King sees the letters IVDAEUS — suggesting Judas. This identity has not been taken

E. LESSING/AMG-IMAGES

seriously before, but King says it is supported by the painting itself, which has the figure reaching out and touching Christ: “Judas Iscariot was the disciple close enough to touch Jesus,” he says. Another name that occurs is George of Trebizond, with whom Bessarion had a long-running scholarly feud.

So which identity is correct for each figure? This is where King’s interpretation departs fundamentally from previous attempts. He argues that there is not just one identity intended for each man, but several, explaining why it has been so difficult to assign the figures to any one person. Like the poem, the painting conceals multiple meanings, depending on how it is read.

Once King was satisfied that the poem matched up with the flagellation scene, he turned his attention to the men on the right. For the bearded figure, King sees the name Bessarion. For the angelic youth, he sees Regiomontanus, and also the names of three talented young men who had been close to Bessarion but were felled by disease — his dead godson Buonconte and two of his friends’ sons, Bernardino Ubaldini and Vangelista Gonzaga. Bessarion transferred all his lost hopes for these young scholars to the promising Regiomontanus, says King. The man on the right is associated with three people: the nobleman Giovanni Bacci, previously suggested as a possible sponsor for the painting, Bernardino’s father and Vangelista’s adoptive father.

Multiple identities

King believes that subtle clues in the painting confirm his interpretation. For example, the angelic face of the young man in red is explained by the dead youths. And the gown of the figure on the right is embroidered with thistles, perhaps hinting at dalla Carda, the name of Bernardino’s father (the Italian for thistle is *cardo*), and holds purse strings, hinting at the sponsor, Bacci.

According to King, many times, events and people are overlaid in one frozen scene. The painting represents not just the flagellation of Christ, but what Bessarion saw as the betrayal of the Eastern Church. It also serves as a consolation for the lost young men, and celebrates the arrival of Regiomontanus. And it demonstrates just how far it is possible to go with the concept described in the painting’s enigmatic

AMG-IMAGES



Cardinal Bessarion (above) was a mentor to the young Viennese astronomer and astrolabe-maker Johannes Regiomontanus (left).



original title: “They came together in one.”

King suggests that when Regiomontanus conceived the inscription, he added a few concealed meanings, mostly relating to the older astrolabe, which he thought would amuse his teacher. But as Bessarion studied the letters, he may have seen other chance combinations — you can see anything in this kind of puzzle if you look hard enough — that meant something to him, and so the idea for a painting may have emerged. Transferring the hidden identities into a painting would have been the ultimate representation of Bessarion’s feelings about his life and the Church.

There is no direct evidence that Bessarion commissioned the painting from Piero, but they were known to each other (Bessarion is featured in Piero’s most famous work, the wall frescoes at Arezzo). And there are several occasions at around the right time when they may have been in the same town.

So how do we know that King is not just seeing what he wants to see, as he believes Bessarion once did? Beyond the hidden characters he has identified in the painting, King says his evidence connecting the astrolabe and the painting is mathematical.

According to King, the epigram and the painting both hint at a ratio called the ‘divine proportion’ or ‘golden ratio’, which is aesthetically pleasing. It describes a line divided such that the ratio of the lengths of the two sections (A:B) is the same as the ratio between the whole line and the larger section (A+B:A). The current view among art historians is that although the ratio was known during the Italian Renaissance, there is no evidence that Piero, or anyone else, used it in their art.

Regiomontanus would have been familiar with the divine proportion from his studies of the geometry of Euclid, and King believes that the dates of the two astrolabes (1062 and 1462), which cut their centuries roughly in the divine proportion, may have reminded him of it.

In King’s interpretation, the eight vertical groupings in the poem match the geometry of the painting by lining up with the eight figures. King identifies two vertical lines at 3/8 and 5/8 of the inscription’s width, drawn through the B and the I of BESSARION (that is, his initials), which each divide the inscription in something close to the divine proportion. These match vertical lines drawn between the eyes of Christ and of the bearded figure, two important figures in the painting (see graphic, opposite).

King believes that contrary to the standard view, Piero may have used the golden ratio in his painting. The vertical line between Christ’s eyes divides the flagellation scene (its edges defined by the bordering columns) almost exactly in the divine proportion. To get this effect, Piero would have had to position the observer’s viewpoint very precisely, thus fixing the position of the ‘vanishing point’ of his carefully worked out perspective.

King is careful to describe his ideas as a “hypothesis”. But he argues that his interpretation fits with what is known, and solves many of the mysteries surrounding the painting. “It’s one of the most spectacular discoveries in the history of science,” he says.

Many disagree. Some art historians have dismissed the idea entirely, describing it to *Nature* as “nonsensical”, “embarrassing”

and “utter rubbish”. Unlike the most widely accepted interpretation of Piero’s painting, by Princeton art historian Marilyn Lavin (see ‘The Establishment view’), they feel King’s hypothesis stretches credulity too far: if you layer enough subjective assumptions on top of each other, they argue, you can find anything you like.

Kemp is one of the more moderate voices from that community. But even he is highly sceptical about any link between the astrolabe

“No art historian has looked at the geometry of the painting.”
— David King

and the painting. "It requires a substantial leap of faith," he says. "What is the concrete reason for making the connection?"

There is more enthusiasm for King's ideas outside the art-history community. João Pedro Xavier, an architect and geometrician in Porto, Portugal, who has studied Piero, finds King's measurements persuasive. Piero wrote extensively about the divine proportion in his mathematical work on regular polyhedrons, Xavier notes, and it follows naturally from his work with perspective. "He knew these relations, he could do it almost exactly." And if Piero was going to use the divine proportion anywhere in his art, "the person to put in such a position is Christ". Of course there is no evidence that Piero intended this golden ratio, but for a painting that has been so intensively studied, "why did nobody notice this before?" Xavier says. "It is strange."

Divided opinion

Neil Graves, a professor of English at the University of Tennessee in Knoxville and an expert in hidden meanings in literary texts, says that in the absence of direct evidence of what an author intended, it is necessary to consider factors such as whether a practice was common at the time, and how likely it is to have occurred by chance.

He is taken with King's and Holzschuh's reading of the astrolabe inscription, and agrees

The Establishment view

The reading of Piero della Francesca's *The Flagellation* most generally accepted by the art world was first published by Princeton art historian Marilyn Lavin in 1968 (see *Piero della Francesca: The Flagellation*, Univ. Chicago Press, 1973).

As is conventional in art history, Lavin answers the questions about the painting by referring to other works of

the time. She identifies the three men on the right on the basis of portraits from the same period.

She believes that the right-hand figure, in his blue and gold cloak, is Ludovico Gonzaga. The man on the left, in Byzantine attire and with the split beard of an astrologer, is the respected astrologer and Gonzaga's life-long friend, Ottaviano

Ubal dini della Carda.

Both these men had lost a son and Lavin suggests that the angelic youth between them is a memorial to an idealized 'beloved son', mirrored by the heavenly beloved son, Christ, on the far left. Lavin believes the painting was probably commissioned by Ubal dini for the ducal palace in Urbino, where he lived.

J.M.

that the odd spacing was probably intentional, to allow extra meanings. Word-play and hidden readings were particularly popular during mediaeval and Renaissance times. Signatures were commonly written as clusters of letters: Christopher Columbus adopted a four-line acrostic that has never been fully decoded.

But both Xavier and Graves balk at King's attempts to link his inscription geometrically with the painting. Both feel that it seems arbitrary to divide the painting vertically at the eyes of Christ and of the bearded figure, and to split the poem at the B and the I. Graves says that King deserves a hearing, however. "I don't think he proves his argument, but he makes an interesting and sensible case."

King is undaunted by the criticism he has received, and believes that some art historians will dismiss his work because they can't understand it. "The epigram and painting are mathematical in nature," he says. "No art historian has ever looked at the basic geometry of the painting".

But even an expert with mathematical training, such as Kemp, says that drawing any conclusions from measurements alone is fraught with problems. Part of the difficulty is deciding what to measure and where to measure it from and to, especially on a complicated painting like *The Flagellation*. "You are likely to hit something," Kemp says. "I want to see direct evidence." Such evidence might be lines drawn underneath the paint.

Like other art historians approached by *Nature*, Ellen Handy of the City College of New York worries that King may be jumping too quickly to conclusions, but she acknowledges that art history often ignores mathematics. "Ironically, many of those who consider themselves as art historians don't have the training that the artists of the time did," she says. Many Renaissance artists, such as Piero, were skilled geometricians. "We are not. We can learn from those who have that mathematical training now."

Architect James Bradburne, also a cultural historian and director general of the Palazzo Strozzi in Florence, acknowledges that proof may never be found, but supports King's ideas nevertheless: "If this is accepted even as a plausible hypothesis, then it says that scientific objects can legitimately be treated as historical documents, in the same way as paintings themselves have been. Scientific objects can be considered part of the puzzle."

Jo Marchant is news editor for *Nature*.

For more information on King's theory

▶ <http://web.uni-frankfurt.de/fb13/ign/>

Code.htm



Controversial codes: King says he can line up hidden names in the couplet with figures in the painting.

SOPRINTENDENZA PATR. STORICO, ART. ET NOANTROPOL. MARCHE

Research loses in hasty changes to medical training

SIR — The new system for specialist medical training currently being implemented by the UK government will have dire consequences for the country's biomedical research. The modernizing medical careers (MMC) framework for training doctors comprehensively fails to recognize the importance of academic research in either the recruitment or the training of future medical consultants. Many young, ambitious UK clinicians engaged in full-time pre- and postdoctoral research recently discovered, to their horror, that their academic and research achievements were essentially dismissed as irrelevant in the new selection process for specialist training.

In many specialities, research has traditionally been an integral, if informal, constituent of becoming a senior hospital consultant. Under the new system, unless

doctors decide at the very beginning of their careers to embark on a separate, dedicated academic pathway of medical training, they will have almost no exposure or opportunity to engage in research.

This is a serious mistake. Proleptically dismissing a research-experienced medical workforce will be of substantial detriment to clinical-science research, medical innovation and the development of scientific and economic partnerships with industry. It neglects the fact that many consultants who are employed fulltime in a purely clinical capacity frequently actively engage in research, often in collaboration with basic scientists and biomedical research companies. This provides mutual benefit to both clinical science and the provision of basic medical care. Furthermore, it overlooks the fact that many leading medical academics

do not develop or discover their passion for research until more advanced stages of their training. If tomorrow's clinicians have no expertise in research, the invaluable and profitable alliance between clinical and academic medicine in the United Kingdom is in jeopardy.

This problem has suddenly become rather urgent, as the new system was introduced with such speed and opaqueness that few saw it coming. The rushed and chaotic implementation should be immediately suspended in favour of an open, balanced and broad debate on the future of medical training and research.

Ben Seymour

The Wellcome Trust Centre for Neuroimaging, University College London, and the National Hospital for Neurology and Neurosurgery, 12 Queen Square, London WC1N 3BG, UK

Confidentiality is essential in misconduct inquiries

SIR — Your News story "Misconduct? It's all academic..." (*Nature* 445, 240–241; 2007) and related articles in the same issue were too eager to find fault with the process universities use to deal with allegations of misconduct in research. As provost (S. M.) and vice president for research (C. R.) of Purdue University, we consider that you failed to give readers a true picture of the realities of these investigations.

A glaring omission is the fact that the US Department of Health and Human Services' integrity guidelines require US institutions to protect "the confidentiality of respondents, complainants, and research subjects" when investigating allegations of misconduct. This confidentiality is inconvenient for journalists. It also is extremely challenging for scientists and administrators who face the unhappy task of judging the integrity of one of their colleagues, but it is necessary if we are to prevent the ruin of good reputations through malicious or erroneous claims.

The process is not perfect. Like the US system of justice, it is frustrating, confusing and tedious, but it is the process we have, and we must follow it carefully until we find a better one. Despite its imperfections, in the end, it usually does the right thing. The process works best when those alleging misconduct document their concerns thoroughly and cooperate fully with all aspects of the inquiry — including the requirement for confidentiality.

An inquiry into a research misconduct allegation is not an inquiry into the verifiability of a research claim. Verifiability is decided by experimentation and debate,

and often takes time to resolve. There can be legitimate differences of opinion regarding a laboratory observation. The Purdue administration's job is not to decide among such opinions.

Purdue University's policy on research integrity states: "The mere suspicion or allegation of wrongdoing, even if totally unjustified, is potentially damaging to a person's career. Consequently, no information about charges of a lack of integrity in research may be disclosed except to the appropriate university and federal authorities." Any response to an allegation of misconduct at Purdue will adhere to the letter and the spirit of that principle. We believe this is true at the vast majority of universities. Readers of *Nature* would not understand that truth from your coverage, nor would they be likely to conclude that a successful and fair inquiry might include a finding of 'not guilty'. **Sally Mason, Charles Rutledge**
Purdue University, 610 Purdue Mall, West Lafayette, Indiana 47907-2040, USA
See News story, page 480.

New species show how little we know of the sea

SIR — Your News Feature "Killer in the kelp" (*Nature* 445, 703–705; 2007) on the killer whale, *Orcinus orca*, states that the genetic analyses of type-C killer whales in Antarctic waters could lead to the naming of the first new whale species since 2003. However, the killer whale is actually a dolphin species belonging to the family Delphinidae, which includes about 30 species of small and mid-sized odontocetes (toothed whales, dolphins and porpoises).

Even if the type-C Antarctica killer whales were to be named a new species, they would still not become the first new cetacean species since *Balaenoptera omurai* was discovered in 2003. In 2005, a new dolphin species, the Australian snubfin dolphin *Orcaella heinsohni* (Cetacea, Delphinidae), was described by a team of scientists from Australia and the United States (I. Beasley *et al. Mar. Mammal Sci.* 21, 365–400; 2005). Genetic and osteological analyses of Irrawaddy dolphin specimens collected from Asian and Australian waters provided significant statistical basis that the Australian specimen was a new species.

In addition, a new species of beaked whale, Perrin's beaked whale *Mesoplodon perrini* (Cetacea, Ziphiidae), was described in 2002, on the basis of five animals stranded on the coast of California between 1975 and 1997 (M. L. Dalebout *et al. Mar. Mammal Sci.* 18, 577–608; 2002). Therefore, if the type-C Antarctica killer whale is recognized as a new species, it will become the first new dolphin species named since 2005, or the third new cetacean species since 2002.

The discovery of three, potentially four, new cetacean species in the first decade of the twenty-first century underscore how little we know about these large mammals of the sea. It is very likely that more new species of whales and dolphins will be discovered and described in the years to come, as more rigorous morphological and genetic investigation are being conducted.

Shane Guan

Office of Protected Resources, National Marine Fisheries Service, Silver Spring, Maryland 20910, USA

Contributions to Correspondence may be submitted to corres@nature.com.

BOOKS & ARTS

All systems go

Three authors present very different views of the developing field of systems biology.

Life: An Introduction to Complex Systems Biology

by Kunihiko Kaneko

Springer: 2006. 383 pp. £61.50, \$99

An Introduction to Systems Biology: Design Principles of Biological Circuits

by Uri Alon

Chapman & Hall: 2006. 320 pp. £28.99

Systems Biology: Properties of Reconstructed Networks

by Bernhard Palsson

Cambridge University Press: 2006.

334 pp. £35, \$75

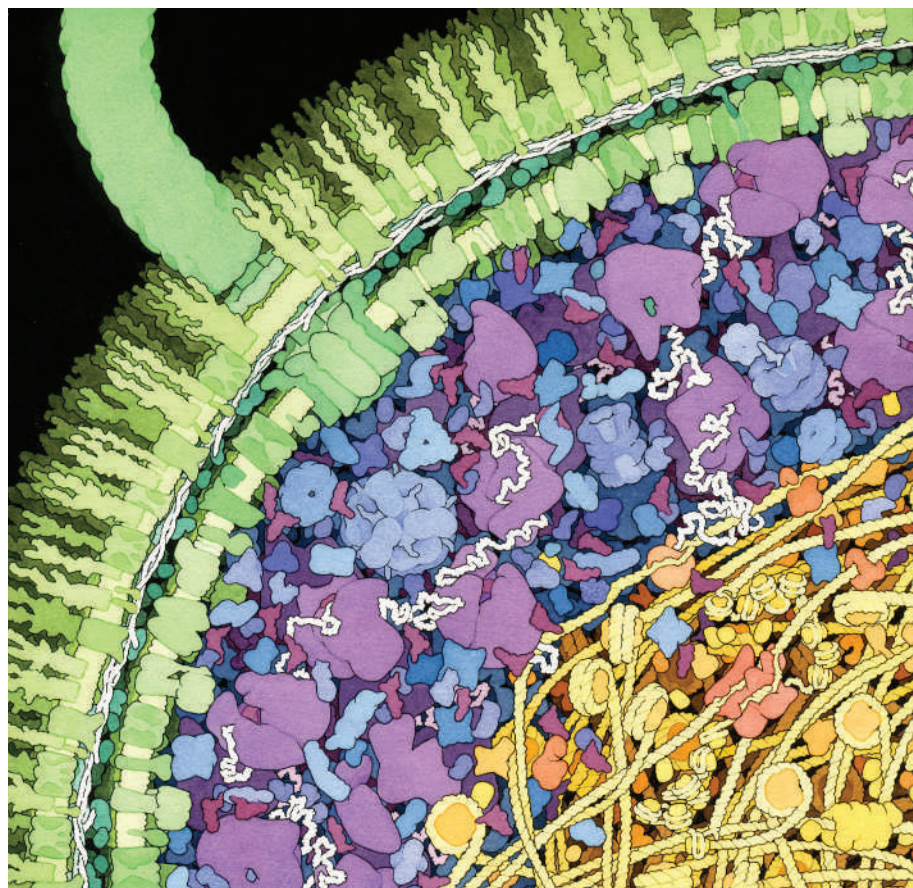
Eric Werner

The authors of three books profess to give an introduction to systems biology, but each takes a very different approach. Such divergence might be expected from a field that is still emerging and broad in scope. Yet systems biology is not as new as many of its practitioners like to claim. It is a mutated soup of artificial life, computational biology and computational chemistry, with a bit of mathematics, physics and computer science thrown in. Because it is so broad and has few recognized boundaries and plenty of funding, it is attractive to anyone who has ever thought about life and has some relevant technical expertise.

The discovery that dynamic systems can exhibit complex, chaotic and self-organizing behaviour made many scientists see analogies with living systems. In *Life*, Kunihiko Kaneko attempts to describe living organisms as complex systems akin to those seen in chemistry and physics. The problem is that the theory of dynamic complex systems used in physics and chemistry may have little to do with biological organisms and the way they grow and function.

For instance, Kaneko views differentiation from a group of uniform cells as resulting from slight stochastic perturbations that are gradually amplified by intracellular and intercellular interactions. After a while, these become fixed, resulting in a pattern of different cell types. One problem with this theory is that it gives no account of how differentiation repeats itself so consistently in the development of organisms. It fails to explain why identical twins remain identical, and why horse embryos develop into horses, not chimpanzees.

Kaneko also claims that stem cells are fundamentally unstable and that this leads to different cell types. But stem cells are not unstable.



The activity of cells is determined by complex interactions governed by a range of control signals.

Rather, when stimulated by signals or by their own genetic clock, they start a very precise process of differentiation that is dependent on internal and external control signals.

There is one big player missing from the dynamic-systems account: the genome. For this reason, it seems to me that dynamic-systems theory fails to give sufficient insight into biological processes. Cells are highly complex agents containing a vast amount of control information that cannot be reduced to a few simple rules (or even sophisticated mathematical functions) that attempt to describe cell dynamics and cell interactions externally without recourse to the information contained in the genome. A similar problem lies at the heart of the failure of Turing-like models to describe embryonic development. Kaneko provides a good summary of the standard weaknesses of Turing's theory of development, but fails to see that some of the same

weaknesses apply to his own ideas as well.

Kaneko assumes that because complex patterns can form from simple interacting physical elements, such interactions can also generate arbitrary complexity. Even a simple counting algorithm that sequentially generates every integer will generate every complex state (binary sequences), but no algorithm can generate any particular number or state and stop without having the information contained in that number or state. Moreover, any process that generates a complex structure and stops must contain the information required to generate that structure. This is why cells need the vast amount of information encoded in their genome. Kaneko and many others who have fallen for the myth of interactionism, complex-systems theory or Turing-like models are in fundamental conflict with the complexity conservation principle, which states that a space-time event generated by a set of agents

D.S. GOODSELL

cannot be more complex than the information available to the agents.

Evolution gets round this principle by the stochastic generation of new states. Stochastic processes can be random so they can generate arbitrary complexity, within physical chemical constraints, because random strings or structures are maximally complex.

Uri Alon's *An Introduction to Systems Biology* is a superb, beautifully written and organized work that takes an engineering approach to systems biology (see also *Connections*, page 497). Alon provides nicely written appendices to explain the basic mathematical and biological concepts clearly and succinctly without interfering with the main text. He starts with a mathematical description of transcriptional activation and then describes some basic transcription-network motifs (patterns) that can then be combined to form larger networks.

The elegance and simplicity of Alon's book might lead the reader to believe that all the basics of the control of living systems have been worked out. It only remains, it seems, to combine the network motifs to get a total understanding of networks in the dynamics and development of living systems.

All is fine except that in the very first page of the book, Alon defines networks as functions that map inputs to protein production. In other words, the meaning of genomic transcription networks is restricted to the production of proteins or cell parts. Granted, some of these proteins are transcription factors that in turn activate other genes and, thereby, are a key part of the network itself. But this prejudices the enterprise by presupposing that protein states are all there is to understanding life. Such a view is bottom-up in the extreme.

What's missing is a relation between higher-level organizational, functional states and networks. This is indicative of a more fundamental problem. Because Alon focuses on very basic low-level circuits, the global organization and its effects are largely ignored.

In some ways, Bernhard Palsson's *Systems Biology* is a more practical book for those wishing to understand and analyse actual biological data and systems. It directly relates chemistry to networks, processes and functions in living systems. The book's main focus is on metabolic networks of single cells such as bacteria. Palsson argues that classical modelling using differential equations requires complete information about the state of the system. Such data, however, are not available for complex biological systems. Palsson's response is to accept biological uncertainty. The approach is to describe a space of all the possible states of a system or network (relative to a set of dimensions of interest) and then use biological and chemical data to constrain this space. This is similar to the process of entropy reduction described in statistical thermodynamics.

Specifically, Palsson espouses a mathematically ingenious method of formalizing metabolic reactions, pathways and networks, and

uses this to formalize uncertainty about biological chemical states. This space of possibilities can then be systematically constrained by high- and low-level information. In this way, he manages to formalize states of uncertainty in a biological system so he can extract useful predictive information about it, despite the fact that many of its parameters and values of variables are unknown.

Unfortunately, Palsson's book is a difficult read. It is not well organized and refers the reader to later chapters to explain concepts needed in earlier ones, and vice versa. Often no explanation of basic concepts is provided; additional appendices would have been helpful. Palsson admits that he had help writing some of the chapters, and the book does feel like the work of a committee. However, it brings together many of Palsson's contributions to metabolic network formalization and analysis and, for this reason, deserves to be part of a systems-biology curriculum. I look forward to

improvements in the promised future editions.

Of the three books, Palsson's is the most practical and immediately relevant to modelling low-level metabolic networks. Alon investigates networks at a higher level, including genomic regulatory networks. He does an excellent job of explaining and motivating a useful toolbox of engineering models and methods using network-based controls. Kaneko's book is conceptually deep but further removed from Palsson's chemical networks and even from Alon's more abstract regulatory networks. Even though I am critical of his approach, the book is filled with insights and useful criticisms of some of the standard models and theories used in systems biology, and in biology generally. All three books will be valuable and non-overlapping additions to a systems-biology curriculum. ■

Eric Werner is in the Department of Physiology, Anatomy and Genetics, University of Oxford, Parks Road, Oxford OX1 3PT, UK.

A little movement

Middle World: The Restless Heart of Matter and Life

by Mark Haw

Macmillan Science: 2006. 256 pp. £16.99, \$24.95

Tom McLeish

The fascinating tale of brownian motion has been looking for a story-teller for a long time. The tangled threads knot together, rather than begin, in the nineteenth century with botanist Robert Brown's original observations of the random, ceaseless motion of particles in pollen grains of *Clarkia pulchella*. The threads lead back in time to medieval theories of matter that tangled physics with theology — a pattern that ran deep through the work of Galileo and Newton — and further back still to the Epicureans. Going forwards from Brown, they twist through the nineteenth century's ambivalence towards molecular theory and the thermodynamics of Sadi Carnot and Lord Kelvin. Weaving through the kinetic theory of James Clerk Maxwell and the statistical mechanics of Ludwig Boltzmann that finally grasped the physics of randomness, they lead to the complementary beauties of Einstein's theory of brownian motion and Jean Baptiste Perrin's experiments that led to modern soft-matter physics and a new understanding of the role of brownian dynamics in molecular biology. This is a remarkable story of science and scientists that leaves no major science untouched and summons onto the stage a colourful and eminent cast from centuries of endeavour.

In *Middle World*, Mark Haw provides an accessible and racy account that succeeds in opening up technical ideas without losing momentum. Haw is not insensitive to dramatic



Jean Baptiste Perrin (above) provided a new understanding of Robert Brown's notion of random motion.



irony, and makes a satisfying conclusion out of the return of brownian motion to illuminate dynamical processes in biology, where it originated, after spending a century wandering the worlds of physics and physical chemistry. We fleetingly visit the role of brownian motion in polymer physics, oxygen capture by myoglobin, the protein-folding problem and the question of how molecular motors (the cell's cargo transporters) can possibly execute controlled and directed motion in a turbulent brownian world. It's not quite T. S. Eliot, but we are almost back where we began, yet knowing for the first time.

Although it is a fitting window onto a selection of hot topics in current science, the final 'contemporary' section drops the connected storyline of the preceding historical material.

I wonder if the role of diffusion in the molecular biology of plant reproduction might have connected this coda more strongly to the earlier narrative.

The research is mostly thorough: Haw has picked up on subtleties often glossed over, such as the prescient role of Michael Faraday in advocating a correct reading of Brown's work, the correct early kinetic theory of the unfortunate John Waterston, who disappeared from science following its rejection, and the extraordinary timeliness of Einstein's molecular theory for the diffusion constant published earlier by the largely overlooked William Sutherland. But the reader has to stay alert — a cost of the narrative's unflagging pace is that people and places flash by all too quickly. I wish we had the time to get to know Perrin, and the shadowy figure of Brown himself, rather better.

Another aspect of the thirst for satisfying narrative is that history seems sometimes to be squeezed into the story's form, rather than the converse. So our sole representative of the middle ages is Hieronymous Bosch, whose portrayals of chaos conveniently prepare the stage for a sea change to order in the enlightened follow-

ing act starring Galileo and Newton. The plot thickens with a return to calculated chaos in statistical mechanics, and so on. A case could be made more strongly for a highly ordered medieval theory of matter than for a chaotic one, and Galileo's corpuscular theory of matter in *The Assayer* in 1623 surely anticipates the underlying chaos of kinetic theory. But perhaps such complaints are churlish: a good yarn withers from too much of "on the other hand".

Such strong selection in historical interpretation, as well as some under-development of character, could well be the results of zealous editing with a younger lay readership in mind. In places the author gives the impression that he would have liked to say more. Perhaps the ambiguity in target readership is also reflected in the uneven style, which alternates ambitious alliteration with colloquialism (it was my first non-fiction read containing, as an entire sentence, "Not."). But these are pitfalls for all authors and publishers of 'popular science', and I would hope there is something for everyone in this highly enjoyable little book. ■

Tom McLeish is professor of polymer physics, University of Leeds, Leeds LS2 9JT, UK.

Roman alphabet. The caliphate — the office of the head of the Muslim religion — was dismissed to make Turkey secular. And on 31 July 1933, to complete the transformation, Atatürk closed down Istanbul's institution of traditional higher learning, the *darülfünun*, dismissing the entire faculty. On the same premises, the very next day, he installed a new Western-style university with a distinguished faculty.

Assembling this faculty required a second, quite different architect, one cognizant of scholarship and competence. That man was Philipp Schwartz, a Hungarian-born pathologist who had been dismissed by the Nazis from his position in Frankfurt and had fled to Switzerland. There he had founded the *Notgemeinschaft Deutscher Wissenschaftler im Ausland*, which compiled and maintained a roster of leading scholars seeking to escape Nazi oppression. Schwartz persuaded the Turkish government that his organization could staff an entire university — so many outstanding academics were being persecuted that they could select the very best.

As Reisman recounts, Istanbul University embraced a wide range of disciplines, although the heart of the university was the medical faculty. Foreign academics had to start at the most elementary level. Before medicine could be taught, a Turkish medical vocabulary had to be devised. Only then could the first modern texts be written in Turkish and medical students taught in their own language. The nation was in dire need of physicians, especially in remote regions of Anatolia. The university trained thousands of young doctors who, in exchange for free schooling, were obliged to provide medical services in understaffed parts of the country for several years after graduation.

The book captures the spirit of the times, the resistance the foreign scholars faced as they sought to modernize Turkey's institutions of higher education, the worries brought on by the war, and the family outings in which foreigners often compared notes and tried to laugh at the sometimes ludicrous problems they faced. What remains with me from these outings, so many years later, is the interest the

A Turkish revolution

Turkey's Modernization: Refugees from Nazism and Atatürk's Vision

by Arnold Reisman

New Academia: 2006. 572 pp. \$28

Martin Harwit

Looking out of the window facing Prague's main railway station that evening, I saw a soldier in an unfamiliar uniform standing guard in the snow. The Germans had arrived. It was 15 March 1939, less than a week after my eighth birthday. By the end of the month, my parents, my sister and I were on a train to Istanbul. My father, whom the Germans had dismissed from his professorship at Charles University, had been offered the chair of biochemistry at Istanbul University. None of the Jewish members of our family who stayed behind survived the German occupation.

Our journey to Istanbul was not unique. Arnold Reisman's insightful book *Turkey's Modernization* documents how, starting in 1933, Turkey provided shelter to more than a hundred eminent European academics and their families, all victims of Nazi persecution. The task of the professors was to initiate the country's first modern university and train a generation of young Turkish scholars able to further expand higher education.

Two men spearheaded the drive to establish Istanbul University. The vision was provided by Mustafa Kemal Atatürk, who founded the modern Turkish Republic on the shards of a crumbled Ottoman empire. As a young military officer in the First World War, Mustafa

Kemal had become a hero to his countrymen, first for repulsing the Allies at the Dardanelles, and later for recapturing the territories that define modern Turkey today. Once in power, he decreed that Turkey would discard its Ottoman past and become a modern state modelled on European lines. A new constitution and newly enacted laws affected every aspect of life.

Men were prohibited from wearing the traditional *fez*. Women were forbidden from hiding their faces behind veils. Polygamy was abolished. Everyone had to adopt a family name; for himself, Mustafa Kemal chose 'Atatürk' — father of the Turks. To eradicate widespread illiteracy, every child now had to be schooled. Arabic script was outlawed and replaced by a



Open-door policy: in the Second World War, Istanbul University welcomed foreign academics fleeing Nazi persecution.

M. BOURKE-WHITE/TIME & LIFE/GETTY IMAGES

professors took in us children. Reisman's richly illustrated book recalls this aspect of family life in the community.

Looking back, some seventy years later, how should we judge the impact of the European academics? The draconian measure of closing the darülfünun to create Istanbul University left deep wounds. The 2006 Nobel laureate in literature, Orhan Pamuk, remarks in his book *Istanbul* (Alfred A. Knopf, 2005) on the unjust dismissal of traditional Ottoman scholars. His concern is the loss of the nation's identity in the

Atatürk reforms. Although distancing Turkey from its Ottoman past, the modernization has not yet led to Turkey's full acceptance as a Western nation.

Nevertheless, as Reisman notes, Istanbul University became established almost overnight and the foreign professors continued to educate Turkish students from 1933 until about 1948. By then a strong academic community had been built with talented young Turks. Dozens of new universities began springing up across the country, and the assistance of

the foreign professors, many of whom went on to productive careers elsewhere, was no longer needed.

Today, Turkish names appear on articles in leading international journals, showing how the vision of one man and the organizational acumen of another laid a foundation on which Turkey has continued to build.

Martin Harwit is former director of the National Air and Space Museum, Washington DC 20560, and is emeritus professor of astronomy at Cornell University, Ithaca, New York 14853, USA.

Gene expression

Sarah Jacobs mutates genetic information into art.

Martin Kemp

How can artists possibly confront the excruciating complexity of the human genome — or any genome for that matter? There are just too many of the letters C, G, A and T. It is possible, however, to make some general artistic statements about the human genome project and its implications, and about genetic engineering as a whole. But it is all too easy to sink to the level of the 'Frankenstein food' headline that appeared in the British newspaper the *Daily Mail* on 13 February 1999.

Sarah Jacobs shows that the complexity can be tackled head on. She has a record of working with the blank poetics of modern scientific discourse, with its studied eschewing of personal expression. Her 92-page e-book *Deciphering Human Chromosome 16: We Report Here* is studded throughout with phrases from the original article, 'The sequence and analysis of duplication-rich human chromosome 16' (*Nature* **432**, 988–994; 2004). "We report here" is one of these, together with "We observed" (of course), "Here we describe", "We constructed", "We adopted a strategy", "We then eliminated", "Finally we identified", and so on. Isolated, phrases that are so much part of scientific normality assume the quality of an incantation.

After the *Nature* article was published, Jacobs googled such terms as "human chromosome 16", "chromosome 16 book" and "chromosome 16 expression". She even searched for odd combinations, such as "chromosome 16" + "Saddam Hussein".

She sifted out around 250 website links on the basis of what appeared intellectually or intuitively interesting and "looked good". The e-book proceeds through simple pages of the incantatory phrases interspersed with coloured lower-case overprinting of the website links with fragments of their text and numbers from the original article in large capitals (see the page shown below).

The result is a doggedly

the original article. They are accompanied by enigmatic fragments from the websites.

Given the vagaries of the production process, each index assumes an individual character. The letters C, G, A and T on every left-hand page are bled to the page borders, and their visible expression on the unbound edge of the closed book varies unpredictably as the result of minute variations in the trimming process.

The report and the index are odd, difficult, perplexing, suggestive

and strangely beautiful — and awesome in their numerical persistence. Jacobs has created something drawn directly from the science and its diffusion, using the tools of a bibliographer. Yet the result subverts the science in the direction of chaos and cacophony. The effect is analogous to the way that the particularity of each individual person seems to confound the overwhelming similarity of our genetic constitutions.

At least, this is one possible interpretation. There are others. Jacobs is, I suspect, resisting any closed or dominant reading. And therein lies the difference between the original *Nature* article and Jacobs' visual play. The scientific exposition provides as little latitude for alternative readings as possible, whereas Jacobs provides a field for interpretative flexibility that triggers thoughts and insights of an unexpected nature — unexpected, perhaps, even to the author herself.

Martin Kemp is professor of the history of art at the University of Oxford, Oxford OX1 1PT, UK. His new book, *Seen | Unseen*, is published by Oxford University Press.



accumulated 'report' on the incredibly rapid Internet diffusion of the knowledge in standard and bizarre forms. The contents are subject to constant mutation, so every six months Jacobs takes screen shots to document the changes.

To accompany the report, Jacobs has now issued an 'index' as a print-on-demand book, with a fixed form of 552 pages (www.informationasmaterial.com). Against the background of the CGAT permutations, the accumulated number of characters is remorselessly spelt out, up to "Sixteen million five hundred and forty-one thousand and nine hundred" — still some way short of the roughly 80 million base pairs noted in



Simplicity in biology

Networks of interactions between thousands of molecules within cells seem to defy comprehension, but shared principles of design may simplify the picture.

Uri Alon

'Complex' is perhaps the most common adjective used to describe biological phenomena. In every cell, complex networks of interactions occur between thousands of metabolites, proteins and DNA. Every interaction is itself a complex dance between exquisitely shaped proteins, designed to interface with each other if the conditions are right. And every protein looks like tangled strands of spaghetti festooned with atomic appendages. So where is the simplicity?

The point I wish to make is not that biology is simple, but that biological networks of interactions are simpler than they might have been. There seems to be a degree of simplicity in several aspects of these networks, which is intriguing given that cells evolved to survive, and not for scientists to understand.

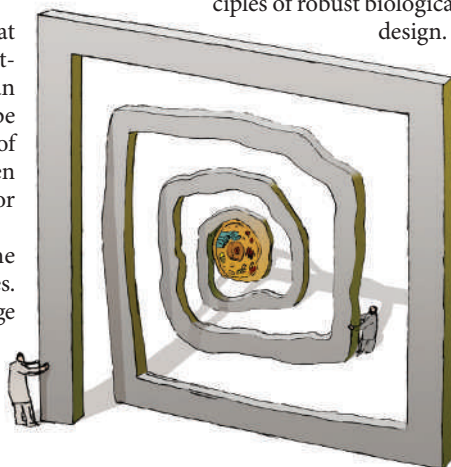
One level of simplicity occurs in the structure of networks that regulate genes. In large networks there is normally a huge number of possible interaction patterns, but biological networks seem to be built, to a good approximation, from only a few types of patterns called network motifs. These motifs appear again and again throughout the network, each time having the same pattern of interactions but with different genes.

Theoretical modelling, and experiments that monitor the dynamics of networks in real time inside living cells, have revealed specific functions of different motifs — such as filtering out fluctuations in input signals. For example, a common network motif in *Escherichia coli* allows the bacteria to respond appropriately to stress even if the signal that triggers the response is disrupted.

When stressed, *E. coli* produce proteins that self-assemble into whip-like projections called flagella, and these enable the bacteria to swim in search of better conditions. A network motif known as a coherent feedforward loop senses the stress signal and coordinates the production of flagella proteins. The motif allows the cells to start making flagella proteins when a stress signal appears, but when the signal is lost, keeps production going for an hour — about the time it takes to assemble a flagella. In this way, this motif protects flagella production from a brief loss of input signal. The same motif appears in hundreds of systems in bacteria and other organisms.

Why are gene-regulation networks built

out of only a handful of network motifs? The small number of motifs seems to result from the strict constraints that biological circuits must meet. For example, circuits must operate despite random fluctuations in the concentrations of the component parts, because such fluctuations seem to be an inherent feature of cells. This demand for robustness reduces the large number of circuits that perform a given function on paper to only a few that can work in the cell. Theoretical and experimental studies have begun to outline the basic principles of robust biological design.



Furthermore, in the case of bacteria, cells often seem to economize; network motifs tend to be the circuits with the fewest components that are able to robustly perform a given function. Also, in many of the systems studied so far, the motifs are wired to each other in a way that does not spoil the independent function of each motif. As a result, combinations of motifs can give rise to new dynamical functions.

The same small set of network motifs, discovered in bacteria, have been found in gene-regulation networks across diverse organisms, including plants and animals. Evolution seems to have 'rediscovered' the same motifs again and again in different systems: circuit duplication, where an ancestral network motif gave rise to existing motifs in several species, would lead to a 'family resemblance' between the proteins that appear in different instances of the motif, but this is rarely found. Such convergent evolution suggests that specific motifs are repeatedly selected because of their properties.

A second type of simplicity is found when one considers the kind of models needed to understand the dynamics of biological networks. Instead of having

to include many of the molecular details referred to at the start of this essay, the dynamics of each motif can be described using mathematical models that have a certain degree of universality. In many cases the models do not require plunging into the details of how every protein works; they only need to include information on whether X activates or inhibits Y, and at what concentration (and perhaps a few additional parameters). Such models seem to capture the essential dynamics of protein circuits, while being, in a sense, insulated from most of the complexity of the proteins themselves.

A further source of simplification in such models is the strong separation of timescales between different processes. For example, networks that control the production of new proteins work on the timescale of tens of minutes, whereas networks that chemically modify existing proteins operate in seconds. Thus, circuits that chemically

modify proteins can complete their work before the slower interactions have begun to change the concentrations of proteins.

Mathematically, the separation of timescales allows us to understand the dynamics on the slow timescale by using steady-state approximations for the interactions on fast timescales.

Some of the biological networks studied so far seem to contain a degree of simplicity. Simplifying principles gives hope that the behaviour of seemingly incomprehensible biological networks will eventually be deciphered. I have emphasized simplicity in biology to encourage the point of view that general principles can be discovered. Without such principles, it is difficult to imagine how we might ever make sense of biology on the level of an entire cell, tissue or organism.

Uri Alon is in the Departments of Molecular Cell Biology and Physics of Complex Systems, Weizmann Institute of Science, Rehovot 76100, Israel.

FURTHER READING

Alon, U. *An Introduction to Systems Biology: Design Principles of Biological Circuits* (CRC Press, 2006).
Ptashne, M. & Gann, A. *Genes and Signals* (Cold Spring Harbor Laboratory Press, 2002).
Simon, H. A. *The Architecture of Complexity in The Sciences of the Artificial* (MIT Press, Cambridge, MA, 1996).
Savageau, M. A. *Biochemical Systems Analysis: A Study of Function and Design in Molecular Biology* (Addison-Wesely, Reading, MA, 1976).

For other essays in this series, see <http://nature.com/nature/focus/arts/connections/index.html>

J. KAPUSTA/IMAGES.COM

CONNECTIONS

CHEMICAL BIOLOGY

A degrading solution to pollution

J. Wade Harper

Environmental pollutants such as dioxins affect human health. It now seems that dioxins exert their effect by forming atypical enzyme complexes that mediate the breakdown of steroid-hormone receptors.

Dioxins are some of the most prevalent and dangerous pollutants in the environment. They are generated as by-products of, among other things, rubbish incineration and industrial processes¹, and act by disrupting the endocrine system. Because dioxins are fat-soluble, they tend to accumulate in the fatty tissue of animals, reaching levels in the food-chain that exceed those considered safe to humans². Endocrine disruptors such as dioxins have been implicated in birth defects, infertility and cancer. However, the molecular mechanisms by which they alter the signalling pathway that is mediated by the components of the endocrine system, steroid hormones, have remained a mystery^{3,4}. On page 562 of this issue, Ohtake and colleagues⁵ describe a possible mechanism by which dioxins regulate steroid signalling: they form atypical ubiquitin-ligase enzymes that specifically mark members of the nuclear steroid-receptor family of gene-transcription factors for degradation.

There are two main ways in which dioxins disrupt the function of nuclear receptors. First, they promote the activation of steroid-receptor-dependent genes in a hormone-independent manner. They do this by forming a complex with the aryl hydrocarbon receptor protein (AhR), the AhR nuclear-translocator protein (ARNT) and a steroid receptor such as the oestrogen receptor, ER α (refs 3, 6) (Fig. 1). AhR–ARNT–ER α complexes recruit transcriptional coactivators to ER α -regulated genes even in the absence of oestrogen. Second, the ER α protein within AhR–ARNT–ER α complexes is less responsive to oestrogen, leading to an imbalance in steroid-dependent gene transcription in oestrogen-responsive tissues^{6,7} and the new findings⁵ of Ohtake *et al.* indicate that dioxins alter the abundance of steroid receptors with the help of the proteasome — a large protein complex that recognizes proteins tagged with a chain of ubiquitin molecules and catalyses their degradation⁸. Protein turnover through the ubiquitin system involves a cascade of ubiquitin-transfer reactions culminating in the attachment of ubiquitin to the target protein through substrate-specific E3 ubiquitin ligases.

The observation of proteasome-mediated,

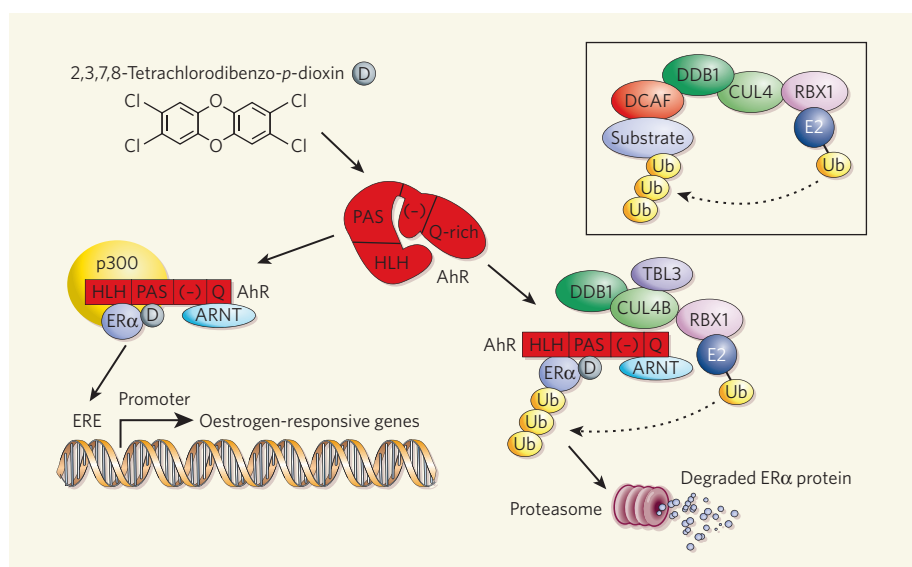


Figure 1 | Dioxins and the degradation of the oestrogen receptor (ER α). Binding of dioxins, such as 2,3,7,8-tetrachlorodibenzo-*p*-dioxin (D), to the AhR protein, which consists of HLH, PAS, acidic (–) and Q-rich structural domains, leads to a conformational change that partitions AhR into two complexes. Previously, Ohtake *et al.*⁶ found that a transcriptionally active complex composed of AhR, ARNT, ER α and a coactivator such as p300 interacts with the oestrogen-responsive element (ERE), causing the promoters of oestrogen-responsive genes to activate transcription in the absence of oestrogen. They now show⁵ that a ubiquitin-ligase complex that targets ER α for degradation by the proteasome also forms through an interaction of the acidic domain of AhR with the amino terminus of CUL4B. Inset, the structure of a conventional CUL4-based E3 complex in which DDB1 functions as an adaptor for assembly of substrate-binding DCAF proteins. Ub, Ubiquitin.

dioxin-dependent degradation of ER α and androgen receptors (AR) led Ohtake *et al.* to search for components of the ubiquitin system that form complexes with AhR. Strikingly, they found that dioxin promotes the formation of an atypical E3 ligase (CUL4B^{AhR}). This ligase has various components: the scaffolding protein CUL4B, the ring-finger protein RBX1/ROC1, which recruits E2 ubiquitin-conjugating enzymes, the β -transducin-like protein TBL3 and the adaptor protein DDB1, as well as ARNT and AhR (Fig. 1). In this complex, AhR functions as a substrate receptor and can interact with both ER α and AR, thereby promoting their ubiquitination and degradation by the proteasome.

Conventional CUL4-based E3s contain CUL4A or CUL4B, together with RBX1, DDB1 and a member of a family of proteins called

DDB1- and CUL4-associated factors (DCAFs), which bind to DDB1 and serve as substrate receptors^{9–12} (Fig. 1; inset). Experiments performed by Ohtake *et al.*⁵ suggest that the binding of dioxin to AhR results in the exposure of an acidic domain of AhR, which can exclusively assemble with the unique amino terminus of CUL4B — a process that is independent of DDB1. Thus, dioxin promotes the formation of an atypical CUL4B^{AhR} complex that is distinct from conventional CUL4^{DCAF} complexes.

Using the technique of RNA interference, Ohtake *et al.* found that depletion of any single component of CUL4B^{AhR} reduces both dioxin-dependent degradation of ER α and the accumulation of ubiquitin chains on ER α and AR. When ER α was stabilized, the dioxin-mediated suppression of oestrogen-dependent gene transcription was blocked. This indicates that

CUL4B-mediated ER α degradation contributes to dioxin's action as an endocrine disruptor.

Ohtake *et al.* also examined the abundance of ER α and AR in the reproductive tissues of hormone-depleted mice lacking AhR and treated with dioxins and/or steroid hormones. In the absence of AhR, high levels of AR and ER α were insensitive to dioxins, and AhR-negative cells, or normal cells depleted of CUL4B, were unable to suppress hormone-dependent activation of gene expression and cell proliferation.

By showing how dioxins convert AhR into an atypical CUL4B-based E3 ubiquitin ligase that targets ER α and AR for proteasomal degradation, Ohtake and colleagues⁵ provide mechanistic insight into the way dioxins disturb endocrine signalling. But several questions remain. Although dioxin promotes the formation of a complex between CUL4B^{AhR} and ER α , a substantial fraction of AhR and ER α exists in CUL4B-independent complexes that are still active in promoting gene transcription⁵. This allows simultaneous hormone-independent activation of steroid-receptor target genes and the blunting of hormone-dependent transcription through steroid-receptor degradation. It is unclear how this partitioning is regulated (Fig. 1) and whether the extent of partitioning is an essential aspect of endocrine disruption.

AhR is best known for its role in detoxification, but it also seems to function in the development of the reproductive organs independently of external ligands such as dioxins¹³. So, another question for the future is whether AhR forms an E3 complex with CUL4B in the context of an as-yet-unidentified natural ligand. There are emerging examples of small molecules that affect the assembly of E3-substrate complexes, such as the interaction of the plant hormone auxin with the TIR1 F-box protein¹⁴. Therefore, it seems possible that small-molecule-dependent, ubiquitin-mediated protein degradation is more widespread than currently appreciated. Finally, the selectivity of AhR for CUL4B is interesting in light of the finding that CUL4B (but not CUL4A) is mutated in human mental-retardation syndromes linked to the X chromosome¹⁵. Understanding what makes CUL4B special will be a focus of future research.

The branch of science known as chemical biology involves screening libraries of small molecules to identify compounds that can modulate cellular mechanisms. This pursuit has led to the identification of many molecules, some of which — like dioxins — are deleterious to cells. Ohtake *et al.*⁵ have provided an example of how analysis of the interaction between environmental toxins and their targets produces a better understanding of cellular control mechanisms that are crucial to human health. Their results are a poignant reminder that our ecosystem is, in fact, a very large chemical-biology experiment, in which we are both the investigator and the subject. Only time will tell if this experiment is as well controlled as we hope it is. ■

J. Wade Harper is in the Department of Pathology, Harvard Medical School, Boston, Massachusetts 02115, USA.
e-mail: wade_harper@hms.harvard.edu

1. Schecter, A., Birnbaum, L., Ryan, J. J. & Constable, J. D. *Environ. Res.* **101**, 419–428 (2006).
2. Thornton, J. W., McCally, M. & Haoulihan, J. *Public Health Rep.* **117**, 315–323 (2002).
3. Brosens, J. J. & Parker, M. G. *Nature* **423**, 545–550 (2003).
4. Petersen, S. L., Krishnan, S. & Hudgens, E. D. *Endocrinology* **147**, S33–S42 (2006).

5. Ohtake, F. *et al.* *Nature* **446**, 562–566 (2007).
6. Ohtake, F. *et al.* *Nature* **423**, 545–550 (2003).
7. Wormke, M. *et al.* *Mol. Cell. Biol.* **23**, 1843–1855 (2003).
8. Pickart, C. M. & Eddins, M. J. *Biochim. Biophys. Acta* **1695**, 55–72 (2004).
9. Jin, J. *et al.* *Mol. Cell* **23**, 709–721 (2006).
10. Angers, S. *et al.* *Nature* **443**, 590–593 (2006).
11. Higa, L. A. *et al.* *Nature Cell Biol.* **8**, 1277–1283 (2006).
12. He, Y. J. *et al.* *Genes Dev.* **20**, 2949–2954 (2006).
13. Baba, T. *et al.* *Mol. Cell. Biol.* **25**, 10040–10051 (2005).
14. Dharmasiri, N., Dharmasiri, S. & Estelle, M. *Nature* **435**, 441–445 (2005).
15. Tarpey, P. S. *et al.* *Am. J. Hum. Genet.* **80**, 345–352 (2007).

MICROSCOPY

Tip-top imaging

Herman Batelaan and Kees Uiterwaal

Images of nanoscale structures can be constructed using the flow of electrons ejected from a metal probe tip by a fast laser pulse. The technique adds new dimensions to established methods of microscopy.

How can we see without eyes? One way is with electric fields. Fishes do this all the time: sharks, for instance, use electroreceptors to 'see' distortions of fields caused by nearby objects, and thus locate their prey. The builder's tool known as a stud finder works in a similar way, using electric fields to locate the load-bearing members inside a wall. Writing in *Physical Review Letters*, Ropers *et al.*¹ demonstrate a way to downscale this kind of depth-imaging capability to nanometre sizes.

Technologies for seeing objects too small for the naked eye have a long history. The Dutchman Antonie van Leeuwenhoek reported "with great wonder" the sight of microorganisms through one of his newly developed optical microscopes more than three centuries ago. Optical microscopy has been an important imaging tool ever since, despite an obvious limitation — it cannot be used to see structures smaller than the wavelength of visible light, roughly a micrometre. This shortcoming was bypassed in the 1930s in Germany, when the first microscope was built that exploited the fact that the electron, as a quantum-mechanical particle, is also a wave. An electron's wavelength becomes shorter the faster it moves: modern, fast electron microscopes can therefore spy out objects 10,000 times smaller than the smallest structures visible with an optical microscope.

But, as physicist Richard Feynman remarked in 1959, in a talk² often considered to mark the birth of nanotechnology, "there is plenty of room at the bottom". Scanning tunnelling microscopy (STM), invented in the 1980s, was the first of a series of revolutionary imaging techniques that can be used to probe surfaces down to their atomic structure. STM reveals a surface's structure by passing a very sharp needle over the surface, rather as the needle of an old-fashioned record player is dragged over a structured surface to reproduce the



D. PLUMMER/ALAMY

Figure 1 | Tip and flow. The discharge of current in a lightning strike bears similarities to the electron-imaging technique developed by Ropers and colleagues¹.

sounds imprinted on it. The shape of an STM tip distorts the electric field around it, causing a tunnelling current to flow to a nearby surface. In much the same way, a metal lightning rod on a tower distorts Earth's electric field, allowing a current of electrons stored in the clouds above to flow to Earth (Fig. 1).

The magnitude of the charge flow in STM depends on the distance between the probe and the surface, so an atomic-scale, contoured

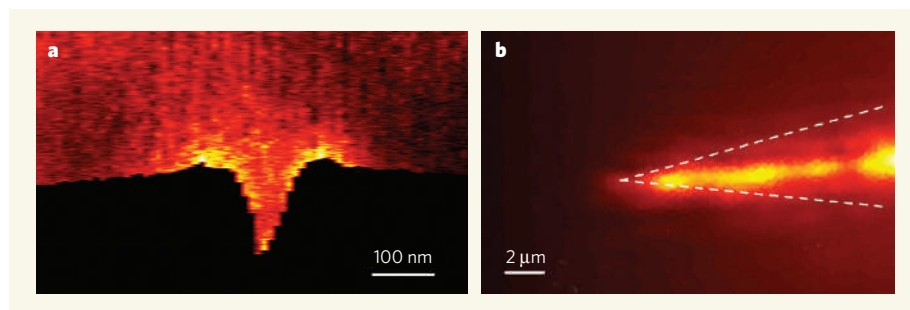


Figure 2 | Into the groove. **a**, Ropers and colleagues' 'tip-enhanced electron emission microscopy'¹ provides a picture of a nanoscale groove in a gold surface. **b**, The laser-illuminated probe tip.

'map' of the surface can be made. What STM cannot easily give us, however, is information on what happens in the third dimension above the surface. Step forward Ropers *et al.*¹, with their 'tip-enhanced electron emission microscopy'.

Like STM, the authors' technique involves measuring the effect of a sample surface on the electrical current flowing through a probe tip. So far, so conventional. But the real beauty of the technique is how that current is generated: it is stimulated by a pulsed laser beam focused on the tip. Because this laser field is affected by any kind of sample that is introduced near to the probe, the device can act in three dimensions. Furthermore, the current flow scales highly nonlinearly with changes in the laser field, making the imaging extremely sensitive to whatever is put near the probe tip.

So what sorts of things could the technique be used to look at? Ropers *et al.* use it to image a nanometre-scale groove on a gold surface (Fig. 2). But anything down to a single metal atom is theoretically possible: the spatial resolution of the authors' technique is given by the size of the metal tip, 20 nanometres, which is certainly scalable to atomic size. Questions such as the distance from which atomic-scale objects would be visible, and whether the technique could also be used for non-conducting nanostructures, will no doubt be addressed soon.

A further dimension is added to Roper and colleagues' technique through its time resolution. The laser pulses that dictate the electron emission are exceedingly short (7 femtoseconds, or 7×10^{-15} s) and have a frequency of 80 megahertz. This admits the exciting prospect of tracking atomic-scale dynamics in real time. For example, the authors suggest¹ that the dynamics of surface polaritons — discrete packets of energy that result from the interaction of an electric field and the vibrations of a material — could be studied using pairs of time-delayed pulses. Surface polaritons have been credited with wide-ranging potential for 'optical' devices that do not suffer the wavelength limitations associated with devices using light propagation.

Another recent study³ has achieved an electron pulse resolution of below 100 femtoseconds using an identical source, and there is promise for entering the attosecond

(10^{-18} s) domain³. Ahmed Zewail, who won the 1999 Nobel Prize in Chemistry for his studies of reaction dynamics using femtosecond spectroscopy, recently observed⁴ that "Ultrafast

electron microscopy should have an impact on all areas of microscopy, including biological imaging". Following Zewail's vision, Ropers *et al.* have made exciting progress in an area that might be called ultrafast near-field microscopy.

Herman Batelaan and Kees Uiterwaal are in the Department of Physics and Astronomy, Behlen Laboratory, University of Nebraska - Lincoln, City Campus, Lincoln, Nebraska 68588-0111, USA. e-mails: hbatelaan2@unl.edu; cuiteraal2@unl.edu

1. Ropers, C., Solli, D. R., Schulz, C. P., Lienau, C. & Elsaesser, T. *Phys. Rev. Lett.* **98**, 043907 (2007).
2. www.its.caltech.edu/~feynman/plenty.html
3. Hommelhoff, P., Kealhofer, C. & Kasevich, M. A. *Phys. Rev. Lett.* **97**, 247402 (2006).
4. Lobastov, V. A., Srinivasan, R. & Zewail, A. H. *Proc. Natl Acad. Sci. USA* **102**, 7069–7073 (2005).

EVOLUTIONARY BIOLOGY

Mass survivals

David Penny and Matthew J. Phillips

The conclusion that the primary divergences of the modern groups of mammals occurred in the mid-Cretaceous requires fresh thinking about this facet of evolutionary history — especially in ecological terms.

On page 507 of this issue, Bininda-Emonds and co-authors¹ present an evolutionary tree of more than 4,500 mammals, and conclude that more than 40 lineages of modern mammals have survived from the Cretaceous, some 100 million to 85 million years (Myr) ago, to the present. This is paralleled by Brown and colleagues' analyses for birds, just published in *Biology Letters*²: they claim that more than 40 avian lineages have likewise survived from before the extinctions at the Cretaceous/Tertiary (K/T) boundary 65 Myr ago. These numbers of surviving lineages push back the evolutionary history of many mammals and birds much further than earlier estimates based on smaller data sets^{3,4}. But strong claims need strong evidence to support them.

However, first things first, concentrating on mammals. Bininda-Emonds *et al.* present an evolutionary tree that includes 99% of living mammal species (4,510 out of 4,554), a major achievement in itself. They used a supertree⁵ approach, in which some 2,500 previously inferred subtrees were integrated into a large supertree (see Fig. 1 of the paper¹ on page 508). To date the supertree, they constructed an alignment that included 66 genes consisting of more than 51,000 nucleotides. These, plus 30 fossil calibration points, were used to estimate the times of the divergences and the rates of net speciation against time (Fig. 1, overleaf). Improvements will undoubtedly be made to the tree and its calibration points. However, inferring a good tree of such scale is groundbreaking, and the methods will be used as a

model for tree-of-life studies — whether of birds, flowering plants, invertebrate groups or other organisms.

An evolutionary tree is just the initial, descriptive, part of a study; from an evolutionary viewpoint, the real interest is using trees to learn about the processes of evolution. For context, the main divisions of existing mammals are the placental mammals (eutherians), the marsupials and the monotremes (such as the platypus). Each has its further subdivisions into order, then family, and so on.

The authors¹ report a period of radiation of placental mammals around 100–85 Myr ago; all modern orders are inferred to have diverged by 75 Myr ago. In contrast, they do not detect any radiation involving current placental lineages near the end of the Cretaceous. However, they do identify various radiations of modern families from the Eocene through to the Miocene (about 55–10 Myr ago). Modern families seem to radiate at slightly different times for the main lineages (such as for marsupials, Afrotheria, Supraprimates; Fig. 1), making it unlikely that a common physical cause was responsible. But the most challenging aspect of the phylogeny is the inference that more than 40 lineages of living mammals (and of birds, as described by Brown *et al.*²) survived from the Cretaceous to the present.

For mammals, there are three important areas of agreement (or at least non-disagreement) between the fossil record and the supertree results¹. The first is the initial radiation of modern eutherian lineages (from around

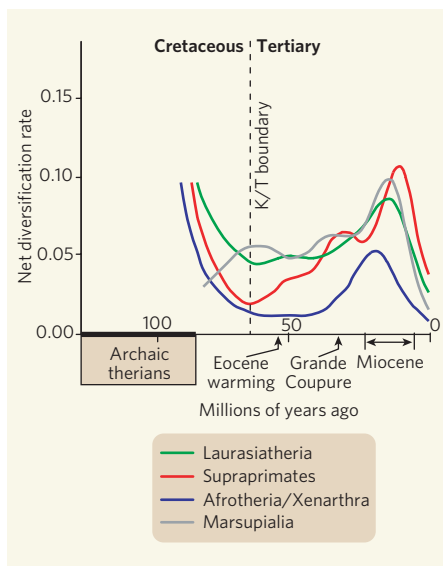


Figure 1 | Mammalian diversification over evolutionary time. The lineages shown are the Laurasiatheria (which include ungulates, whales, carnivores, core insectivores, bats), Supraprimates (primates, rodents, rabbits), and Afrotheria (elephants, sea cows, hyraxes, tenrecs, elephant shrews) and Xenarthra (armadillos, sloths, anteaters). The Marsupialia are non-placental mammals such as kangaroos. Note the overall lack of dramatic change at the K/T boundary¹. The 'Grande Coupure' is the rapid turnover of many mammal groups, at least in Europe, Asia and North America, around the end of the Oligocene (34 Myr ago). Major diversifications of many modern families date from around this time. Archaic therians are extinct relatives of later placental and marsupial mammals. (Net diversification rate = net speciation events, per lineage, per million years. Figure based on Supplementary Information, ref. 1.)

100–85 Myr ago)⁶. This is roughly coincident with the decline in frequency of earlier fossil mammalian groups⁷ (such as triconodonts, symmetrodonts and 'archaic' therians) and their replacement in several regions by placental and marsupial lineages of uncertain affinities, for example in Uzbekistan⁸. This is a key period for future work, although it may be hindered by a relatively poor fossil record from 95 to 80 Myr ago⁹.

The second area of agreement is that the radiation of eutherian mammals in the Early Tertiary (65–60 Myr ago), following the end-Cretaceous impact, was not primarily of existing placental lineages, but rather of now extinct groups including 'archaic' ungulates (omnivores), plesiadapiformes (primate relatives) and multituberculates (which might have filled a rodent-like niche). It had earlier been considered that the decline and eventual extinction of dinosaurs 'allowed' modern mammals to diversify, but it is clear that there were intermediate lineages, now extinct. The first two areas of agreement change the focus for the primary radiation of placental mammals (and for birds^{2,10}) back into the mid-Cretaceous. The third area of agreement between molecules

and fossils is that the modern families do not radiate until the Late Eocene through to the Miocene (Fig. 1). These agreements are a major achievement of the whole supertree approach. The results eliminate any direct suppression of modern orders of mammals by dinosaurs during the Late Cretaceous.

Taken together, these three areas of agreement mean that the pivotal macroevolutionary events in the evolution of existing placental mammals occurred either well before, or well after, the K/T boundary. The former events are the divergence between orders; the latter the radiation of families. It is notable that both the mammal¹ and avian¹¹ data sets were generated by teams that included both palaeontologists and specialists in molecular evolution. That combination allows questions to be addressed that neither group can do well independently. Each endeavour still has its own areas of uncertainty and issues that are independent of the other, but attempts at tackling many questions benefit from these interactions. In the future, integrative studies will need to go further in incorporating both biogeography and macroecology, including long-term niche stability. A view of the past¹² in which the main taxonomic divisions of mammals occur in the Cretaceous has many such consequences that will require more thought.

For example, the results reopen the intriguing question of the ecological roles of the early mammals and birds. Here, the present is the key to the past. For example, in the present, juvenile reptiles have different ecological niches from adults^{12,13}, and interactions between adult mammals and juvenile reptiles can be instructive. Thus, a small rat (*Rattus exulans*), whether by direct or indirect competition with the

young of tuatara (*Sphenodon*), eliminates this New Zealand reptile, which has 20 times the rat's adult body weight¹⁴ — even though adult tuatara are not directly affected. For longer-term effects, diversification of new groups can be studied in cases such as the past invasion of South America by placental mammals from the north, or the arrival of rodents in Australia. Bininda-Emonds and colleagues' study¹ illustrates how major improvements in evolutionary trees open up new research programmes, including studies of the present to explain the past.

David Penny and Matthew J. Phillips are at the Allan Wilson Center for Molecular Ecology and Evolution, Massey University, Palmerston North, New Zealand.

e-mails: d.penny@massey.ac.nz;
m.j.phillips@massey.ac.nz

- Bininda-Emonds, O. R. P. *et al.* *Nature* **446**, 507–512 (2007).
- Brown, J. W., Payne, R. B. & Mindell, D. P. *Biol. Lett.* doi:10.1098/rsbl.2006.0611 (2007).
- Cooper, A. & Penny, D. *Science* **275**, 1109–1113 (1997).
- Springer, M. S., Murphy, W. J., Eizirik, E. & O'Brien, S. J. *Proc. Natl Acad. Sci. USA* **100**, 1056–1061 (2003).
- Bininda-Emonds, O. R. P., Gittleman, J. L. & Steel, M. A. *Annu. Rev. Ecol. Syst.* **33**, 265–289 (2002).
- Benton, M. J. & Donoghue, P. C. J. *Mol. Biol. Evol.* **24**, 26–53 (2007).
- Kielan-Jaworowska, Z., Cifelli, R. L. & Luo, Z.-X. *Mammals from the Age of Dinosaurs: Origins, Evolution and Structure* (Columbia Univ. Press, New York, 2005).
- Archibald, J. D., Averianov, A. O. & Eklund, E. G. *Nature* **414**, 62–65 (2001).
- Benton, M. J. *BioEssays* **21**, 1043–1051 (1999).
- Slack, K. E. *et al.* *Mol. Biol. Evol.* **23**, 1144–1155 (2006).
- Ericson, P. J. P. *et al.* *Biol. Lett.* **4**, 543–547 (2006).
- Penny, D. & Phillips, M. J. *Trends Ecol. Evol.* **19**, 516–522 (2004).
- Murphy, J. B. *et al.* (eds) *Komodo Dragons* (Smithsonian Press, Washington DC, 2002).
- Towns, D. R., Atkinson, I. A. E. & Daugherty, C. H. *Biol. Invasions* **8**, 863–891 (2006).

BEHAVIOURAL GENETICS

Sex, flies and acetate

Charalambos P. Kyriacou

A receptor molecule in the fruitfly *Drosophila melanogaster* responds to a male pheromone in both sexes. But the effect of this response on sexual behaviour is not the same in males and females.

Courtship in the fruitfly *Drosophila* involves visual, gustatory, olfactory and acoustic sensations that mediate male advances and, until she mates, poorly understood female rejections¹. Cuticular pheromones have been implicated in sexual behaviour both within and between *Drosophila* species^{2,3}, but the only known volatile pheromone is 11-*cis*-vaccenyl acetate (cVA), a male-specific lipid that is transferred in the ejaculate to females during copulation⁴. When deposited on eggs or food, cVA causes flies to aggregate⁵ but, somewhat controversially⁶, cVA has also been reported to act as an 'anti-aphrodisiac', inhibiting the courtship

of males with previously mated females⁷. Perhaps as a consequence, interest in cVA in *Drosophila* waned rather. It has made a comeback in recent years⁸, however, and with three new papers — one by Kurtovic and colleagues on page 542 of this issue⁹, and a brace in *Current Biology*^{10,11} — the role of cVA and its receptors has been clarified.

To study the role of cVA, Ejima and collaborators¹⁰ exploited the principle that when a male fly is trained by courting an unreceptive, mated female, he remembers his experience, and subsequently shows less interest in courting a virgin female. They found that when

male flies were exposed to volatile fly extracts or cVA during the training session, either cVA, or mated female extract or male extracts, could generate the subsequent courtship inhibition, but that virgin female material could not (Table 1). Chromatographic analysis of volatile and non-volatile cuticular extracts revealed that the only significant difference between mated and virgin females was the presence of cVA, suggesting that this chemical might be responsible for the inhibitory effect on male courtship.

Several laboratories have studied the structure–function relationships of the 1,300 or so olfactory receptor neurons (ORNs) on the fly's antenna and maxillary palps^{12–14}. Up to four dendrites from ORNs are encapsulated within three types of chemosensory receptor cell — the basiconic, coeloconic and trichoid sensilla — and each neuron expresses one of about 60 G-protein-coupled odorant receptors encoded in the fly genome (Fig. 1). A putative receptor for cVA was initially identified by studies of the mutant *lush*. The normal *lush* gene encodes a protein that is expressed in the 150 or so singly innervated (T1) trichoid sensilla. The mutant was unexpectedly found to be insensitive to cVA, both by physiological recordings from ORNs in T1 sensilla and in behavioural aggregation assays⁸. The product of the *lush* gene is a putative odorant-binding protein for the receptor Or67d, which is co-expressed with it in T1 sensilla.

Van der Goes van Naters and Carlson¹¹ administered fly odours close to the T1, T2 and T3 trichoid sensilla, which make up about 20% of the antennal sensilla. They confirmed the ORN responses in T1 sensilla to cVA as above, but also observed an elevated impulse rate in a more disto-lateral group of T3 sensilla (Fig. 1a). The T1 sensilla were sensitive to male cuticular extracts, but were insensitive to those from virgin females, whereas the T2 and T3 sensilla, which have multiple ORNs, responded to both male and female extracts.

Using an 'empty neuron' *in vivo* system developed previously¹², van der Goes van Naters and Carlson expressed each of the 12 known trichoid odorant receptors within a neuron lacking its endogenous receptor gene, and measured their physiological responses to male and female cuticular extracts, as well as to cVA. This time, two receptors — Or67d and Or65a (the latter expressed in one of three T3 neurons) — responded to cVA¹¹. These two receptors also generated signals to extracts from males and mated females, but not to virgin female extracts, with Or67d giving the strongest responses. Two other receptors, Or47b and Or88a, responded to both male and female extracts but not to cVA. Therefore, activation of Or47b and Or88a

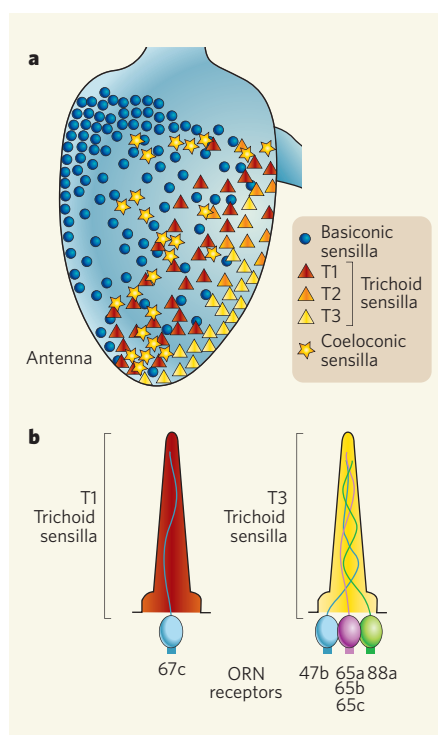


Figure 1 | The organization of antennal sensilla and their components. **a**, In *Drosophila*, three types of chemosensory receptor cell are found on the antenna — basiconic, trichoid and coeloconic. Trichoid sensilla are further divided into three subtypes: T1, T2 and T3. **b**, Each sensilla encapsulates olfactory receptor neurons (ORNs), so called because they express receptors that mediate perception of odours. The three papers discussed here^{9–11} describe the perception of the fly sex pheromone cVA through this system in males and females. (Figure redrawn from ref. 14.)

receptors might signal whether a fly is nearby, whereas activation of Or65a and Or67d receptors might report whether the fly is a virgin female or not.

In a different approach, Kurtovic *et al.*⁹ incorporated the gene encoding the yeast Gal4

activator of gene transcription into the *Or67d* locus, creating the *Or67d^{GAL4}* mutant, which allows Gal4-mediated expression of any gene under the control of the promoter and enhancers for the endogenous *Or67d* gene. Using a Gal4-responsive neuronal marker, they pinpointed the location of Or67d-expressing neurons in a specific cluster of nerve fibres in the antennal lobe and their incoming projections from the T1 sensilla in males and females.

Physiological recordings in an air-flow assay revealed equally robust responses of T1 sensilla to cVA in both sexes, suggesting that cVA has a function in the sexual response of both males and females. Indeed, they observed that male *Or67d^{GAL4}* mutants court virgin females normally, but when paired with other males, their behaviour was significantly more homosexual than that of normal flies, exposing again the inhibitory effect of cVA, but this time on male–male interactions.

The authors also found that when female *Or67d^{GAL4}* mutants were paired with normal males they played hard to get, even though males apparently found them as sexy as wild-type females; this suggests that cVA has a stimulatory effect on a female's receptivity. Smearing cVA on the abdomens of virgin females caused a suppression of normal male courtship but, predictably, not in male *Or67d^{GAL4}* mutants.

Kurtovic *et al.*⁹ also found that the separate expression, under *Or67d^{GAL4}* control, of receptors for two moth pheromones in place of Or67d enabled responses in the fly's T1 sensilla to moth-specific pheromones — silk-moth bombykol and tobacco-budworm (Z)-11-hexadecenal. Application of these moth pheromones to the abdomen of female flies resulted in a suppression of courtship towards them by the respective receptor-replaced males. Thus, activation of these Or67d-expressing neurons solely through olfaction of cVA seems sufficient to inhibit male courtship, and this single olfactory channel seems to have survived the evolutionary haze of 300 million years of divergence between the orders Lepidoptera and Diptera, to which moths and fruitflies respectively belong.

Or67d-expressing ORNs connect to other neurons that project to putative higher olfactory processing centres, which show sex-related differences in size¹⁵. Perhaps the switch between male-like and female-like responses to cVA lies in subtle sex-specific wiring patterns in these regions, which engage different downstream pathways in the two sexes. Another puzzle is that, in females, cVA is an attractant for both sex and aggregation, whereas in males it is aversive in a sexual context, but attractive for aggregation. The differing sex-specific behavioural responses in aggregation and sexual contexts may thus require additional olfactory signals

Table 1 | Odorant receptors and courtship in the fruitfly *Drosophila*. Synopsis of results from refs 9–11. WT, wild type.

Odour	Subject	Courtship response	Or67d, Or65a receptors	Or47b receptor	Or88b receptor
Mated female	Male WT	Inhibited	On	Off	On
Virgin female	Male WT	Activated	Off	On	On
Male	Male WT	Inhibited	On	On	On
cVA	Male WT	Inhibited	On	Off	Off
Male	Male <i>Or67^{GAL4}</i>	Activated	–	–	–
Virgin female	Male <i>Or67^{GAL4}</i>	Activated	–	–	–
Male	Female <i>Or67^{GAL4}</i>	Inhibited	–	–	–
Moth pheromone	Male <i>Or67^{GAL4}</i> -expressing UAS moth receptor	Activated	–	–	–



50 YEARS AGO

The Chemistry and Mode of Action of Plant Growth Substances — This volume is a collection of the full texts of papers contributed at the third International Conference on Plant Growth Substances... Since much of the data have appeared, or will be appearing, in botanical or chemical journals, the value of such a publication is left in some doubt... The great advantage of such meetings is that it allows scientists to 'stick out their necks'. The prospect of appearing in print is likely to inhibit this completely. The book is nevertheless an excellent technical production, and will doubtless be of great interest to all workers in the auxin field.

From *Nature* 30 March 1957.

100 YEARS AGO

In reference to the weight-judging competition, Mr Galton says that "the average competitor was probably as well fitted for making a just estimate of the dressed weight of the ox as the average voter is of judging the merits of most political issues on which he votes." These competitions are very popular in Cornwall; but I do not think that Mr Galton at all realises how large a percentage of the voters—the great majority, I should suspect—are butchers, farmers, or men otherwise occupied with cattle... I am afraid that the vast majority of such competitors know far more of their business, are far better trained, and are better fitted to form a judgment, than are the majority of voters of any party, and of either the uneducated or the so-called "educated" classes. I heartily wish that the case were otherwise.

F. H. Perry-Coste

I inferred that many non-experts were among the competitors... It would be of service in future competitions if a line headed "Occupation" were inserted in the cards, after those for the address.

Francis Galton

From *Nature* 28 March 1907.

acting through other receptors. These two unresolved issues might provide the basis for more immediate future investigations on this complex but tractable animal communication system.

Charalambos P. Kyriacou is in the Department of Genetics, University of Leicester, Leicester LE1 7RH, UK.
e-mail: cpk@leicester.ac.uk

- Hall, J. C. *Science* **264**, 1702–1714 (1994).
- Savarit, F., Sureau, G., Cobb, M. & Ferveur, J. F. *Proc. Natl Acad. Sci. USA* **96**, 9015–9020 (1999).
- Siwicki, K. K. *et al. Learn. Mem.* **12**, 636–645 (2005).
- Brieger, G. & Butterworth, F. M. *Science* **167**, 1262 (1970).
- Bartelt, R. J. *et al. J. Chem. Ecol.* **11**, 1747–1756 (1985).
- Scott, D. & Richmond, R. L. *J. Insect Physiol.* **33**, 363–369 (1967).
- Jallon, J.-M., Antony, C. & Benamar, O. C. R. *Acad. Sci., Paris* **292**, 1147–1149 (1981).
- Ha, T. S. & Smith, D. P. *J. Neurosci.* **26**, 8727–8733 (2006).
- Kurtovic, A., Widmer, A. & Dickson, B. J. *Nature* **446**, 542–546 (2007).
- Ejima, A. *et al. Curr. Biol.* doi:10.1016/j.cub.2007.01.053 (2007).
- van der Goes van Naters, W. & Carlson, J. R. *Curr. Biol.* doi:10.1016/j.cub.2007.02.043 (2007).
- Hall, E. A., Ho, M. G. & Carlson, J. R. *Cell* **117**, 965–979 (2004).
- Fishilevich, E. & Vosshall, L. B. *Curr. Biol.* **15**, 1548–1553 (2005).
- Couto, A., Alenius, M. & Dickson, B. J. *Curr. Biol.* **15**, 1535–1547 (2005).
- Stockinger, P., Kvitsiani, D., Rotkopf, S., Tirian, L. & Dickson, B. J. *Cell* **121**, 795–807 (2005).

SOLID-STATE PHYSICS

Vacillating valence

Robert C. Albers and Jian-Xin Zhu

Electrons in one particular solid phase of plutonium are complex characters: while bound to atoms, in a quantum-mechanical mixture of two different valence states, they also roam freely throughout the crystal.

Plutonium is the most puzzling element of the generally bizarre actinides, the group of metals that, together with the lanthanides, nestles below the standard periodic table. It is extremely sensitive to added impurities, and comes in six distinct solid phases below its melting point of just over 900 kelvin. In particular, its δ phase at 600 K is characterized by a hugely increased volume per atom, around 25% greater than that of its room-temperature (300 K) α phase¹.

On page 513 of this issue², Shim, Haule and Kotliar explain the odd behaviour of the δ phase in terms of an underlying instability in its electronic structure. Electrons in a solid can be either atomic — strongly bound and localized deep in the core of an atom — or metallic, delocalized and overlapping with the electrons of neighbouring atoms to form bonding or itinerant states. But the electrons in the outermost (5f) orbitals of plutonium's δ phase, which should be metallic, actually show qualities of both atomic and metallic electrons³. Shim *et al.* investigate this split personality in detail, and show that it arises from a mixture of two different atomic valence states. Previous work focused mainly on the metallic aspects of these electrons; this work allows us to penetrate the complexity of electronic states on the boundary of localization.

The dilemma of the dual nature of the δ phase 5f electrons is reminiscent of the early days of quantum mechanics, when controversy raged as to whether electrons were particles or waves. Eventually, it was decided that they were both. The 5f duality similarly has a quantum-mechanical origin, but this time it is in the 'correlated electron' problem. Electrons

have the same negative charge and so repel each other electrostatically. In simple, crystalline metals, this effect is weak, and the effect of all other electrons on one individual electron can be calculated using an averaged effective repulsive potential.

This 'self-consistent mean-field approximation' predicts itinerant electronic states, and provides generally accurate predictions of a metal's bonding, phase stability, equation of state, and so on. But where electrons are more strongly localized (atomic), the approximation starts to fail. New approaches must take into account not only how electron wavefunctions dance round each other in a correlated fashion so as to lower the total energy of the system, but also phenomena, such as the Pauli repulsion between two electrons of the same spin, that affect the metal's magnetic properties.

Calculating these correlation effects is fiendishly complex. It means ascertaining the detailed motion of every relevant electron — in a solid, some 10^{23} per cubic centimetre! An approximation is needed, and Shim *et al.*² use a promising approach called dynamical mean-field theory⁴. This technique makes the reasonable assumption that electronic correlations are strongest between electrons on the same atoms. Such an assumption makes it well suited to exploring the 5f electrons in δ -plutonium, whose wavefunctions only weakly overlap those of neighbouring atoms owing to the phase's lower atomic density.

An important test of any model of plutonium's electronic structure is whether it quenches magnetic tendencies. Localized electrons often have large quantum-mechanical 'exchange energies', which cause the alignment of electron

spins or orbital moments — in other words, magnetic behaviour. Most mean-field treatments that explain anomalies of the plutonium δ phase, such as its expanded volume, also predict that the phase is magnetic. Experimentally, this is not the case⁵. Shim *et al.*² and the authors of another recent paper⁶ show, however, that dynamical mean-field theory treats correlations sufficiently well to correctly predict a non-magnetic ground state.

Shim and colleagues also present² a more refined physical picture of this lack of magnetism, and in particular the role of the $5f$ orbitals. Plutonium is normally described as a trivalent metal with eight valence electrons in total; of these, three metallic electrons occupy the s , p and d orbitals. The authors' approach, which predicts about five electrons occupying δ -plutonium's $5f$ shell, is consistent with this picture. Other calculations^{6–8} come up with closer to six $5f$ electrons. The number six is significant, because the f shell in plutonium is split by strong spin–orbit interactions into two subshells, the lower-energy one of which, denoted by $f^{5/2}$, can contain six electrons. Filled subshells are magnetically inert: americium, the element with one atomic number higher than plutonium in the actinide series, is non-magnetic on account of having six localized $5f$ electrons.

Increasing plutonium's $5f$ electron occupation towards six would thus make it more like americium and naturally suppress magnetism, as well as correlation effects. Shim and colleagues' calculation of five electrons is therefore especially interesting because it shows that the lack of magnetism arises not from a full subshell, but from a competition between the localization tendencies of the $5f$ electrons and their coupling to the other metallic electrons — a signature of strong electron correlation. The authors' results are consistent with a range of experimental evidence for a significant amount of correlated-electron behaviour in this plutonium phase⁵.

Going beyond this, Shim *et al.* do not find that the $5f$ shell of δ -plutonium is filled by exactly five electrons, but, on average, slightly more (about 5.2). The explanation is that, in quantum-mechanical terms, the electrons can, for short periods of time, preserve their atomic character in a superposition of two atomic valence states with five and six $5f$ electrons, while at the same time also maintaining their metallic, delocalized hopping from atom to atom. With their calculations of the probability of occupation of the various valence states, the authors provide a remarkably detailed picture of the atomic character of these electrons. That extends even to the fine splittings of allowed energy levels typically seen in individual atoms, and how these are related to structure observed in the experimental photoemission spectra.

The authors extend their calculations to curium, the actinide metal one beyond the inert americium. Their model correctly predicts this material to be magnetic, with predominantly

one valence state of seven $5f$ electrons. These localized, magnetic, atomic-like electrons have an energy that overlaps those of the other metallic, valence-band electrons in the s , p and d orbitals, instead of having a lower energy as they do in the lanthanide series.

It is often said that the actinide metals with an atomic number equal to or greater than americium form a second lanthanide series⁹. But Shim and colleagues' calculations² imply that the electronic structure of these actinides is actually far more complex than a simple localized $5f$ shell. Confirmatory experiments — for example, measurement of photoemission and of the materials' specific heat and transport properties — are difficult, but it seems that there is new and interesting physics to be discovered. How electron duality might affect the

electronic, magnetic and other properties of elements even closer to the limit of the periodic table is an exciting, unexplored frontier. ■

Robert C. Albers and Jian-Xin Zhu are in the Condensed Matter and Statistical Physics Group, Theoretical Division, Los Alamos National Laboratory, Los Alamos, New Mexico 87545, USA. e-mail: rca@lanl.gov

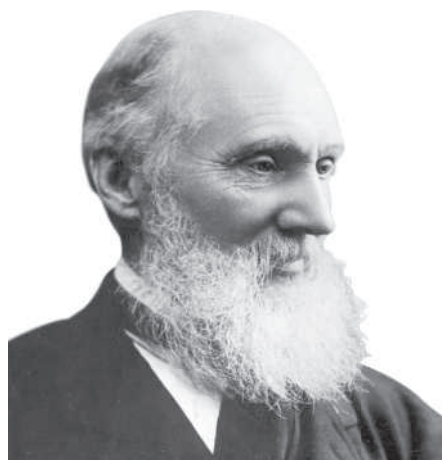
1. Hecker, S. S., Harbur, D. R. & Zocco, T. G. *Prog. Mater. Sci.* **49**, 429–485 (2004).
2. Shim, J. H., Haule, K. & Kotliar, G. *Nature* **446**, 513–516 (2007).
3. Albers, R. C. *Nature* **410**, 759–761 (2001).
4. Georges, A. *et al. Rev. Mod. Phys.* **68**, 13–125 (1996).
5. Lashley, J. C. *et al. Phys. Rev. B* **72**, 054416 (2005).
6. Pourvorskii, L. V. *et al. Europhys. Lett.* **74**, 479–485 (2006).
7. Shorikov, A. O. *et al. Phys. Rev. B* **72**, 024458 (2005).
8. Shick, A. B., Drchal, V. & Havela, L. *Europhys. Lett.* **69**, 588–594 (2005).
9. Lander, G. H. *Science* **301**, 1057–1058 (2003).

CHEMISTRY

Compliments from Lord Kelvin

Laurence D. Barron

Telling if a molecule is right-handed or left-handed is a venerable problem, but traditional approaches cannot touch the subtlest cases. As so often, technical innovation has provided the way forward.



Were he alive today, Lord Kelvin (above) would be impressed with the work of Haesler *et al.*¹ reported on page 526 of this issue. Kelvin² was the first to introduce the word 'chirality', meaning right- or left-handedness, into science, and was equally adept at experimental and theoretical physics. He would have enjoyed the combination of exquisite instrumentation and advanced theoretical simulation with which the authors have confirmed the absolute configuration (handedness) of a small organic molecule designed to possess structural chirality of the utmost delicacy.

Kelvin's original definition is essentially that still used in stereochemistry today^{3,4}: "I call any geometrical figure or group of points *chiral*, and say that it has chirality if its image in a plane mirror, ideally realized, cannot be

brought into coincidence with itself"². The principle is illustrated in Figure 1 (overleaf), with the two possible non-superposable mirror-image structures (enantiomers) of the small archetypal chiral molecule bromochlorofluoromethane (CHFCIBr). A fundamental problem in stereochemistry is that, given a sample of a pure enantiomer, how do you know, using physical methods alone (rather than chemical or biochemical inferences), which of the two enantiomers it is? The definitive method for determining absolute configuration⁵ actually 'sees' the absolute handedness directly through anomalous X-ray scattering. But this requires the introduction of a heavy atom into the structure and cannot be used for most molecules.

Chirality has a rich history^{3,4}. The classic manifestation, discovered in the early years of the nineteenth century, is natural optical rotation of the plane of polarization of linearly polarized light by a chiral medium, such as a solution of chiral molecules. This was subsequently shown to originate in different refractive indices of the chiral material for right- and left-circularly polarized light. It was followed in 1848 by Louis Pasteur's epoch-making discovery that mirror-image enantiomers generate equal and opposite optical-rotation angles. The reason optical rotation is sensitive to chirality is that circularly polarized light, being itself intrinsically chiral, acts as a chiral probe⁴. The correspondence between the (+) or (–) sign of the optical rotation at a particular wavelength and the absolute configuration is used as a

macroscopic label, as in (*S*)(+)- and (*R*)(-)-CHFCIBr in Figure 1. Here, *R* (for *rectus*) and *S* (for *sinister*) are the absolute configurations in the standard nomenclature³.

Optical rotation and circular dichroism (a small difference in the absorption of right- and left-circularly polarized light) at visible and ultraviolet wavelengths measure natural optical activity in the electronic spectrum of a molecule. It had long been appreciated that extending natural optical activity into the vibrational spectrum could provide more detailed and reliable stereochemical information, because a vibrational spectrum contains many more bands sensitive to the details of the molecular structure⁴. This was finally achieved in the early 1970s, when vibrational optical activity was first observed in small chiral molecules in fluid media using two complementary techniques: a circular-polarization dependence of vibrational Raman scattering of visible laser light⁶, and circular dichroism of infrared radiation⁷. These are now known as Raman optical activity (ROA) and vibrational circular dichroism (VCD), respectively.

Haesler *et al.*¹ tested the limits of a new ROA instrument developed in their laboratory by applying it to a chiral molecule for which it would be very difficult, if not impossible, to determine the absolute configuration using any other existing physical technique. They chose (*R*)-[²H₁,²H₂,²H₃]-neopentane, which is C(CH₃)₄ rendered chiral through isotopic substitution — deuteration — of three of the four methyl groups (Fig. 2). In other words, chirality was induced by replacing ordinary hydrogen (¹H) in three of the four CH₃ groups with deuterium (²H, or D), producing one each of CH₃, CH₂D, CHD₂ and CD₃.

Haesler and colleagues' synthesis¹ of (*R*)-[²H₁,²H₂,²H₃]-neopentane with high enantiomeric purity was itself an achievement, and was attempted only after calculations⁸ suggested that the ROA might be measurable. It is a gas at room temperature, but was collected as a

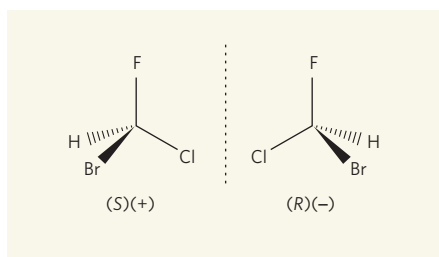


Figure 1 | Chiral archetype. Lord Kelvin's classic definition of chirality² emphasizes the non-superposability of a chiral object and its mirror image, exemplified here by the enantiomers of bromochlorofluoromethane, CHFCIBr.

liquid for ROA measurements by distilling into a cooled capillary tube that was subsequently sealed. Three distinct orientations of each of the CH₂D and CHD₂ groups are possible, generating nine distinct rotational 'conformers' that all contribute to chiroptical observable properties and tend to cancel.

The ROA turned out to be just detectable at the limit of sensitivity of the authors' new instrument, which measures tiny circularly polarized components in the vibrational Raman bands down to a few parts in 10⁻⁵ of the total band intensity (Fig. 2). This instrument separates the right- and left-circularly polarized components of the backscattered light and collects them into the ends of two fibre-optic strands. This allows separate Raman spectra for the right- and left-circularly polarized components of the scattered light to be dispersed simultaneously, one above the other, onto a multichannel detector. Subtraction then provides the required ROA spectrum. Because the right- and left-circularly polarized Raman spectra are measured during the same acquisition period, the 'flicker noise' arising from dust particles, density fluctuations, fluctuations in laser power and so on cancels out, resulting in greatly superior signal-to-noise characteristics compared with earlier designs of the instrument. Other novel features provide a high

degree of suppression of the spurious signals that can plague this type of delicate polarization measurement.

Haesler *et al.*¹ simulated the ROA spectrum of the chiral neopentane using *ab initio* quantum-chemical protocols⁸. They summed the partially cancelling ROA spectra computed for each of the nine possible rotational conformers present at thermal equilibrium. The resulting theoretical spectrum was close enough to the observed spectrum with respect to the signs and magnitudes of the ROA bands for the *R* absolute configuration to be assigned unequivocally to their neopentane sample. This highlights the power of vibrational optical activity generally — VCD (ref. 9) as well as ROA — for determining absolute configuration: as there are numerous bands, a calculation that reproduces the signs of most, if not all, of them correctly will provide an absolute configuration on which one might stake one's life.

As well as probing the most delicate sources of chirality in small molecules, ROA provides valuable information about very large chiral molecular structures, such as proteins, sugars and nucleic acids¹⁰. Even intact viruses are accessible to ROA measurements, and from these, for instance, details about the folds of coat proteins and the nucleic-acid structure may be deduced. The power of chiroptical spectroscopic techniques for biomolecular applications derives from their ability to cut through the complexity of conventional spectra (which are 'blind' to chirality), to reveal three-dimensional information about the most rigid, twisted chiral parts of the structure. These are usually found within the backbone in large biomolecules, and generate the largest chiroptical signals. The decisive advances in ROA instrumentation reported by Haesler *et al.*¹, backed up by powerful theoretical simulation techniques, should facilitate widespread exploitation of vibrational optical activity in chemical and biomolecular science. ■

Laurence D. Barron is in the Department of Chemistry, University of Glasgow, Glasgow G12 8QQ, UK.
e-mail: laurence@chem.gla.ac.uk

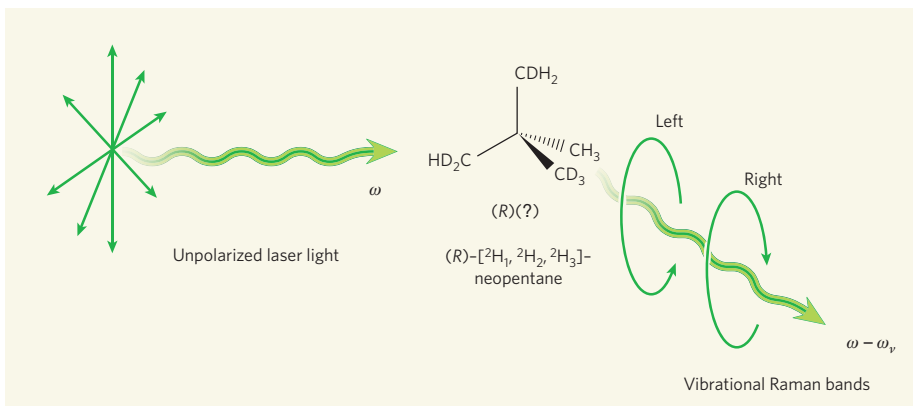


Figure 2 | Determination of the absolute configuration of (*R*)-[²H₁,²H₂,²H₃]-neopentane. Unpolarized laser light incident on the deuterated molecule produces tiny but measurable right- or left-circularly polarized components in the bands of the resulting vibrational Raman spectrum. ω is the angular frequency of the incident visible laser beam and $\omega - \omega_v$ that of one of the many vibrational Raman bands. By comparing these measurements with the expectations of *ab initio* simulations, Haesler *et al.*¹ could assign the *R* absolute configuration to their sample. No (+) or (−) sign is associated with the *R* absolute configuration because there was insufficient material to measure the corresponding optical rotation.

- Haesler, J., Schindelhof, I., Riguet, E., Bochet, C. G. & Hug, W. *Nature* **446**, 526–529 (2007).
- Lord Kelvin *Baltimore Lectures* (Clay, London, 1904).
- Eliel, E. L. & Wilen, S. H. *Stereochemistry of Organic Compounds* (Wiley, New York, 1994).
- Barron, L. D. *Molecular Light Scattering and Optical Activity* 2nd edn (Cambridge Univ. Press, 2004).
- Bijvoet, J. M. *et al.* *Nature* **168**, 271–272 (1951).
- Barron, L. D., Bogaard, M. P. & Buckingham, A. D. *J. Am. Chem. Soc.* **95**, 603–605 (1973).
- Holzwarth, G. *et al.* *J. Am. Chem. Soc.* **96**, 251–252 (1974).
- Hug, W. & Haesler, J. *Int. J. Quantum Chem.* **104**, 695–715 (2005).
- Stephens, P. J. & Devlin, F. J. *Chirality* **12**, 172–179 (2000).
- Barron, L. D. *Curr. Opin. Struct. Biol.* **16**, 638–643 (2006).

Correction

In the News & Views Q&A article "Organometallic chemistry: C–H activation" by Robert G. Bergman (*Nature* **446**, 391–393; 2007), the e-mail address given for the author was incorrect. The correct address is rbergman@berkeley.edu

ECOLOGY

Diversity and stability in plant communities

Arising from: D. Tilman, P. B. Reich & J. M. H. Knops *Nature* 441, 629–632 (2006)

The relationship between species diversity and ecosystem stability is controversial^{1,2}. Tilman *et al.*³ analyse biomass patterns over a decade in a grassland experiment with artificial plant communities, and provide evidence for a positive relationship between the number of plant species and the temporal stability of the ecosystem. Here we use data from a long-term biodiversity experiment with plant communities that were not controlled by weeding⁴ in order to show that diverse systems can be both stable and unstable.

In 1996, we established plant communities by sowing low-diversity (4 species) and high-diversity (15 species) seed mixtures, and compared the development of the plant communities with those of unsown plots⁴. After sowing, by contrast with other diversity trials^{3,5}, plots were not weeded so that subsequent development of the plant community was due to natural colonization and plant-community assemblage processes. In the following nine years, plant diversity and above-ground biomass were higher in plots sown with 15, rather than 4, species (Fig. 1a–c). The results were the same when we excluded the initial years after sowing, which excludes the possibility that the starting conditions caused the observed effects (Table 1). Increasing the seed-mixture diversity enhanced biomass production, as in plant communities in which diversity was maintained by hand-weeding^{3,5}. However, the richness and diversity of the species were consistently highest in non-sown plots, which had the lowest biomass production (Fig. 1a–c; Table 1).

Temporal stability, based on biomass production³, was lowest in the non-sown plots and highest in plant communities that were initially sown with 15 species (Fig. 1d). The stability of individual species was also lowest in non-sown plots. Annual rates of extinction and colonization were higher in non-sown than in sown plots, and in plots sown with 4 species rather than 15 species (Fig. 1e,f; Table 1).

Most plant species occurred in all plots, but at different densities. A total of 58 plant species were recorded, with cover being greater than or equal to 1% per square metre on at least one sampling occasion. Of these, only four species were recorded exclusively in some of the non-sown plots and one in plots sown with four species. In almost all cases, those species were rare locally and did not contribute significantly to biomass production (see Methods). Moreover, the observed differences in the rates of extinction and colonization could not be attributed to the presence or absence of those species.

Temporal stability was not related to species

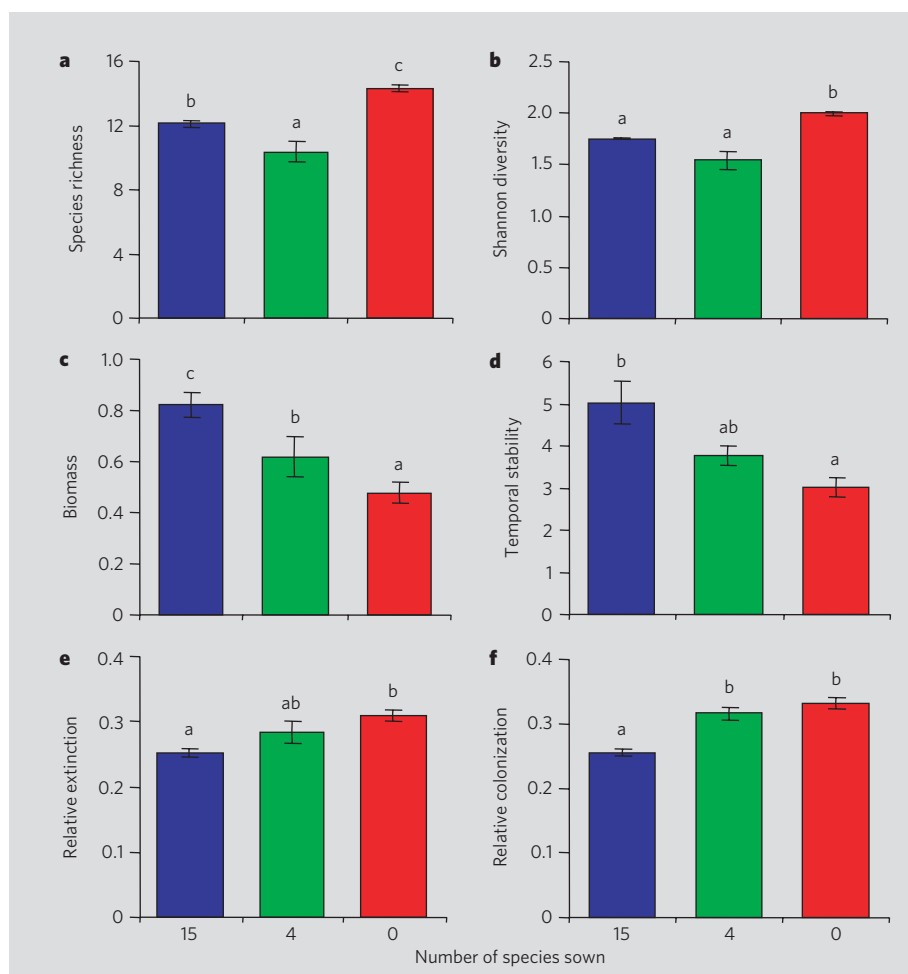


Figure 1 | Initial seed-diversity level (15, 4 or 0 species) determines long-term ecosystem characteristics in unweeded grassland plots. Means for 1997–2005 are shown (\pm s.e.) for: **a**, species richness (number per square metre); **b**, Shannon diversity; **c**, above-ground biomass (kilograms per square metre); **d**, temporal stability (calculated as the mean biomass of each plot over the study period, divided by the standard deviation for that period); **e**, relative annual extinction rate (number of species in 1-m² subplots going extinct between two subsequent years, divided by mean number of species present in those two years); and **f**, relative annual colonization rate (number of species in 1-m² subplots colonizing between two subsequent years, divided by the mean number of species present in those two years). Within in each panel, letters above bars indicate significant differences ($P < 0.05$) between individual sowing treatments (0, 4, 15 species), based on a Tukey HSD test after the ‘between’ analysis (see Table 1).

richness, but there was a positive relationship with biomass ($r = 0.62$), whereas productivity was negatively related to extinction ($r = -0.89$) and colonization rates ($r = -0.68$). Biomass, in turn, was strongly positively related to legume abundance ($r = 0.82$), which was lowest in non-sown plots. Legume abundance therefore strongly influences relationships between diversity and functioning in plant communities, as in artificially assembled communities⁶.

Our results show that a long-term positive relationship between biodiversity and ecosystem stability also occurs in plant

communities that have not been weeded after sowing. However, in the non-sown, completely self-assembled plant communities, we found that high species diversity coincided with low temporal stability, and high extinction and colonization. We conclude that diversity–stability relationships are strongly context dependent.

Methods. Experimental plots were 100 m², with five replicate plots per diversity treatment (15, 4 or 0 species sown). After sowing, plots were not weeded, but above-ground biomass was removed annually in

September. Abundance of individual plant species and above-ground biomass were recorded annually in 12 permanent subplots. Data (averaged per plot) were analysed for the period 1997–2005, thereby omitting the establishment year (1996). For further information, see www.nioo.knaw.nl/ppages/mbezemer/.

T. Martijn Bezemer*†‡, **Wim H. van der Putten***†

*Department of Multitrophic Interactions, Netherlands Institute of Ecology, PO Box 40, 6666 ZG Heteren, the Netherlands

†Laboratory of Nematology, Wageningen University and Research Centre, PO Box 8123, 6700 ES Wageningen, the Netherlands
e-mail: martijn.bezemer@wur.nl

‡Laboratory of Entomology, Wageningen University and Research Centre, PO Box 8031 6700 EH Wageningen, the Netherlands

Received 15 June 2006; accepted 27 February 2007.

1. Lehman, C. L. & Tilman, D. *Am. Nat.* **156**, 534–552 (2000).
2. Pfisterer, A. B. & Schmid, B. *Nature* **416**, 84–86 (2002).
3. Tilman, D., Reich, P. B. & Knops, J. M. H. *Nature* **441**, 629–632 (2006).
4. Fukami, T., Bezemer, T. M., Mortimer, S. R. & van der Putten, W. H. *Ecol. Lett.* **8**, 1283–1290 (2005).
5. Hector, A. et al. *Science* **286**, 1123–1127 (1999).
6. Hooper, D. U. et al. *Ecol. Monogr.* **75**, 3–35 (2005).

Competing financial interests: declared none.
doi:10.1038/nature05749

Table 1 | Results of repeated measures analysis of variance (ANOVA) (F and P values)

	Between effect		Time × treatment interaction	
	F	P	F	P
Test for 0, 4, 15 species				
Species richness	20.60	0.0005	2.56	0.004
Shannon diversity	18.87	0.0009	5.64	<0.0001
Above-ground biomass	42.33	<0.0001	1.65	0.08
Temporal stability	8.28	0.01		
Relative colonization rate	38.66	<0.0001	8.07	<0.0001
Relative extinction rate	9.75	0.007	2.79	0.0032
Test for 4, 15 species				
Species richness	7.33	0.05	3.03	0.01
Shannon diversity	5.44	0.07	8.32	0.0002
Above-ground biomass	23.03	0.009	0.58	0.8
Temporal stability	6.29	0.07		
Relative colonization rate	40.26	0.003	6.09	0.0002
Relative extinction rate	4.16	0.1	2.99	0.02
Test for sown, non-sown plots				
Species richness	15.19	0.003	2.53	0.02
Shannon diversity	16.60	0.003	4.73	0.0001
Above-ground biomass	15.41	0.003	2.82	0.009
Temporal stability	8.19	0.02		
Relative colonization rate	4.61	0.06	5.36	<0.0001
Relative extinction rate	8.91	0.02	1.54	0.2

Between effects are independent of time, whereas the time × treatment interaction tests for differences in the response of treatments over the period 1997 to 2005. Three tests were carried out: one that compared all three sowing treatments, one that compared the two diversity levels of sown plots, and one that compared sown with unsown plots. Temporal stability was calculated over the whole time period and was analysed with ANOVA. To obtain normality, data were log-transformed before analysis when appropriate. The effect of sowing diversity (4 versus 15 species) remains significant for species richness and Shannon diversity when the first three years after establishment (1997–99) are omitted from the analyses.

ECOLOGY

Tilman et al. reply

Replying to: T. M. Bezemer & W. H. van der Putten *Nature* **446**, doi: 10.1038/nature05749 (2007)

Bezemer and van der Putten¹ observe that greater initial plant diversity is associated with greater productivity (total above-ground plant biomass), greater ecosystem temporal stability and greater stability of plant community composition (that is, lower per-species extinction and colonization rates). Their results are consistent with the results of our biodiversity experiment² and with predictions of theory³, but with an intriguing twist.

In their study, initial plant diversity (number of species sown) had a strong and long-lasting effect on ecosystem productivity (biomass) and temporal stability (see their Fig. 1 c, d), whereas the number of species acquired through natural community assembly seems to have no consistent effect on productivity and ecosystem stability. In particular, if the species-richness data of their Fig. 1a are used as the independent variable and the associated data on biomass (their Fig. 1c) and temporal stability (their Fig. 1d) as dependent variables, the resulting graphs indicate that there is no relationship between assembled species richness and these two variables.

Why might initial planted diversity matter,

but not the diversity that results from subsequent community invasion during assembly? Field experiments that have controlled for both plant species number and species composition by use of randomized designs have shown that both diversity and composition are significant determinants of productivity^{4–6} and temporal stability². Bezemer and van der Putten¹ do not control for species composition but rather allow natural community assembly to determine composition and, ultimately, the number of plant species, which confounds diversity and composition. They reported earlier that the assembly process did not lead to convergent compositions, and that compositions of their three seeding treatments (seeding plots with 0, 4 or 15 species) remained as different after nine years as they had been after their first year of growth⁷.

It seems likely that many of the species that invaded the unsown plots were early successional species, and so may have been better colonists but poorer competitors, with lower nutrient-use efficiencies than the sown species. If so, rather than clouding earlier results, their results reinforce the concept

that ecosystem functioning depends just as much on which species are present as on how many are present. The two experiments are hence easily reconciled — in our experiment, diversity effects were examined while holding composition neutral, whereas composition effects swamped the diversity effect in the experiments of Bezemer and van der Putten¹.

Additionally, their results offer an insight into restoration ecology. Planting a disturbed site with a higher number of native, late successional species (their 15-species treatment) led to greater productivity and to greater temporal stability than did planting fewer such species (their four-species treatment), which, even after nine years, had a similar advantage over the unrestored (unsown) plots that were undergoing succession. More complete restoration caused better ecosystem functioning. It will be interesting to see, if the experiment continues, if or when the three treatments converge in their productivity and temporal stability.

David Tilman*, **Peter B. Reich**†, **Johannes Knops**‡

*Department of Ecology, Evolution and Behavior,

and ‡Department of Forest Resources, University of Minnesota, St Paul, Minnesota 55108, USA
e-mail: tilman@umn.edu

§School of Biological Sciences, University of Nebraska, Lincoln, Nebraska 68588-0118, USA

1. Bezemer, T. M. & van der Putten, W. H. *Nature* **446**, doi: 10.1038/nature05749 (2007).
2. Tilman, D., Reich, P. B. & Knops, J. M. H. *Nature* **441**, 629–632 (2006).
3. Lehman, C. L. & Tilman, D. *Am. Nat.* **156**, 534–552 (2000).
4. Tilman, D. *et al. Science* **294**, 843–845 (2001).
5. Hooper, D. U. *et al. Ecol. Monogr.* **75**, 3–35 (2005).
6. Reich, P. B. *et al. Proc. Natl Acad. Sci. USA* **101**, 10101–10106 (2004).
7. Fukami, T., Bezemer, T. M., Mortimer, S. R. & van der Putten, W. H. *Ecol. Lett.* **8**, 1283–1290 (2005).

doi: 10.1038/nature05750

The delayed rise of present-day mammals

Olaf R. P. Bininda-Emonds^{1†}, Marcel Cardillo^{2†}, Kate E. Jones⁴, Ross D. E. MacPhee⁵, Robin M. D. Beck⁶, Richard Grenyer⁷, Samantha A. Price⁸, Rutger A. Vos⁹, John L. Gittleman¹⁰ & Andy Purvis^{2,3}

Did the end-Cretaceous mass extinction event, by eliminating non-avian dinosaurs and most of the existing fauna, trigger the evolutionary radiation of present-day mammals? Here we construct, date and analyse a species-level phylogeny of nearly all extant Mammalia to bring a new perspective to this question. Our analyses of how extant lineages accumulated through time show that net per-lineage diversification rates barely changed across the Cretaceous/Tertiary boundary. Instead, these rates spiked significantly with the origins of the currently recognized placental superorders and orders approximately 93 million years ago, before falling and remaining low until accelerating again throughout the Eocene and Oligocene epochs. Our results show that the phylogenetic 'fuses' leading to the explosion of extant placental orders are not only very much longer than suspected previously, but also challenge the hypothesis that the end-Cretaceous mass extinction event had a major, direct influence on the diversification of today's mammals.

Molecular data and the fossil record can give conflicting views of the evolutionary past. For instance, empirical palaeontological evidence by itself tends to favour the 'explosive model' of diversification for extant placental mammals¹, in which the orders with living representatives both originated and rapidly diversified soon after the Cretaceous/Tertiary (K/T) mass extinction event that eliminated non-avian dinosaurs and many other, mostly marine², taxa 65.5 million years (Myr) ago^{1,3,4}. By contrast, molecular data consistently push most origins of the same orders back into the Late Cretaceous period^{5–9}, leading to alternative scenarios in which placental lineages persist at low diversity for some period of time after their initial origins ('phylogenetic fuses'; see ref. 10) before undergoing evolutionary explosions^{1,11}. Principal among these scenarios is the 'long-fuse model'¹, which postulates an extended lag between the Cretaceous origins of the orders and the first split among their living representatives (crown groups) immediately after the K/T boundary⁸. Some older molecular studies advocate a 'short-fuse model' of diversification¹, where even the basal crown-group divergences within some of the larger placental orders occur well within the Cretaceous period^{5–7}.

A partial molecular phylogeny emphasizing divergences among placental orders suggested that over 20 lineages with extant descendants (henceforth, 'extant lineages') survived the K/T boundary⁸. However, the total number of extant lineages that pre-date the extinction event and whether or not they radiated immediately after it remain unknown. The fossil record alone does not provide direct answers to these questions. It does reveal a strong pulse of diversification in stem eutherians immediately after the K/T boundary^{4,12}, but few of the known Palaeocene taxa can be placed securely within the crown groups of extant orders comprising Placentalia⁴. The latter only rise to prominence in fossils known from the Early Eocene epoch onwards (~50 Myr ago) after a major faunal reorganization^{4,13,14}. The geographical patchiness of the record complicates interpretations of this near-absence of Palaeocene crown-group fossils^{14–16}: were these clades radiating throughout the Palaeocene epoch in parts of the

world where the fossil record is less well known; had they not yet originated; or did they have very long fuses, remaining at low diversity until the major turnover at the start of the Eocene epoch?

The pattern of diversification rates through time, to which little attention has been paid so far, might hold the key to answering these questions. If the Cretaceous fauna inhibited mammalian diversification, as is commonly assumed¹, and all mammalian lineages were able to radiate after their extinction, then there should be a significant increase in the net per-lineage rate of extant mammalian diversification, r (the difference between the per-lineage speciation and extinction rates), immediately after the K/T mass extinction. This hypothesis, along with the explosive, long- and short-fuse models, can be tested using densely sampled phylogenies of extant species, which contain information about the history of their diversification rates^{17–20}.

Using modern supertree algorithms^{21,22}, we construct the first virtually complete species-level phylogeny of extant mammals from over 2,500 partial estimates, and estimate divergence times (with confidence intervals) throughout it using a 66-gene alignment in conjunction with 30 cladistically robust fossil calibration points. Our analyses of the supertree indicate that the principal splits underlying the diversification of the extant lineages occurred (1) from 100–85 Myr ago with the origins of the extant orders, and (2) in or after the Early Eocene (agreeing with the upturn in their diversity known from the fossil record^{4,13,14}), but not immediately after the K/T boundary, where diversification rates are unchanged. Our findings—that more extant placental lineages survived the K/T boundary than previously recognized and that fewer arose immediately after it than previously suspected—extend the phylogenetic fuses of many extant orders and indicate that the end-Cretaceous mass extinction event had, at best, a minor role in driving the diversification of the present-day mammalian lineages.

A supertree with divergence times for extant mammals

The supertree contains 4,510 of the 4,554 extant species recorded in ref. 23, making it 99.0% complete at the species level (Fig. 1; see also

¹Lehrstuhl für Tierzucht, Technical University of Munich, 85354 Freising-Weihenstephan, Germany. ²Division of Biology, and ³NERC Centre for Population Biology, Imperial College, Silwood Park campus, Ascot SL5 7PY, UK. ⁴Institute of Zoology, Zoological Society of London, Regents Park, London NW1 4RY, UK. ⁵Division of Vertebrate Zoology, American Museum of Natural History, New York, New York 10024, USA. ⁶School of Biological, Earth and Environmental Sciences, University of New South Wales, Sydney, New South Wales 2052, Australia. ⁷Jodrell Laboratory, Royal Botanic Gardens, Kew, Richmond, Surrey TW9 3AB, UK. ⁸National Evolutionary Synthesis Center (NESCent), Durham, North Carolina 27705, USA. ⁹Department of Zoology, University of British Columbia, Vancouver, British Columbia V6T 1Z4, Canada. ¹⁰Institute of Ecology, University of Georgia, Athens, Georgia 30602, USA. [†]Present addresses: Institut für Spezielle Zoologie und Evolutionsbiologie mit Phyletischem Museum, Friedrich-Schiller-Universität Jena, 07743 Jena, Germany (O.R.P.B.-E.); Centre for Macroevolution and Macroecology, School of Botany and Zoology, Australian National University, Canberra 0200, Australia (M.C.).

Supplementary Fig. 1 and Supplementary Table 1). Most major clades have complete taxonomic coverage and all are more than 90% complete except for Afrotheria (tenrecs and golden moles; 78.6%). The supertree is 46.7% resolved compared to a fully bifurcating tree, with poorly resolved areas being generally found closer to the tips of the tree, particularly within Muridae and other rodent families (Supplementary Table 1). Roughly 63% of the 2,108 nodes in the tree were dated on the basis of one or more estimates from molecular sequence data and/or cladistically robust fossil estimates (Supplementary Table 2).

The two earliest splits in the phylogeny established Monotremata by 166.2 Myr ago, and then Marsupialia and Placentalia by 147.7 Myr ago (Table 1). After nearly 50 Myr without the origination of any further extant groups, all four placental superorders (Afrotheria, Euarchontoglires, Laurasiatheria and Xenarthra) arose within 2.4 Myr of

one another around 100 Myr ago. This period seems to mark the start of a temporal hotspot of eutherian diversification: nearly all extant placental orders originated by 85 Myr ago, and all had appeared by 75 Myr ago, some 10 Myr before the K/T boundary. This interval of rapid eutherian radiation from 100–85 Myr ago is also notable for many other events in Earth history (for example, the rise of angiosperms; general reduction in worldwide temperatures to the Campanian low at 75 Myr ago; the Cenomanian/Turonian boundary ocean anoxic event at 93.5 Myr ago), but whether the co-occurrence is more than coincidence is beyond the scope of this work. The phylogeny suggests that 43 placental lineages with extant descendants survived the K/T boundary, nearly twice as many as previously identified⁸. This taxic diversity is consistent with the hypothesis that placentals diversified ecologically in the Cretaceous period (model 5 of ref. 11), although phylogenies alone are mute

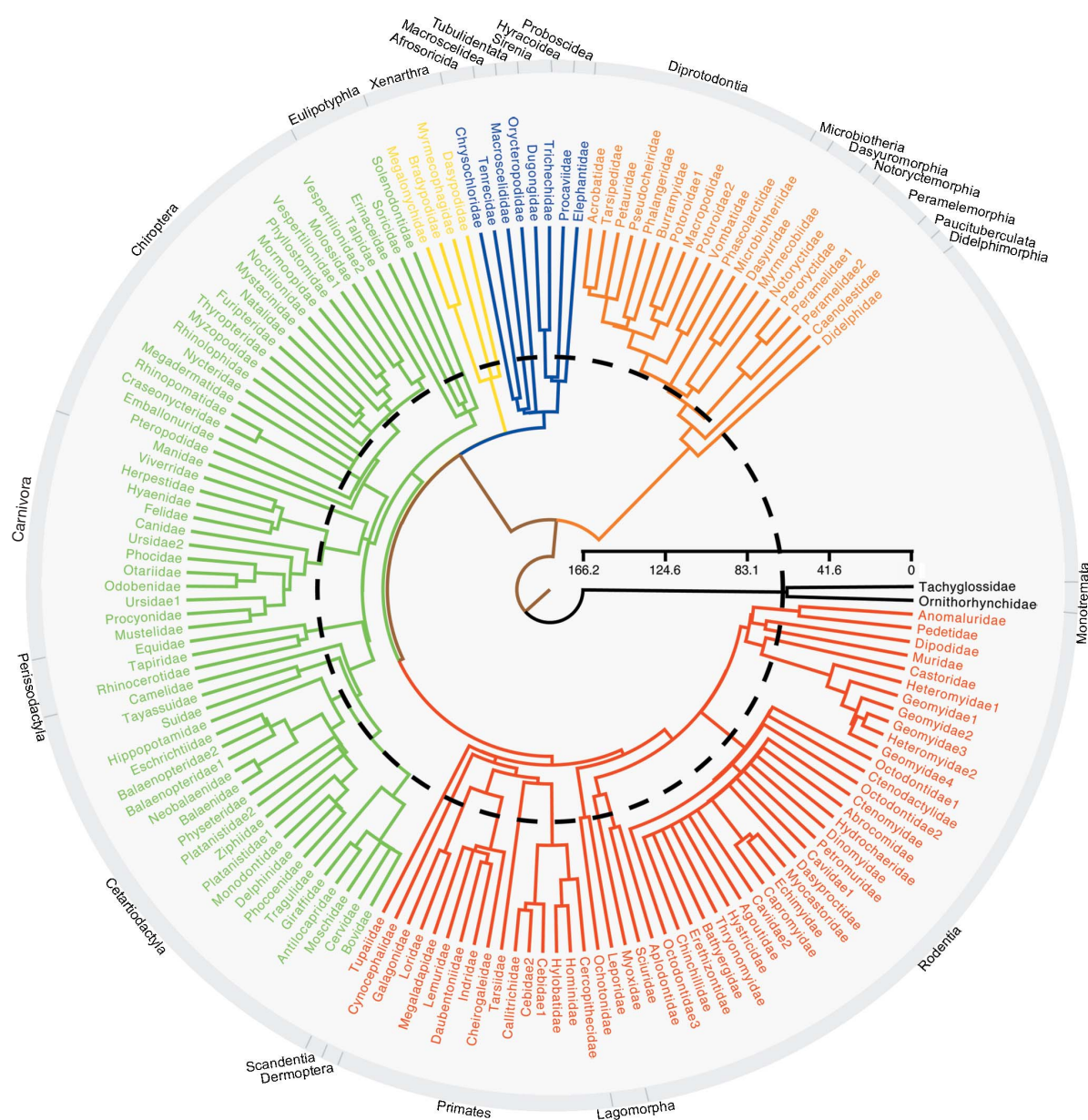


Figure 1 | Partial representation of the mammalian supertree showing the relationships among the families (following ref. 23). All orders are labelled and major lineages are coloured as follows: black, Monotremata; orange, Marsupialia; blue, Afrotheria; yellow, Xenarthra; green, Laurasiatheria; and red, Euarchontoglires. Families that were reconstructed as non-

monophyletic are represented multiple times and numbered accordingly. Branch lengths are proportional to time, with the K/T boundary indicated by a black, dashed circle. The scale indicates Myr. The base tree was drawn using FigTree v1.0 (<http://evolve.zoo.ox.ac.uk/software.html?id=figtree>).

Table 1 | Divergence times for major mammalian lineages.

Taxon	Crown-group size	Time of origin	Time of basal diversification	Waiting time to first split	
				Absolute	Percentage
Mammalia	4,510	N/A	166.2 (fixed)	N/A	N/A
Monotremata	3	166.2 (fixed)	63.6 ± 11.4	102.6	61.7
Placentalia	4,249	147.7 ± 5.5	101.3 ± 7.4	46.4	31.4
Euarchotheria	2,302	98.9 ± 2.7	94.5 ± 2.0	4.4	4.4
Rodentia	1,969	91.8 ± 1.3	85.3 ± 3.0	6.5	7.1
Lagomorpha	79	91.8 ± 1.3	66.8 ± 5.1	25.0	27.2
Primates	233	91.3 ± 2.6	87.7 ± 2.7	3.6	3.9
Dermoptera	2	91.3 ± 2.6	13.0 ± 5.2	78.3	85.8
Scandentia	19	94.3 ± 2.3	32.7 ± 2.6	61.6	65.3
Laurasiatheria	1,851	98.9 ± 2.7	91.8 ± 2.6	7.1	7.2
Cetartiodactyla	290	87.3 ± 1.5	74.1 ± 3.1	13.2	15.1
Perissodactyla	17	87.3 ± 1.5	58.2 ± 4.9	29.1	33.3
Carnivora	268	84.9 ± 3.6	67.1 ± 3.8	17.8	21.0
Pholidota	7	84.9 ± 3.6	19.9 ± 20.7	65.0	76.6
Chiroptera	915	88.7 ± 2.0	74.9 ± 3.3	13.8	15.6
Eulipotyphla	354	91.8 ± 2.6	84.2 ± 2.1	7.6	8.3
Xenarthra	29	101.1 ± 3.3	72.5 ± 5.1	28.6	28.3
Afrotheria	67	101.3 ± 7.4	93.4 ± 3.0	7.9	7.8
Afrosoricida	39	91.2 ± 2.6	85.2 ± 4.2	6.0	6.6
Macroscelidea	15	91.2 ± 2.6	50.7 ± 7.6	40.5	44.4
Tubulidentata	1	93.2 ± 3.0	N/A	N/A	N/A
Sirenia	4	75.9 ± 3.9	52.2 ± 14.4	23.7	31.2
Hyracoidea	6	75.9 ± 3.9	19.1 ± 0.8	56.8	74.8
Proboscidea	2	77.8 ± 3.6	19.5 ± 12.1	58.3	74.9
Marsupialia	258	147.7 ± 5.5	82.5 ± 11.1	65.2	44.1
Diprotodontia	109	63.6 ± 0.6	54.5 ± 1.7	9.1	14.3
Microbiotheria	1	63.6 ± 0.6	N/A	N/A	N/A
Dasyuromorphia	61	58.5 ± 8.0	32.8 ± 20.0	25.7	43.9
Notoryctemorphia	2	58.5 ± 8.0	9.3 ± 0.9	49.2	84.1
Peramelemorphia	18	66.8 ± 5.2	36.2 ± 5.6	30.6	45.8
Paucituberculata	5	73.8 ± 2.7	33.3 ± 6.9	40.5	54.9
Didelphimorphia	62	82.5 ± 11.1	56.1 ± 10.9	26.4	32.0

Hierarchical nesting of taxa is indicated using an indented taxonomy. Divergence times are in Myr ago ± 95% confidence intervals. Waiting times indicate the temporal gap (phylogenetic-fuse length) between the time of origin and of the basal diversification of the existing members of the crown group, both in absolute (Myr) and relative terms (percentage, relative to time of origin). See also Supplementary Table 2.

about ecological diversity¹². Marsupialia did not diversify until 82.5 Myr ago, nearly 20 Myr after placentals, with four lineages crossing the K/T boundary. Diversification of the surviving Monotremata is even later, with the single lineage that crossed the boundary first diversifying shortly thereafter (63.6 Myr ago).

Purely on the basis of the timings of the interordinal and first intraordinal splits, all three diversification models are present in mammals (Table 1). The short-fuse model is found for all placental crown groups that include at least 29 species, where the basal splits within these clades occur shortly after their origins (average fuse length = 13.6 Myr or 14.8%), and average some 10 Myr before the K/T boundary (77.5 Myr ago; range = 66.8–87.7 Myr ago). Crown-group marsupials instead approximate the explosive model, with the K/T boundary being within the confidence intervals of the dates of origin of most orders (although two orders did arise significantly earlier and most intraordinal divergences are significantly later). Finally, the long-fuse model characterizes Monotremata, the depauperate placental super-order Xenarthra, and the less diverse extant placental orders. For many of these groups, the long fuses (average = 57.3 Myr or 60.9%) reflect that these taxa have often been more diverse in the past, with the present crown group encompassing little of their early evolutionary history (for example, Proboscidea, Perissodactyla, Monotremata).

The tempo of mammalian diversification

To identify times of unusually rapid net diversification ('evolutionary explosions'), we use lineages-through-time plots¹⁷ to gain insight into the history of mammalian diversification rates. If speciation and extinction rates have been constant through time, the logarithm of the number of phylogenetic lineages with extant descendants should rise linearly with time for much of a clade's history¹⁹, with a slope that estimates the net rate of diversification, r . An increase in slope at the K/T boundary would indicate that r rose at that point, whereas a step-like increase would signify a burst of speciation¹⁸. Lineages-through-time plots from the supertree (Fig. 2a), however, show no evidence of any significant

upturn in r at any time around the K/T boundary. This result is confirmed by two-tailed γ -tests²⁰, which show that no significant temporal trend in r exists for mammals as a whole from the origin of crown-group mammals to 50 Myr ago ($\gamma = -0.575$, $P = 0.56$), with placental diversification actually slowing significantly over this period ($\gamma = -2.084$, $P = 0.04$). However, the placental data are more consistent with a step-change in diversification rate than a gradual trend (corrected Akaike information criterion, $AIC_c = 232.21$ and 239.04 , respectively; evidence weight for step-change = 96.8%), with the rate decrease inferred to have taken place at 85 Myr ago. Although marsupials do show a jump at the K/T boundary, the number of lineages involved (from three to six lineages) is very small, making firm conclusions difficult (see Supplementary Results).

Regression models in which r is a smooth function of time substantiate these findings (Fig. 2b). The temporal variation in r before 25 Myr ago is highly significant ($\chi^2_9 = 31.3$, $P < 0.001$). There is a peak at 93.1 Myr ago coincident with the Cenomanian/Turonian boundary, after which r declined to a minimum around the K/T boundary. After the latter, r remained low until the late Palaeocene, after which it increased more or less continuously until the Miocene epoch. Net diversification rates did not rise suddenly at any time around the K/T event: no significant rate difference exists between the latest Cretaceous (Maastrichtian) and earliest Tertiary (Danian) (general linear model with Poisson errors: $z = 0.479$, degrees of freedom = 104, $P = 0.63$). Results from parallel analyses broken down according to the major lineages of mammals or based on the 95% confidence interval dates are very similar (see Supplementary Results and Supplementary Figs 2–4).

The supertree therefore contains no evidence that the diversification rate of the extant mammalian lineages increased soon after non-avian dinosaurs went extinct. Although there is strong palaeontological evidence that mammalian diversity, driven by a massively elevated rate of speciation, generally rose rapidly immediately after the K/T boundary⁴, there is in fact no conflict between the palaeontological

and neontological interpretations of the known facts. Most diversifications immediately after the K/T boundary were in groups such as multituberculates, plesiadapiforms and 'archaic' ungulates⁴, as plots of the numbers of genera known in each sub-epoch indicate (Fig. 2c). These groups declined or went extinct early in the Cenozoic era and so are barely, if at all, represented in the phylogeny of living species. The continuing low rates of extant mammalian diversification through this period imply that the dearth of Palaeocene crown-group fossils is a real reflection of the low diversity of those clades. The low rates are also consistent with (but not direct evidence for) the hypothesis that extant lineages were inhibited in some manner by the diversity of the predominantly Palaeocene groups, and only started to diversify with the decline of the latter (Fig. 2c). However, like most other proposed competitive exclusion scenarios (for example, see refs 24, 25), this conjecture is based purely on the negative correlation of taxon diversities rather than direct evidence of exclusion.

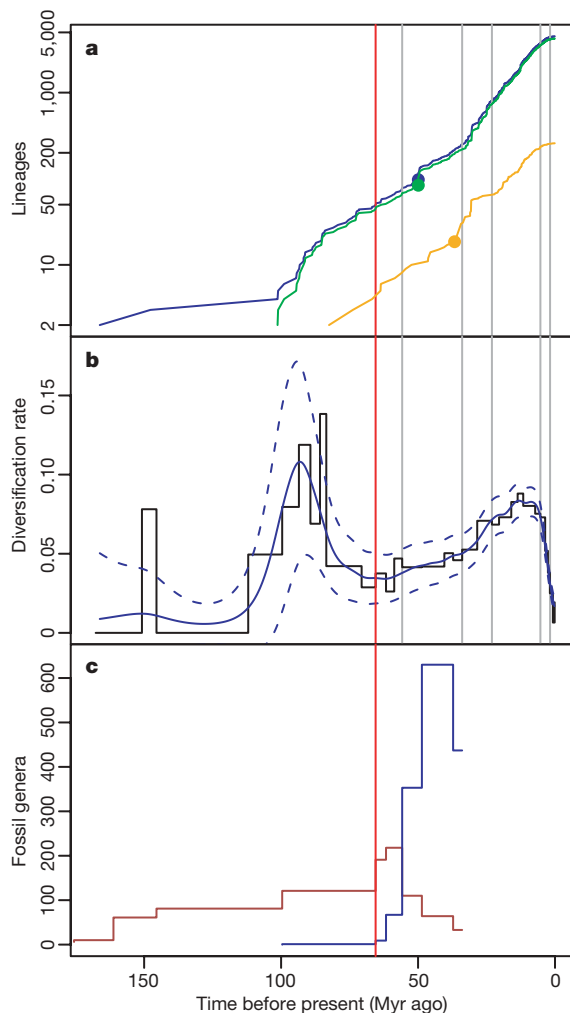


Figure 2 | Temporal patterns of mammalian diversification. **a**, Lineages-through-time plot for all (blue), placental (green) and marsupial (orange) mammals. Filled circles indicate when resolution in the phylogeny dropped below 85%. **b**, Net diversification rates: stepped line, rate in each age or sub-epoch; solid blue curve, rate inferred from a GAM of rate against time ($\chi^2 = 241.5$, estimated degrees of freedom = 14.75, $P \ll 0.001$, adjusted $R^2 = 77.6\%$, deviance explained = 20.3%); dashed curves, 95% confidence intervals. **c**, Counts of mammalian genera in each sub-epoch (Late Triassic to Late Eocene) according to the Unitaxon database (based on ref. 42). Red and blue lines represent genera whose families diversified predominantly before or after the Palaeocene/Eocene boundary, respectively. Throughout, the red vertical line is the K/T boundary and grey lines separate Cenozoic epochs.

Conclusions

As unquestionably useful as molecular data have been for untangling mammalian evolutionary history²⁶, no current molecular phylogeny is sufficiently complete to provide a clear view of dynamics so far in the past. Our analysis of a near-complete, species-level phylogeny of extant mammals sheds new light on how one of the best-known mass extinctions in Earth history affected their macroevolutionary dynamics. In particular, we challenge the widely accepted importance of the K/T extinction event for the origin and diversification of extant mammalian lineages. The pulse of mammalian diversification immediately after the K/T event was mainly or wholly in groups that declined subsequently or died out, without contributing markedly to those lineages with extant descendants, for which the diversification rate remained flat across the boundary. Only selected marsupial orders agree with the explosive model to any extent, and then only in their times of origin. Instead, the pivotal macroevolutionary events for extant mammalian lineages occur either well before the boundary (significant decrease in diversification rate at approximately 85 Myr ago, after establishment and initial radiations of the placental superorders and major orders at approximately 93 Myr ago) or well afterwards, from the Early Eocene onwards (when net diversification began to accelerate). The supertree and fossil record provide different parts of this picture, attesting to the value of using both approaches together: the supertree provides no information about the dynamics of extinct lineages, whereas the fossil record probably underestimates the timing of crown-group diversification in the past. Together, both lines of evidence indicate that the phylogenetic fuses throughout mammals, but especially in placentals, are much longer than previously suspected.

Therefore, the demise of the non-avian dinosaurs, and the K/T mass extinction event in general, do not seem to have had a substantial direct impact on the evolutionary dynamics of the extant mammalian lineages. What, then, was delaying the diversification of present-day mammals? Clearly, the priority is to identify why net rates of diversification remained low for so long after the major lineages became established. Time lags are also known for other groups^{10,27}; however, our values are much longer. Future tests are needed to see whether the time lag might involve inhibition by not only the Cretaceous fauna, but also by the major Palaeocene mammal groups. Net diversification rates might also have been shaped in part by abiotic factors that were more favourable for the modern groups: r starts to rise at around the time of the Cenozoic thermal maximum and subsequent Early Eocene Climatic Optimum (approximately 55–50 Myr ago)²⁸. Discriminating among all these scenarios will be demanding, requiring a highly integrative approach combining phylogenetic, palaeontological, palaeoclimatic and geographical data at both regional and global scales.

METHODS

The supertree was constructed in a hierarchical framework, combining pre-existing supertrees for Carnivora, Chiroptera, 'Insectivora' (split into Afrosoricida and Eulipotyphla) and Lagomorpha with new ones for the remaining groups, including the base supertree of all extant families (see Supplementary Table 1). All new supertrees were built using an explicit source tree collection protocol²⁹ to minimize both data duplication (for example, where the same data set underlies more than one source tree) and the inclusion of source trees of lesser quality (for example, taxonomies or those based on appeals to authority). Species names in the source trees were standardized to those found in ref. 23, and extinct taxa (following the 2004 IUCN Red List; <http://www.redlist.org>) were pruned from the final supertree. All supertrees were obtained using Matrix Representation with Parsimony (MRP^{30,31}), with the parsimony analyses for the new supertrees being performed in PAUP* v4.0b10 (ref. 32).

Recognizing that fossils provide minimum divergence-time estimates³³, divergence times throughout the supertree were either estimated by a combination of fossil and/or molecular dates under the assumption of a local molecular clock³⁴ (1,322 of 2,108 nodes) or interpolated from these empirically dated nodes using a pure birth model³⁴ (786 nodes) using the Perl scripts relDate v.2.2 and chronoGrapher v1.3.3, respectively (<http://www.personal.uni-jena.de/~b6biol2/>). The interpolated dates were not used in any of the statistical analyses reported

here. Because of the crucial nature of fossil calibration points, we restricted ourselves to fossils placed within crown groups of major lineages (generally orders) on the basis of one or more shared derived features as demonstrated in robust cladistic analyses. The 30 fossil dates so obtained represented minimum age constraints for their respective nodes (Supplementary Table 3). The root of the mammalian tree (age of the crown group) was estimated at 166.2 Myr ago based on the Middle Jurassic (Bathonian) Malagasy fossil *Ambondro mahabo*³⁵.

Relative molecular date estimates were obtained by fitting sequence data to the topology of the supertree under a maximum-likelihood framework in PAUP* to determine the branch lengths (following ref. 36). Sequence data were mined from the mammal section of GenBank release 144 (15 October 2004) using the Perl script GenBankStrip v2.0 (<http://www.personal.uni-jena.de/~b6biol2/>). Individual gene data sets were post-processed to retain only those sampled for at least 50 species and meeting minimum length and quality requirements before alignment (see Supplementary Methods). The final data set consisted of 51,089 base pairs from 66 genes (32 nuclear DNA, 19 transfer RNA and 15 other mitochondrial DNA), distributed across a total of 2,182 mammalian species (Supplementary Table 4). Representative outgroup sequences from the chicken (*Gallus gallus*) and/or either of the African or western clawed frogs (*Xenopus laevis* and *Xenopus tropicalis*, respectively) were added to each data set. Variation among the relative molecular date estimates provided by each gene was used to establish 95% confidence intervals for each divergence time estimate (see Supplementary Methods).

Two-tailed γ -tests²⁰ based on a lineages-through-time plot¹⁷ of the dated supertree were used to test the significance of any trends in the net diversification rate, r , over time in placentals, marsupials and mammals as a whole; under the null distribution, γ has a standard normal distribution. This test requires the tree to be highly resolved²⁰; we therefore used it only for the time window in which our tree is more than 85% resolved (before 50 Myr ago for placentals and all mammals, Fig. 2a; all dates within this portion of the tree were also estimated directly, rather than interpolated). On finding a trend within placentals, we compared the goodness-of-fit of linear and stepwise regression models to test whether the change in r was gradual or sudden. An additional test used only those lineages for which neither the beginning nor end dates were interpolated, and which did not start at a polytomy. These lineages can be informative about dynamics over a wider range of times (here, from the root of the tree up to about 25 Myr ago, after which point artefacts become increasingly important; see Supplementary Methods). Survival analysis³⁷ was used to estimate r within each geological age (pre-Pleistocene) or sub-epoch (Pleistocene). Temporal constancy in rate was tested by modelling r (as estimated from the number of speciation events per unit branch length within 0.1-Myr bins) as a function of time using generalized additive models (GAMs)³⁸. All analyses were repeated using the 95% confidence interval dates. All statistical analyses were performed in R³⁹ using the packages *ape*⁴⁰ and *mgcv*⁴¹.

Received 26 October 2006; accepted 31 January 2007.

- Archibald, J. D. & Deutschmann, D. H. Quantitative analysis of the timing of the origin and diversification of extant placental orders. *J. Mamm. Evol.* **8**, 107–124 (2001).
- Benton, M. J. Diversification and extinction in the history of life. *Science* **268**, 52–58 (1995).
- Asher, R. J. *et al.* Stem Lagomorpha and the antiquity of Glires. *Science* **307**, 1091–1094 (2005).
- Alroy, J. New methods for quantifying macroevolutionary patterns and processes. *Paleobiology* **26**, 707–733 (2000).
- Penny, D., Hasegawa, M., Waddell, P. J. & Hendy, M. D. Mammalian evolution: timing and implications from using the LogDeterminant transform for proteins of differing amino acid composition. *Syst. Biol.* **48**, 76–93 (1999).
- Kumar, S. & Hedges, S. B. A molecular timescale for vertebrate evolution. *Nature* **392**, 917–920 (1998).
- Springer, M. S. Molecular clocks and the timing of the placental and marsupial radiations in relation to the Cretaceous-Tertiary boundary. *J. Mamm. Evol.* **4**, 285–302 (1997).
- Springer, M. S., Murphy, W. J., Eizirik, E. & O'Brien, S. J. Placental mammal diversification and the Cretaceous-Tertiary boundary. *Proc. Natl Acad. Sci. USA* **100**, 1056–1061 (2003).
- Bromham, L., Phillips, M. J. & Penny, D. Growing up with dinosaurs: molecular dates and the mammalian radiation. *Trends Ecol. Evol.* **14**, 113–118 (1999).
- Cooper, A. & Fortey, R. Evolutionary explosions and the phylogenetic fuse. *Trends Ecol. Evol.* **13**, 151–155 (1998).
- Penny, D. & Phillips, M. J. The rise of birds and mammals: are microevolutionary processes sufficient for evolution? *Trends Ecol. Evol.* **19**, 516–522 (2004).
- Alroy, J. The fossil record of North American mammals: evidence for a Paleocene evolutionary radiation. *Syst. Biol.* **48**, 107–118 (1999).
- Gingerich, P. D. Environment and evolution through the Paleocene-Eocene thermal maximum. *Trends Ecol. Evol.* **21**, 246–253 (2006).
- Bowen, G. J. *et al.* Mammalian dispersal at the Paleocene/Eocene boundary. *Science* **295**, 2062–2065 (2002).
- Foote, M., Hunter, J. P., Janis, C. M. & Sepkoski, J. J. Jr. Evolutionary and preservational constraints on origins of biologic groups: divergence times of eutherian mammals. *Science* **283**, 1310–1314 (1999).
- Rose, K. D. *The Beginning of the Age of Mammals* (John Hopkins Univ. Press, Baltimore, 2006).
- Nee, S. & Mooers, A. Ø. & Harvey, P. H. Tempo and mode of evolution revealed from molecular phylogenies. *Proc. Natl Acad. Sci. USA* **89**, 8322–8326 (1992).
- Kubo, T. & Iwasa, Y. Inferring the rates of branching and extinction from molecular phylogenies. *Evolution* **49**, 694–704 (1995).
- Harvey, P. H., May, R. M. & Nee, S. Phylogenies without fossils. *Evolution* **48**, 523–529 (1994).
- Pybus, O. G. & Harvey, P. H. Testing macro-evolutionary models using incomplete molecular phylogenies. *Proc. R. Soc. Lond. B* **267**, 2267–2272 (2000).
- Sanderson, M. J., Purvis, A. & Henze, C. Phylogenetic supertrees: assembling the trees of life. *Trends Ecol. Evol.* **13**, 105–109 (1998).
- Bininda-Emonds, O. R. P., Gittleman, J. L. & Steel, M. A. The (super)tree of life: procedures, problems, and prospects. *Annu. Rev. Ecol. Syst.* **33**, 265–289 (2002).
- Wilson, D. E. & Reeder, D. M. (eds) *Mammal Species of the World: a Taxonomic and Geographic Reference* (Smithsonian Institution Press, Washington, 1993).
- Krause, D. W. in *Vertebrates, Phylogeny and Philosophy: a Tribute to George Gaylord Simpson* (eds Flanagan, K. M. & Lillegraven, J. A.) 95–117 (Univ. Wyoming, Laramie, Wyoming, 1986).
- Maas, M. C., Krause, D. W. & Strait, S. G. The decline and extinction of Plesiadapiformes (Mammalia: ?Primates) in North America: displacement or replacement? *Paleobiology* **14**, 410–431 (1988).
- Springer, M. S., Stanhope, M. J., Madsen, O. & de Jong, W. W. Molecules consolidate the placental mammal tree. *Trends Ecol. Evol.* **19**, 430–438 (2004).
- Moreau, C. S., Bell, C. D., Vila, R., Archibald, S. B. & Pierce, N. E. Phylogeny of the ants: diversification in the age of angiosperms. *Science* **312**, 101–104 (2006).
- Falkowski, P. G. *et al.* The rise of oxygen over the past 205 million years and the evolution of large placental mammals. *Science* **309**, 2202–2204 (2005).
- Bininda-Emonds, O. R. P. *et al.* in *Phylogenetic Supertrees: Combining Information to Reveal the Tree of Life* (ed. Bininda-Emonds, O. R. P.) 267–280 (Kluwer, Dordrecht, the Netherlands, 2004).
- Baum, B. R. Combining trees as a way of combining data sets for phylogenetic inference, and the desirability of combining gene trees. *Taxon* **41**, 3–10 (1992).
- Ragan, M. A. Phylogenetic inference based on matrix representation of trees. *Mol. Phylogenet. Evol.* **1**, 53–58 (1992).
- Swofford, D. L. *PAUP*. Phylogenetic Analysis Using Parsimony (*and Other Methods)* Version 4 (Sinauer Associates, Sunderland, Massachusetts, 2002).
- Tavaré, S., Marshall, C. R., Will, O., Soligo, C. & Martin, R. D. Using the fossil record to estimate the age of the last common ancestor of extant primates. *Nature* **416**, 726–729 (2002).
- Purvis, A. A composite estimate of primate phylogeny. *Phil. Trans. R. Soc. Lond. B* **348**, 405–421 (1995).
- Flynn, J. J., Parrish, J. M., Rakotosamimanana, B., Simpson, W. F. & Wyss, A. R. A Middle Jurassic mammal from Madagascar. *Nature* **401**, 57–60 (1999).
- Jones, K. E., Bininda-Emonds, O. R. P. & Gittleman, J. L. Bats, rocks and clocks: diversification patterns in Chiroptera. *Evolution* **59**, 2243–2255 (2005).
- Crawley, M. J. *Statistical Computing: an Introduction to Data Analysis Using S-Plus* (John Wiley & Sons, New York/Chichester, 2002).
- Wood, S. N. *Generalized Additive Models: an Introduction with R* (Chapman & Hall/CRC, Boca Raton, Florida, 2006).
- R Development Core Team. R: a language and environment for statistical computing, reference index version 2.2.1. (R Foundation for Statistical Computing, Vienna, 2005) (<http://www.R-project.org>).
- Paradis, E., Claude, J. & Strimmer, K. APE: analyses of phylogenetics and evolution in R language. *Bioinformatics* **20**, 289–290 (2004).
- Wood, S. N. *mgcv*: GAMs and generalized ridge regression for R. *R News* **1**, 20–25 (2001).
- McKenna, M. C. & Bell, S. K. *Classification of Mammals Above the Species Level* (Columbia Univ. Press, New York, 1997).

Supplementary Information is linked to the online version of the paper at www.nature.com/nature.

Acknowledgements D. Wong and A. Mooers provided their unpublished supertree of Geomyoidea. T. Barraclough, J. Bielby, N. Cooper, T. Coulson, M. Crawley, J. Davies, S. Fritz, N. Isaac, A. Lister, K. Lyons, G. Mace, S. Meiri, D. Orme, G. Thomas and N. Toomey all provided support and/or suggestions to improve the manuscript. Funding came from the NCEAS Phylogeny and Conservation Working Group; the BMBF; a DFG Heisenberg Scholarship; NERC studentships and grants; the Leverhulme Trust; the NSF; an Earth Institute Fellowship; and a CIPRES postdoctoral fellowship.

Author Contributions O.R.P.B.-E. developed data and computer protocols underlying the supertree and dating analyses, contributed to or performed many of the supertree analyses, generated the molecular data set and dated the supertree, and wrote major portions of the manuscript; M.C. helped develop data protocols,

contributed source trees and performed many of the intraordinal supertree analyses, and helped write parts of the manuscript; K.E.J. contributed source trees, developed data protocols, collected the fossil database and performed associated analysis; R.D.E.M. provided relevant palaeontological information and first appearance dates of major clades, and collected the fossil database and performed associated analysis; R.M.D.B. contributed to and performed selected supertree analyses, and provided relevant palaeontological information; R.G. developed protocols for and performed supertree construction and macroevolutionary analyses, and contributed to the writing of the manuscript; S.A.P. developed data protocols, collected source trees for and built the cetartiodactyl and perissodactyl

portions of the supertree; R.A.V. provided source trees for Primates; J.L.G. provided source trees and ideas for comparative tests; and A.P. developed, conceived and performed the macroevolutionary analyses, wrote the corresponding sections of the manuscript and developed data protocols. All authors provided comments on the manuscript.

Author Information Reprints and permissions information is available at www.nature.com/reprints. The authors declare no competing financial interests. Correspondence and requests for materials should be addressed to O.R.P.B.-E. (olaf.bininda@uni-jena.de).

CORRIGENDUM

doi:10.1038/nature07347

The delayed rise of present-day mammals

Olaf R. P. Bininda-Emonds, Marcel Cardillo, Kate E. Jones,
Ross D. E. MacPhee, Robin M. D. Beck, Richard Grenyer,
Samantha A. Price, Rutger A. Vos, John L. Gittleman & Andy Purvis

Nature 446, 507–512 (2007)

We have discovered a bug in the Perl script relDate v.2.2 that was used in part to date the nodes in the species-level mammalian supertree presented and analysed in our Article. The bug affected all but 80 of the 2,109 published dates, generally causing them to be slightly inflated, with the effect being stronger in more recent nodes. The absolute errors are mostly small (mean and median change of 1.32 and 0.70 million years, respectively), and a strong correlation between the two sets of dates exists ($r = 0.990$); however, 25 dates (all within Chiroptera) do change by more than 10 million years. Four of these dates are associated with the paraphyletic genus *Hipposideros*, whereas the remaining 21 cover most of Molossidae. The errors do not affect the results or overall conclusions of our paper qualitatively.

The Supplementary Information, including the tree files, has now been amended and can be accessed through the Supplementary Information link of the original Article. An additional file with a version of the amended Article can be accessed at <http://www.uni-oldenburg.de/molekularesystematik/> under the 'Publikationen/Publications' link.

CORRIGENDUM

doi:10.1038/nature07432

STING is an endoplasmic reticulum adaptor that facilitates innate immune signalling

Hiroki Ishikawa & Glen N. Barber

Nature 455, 674–678 (2008)

We inadvertently failed to notice that STING protein is encoded by the same gene as the previously described plasma membrane tetraspanner MPYS¹.

1. Jin, L. *et al.* MPYS, a novel membrane tetraspanner, is associated with major histocompatibility complex class II and mediates transduction of apoptotic signals. *Mol. Cell. Biol.* 28, 5014–5026 (2008).

CORRIGENDUM

doi:10.1038/nature07514

A role for clonal inactivation in T cell tolerance to Mls-1^a

Marcia A. Blackman, Hans-Gerhard Burgert, David L. Woodland,
Ed Palmer, John W. Kappler & Philippa Marrack

Nature 345, 540–542 (1990)

In this Article, the name of Hans-Gerhard Burgert was incorrectly listed as Hans Gerhard-Burgert.

ADDENDUM

doi:10.1038/nature07566

Genes mirror geography within Europe

John Novembre, Toby Johnson, Katarzyna Bryc, Zoltán Kutalik,
Adam R. Boyko, Adam Auton, Amit Indap, Karen S. King,
Sven Bergmann, Matthew R. Nelson, Matthew Stephens
& Carlos D. Bustamante

Nature 456, 98–101 (2008)

A related manuscript arriving at broadly similar conclusions based on partially overlapping data has recently been published¹. Specifically, 661 of the 3,192 samples from the POPRES collection² analysed in our paper were also analysed by Lao *et al.*¹.

1. Lao, O. *et al.* Correlation between genetic and geographic structure in Europe. *Curr. Biol.* 18, 1241–1248 (2008).
2. Nelson, M. R. *et al.* The population reference sample, POPRES: a resource for population, disease, and pharmacological genetics. *Am. J. Hum. Genet.* 83, 347–358 (2008).

CORRIGENDUM

doi:10.1038/nature07515

Structural basis for specific cleavage of Lys 63-linked polyubiquitin chains

Yusuke Sato, Azusa Yoshikawa, Atsushi Yamagata,
Hisatoshi Mimura, Masami Yamashita, Kayoko Ookata,
Osamu Nureki, Kazuhiro Iwai, Masayuki Komada & Shuya Fukai

Nature 455, 358–362 (2008)

In this Fig. 3c of this Article, Asp 324 was incorrectly labelled as Glu 324.

Fluctuating valence in a correlated solid and the anomalous properties of δ -plutonium

J. H. Shim¹, K. Haule¹ & G. Kotliar¹

Although the nuclear properties of the late actinides (plutonium, americium and curium) are fully understood and widely applied to energy generation, their solid-state properties do not fit within standard models and are the subject of active research¹. Plutonium displays phases with enormous volume differences, and both its Pauli-like magnetic susceptibility and resistivity are an order of magnitude larger than those of simple metals². Curium is also highly resistive, but its susceptibility is Curie-like at high temperatures and orders antiferromagnetically³ at low temperatures. The anomalous properties of the late actinides stem from the competition between itinerancy and localization of their *f*-shell electrons, which makes these elements strongly correlated materials. A central problem in this field is to understand the mechanism by which these conflicting tendencies are resolved in such materials. Here we identify the electronic mechanisms responsible for the anomalous behaviour of late actinides, revisiting the concept of valence using a theoretical approach that treats magnetism, Kondo screening, atomic multiplet effects and crystal field splitting on the same footing. We find that the ground state in plutonium is a quantum superposition of two distinct atomic valences, whereas curium settles into a magnetically ordered single valence state at low temperatures. The f^7 configuration of curium is contrasted with the multiple valences of the plutonium ground state, which we characterize by a valence histogram. The balance between the Kondo screening and magnetism is controlled by the competition between spin–orbit coupling, the strength of atomic multiplets and the degree of itinerancy. Our approach highlights the electronic origin of the bonding anomalies in plutonium, and can be applied to predict generalized valences and the presence or absence of magnetism in other compounds starting from first principles.

To understand the unique properties of elemental plutonium and its distinctive placement in the periodic table, it is essential to build a theory of actinides that can describe itinerant actinides as well as late actinides beyond plutonium. In the late rare-earth materials, the spin–orbit coupling and the hybridization is weak. The direct exchange promotes a ferromagnetic Kondo interaction between the *spd* and *f*electrons that results in a decoupling of *spd* and *f*electrons at low energies. In the late actinides the net Kondo interaction is antiferromagnetic, leading to strong correlation phenomena such as anomalously high room-temperature resistivities⁴. Curium, which follows americium in the periodic table, provides a very useful analogue to plutonium expanded beyond the equilibrium volume of its δ -phase. Curium is obtained by adding an electron to americium's inert *5f* shell (total angular momentum $J = 0$), while plutonium is obtained by creating a hole in the shell. The ability to predict magnetism in curium and its absence in plutonium is a strong test for our methodology, and we will use it as a benchmark for the quality of our theory of actinides.

To treat realistic multiplets and band structure, we use a new implementation of the merger of the local density approximation and the dynamical mean field theory (LDA+DMFT)^{5,6}. The DMFT method requires a solution of a quantum impurity problem which was here accomplished by an accurate impurity solver (which employed a vertex corrected one-crossing approximation⁶) and the results were further crosschecked against a continuous time quantum Monte Carlo method^{7,8}. We treat the full atomic physics (all the Slater integrals F_0 , F_2 , F_4 and F_6) on the same footing with the realistic band structure obtained by the relativistic version of the linear muffin-tin orbital method⁹. This LDA+DMFT approach treats magnetism and Kondo physics on an equal footing, and takes into account all the multiplet structure and crystal fields. As in all the earlier studies¹⁰ we take Coulomb interaction $U = 4.5$ eV and we compute the rest of the Slater integrals (F_2 , F_4 and F_6) from atomic physics¹¹, which, following the usual practice, are rescaled to 80% of their value.

Underlying the dynamical mean field approach⁵ is a physical picture in which the *f* electrons fluctuate among the different atomic configurations by exchanging electrons with a reservoir. The properties of the reservoir are determined self-consistently from the knowledge of the local spectral function. The self-consistency condition allows solutions with partially delocalized *f* electrons forming quasiparticle bands, but at the same time, the *f* electrons are allowed to preserve their atomic character for a short period of time, which leads to formation of Hubbard bands in the spectral function. When the *f* electrons get sufficiently localized, magnetic solutions are possible and become more energetically favourable than paramagnetic solutions at low temperature.

The fingerprint of strong correlations is encoded in the many-body self-energy, which becomes a 14×14 matrix dependent on frequency ω but not momentum \mathbf{k} . Adding this to the hamiltonian matrix, which also contains *spd* electrons, gives rise to the Green's function of the problem, $G(\omega, \mathbf{k})$. Integrated over momentum, it results in the local spectral function, which is measured in photoemission and inverse photoemission experiments.

To investigate phases with antiferromagnetic long-range order, the self-energy is allowed to be spin dependent, and the lattice is partitioned into two different sublattices, A and B, which experience different environments. The solution of two single impurity problems, coupled through the self-consistency condition, gives the self-energies in both sublattices A and B (ref. 5). We start from a magnetic state where the effective mediums for the different projections of the *z* component of the electron total angular momentum j_z at the A and B sublattices are different, and we watch how they evolve under iteration. We find that plutonium does not take advantage of the possibility of a broken symmetry and hence is non-magnetic, whereas curium does.

Starting from a general initial condition, upon iteration the plutonium spectral functions converge to a j_z independent spectral

¹Department of Physics and Astronomy and Center for Condensed Matter Theory, Rutgers University, Piscataway, New Jersey 08854-8019, USA.

function. On the other hand, curium has 14 non-equivalent spectral functions, reflecting the low-temperature antiferromagnetism, as displayed in Fig. 1. Notice the Hubbard bands, atomic-like features, and the Kondo resonance, which is present in plutonium but not in curium. Multiplet effects are clearly visible and provide widths to the Hubbard bands, as pointed out previously in studies of americium¹². Here we show that they play an even more important role in determining the renormalized Fermi energy, or the Kondo scale. For plutonium we obtain a Kondo energy of the order of 800 K, which compares favourably with the measured specific heat of the order of $60 \text{ mJ mol}^{-1} \text{ K}^{-1}$ (ref. 13). Turning off the Hund's rule coupling, which is possible theoretically but not experimentally, would result in a much larger Kondo energy in plutonium and in a non-magnetic heavy fermion state in curium in disagreement with experiments. Hence the Hund's rule coupling plays an unexpected role in the actinide series, renormalizing down the Kondo energy. Although the f - spd hybridization and the f - f hopping is larger in actinides than in lanthanides, it is still much smaller than the correlation strength in the form of the Hubbard interaction, and the width of the Hubbard bands is the result of the multiplet splitting, rather than coherent propagation, unlike the Kohn Sham bands in the standard model of solids.

To define valence, we focus on the reduced density matrix of the f states at a given site, which is obtained from the exact density matrix of the solid by tracing over all degrees of freedom except for those of the $5f$ shell at a given site (see Supplementary Information). The eigenvalues of this reduced density matrix give the probability of observing different f -electron atomic configurations at a given unit cell associated with an actinide nucleus. The solution of the DMFT impurity model allows us to visualize the f electrons as fluctuating between various atomic configurations and exchanging electrons with the surrounding medium. As a function of time, the f electrons in the atom change their atomic configuration while absorbing and

emitting electrons into the medium. We keep track of the different atomic configurations visited and draw them as histograms, which give complementary information to the photoemission spectra. These histograms for δ -plutonium and curium are presented in Fig. 2. Notice that plutonium does not have a well defined valence; its f electrons live a double life, spending considerable time in several atomic configurations, even though plutonium's average f electron count is close to $5f^5$. We describe this situation with a histogram which is peaked for a few atomic eigenstates, including atomic ground states of $5f^5$ and $5f^6$. The system is in a mixed valence state¹⁴ with an average f occupation of $n_f \approx 5.2$. In curium the f electrons are locked into one $5f^7$ dominant configuration, and the histogram is peaked only for the ground state of the atom.

X-ray absorption spectroscopy and electron energy-loss spectroscopy from the core $4d$ states are powerful probes of the valence. The strong spin-orbit coupling of the core states gives rise to two spin-orbit split absorption lines, representing $4d_{5/2} \rightarrow 5f$ and $4d_{3/2} \rightarrow 5f$ transitions¹⁵. The branching ratio B , that is, the relative strength of the $4d_{5/2}$ absorption, is a measure of the strength of the spin-orbit coupling interaction in the f shell. Ignoring the electrostatic interaction between core and valence electrons, known to be negligible in plutonium¹⁶, results in the following general expression obtained first by Van der Laan and collaborators¹⁵:

$$B = \frac{A_{5/2}}{A_{5/2} + A_{3/2}} = \frac{3}{5} - \frac{4}{15} \frac{1}{14 - \langle n_{5/2} \rangle - \langle n_{7/2} \rangle} \sum_{i \in f} \langle \mathbf{l}_i \cdot \mathbf{s}_i \rangle \quad (1)$$

$$\sum_{i \in f} \langle \mathbf{l}_i \cdot \mathbf{s}_i \rangle = \frac{3}{2} \langle n_{7/2} \rangle - 2 \langle n_{5/2} \rangle$$

where $A_{5/2}$ and $A_{3/2}$ are associated with area under the peaks corresponding to $4d_{5/2} \rightarrow 5f$ and $4d_{3/2} \rightarrow 5f$ transitions, respectively. The term $\sum_{i \in f} \langle \mathbf{l}_i \cdot \mathbf{s}_i \rangle$ measures the strength of the spin-orbit coupling

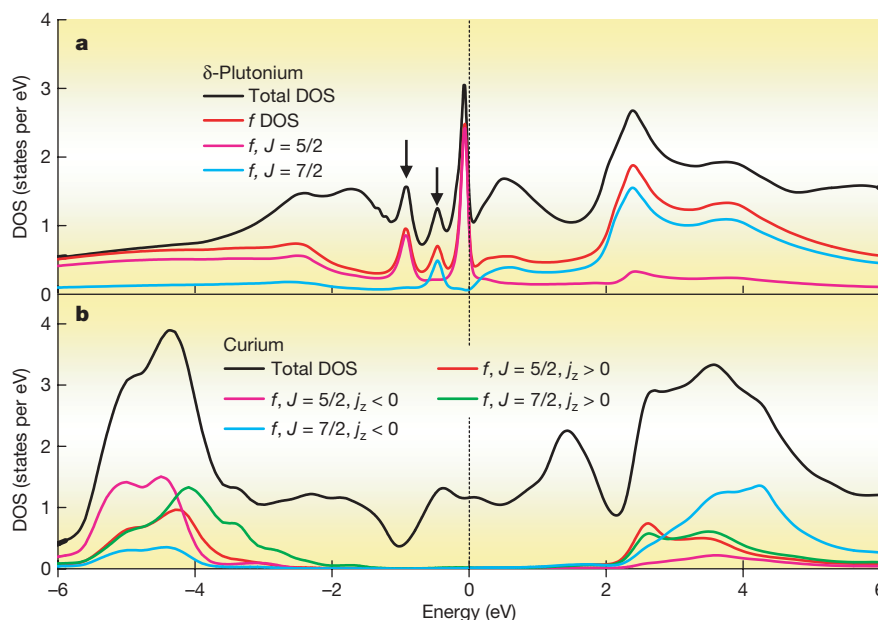


Figure 1 | The spectral functions of δ -plutonium and face-centred-cubic curium. **a**, δ -Plutonium is in a paramagnetic state with its moment totally screened by the Kondo effect, which is observed as a resonance at the Fermi level in the f spectra. In addition to the broad Hubbard band and sharp Kondo peak, two additional peaks below the Fermi level appear in our spectral function (marked with arrows), which were recently identified in photoemission experiments^{28–30}. The virtual charge fluctuations are primarily between the blue central peak in Fig. 2 (ground state of the atomic sector with $N_f = 5$ atoms) and the green side peak $|N_f = 6, J = 0, \gamma = 0\rangle$ (ground state of $N_f = 6$) in the same panel; γ is defined in Fig. 2 legend. The two arrowed sub-bands around 0.5 and 0.85 eV come mostly from the charge

fluctuations between the second blue peak $|N_f = 5, J = 7/2, \gamma = 0\rangle$ and the ground state of $N_f = 6$, and between $|N_f = 5, J = 5/2, \gamma = 1\rangle$ and the same ground state of $N_f = 6$, respectively. They disappear above the coherence temperature, so they are part of the coherent many-body spectra. **b**, The curium spectral function in the antiferromagnetic state. The diagonal components of the 14×14 matrix spectral function are shown separately for the positive and negative components of the electron spin j_z . The theoretical total density of states (DOS) displays the experimentally observed features at approximately the same energies, and calls for more detailed comparisons with experiment, which would require incorporating the photoemission matrix elements into the theory.

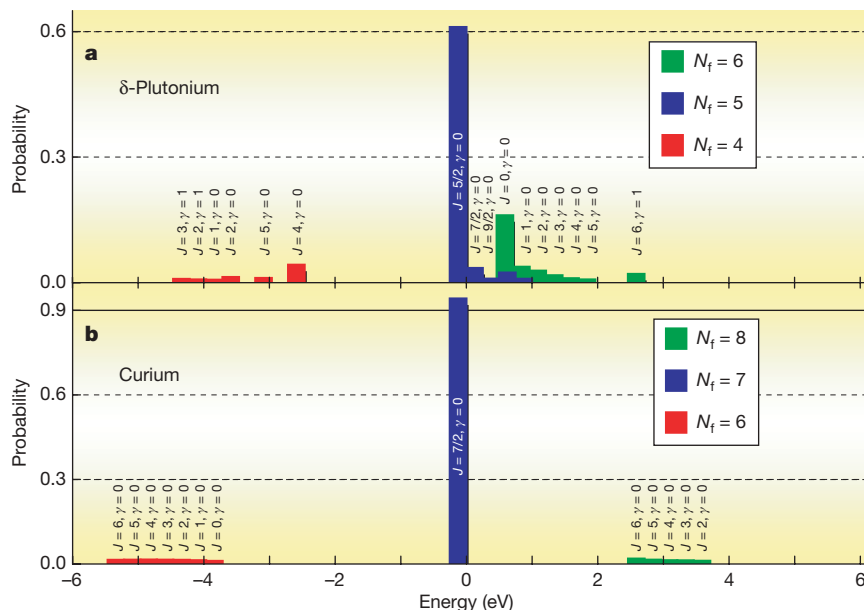


Figure 2 | Projection of the DMFT ground state to various atomic configurations. The histograms describe the generalized concept of valence, where the f electron in the solid spends appreciable time in a few atomic configurations. The height of the peak corresponds to the fraction of the time the f electron of the solid spends in one of the eigenstates of the atom, denoted by the total spin J of the atom. We summed up the probabilities for

the atomic states that differ only in the z component of the total spin J_z . The rest of the atomic quantum numbers are grouped into a single quantum number $\gamma = 0, 1, \dots$. The x axis indicates the energy of the atomic eigenstates defined by: $\text{energy}(N_f - 1, J_\gamma) = E_{\text{atom}}(N_f \text{ ground state}) - E_{\text{atom}}(N_f - 1, J_\gamma)$ and $\text{energy}(N_f + 1, J_\gamma) = E_{\text{atom}}(N_f + 1, J_\gamma) - E_{\text{atom}}(N_f \text{ ground state})$, where N_f is 5 and 7 for δ -plutonium and curium, respectively.

in the valence f states, and $n_{5/2}$ and $n_{7/2}$ are averaged partial occupations of the f valence states.

Comparison of measured branching ratios in actinides¹⁷ with atomic physics computations¹⁶ indicated the important role of spin-orbit coupling and gave strong evidence in favour of a $5f^5$ configuration. We now evaluate B for both curium and plutonium, using DMFT, which goes beyond atomic physics by incorporating the effects of itinerancy and multiple valences. The DMFT results are summarized in Table 1 and are compared with experiment¹⁷ where available. We stress the importance of first principles calculations including spin-orbit coupling, itinerancy and multiplet effects, as these are competing effects. Whereas the spin-orbit coupling increases faster than the Hund's coupling (Slater F_2) with increasing number of f electrons, the changes in the degree of itinerancy are of comparable magnitude and affect the relative strength of the effective spin-orbit coupling compared to the Hund's coupling and crystal fields. As a result, the effective spin-orbit coupling is smaller in curium than plutonium, placing curium much closer to the Russell-Saunders (L - S) coupling than plutonium¹⁸ (see last column in Table 1). The resulting curium moment $\mu \approx 2\sqrt{S(S+1)} \approx 7.9\mu_B$ (where μ_B is the Bohr magneton and S is the spin) is close to the observed experimental value³, which is clearly incompatible with j - j coupling (one $f_{7/2}$ electron would result in a moment of $l + 2s = 3 + 1\mu_B$).

We now contrast our findings with earlier approaches. Spin density functional theory (SDFT) calculations predict that all late actinides (plutonium, americium and curium) are magnetic, with large ordered magnetic moments of the order of a few μ_B (ref. 19). Experimentally, it is now established that no fluctuating or ordered

moments exist in metallic plutonium² and americium²⁰, whereas curium orders magnetically with a large magnetic moment. SDFT can be viewed as a form of static mean-field theory, which is known to sometimes produce spurious magnetic states in order to mimic the effect of correlations.

Other theories of plutonium posit that in this material some $5f$ electrons are localized and some are itinerant. The mixed level model²¹ assumes that four electrons are localized, that is, condensed into an atomic like singlet, while one f electron is itinerant. In the self-interaction corrected LDA, the valence of the f is frozen, and the total energy is determined for each valence to select the one with the lowest total energy. The latter approach²² finds that configurations with four, three, two, one or zero localized $5f$ electrons are almost degenerate. This can be taken as an indication that the dynamical treatment of valence presented in this Letter is needed for plutonium.

Other calculations (LDA + U ^{23,24}, DMFT-FLEX²⁵) suggest that plutonium is close to an inert $5f^6$ configuration with a singlet formed out of six localized f electrons. A non-magnetic configuration naturally accounts for the absence of moments in plutonium, but is too inert to account for the fact that the specific heats in α and δ phases differ by more than a factor of two². Furthermore, X-ray absorption experiments²⁶ and photoemission on thin plutonium layers²⁷, as well as previous DMFT calculations for plutonium¹⁰, are very suggestive that the f electrons are close to $5f^5$ configuration.

The full dynamic treatment of multiplets and Kondo physics, carried out in this Letter, brings a significant admixture of $5f^6$ valence, establishing continuity with weak coupling treatments²⁵, while accounting for the mass enhancement in α - and δ -plutonium. Our technical and conceptual advances in understanding δ -plutonium and curium lead to several experimental predictions. In the paramagnetic state, the volume enclosed by the Fermi surface of plutonium should contain an even number of electrons, whereas that of curium should contain an odd number of electrons, that is, its three spd electrons. These predictions can be tested by de Haas-van Alphen experiments or angle-resolved photoemission experiments. Furthermore, the physical picture of plutonium as a mixed-valence metal provides a natural explanation for the large sensitivity of its volume to small changes in temperature, pressure or doping. Moreover, the

Table 1 | Branching ratio

	f count	$B_{\text{DMFT theory}}$	B_{exp} (ref. 16)	B_{L-S}	B_{jj}	$(B_{\text{DMFT}} - B_{L-S}) / (B_{jj} - B_{L-S})$
δ -Plutonium	5.2	0.83	0.847	0.69	0.90	0.67
Curium	7.0	0.75		0.6	1.0	0.38

The f -electron count and branching ratio, B , of the $4d \rightarrow 5f$ edge spectra of δ -plutonium and curium. B_{L-S} and B_{jj} correspond to limiting cases of the pure Russell-Saunders and j - j coupling, respectively.

mixed-valence nature of plutonium can be probed by optical conductivity experiments, which should display a hybridization gap on a scale corresponding to several times the Kondo energy. In addition to the standard low-energy Drude peak, the optical conductivity should display a hybridization dip around $1,000\text{ cm}^{-1}$ and a broad mid-infrared peak between $3,000$ and $4,000\text{ cm}^{-1}$. The one-electron spectra and the X-ray branching ratio of curium are further quantitative theoretical predictions, which can be tested experimentally via photoemission and X-ray absorption measurements.

Finally, the use of DMFT for extracting valence histograms and thinking about mixed valences should have applications for many other strongly correlated compounds. Two pressing examples are UO_2 and PuO_2 (important by-products in nuclear reactors), whose valence properties are not well understood.

Received 2 November 2006; accepted 26 January 2007.

- Lander, G. Sensing electrons on the edge. *Science* **301**, 1057–1059 (2003).
- Lashley, J. C., Lawson, A., McQueeney, R. J. & Lander, G. H. Absence of magnetic moments in plutonium. *Phys. Rev. B* **72**, 054416 (2005).
- Huray, P. G., Nave, S. E., Peterson, J. R. & Haire, R. G. The magnetic susceptibility of ^{248}Cm metal. *Physica B* **102**, 217–220 (1980).
- Brodsky, M. B. Magnetic properties of the actinide elements and their metallic compounds. *Rep. Prog. Phys.* **41**, 1547–1608 (1978).
- Georges, A., Kotliar, G., Krauth, W. & Rozenberg, M. J. Dynamical mean-field theory of strongly correlated fermion systems and the limit of infinite dimensions. *Rev. Mod. Phys.* **68**, 13–125 (1996).
- Kotliar, G. *et al.* Electronic structure calculations with dynamical mean-field theory. *Rev. Mod. Phys.* **78**, 865–951 (2006).
- Werner, P., Comanac, A., de' Medici, L., Troyer, M. & Millis, A. J. Continuous-time solver for quantum impurity models. *Phys. Rev. Lett.* **97**, 076405 (2006).
- Haule, K. Quantum Monte Carlo impurity solver for cluster DMFT and electronic structure calculations in adjustable base. Preprint at (<http://arxiv.org/cond-mat/0612172>) (2006).
- Savrasov, S. Y. Linear-response theory and lattice dynamics: A muffin-tin-orbital approach. *Phys. Rev. B* **54**, 16470–16486 (1996).
- Savrasov, S. Y., Kotliar, G. & Abrahams, E. Correlated electrons in δ -plutonium within a dynamical mean-field picture. *Nature* **410**, 793–795 (2001).
- Cowan, R. D. *The Theory of Atomic Structure and Spectra* (Univ. California Press, Berkeley, 1981).
- Savrasov, S. Y., Haule, K. & Kotliar, G. Many-body electronic structure of americium metal. *Phys. Rev. Lett.* **96**, 036404 (2006).
- Lashley, J. C. *et al.* Experimental electronic heat capacities of α - and δ -plutonium: Heavy-fermion physics in an element. *Phys. Rev. Lett.* **91**, 205901 (2003).
- Varma, C. M. Mixed-valence compounds. *Rev. Mod. Phys.* **48**, 219–238 (1976).
- Thole, B. T. & van der Laan, G. Linear relation between x-ray absorption branching ratio and valence-band spin-orbit expectation value. *Phys. Rev. A* **38**, 1943–1947 (1988).
- van der Laan, G. *et al.* Applicability of the spin-orbit sum rule for the actinides 5f states. *Phys. Rev. Lett.* **93**, 097401 (2004).
- Moore, K. T., van der Laan, G., Haire, R. G., Wall, M. A. & Schwartz, A. J. Oxidation and aging in U and Pu probed by spin-orbit sum rule analysis: Indications for covalent metal-oxide bonds. *Phys. Rev. B* **73**, 033109 (2006).
- Moore, K. T. *et al.* Failure of Russell-Saunders coupling in the 5f states of plutonium. *Phys. Rev. Lett.* **90**, 196404 (2003).
- Solovyev, I. V., Liechtenstein, A. I., Gubanov, V. A., Antropov, V. P. & Andersen, O. K. Spin-polarized relativistic linear-muffin-tin-orbital method: Volume-dependent electronic structure and magnetic moment of plutonium. *Phys. Rev. B* **43**, 14414–14422 (1991).
- Kanellakopoulos, B., Blaise, A., Fournier, J. M. & Müller, W. The magnetic susceptibility of americium and curium metal. *Solid State Commun.* **17**, 713–715 (1975).
- Wills, J. M. *et al.* A novel electronic configuration of the 5f states in δ -plutonium as revealed by the photo-electron spectra. *J. Electron Spectrosc. Relat. Phenom.* **135**, 163–166 (2004).
- Svane, A., Petit, L., Szotek, Z. & Temmerman, W. M. Self-interaction corrected local spin density theory of 5f electron localization in actinides. Preprint at (<http://arxiv.org/cond-mat/0610146>) (2006).
- Shorikov, A. O., Lukoyanov, A. V., Korotin, M. A. & Anisimov, V. I. Magnetic state and electronic structure of the δ and α phases of metallic Pu and its compounds. *Phys. Rev. B* **72**, 024458 (2005).
- Shick, A. B., Drchal, V. & Havela, L. Coulomb-U and magnetic-moment collapse in δ -Pu. *Europhys. Lett.* **69**, 588–594 (2005).
- Pourvorskii, L. V. *et al.* Nature of non-magnetic strongly-correlated state in δ -plutonium. *Europhys. Lett.* **74**, 479–485 (2006).
- Tobin, J. G. *et al.* Competition between delocalization and spin-orbit splitting in the actinide 5f states. *Phys. Rev. B* **72**, 085109 (2005).
- Gounder, T., Havela, L., Wastin, F. & Rebizant, J. Evidence for the 5f localisation in thin Pu layers. *Europhys. Lett.* **55**, 705–711 (2001).
- Arko, A. J. *et al.* Electronic structure of α - and δ -Pu from photoelectron spectroscopy. *Phys. Rev. B* **62**, 1773–1779 (2000).
- Gouder, T., Eloirdi, R., Rebizant, J., Boulet, P. & Huber, F. Multiplet structure in Pu-based compounds: A photoemission case study of PuSi_x ($0.5 \leq x \leq 2$) films. *Phys. Rev. B* **71**, 165101 (2005).
- Tobin, J. G. *et al.* Resonant photoemission in f-electron systems: Pu and Gd. *Phys. Rev. B* **68**, 155109 (2003).

Supplementary Information is linked to the online version of the paper at www.nature.com/nature.

Acknowledgements This work was supported by the Basic Energy Science division of the DOE. J.H.S. acknowledges a grant from the Korean Research Foundation.

Author Information Reprints and permissions information is available at www.nature.com/reprints. The authors declare no competing financial interests. Correspondence and requests for materials should be addressed to K.H. (haule@physics.rutgers.edu).

Transmission resonances through aperiodic arrays of subwavelength apertures

Tatsunosuke Matsui^{1*}, Amit Agrawal^{2*}, Ajay Nahata² & Z. Valy Vardeny¹

Resonantly enhanced light transmission through periodic sub-wavelength aperture arrays perforated in metallic films¹ has generated significant interest because of potential applications in near-field microscopy, photolithography, displays, and thermal emission². The enhanced transmission was originally explained by a mechanism where surface plasmon polaritons (collective electronic excitations in the metal surface) mediate light transmission through the grating^{1,3}. In this picture, structural periodicity is perceived to be crucial in forming the transmission resonances. Here we demonstrate experimentally that, in contrast to the conventional view, sharp transmission resonances can be obtained from aperiodic aperture arrays. Terahertz transmission resonances are observed from several arrays in metallic films that exhibit unusual local n -fold rotational symmetries, where $n = 10, 12, 18, 40$ and 120 . This is accomplished by using quasicrystals with long-range order, as well as a new type of 'quasicrystal approximates' in which the long-range order is somewhat relaxed. We find that strong transmission resonances also form in these aperiodic structures, at frequencies that closely match the discrete Fourier transform vectors in the aperture array structure factor. The shape of these resonances arises from Fano interference⁴ of the discrete resonances and the non-resonant transmission band continuum related to the individual holes⁵. Our approach expands potential design parameters for aperture arrays that are aperiodic but contain discrete Fourier transform vectors, and opens new avenues for optoelectronic devices.

Periodicity, or the lack of it, is of fundamental importance in a broad range of science and engineering disciplines. In particular, two-dimensional (2D) aperture arrays can be described in terms of long-range order, short-range order, and local rotational symmetry that may be revealed in the Fourier transform structure factor. Several 2D array classes exist, including: (1) periodic lattices having both long-range and short-range order, and discrete Fourier transform vectors, but their n -fold rotational symmetry in real and reciprocal space is limited to $n = 2, 3, 4$ and 6 ; (2) quasicrystals with long-range order but no short-range order, but their discrete Fourier transform vectors possess unusual n -fold rotational symmetry with $n = 5, 8, 12$, and so on⁶; (3) aperiodic structures having no long-range or short-range order, but their structure factor may contain a number of discrete Fourier transform vectors with even more unusual n -fold rotational symmetry; and finally (4) randomly distributed holes with no discrete Fourier transform vectors at all. Patterns that fall into categories (2) and (3) can be referred to generically as aperiodic structures, although quasicrystals⁶ are unique in that their patterns can be developed using well-defined algorithms. The lack of periodicity in these two categories excludes the possibility of describing them using well-established analytical tools (such as Brillouin zones and the Bloch theorem) that are unique to Bravais lattices.

In this investigation, we examine resonantly enhanced transmission of the terahertz (THz) electric field through metallic films perforated with several 2D aperiodic aperture arrays using THz time-domain spectroscopy (see Supplementary Information)⁷. Two-dimensional aperture arrays were fabricated in an $\sim 5\text{ cm} \times 5\text{ cm}$ area of $75\text{-}\mu\text{m}$ -thick free-standing stainless steel metal foils. Six different aperture array sample sets were fabricated with differing hole diameter, nearest-neighbour hole distance, and local rotational symmetry. Most of these structures were designed to have the same fractional aperture area of $\sim 12\%$. One set of samples consisted of randomly distributed holes; the other five sets contained some samples that were in the form of 2D quasicrystals exhibiting five-fold⁸ and 12-fold⁹ rotational symmetry, and some samples that were novel quasicrystal approximates exhibiting 18-, 40- and 120-fold rotational symmetry. 2D fast Fourier transform (FFT) was applied to the individual array patterns to determine their underlying geometrical structure factor.

Figure 1 summarizes our studies on perforated metallic films with randomly distributed apertures for which the FFT contains no discrete components. Figure 1a shows the THz transmission spectra, $T(\nu)$, up to $\nu = 0.5\text{ THz}$ for three perforated films with a differing number of apertures. In each case, the hole diameter, D , is 0.4 mm . $T(\nu)$ increases at high frequencies, reaching a broad maximum that scales linearly with the number of holes in the film (Fig. 1a inset), indicating that it is due to transmission through uncorrelated individual holes. Figure 1b shows $T(\nu)$ for three different perforated films in which D varies, and the number of holes was altered to keep the fractional aperture area constant at $\sim 12\%$. It is apparent that $T(\nu)$ increases at an onset frequency that scales with D (Fig. 1b inset). Therefore, the increase in $T(\nu)$ at short wavelengths can be attributed to a waveguide cut-off phenomenon at frequency ν_c , where the propagation of electromagnetic radiation through the holes is increasingly suppressed for $\nu < \nu_c$. Also, the maximum transmission, T_{max} , of $\sim 20\%$ is greater than that predicted from the fractional aperture area ($\sim 12\%$).

The origin of these deviations from theory¹⁰ was recently explained using an analytical approach based on induced magnetic and electric dipoles on either side of the metallic film through an individual hole⁵. The good fit between our experimental $T(\nu)$ spectrum seen in Fig. 1a and this model (using $D = 0.42\text{ mm}$) validates both the assumption that the transmission spectrum is due to uncorrelated holes, and the model calculation. Thus, when electromagnetic radiation is incident on a perforated metallic film, it scatters from the holes into free space, as well as into surface waves on the metal–air interfaces¹¹. If more than one aperture is fabricated in the metal film, it is conceivable that the scattered surface waves would interfere. For films containing randomly distributed holes, we would not expect strong interference, explaining the lack of sharp resonances in $T(\nu)$. The situation is very

¹Physics Department, ²Department of Electrical and Computer Engineering, University of Utah, Salt Lake City, Utah 84112, USA.

*These authors contributed equally to this work.

different, however, for films that show discrete Fourier transform vectors in their structure factor even with aperiodic structure, such as quasicrystals and their approximates.

Figure 2 summarizes our studies on 2D quasicrystal aperture arrays fabricated in metal films that exhibit local five-fold and 12-fold rotational symmetry. Figure 2a shows a Penrose-type quasicrystal¹² in which the apertures were fabricated at the vertices of the thin and thick rhomb tiles having tile side length d_3 (Fig. 2a). Figure 2b shows the geometrical structure factor of the Penrose quasicrystal, which possesses ten-fold rotational symmetry about the centre, with four series of circular spots about it. These spots can be associated with vectors \mathbf{F} in reciprocal space, referred to as reciprocal vectors⁸, that satisfy the relation $\exp(i\mathbf{F}\cdot\mathbf{R}) = 1$ for all the apertures having coordinates \mathbf{R} . In contrast to the case of a periodic pattern such as a lattice, in which the structure factor is in the form of a Bravais lattice spanned in 2D by two primitive vectors¹, the quasicrystal reciprocal vectors may be conveniently indexed according to their distance from the centre. These distances, in turn, may be related directly to specific real-space distances in the Penrose structure^{8,12} (Fig. 2a and Supplementary Information).

Figure 2c shows $T(\nu)$ of three perforated films with different values of d_3 , keeping the fractional aperture area at 12%. Each $T(\nu)$ consists of three well pronounced transmission bands (or resonances) referenced as $F^{(1)}$, $F^{(2)}$ and $F^{(3)}$ that are directly related to the reciprocal vectors in Fig. 2b, as well as a less pronounced resonance $F^{(4)}$. We note that the resonance frequencies, $\nu^{(i)}$, scale with the magnitude of the corresponding reciprocal vectors in Fig. 2b, clearly demonstrating that the reciprocal vectors are in fact the wave-vectors \mathbf{k} at resonance (Supplementary Information).

To demonstrate that transmission resonances are more generally observed from quasiperiodic aperture arrays, Fig. 2d shows a structure that exhibits local 12-fold rotation symmetry¹³. Figure 2e shows that the FFT of this structure contains five series of reciprocal vectors,

referred to as $\mathbf{T}^{(i)}$, about the centre point. The magnitudes of these reciprocal vectors correspond to real distances in the quasicrystal structure (Fig. 2e and Supplementary Information).

Figure 2f shows typical $T(\nu)$ spectra of this quasicrystal structure having two different aperture diameters in the metal film. We see three primary resonances that correspond to the reciprocal vectors $\mathbf{T}^{(1)}$, $\mathbf{T}^{(3)}$ and $\mathbf{T}^{(4)}$, as summarized in Supplementary Table 2. $T(\nu)$ also contains several accompanying anti-resonances, each on the high-energy side of each resonance band. Importantly we note that the lowest resonance, $\mathbf{T}^{(1)}$, is hardly seen in Fig. 2f(bottom trace) for $D = 0.35$ mm; in turn, the $\mathbf{T}^{(3)}$ and $\mathbf{T}^{(4)}$ resonances cannot be clearly identified in Fig. 2f (top trace) for $D = 0.58$ mm. In addition, the resonance $\mathbf{T}^{(1)}$ shifts to higher frequency when D decreases, whereas the anti-resonance frequency remains unchanged. Recently Sun *et al.* reported enhanced transmission through aperture arrays based on eight-fold quasicrystals at optical frequencies¹⁴. However, they concluded that both long-range order and periodicity are very important for substantial surface plasmon polariton (SPP) coupling, and also did not observe the important anti-resonance features in $T(\nu)$. In contrast, it is clear from our findings that periodicity is not crucial for observing transmission resonances in perforated films. Additionally, we have found that the anti-resonances are crucial in determining the resonance shape in $T(\nu)$. Also, another recent report¹⁵ found enhanced transmission bands for a Penrose quasicrystal in the visible spectral range, but claimed that the resonances are broader than those based on periodic structures. Our data show, however, that at least in the THz range, the transmission resonances of quasicrystal structures are as sharp as those based on periodic arrays.

Numerous models have been put forward to explain the phenomenon of resonantly enhanced transmission through periodically perforated metallic films, but a general consensus has not emerged yet. The transmission resonances with aperiodic arrays found here may have the potential to clarify the underlying physics of the anomalous transmission phenomenon. In the model most commonly used to describe this effect^{1,3}, the incident light couples to SPP excitations with resonant wave-vector \mathbf{k}_{SPP} associated with the aperture array grating, via the quasi-momentum conservation rule:

$$\mathbf{k}_{\parallel} + \mathbf{k}_{\text{SPP}} = \mathbf{G}^{(i)} \quad (1)$$

Here, $\mathbf{k}_{\parallel} = 2\pi\sin\theta/\lambda$ is the light wave-vector parallel to the film surface, θ is the angle between the light wave-vector and the surface normal, and $\mathbf{G}^{(i)}$ is a reciprocal lattice vector. Whereas equation (1) is typically associated with arrays that are strictly periodic, such arrays in practice are always finite, and thus $\mathbf{G}^{(i)}$ are not very well defined. For sufficiently large arrays, however, this equation appears to adequately describe the underlying physics. Quasicrystals are aperiodic but exhibit long-range order. Nevertheless, as with finite periodic arrays, an appropriately modified version of equation (1) may still describe the transmission resonance properties, except that the $\mathbf{G}^{(i)}$ would be replaced by the discrete Fourier transform vectors in the structure factor, namely the reciprocal vectors. Thus sharp transmission resonances would be formed for any structure that contains reciprocal vectors in its FFT geometry.

Transmission resonances associated with aperture arrays on metal films studied with visible light are characterized by broad lineshapes that are largely symmetric about the spectral peaks. Although anti-resonance features are discernible, they are not sharply defined¹⁶. In contrast, the resonances observed here in the THz range are sharply asymmetric and characterized by well-defined anti-resonances on the high-frequency side. We propose that these spectral features arise from the interference between discrete resonances caused by the diffraction from the aperture array, and the broad (continuum) transmission spectrum associated with the individual apertures on the metal film (Fig. 1). This interaction is well described by Fano interference¹⁷. It can be readily recognized that the resonances in $T(\nu)$ (Fig. 2c and f) are superimposed on the continuum spectrum of the

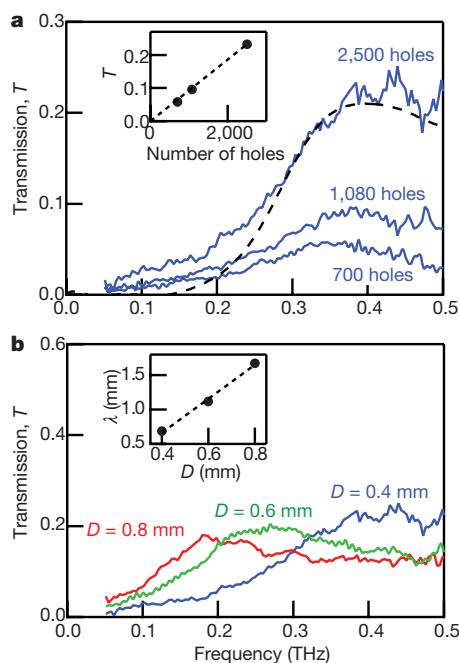


Figure 1 | THz electric field transmission, $T(\nu)$, through random apertures in stainless steel foils. **a**, Data for three films with different numbers of holes having diameter $D = 0.4$ mm; the dashed line through the data points is a fit using the individual hole transmission model of ref. 5 with $D = 0.42$ mm. The inset shows the transmission maximum at 0.4 THz versus the number of holes in the film. **b**, Perforated films with apertures of different D with the number of holes adjusted to keep the fractional aperture area constant at $\sim 12\%$; the inset shows the dependence of the onset wavelength versus D .

individual apertures (Fig. 1a). Fano interference also explains the relative enhancements observed in Fig. 2f. For small D , the continuum band blue-shifts to higher frequencies (Fig. 1b), and thus discrete resonances having higher frequencies become more apparent. The reverse situation occurs at large D , in which case the continuum band red-shifts (Fig. 1b), and thus discrete resonances with lower frequencies are better resolved.

Fano interferences are known to result in anti-resonances on the high-frequency side of the resonance bands^{4,18}. Although more theoretical work is needed to elucidate the coupling between the discrete

resonances and the continuum band, it is clear that because of the Fano interference, the apparent peak frequencies are red-shifted with respect to the true resonances^{4,19}, and thus may change with D . In contrast, the anti-resonance frequencies remain unchanged¹⁷.

We demonstrate here that sharp transmission resonances are also formed in metal films perforated with a much broader range of aperiodic arrays, such as 'approximate' 2D quasicrystal structures, for which geometric tilings are not available or known. Figure 3a shows the design procedure²⁰ for an 'approximate' 18-fold 2D quasicrystal patterned on the metal film. We note that the distances, d_i ,

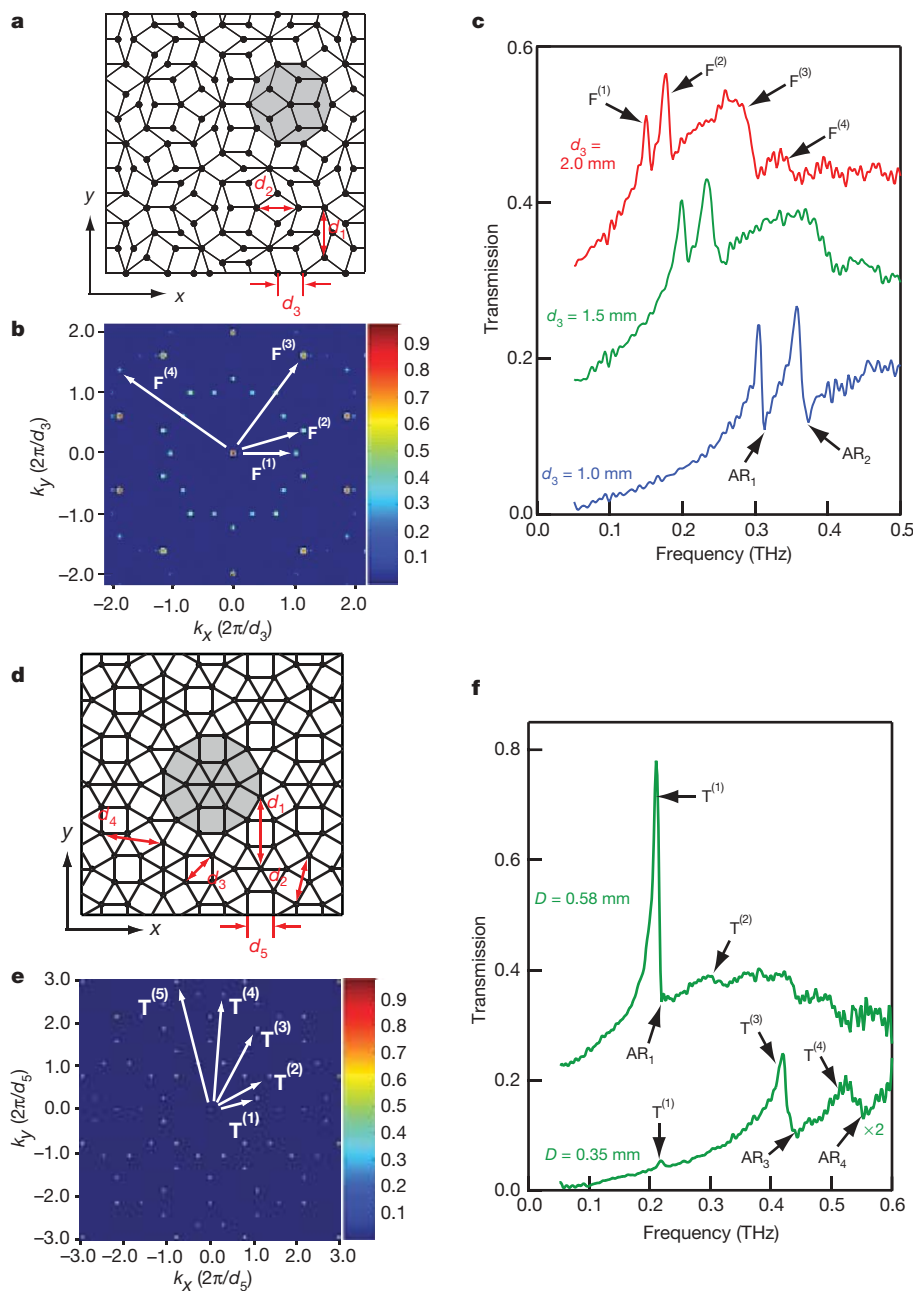


Figure 2 | THz time-domain spectroscopy studies of stainless steel foils perforated with apertures patterned in 2D quasicrystal structures. **a**, A Penrose quasicrystal exhibiting local five-fold rotational symmetry (shaded area) with apertures at the vertices, constructed of thin and thick rhomb tiles. The distances, d_i , between the vertices are assigned, with d_3 referring to the length of the rhomb side. **b**, The structure factor of the quasicrystal in **a** calculated using a 2D FFT. The reciprocal vectors, $\mathbf{F}^{(i)}$, which exhibit ten-fold rotational symmetry, are assigned. **c**, $T(v)$ of three Penrose type quasicrystal perforated films with different rhomb side lengths, d_3 , showing

resonances $\mathbf{F}^{(i)}$ and anti-resonances AR_i . **d**, Same as in **a** but for a 2D quasicrystal structure with local 12-fold rotational symmetry and dominant tile length d_5 . **e**, The structure factor of the quasicrystal in **d**; the reciprocal vectors, $\mathbf{T}^{(i)}$, with 12-fold rotational symmetry are assigned. **f**, $T(v)$ of two quasicrystals with 12-fold rotational symmetry perforated in metal films with a hole diameter $D = 0.35$ mm ($\times 2$) and 0.58 mm, respectively. For both spectra, the side length was $d_5 = 1.5$ mm, and the resonances $\mathbf{T}^{(i)}$ and anti-resonances AR_i are denoted.

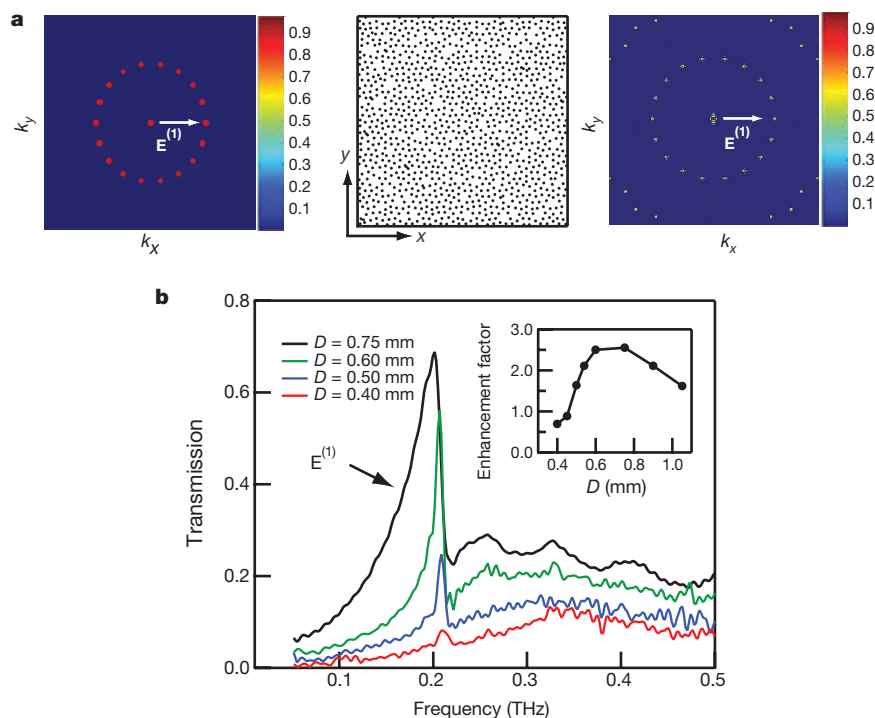


Figure 3 | Design and THz time-domain spectroscopy studies of stainless steel foils perforated with 2D aperiodic aperture arrays. **a**, Numerical approach for obtaining aperiodic arrays. Left panel, the desired 2D diffraction pattern for 18-fold rotational symmetry. Centre panel, the discretized magnitude of the inverse Fourier transform. The inverse Fourier transform is continuous and therefore requires threshold cutting to obtain discrete points. These points are the locations of the apertures in real space. Right panel, Fourier transform of the real space aperture locations for

obtaining the final structure factor properties. **b**, Electric field transmission spectra of four aperiodic arrays with 18-fold rotational symmetry perforated in metal films with aperture diameters of $D = 0.4, 0.5, 0.6$ and 0.75 mm, respectively; the resonant band $E^{(1)}$ is assigned. In each case, the average hole spacing was 1.5 mm. The inset shows the enhancement factor (that is, the ratio of $E^{(1)}$ peak magnitude to the saturated transmission magnitude at high ν) as a function of D .

between apertures in more traditional quasicrystals created using tiling are well-defined, in contrast to the aperiodic structures obtained using the numerical procedure described here. Therefore, the approximate quasicrystal structures are not quasiperiodic, but more correctly aperiodic. Nevertheless, well-defined resonances in $T(\nu)$ still exist.

Figure 3b shows $T(\nu)$ of four 18-fold aperiodic structures with various aperture diameters, in which the average hole spacing is 1.5 mm. In each case, we see only one prominent transmission resonance, $E^{(1)}$ at 0.21 THz, which is in agreement with the numerically obtained reciprocal vectors in the structure factor shown in Fig. 3a (panel #3). Furthermore, there is an apparent monotonic increase in the magnitude of the transmission peak with increasing D up to 750 μm . The inset of Fig. 3b summarizes the dependence on D of the ratio of the resonance peak magnitude to the continuum band saturation level (that is, the enhancement factor). We find that the optimal diameter for transmission enhancement is ~ 750 μm . This may be explained as follows: as D increases, the individual aperture continuum band in $T(\nu)$ red-shifts (Fig. 1b), thereby increasing the prominence of low-frequency transmission resonances. This demonstrates the intimate relation that exists in $T(\nu)$ between the discrete resonances and the continuum band. At $D > 750$ μm , where the apertures no longer can act as cut-off waveguides, the enhancement factor decreases. Finally, as with quasicrystal structures, we again see that the resonant frequency $E^{(1)}$ shifts with the aperture diameter, D , while the corresponding anti-resonance frequency does not.

The true value of the numerical approach described here is that it allows for the generation of arbitrary aperiodic arrays with exotic structures that form a variety of designed transmission properties. Using this general numerical approach we have created, for example, aperiodic arrays that exhibit local n -fold rotational symmetry, with

$n = 40$ and 120 (Supplementary Information). We have also created other, more exotic, aperture array structures that do not exhibit any n -fold rotational symmetry, but nevertheless exhibit resonant transmission bands (T.M., A.A., A.N. and Z.V.V., unpublished results).

Our results show that the THz transmission spectra obtained using quasiperiodic, as well as more generalized aperiodic, aperture structures in metal films also possess enhanced transmission resonances with lineshapes that are comparable in width to those of resonances obtained with periodic structures⁷. We also show that these resonances can be engineered to yield desirable transmission properties. Further exploration of these structures is expected to lead to new optoelectronic device embodiments²¹ that are expected to be particularly important in the THz spectral range, which is largely devoid of usable optoelectronic devices.

Received 14 June 2006; accepted 19 January 2007.

1. Ebbesen, T. W., Lezec, H. J., Ghaemi, H. F., Thio, T. & Wolff, P. A. Extraordinary optical transmission through sub-wavelength hole arrays. *Nature* **391**, 667–669 (1998).
2. Barnes, W. L., Dereux, A. & Ebbesen, T. W. Surface plasmon subwavelength optics. *Nature* **424**, 824–830 (2003).
3. Ghaemi, H. F., Thio, T., Grupp, D. E., Ebbesen, T. W. & Lezec, H. J. Surface plasmons enhance optical transmission through subwavelength holes. *Phys. Rev. B* **58**, 6779–6782 (1998).
4. Genet, C., van Exter, M. P. & Woerdman, J. P. Fano-type interpretation of red shifts and red tails in hole array transmission spectra. *Opt. Commun.* **225**, 331–336 (2003).
5. Garcia de Abajo, F. J., Saenz, J. J., Campillo, I. & Dolado, J. S. Site and lattice resonances in metallic hole arrays. *Opt. Express* **14**, 7–18 (2006).
6. Janot, C. *Quasicrystals: A Primer* 2nd edn (Oxford Univ. Press, New York, 1994).
7. Cao, H. & Nahata, A. Influence of aperture shape on transmission properties of a periodic array of subwavelength apertures. *Opt. Express* **12**, 3664–3672 (2004).

8. Kaliteevski, M. A. *et al.* Diffraction and transmission of light in low-refractive index Penrose-tiled photonic quasicrystals. *J. Phys. Condens. Matter* **13**, 10459–10470 (2001).
9. Oxborrow, M. & Henley, L. C. Random square-triangle tilings: A model for twelve fold-symmetric quasicrystals. *Phys. Rev. B* **48**, 6966–6998 (1993).
10. Bethe, H. A. Theory of diffraction by small holes. *Phys. Rev.* **66**, 163–182 (1944).
11. Agrawal, A. & Nahata, A. Time-domain radiative properties of a single subwavelength aperture surrounded by an exit side surface corrugation. *Opt. Express* **14**, 1973–1981 (2006).
12. Penrose, R. The role of aesthetics in pure and applied mathematical research. *Bull. Inst. Math. Appl.* **10**, 266–271 (1974).
13. Zoorob, M. E., Charlton, M. D. B., Parker, G. J., Baumberg, J. J. & Netti, M. C. Complete photonic bandgaps in 12-fold symmetric quasicrystals. *Nature* **404**, 740–743 (2000).
14. Sun, M. *et al.* The role of periodicity in enhanced transmission through subwavelength hole arrays. *Chin. Phys. Lett.* **23**, 486–488 (2006).
15. Przybilla, F., Genet, C. & Ebbesen, T. W. Enhanced transmission through Penrose subwavelength hole arrays. *Appl. Phys. Lett.* **89**, 121115 (2006).
16. Koerkamp, K. J. K., Enoch, S., Segerink, F. B., van Hulst, N. F. & Kuipers, L. Strong influence of hole shape on extraordinary transmission through periodic arrays of subwavelength holes. *Phys. Rev. Lett.* **92**, 183901 (2004).
17. Fano, U. Effects of configuration interaction on intensities and phase shifts. *Phys. Rev.* **124**, 1866–1873 (1961).
18. Österbacka, R., Jiang, X. M., An, C. P., Horovitz, B. & Vardeny, Z. V. Photoinduced quantum interference antiresonances in π -conjugated polymers. *Phys. Rev. Lett.* **88**, 226401 (2002).
19. Sarrazin, M., Vigneron, J. P. & Vigoureux, J. M. Role of Wood anomalies in optical properties of thin metallic films with bidimensional array of subwavelength holes. *Phys. Rev. B* **67**, 085415 (2003).
20. Lee, T. D. M., Parker, G. J., Zoorob, M. E., Cox, S. J. & Charlton, M. D. B. Design and simulation of highly symmetric photonic quasi-crystals. *Nanotechnology* **16**, 2703–2706 (2005).
21. Matsui, T., Agrawal, A., Nahata, A. & Vardeny, Z. V. Enhanced transmission properties of aperiodic aperture arrays in metallic and semiconductor films and their application to optoelectronic devices. *University of Utah Patent Disclosure*, (2006).

Supplementary Information is linked to the online version of the paper at www.nature.com/nature.

Acknowledgements This work was supported in part by the Army Research Office and the SYNERGY programme at the University of Utah.

Author Information Reprints and permissions information is available at www.nature.com/reprints. The authors declare no competing financial interests. Correspondence and requests for materials should be addressed to Z.V.V. (val@physics.utah.edu) or A.N. (nahata@ece.utah.edu).

LETTERS

Magnetic exchange force microscopy with atomic resolution

Uwe Kaiser¹, Alexander Schwarz¹ & Roland Wiesendanger¹

The ordering of neighbouring atomic magnetic moments (spins) leads to important collective phenomena such as ferromagnetism and antiferromagnetism. A full understanding of magnetism on the nanometre scale therefore calls for information on the arrangement of spins in real space and with atomic resolution. Spin-polarized scanning tunnelling microscopy accomplishes this¹ but can probe only conducting materials. Force microscopy can be used on any sample independent of its conductivity. In particular, magnetic force microscopy² is well suited to exploring ferromagnetic domain structures. However, atomic resolution cannot be achieved because data acquisition involves the sensing of long-range magnetostatic forces between tip and sample. Magnetic exchange force microscopy has been proposed³ for overcoming this limitation: by using an atomic force microscope⁴ with a magnetic tip, it should be possible to detect the short-range magnetic exchange force between tip and sample spins. Here we show for a prototypical antiferromagnetic insulator, the (001) surface of nickel oxide, that magnetic exchange force microscopy can indeed reveal the arrangement of both surface atoms and their spins simultaneously. In contrast with previous attempts to implement this method^{5–8}, we use an external magnetic field to align the magnetic polarization at the tip apex so as to optimize the interaction between tip and sample spins. This allows us to observe the direct magnetic exchange coupling between the spins of the tip atom and sample atom that are closest to each other, and thereby demonstrate the potential of magnetic exchange force microscopy for investigations of inter-spin interactions at the atomic level.

Figure 1 sketches the general concept of magnetic exchange force microscopy (MExFM) for the (001) surface of the antiferromagnetic insulator nickel oxide studied here (see also Supplementary Information). The main feature of this force microscopy approach is that the atomic resolution capabilities of atomic force microscopy (AFM) are combined with spin sensitivity by using as a force sensor a magnetic tip mounted on the free end of a cantilever. Force is detected by the frequency-modulation technique⁹: the cantilever self-oscillates with constant amplitude A_0 , with tip-sample interactions shifting the actual cantilever frequency f by $\Delta f = f - f_0$ from the resonance frequency f_0 of the free cantilever ($\Delta f < 0$ and $\Delta f > 0$ for attractive and repulsive forces, respectively). During scanning in the x - y plane, Δf is kept constant by adjusting the z position of the tip relative to the surface so that the recorded $z(x, y)$ map, or topographic image, provides contour lines of constant tip-sample interaction force. Selecting a more negative Δf set-point increases the attractive interaction; that is, the tip-sample distance is reduced. This method permits atomic resolution on conducting and non-conducting surfaces in the non-contact regime^{10,11}, with height differences (or contrast) in the topography image reflecting variations of the short-range forces between the foremost tip atom and different atomic species of a surface.

The sample material nickel oxide crystallizes in the rock salt structure ($a = 417$ pm) and exhibits a nearly perfectly bulk terminated (001) surface¹². Below its Néel temperature of 525 K, it is a collinear antiferromagnet with ferromagnetic {111} sheets stacked in an antiferromagnetic order as indicated in Fig. 1. According to the superexchange model, the magnetic exchange interaction between the localized Ni d -states is mediated through the oxygen atoms¹³. Within each sheet the spins of the nickel atoms point in one of the 12 possible $\langle 211 \rangle$ orientations. X-ray linear magnetic dichroism data of single crystals indicate that the surface magnetic structure is bulk terminated¹⁴. The spin orientation therefore alternates on neighbouring rows along $\langle 110 \rangle$ directions on the (001) surface, and only the short-range magnetic exchange interaction varies between the chemically and structurally equivalent neighbouring nickel rows. For this reason, the exchange interaction can be distinguished unambiguously from all other long-range and short-range tip-sample interactions.

To prepare a clean (001) surface, the crystal is cleaved in ultrahigh vacuum and heated to 483–493 K for about 15 min to remove residual charges. All measurements are then performed with a silicon

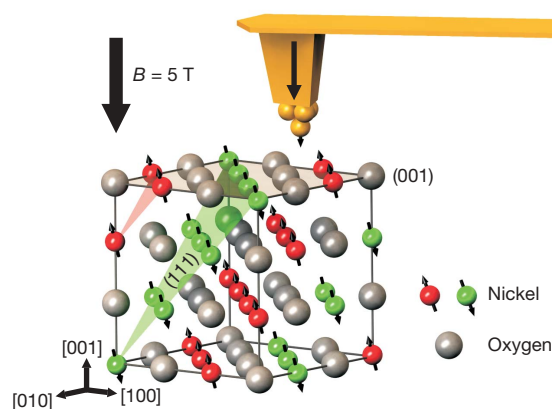


Figure 1 | Concept of MExFM on the insulating antiferromagnet nickel oxide. Nickel magnetic moments (spins) within {111} planes are ordered ferromagnetically and point in $\langle 211 \rangle$ directions. Because neighbouring {111} planes are aligned antiferromagnetically, nickel spins of opposite orientations (red and green) alternate along $\langle 110 \rangle$ directions on the (001) surface. To perform MExFM, a cantilever with an iron-coated tip is scanned above the (001) surface. An external magnetic field of $\mu_0 H = B = 5$ T maximizes the sensitivity of the tip apex to the out-of-plane component of the canted spins at the nickel atoms. A purely chemical and structural contrast would reflect only the arrangement of nickel and oxygen atoms. If the magnetic exchange interaction between the spins of the foremost iron atom at the tip apex and the nickel atom directly below is detected, an additional contrast modulation between neighbouring rows of nickel atoms should appear in an image of the (001) surface.

¹Institute of Applied Physics and Microstructure Research Center, University of Hamburg, Jungiusstrasse 11, 20355 Hamburg, Germany.

cantilever (which had been coated *in situ* with a 22-nm-thick ferromagnetic iron film), using our home-built low-temperature force microscope¹⁵. As a result of its shape anisotropy, the preferred magnetic polarization at the tip apex is in-plane with respect to the (001) surface (see Supplementary Fig. S4b). However, application of an external magnetic field of $\mu_0 H_{\text{ext}} = B_{\text{ext}} = 5$ T perpendicular to the sample surface aligns the magnetic polarization of the iron film along the field direction. In this configuration, the tip apex becomes mainly sensitive to the out-of-plane component of the spins at the sample surface¹⁶ (see Supplementary Fig. S4a). Note that because the exchange coupling between the spins of the nickel atoms is much stronger than the Zeeman energy, the antiferromagnetic order in the nickel oxide crystal is not affected.

According to the Heisenberg model the magnitude of the interaction between two spins \mathbf{S}_1 and \mathbf{S}_2 is given by their scalar product $\mathbf{H} = J_{12}\mathbf{S}_1 \cdot \mathbf{S}_2$, where J_{12} is the exchange integral. Thus, the interaction between tip spins and sample spins is strongest for either parallel or antiparallel spin orientations. In the sample, all 12 possible $\langle 211 \rangle$ spin orientations of the nickel atoms possess a significant in-plane component as well as an out-of-plane component with respect to the (001) surface. In the absence of a magnetic field, the coated tips have an in-plane magnetic polarization with no preferred spin orientation within the plane. Spins at the apex of such tips can therefore exhibit any angle with respect to the in-plane component of the spins at the nickel atoms, including unfavourable relative orientations characterized by vanishing magnetic exchange forces (see Supplementary Information). Applying an external magnetic field and probing the interaction between tip spins and the out-of-plane component of the sample spins overcomes this problem, because the spins are always either parallel or antiparallel. We note that such controlled manipulation of the tip apex spins into the favourable out-of-plane direction is the main difference between this study and all previous MExFM measurements on NiO(001) with magnetically coated tips in zero field^{5–8} (see Supplementary Information). An external magnetic field is not a prerequisite for MExFM, but alignment of the spins at the tip apex in a favourable direction with respect to the spins at the sample surface improves the overall measurement performance significantly. Such alignment can be induced by an external magnetic field as in this study, or by choosing different magnetic materials and appropriate growth modes to control the easy axis of the magnetic polarization.

Figure 2 shows two atomically resolved unfiltered data sets for NiO(001). Both sets were acquired on the same sample area with the use of the same iron-coated tip and with a bias voltage $U_{\text{bias}} = -1.2$ V applied between tip and sample to minimize electrostatic forces (see also Supplementary Information). No evidence for changes in tip characteristics was observed during data acquisition. The topographic image recorded at $\Delta f = -22.0$ Hz (Fig. 2a) exhibits maxima and minima that reflect the (1×1) symmetry of the chemical surface unit cell. In the Fourier transform of the data (Fig. 2c), the chemical unit cell is represented by four spots, which appear as peaks in the two line sections along the diagonals of the Fourier transform (Fig. 2e). The apparent height difference between minima and maxima along the [100] direction in Fig. 2a is about 4.5 pm. Because the total valence charge density is largest above the oxygen atoms¹⁷ and the chemical affinity between oxygen and iron is larger than that between nickel and iron¹⁸, the protrusions correspond to the oxygen sites¹⁹ (see also Supplementary Information).

The image in Fig. 2b was acquired at $\Delta f = -23.4$ Hz; in comparison with the data in Fig. 2a, this corresponds to the sample's having been moved by about 30 pm towards the cantilever. However, the stronger attractive interactions at shorter distances pull the tip-apex atoms towards the surface atoms and vice versa, so the true distance between the foremost tip atom and the surface atom underneath can be reduced significantly further¹⁹. When the raw data sets are compared, an additional modulation is apparent in Fig. 2b: every second row of nickel atoms along the [110] direction seems more depressed,

as indicated by the black arrows. In the Fourier transform (Fig. 2d), this is reflected by the appearance of one additional pair of peaks located halfway between the centre and two (opposing) peaks corresponding to the chemical unit cell. The line sections through the Fourier transform (Fig. 2f) confirm that the additional peaks are only present along one diagonal, as expected. When the scan direction is rotated by 30° , the chemical contrast and the additional modulation on neighbouring nickel rows are rotated accordingly (see Supplementary Information); this excludes the possibility of an oscillatory noise source in phase with the lattice periodicity causing the additional peaks seen in Fig. 2b, d, f. Note that a multiatom tip apex interacting in a purely non-magnetic fashion with the sample also cannot generate the modulation between structurally identical neighbouring nickel rows (see Supplementary Information), which we observed with several different iron-coated tips on different nickel oxide crystals. We therefore conclude that the observed additional contrast modulation on neighbouring nickel rows and the corresponding pair of peaks in the Fourier transform reflect the (2×1) antiferromagnetic surface unit cell of NiO(001), which demonstrates the feasibility of MExFM.

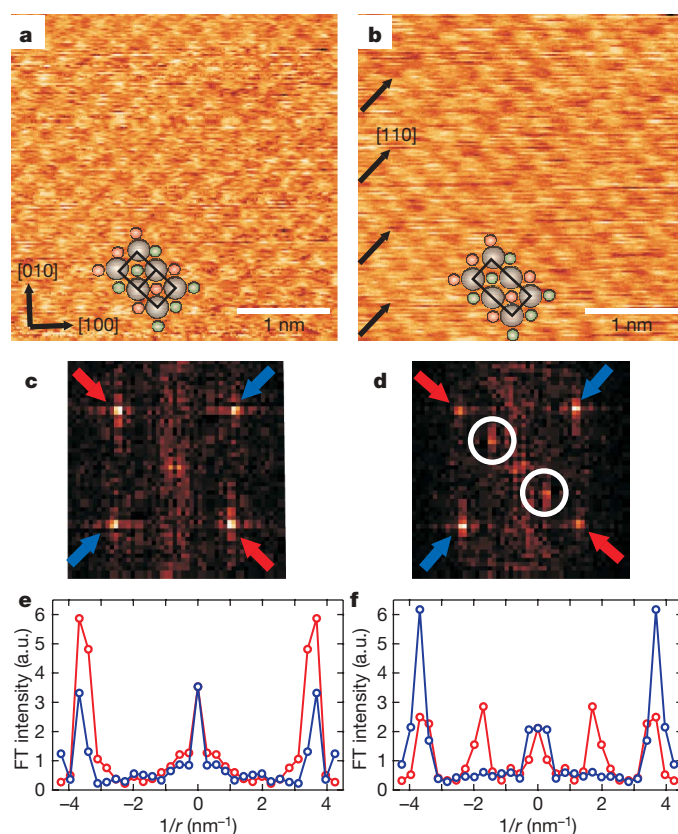


Figure 2 | Chemical and magnetic exchange contrast with atomic resolution on NiO(001). **a, b**, Unfiltered raw data obtained with the same tip at 7.9 K in 5 T on the same $3.5 \text{ nm} \times 3.5 \text{ nm}$ area. **a**, Image recorded at a constant frequency shift of -22.0 Hz. Protrusions and depressions reflect the arrangement of oxygen and nickel atoms, respectively. **c**, Fourier transform of **a**, in which the four spots correspond to the chemical surface unit cell. **b**, Image recorded at a smaller tip-sample distance realized by setting a larger negative frequency shift of -23.4 Hz. It displays an additional contrast modulation along neighbouring rows of nickel atoms (arrows) that results from the arrangement of spins at the NiO(001) surface (compare with Fig. 1). **d**, Fourier transform of **b**, in which the additional modulation is visible as an additional pair of peaks representing the size of the magnetic surface unit cell. **e, f**, Line sections across the Fourier transforms in **c** and **d**, respectively, clearly showing that the additional pair of peaks is visible only at smaller tip sample separations and only along one diagonal. The cantilever parameters were as follows: spring constant $\approx 34 \text{ N m}^{-1}$, $f_0 = 159 \text{ kHz}$, mechanical Q factor at 5 T = 27.720, $A_0 = 6.65 \text{ nm}$, $U_{\text{bias}} = -1.2 \text{ V}$.

To quantify the chemical and magnetic atomic scale contrast, we averaged over all chemical unit cells in Fig. 2a and over all magnetic unit cells in Fig. 2b. The left-hand panels in Fig. 3 show zooms of the raw data in Fig. 2, together with insets constructed by tiling together the respective single unit cell image obtained through averaging. The right-hand panels give the line sections along the [100] direction, from which all relevant apparent height differences h between chemically and magnetically different atoms can be determined. The data in Fig. 3a are consistent with detection of only purely chemical interactions between nickel or oxygen atoms and the iron tip: the apparent height differences are constant, with $h_{\text{Ni}|-\text{O}} = h_{\text{Ni}|-\text{O}} = h_{\text{Ni}|-\text{O}} \approx 4.5$ pm. This contrasts with the data in Fig. 3b, where apparent height differences between oxygen and nickel atoms are seen to depend on the spin orientation of the latter: $h_{\text{Ni}|-\text{O}} \approx 3.7$ pm and $h_{\text{Ni}|-\text{O}} \approx 5.2$ pm, respectively, for nickel atoms with opposite spin orientations ($\text{Ni}\uparrow$ and $\text{Ni}\downarrow$). Thus, the resulting apparent height difference due to the magnetic exchange interactions is $h_{\text{Ni}\downarrow-\text{Ni}\uparrow} = |h_{\text{Ni}\downarrow-\text{O}} - h_{\text{Ni}\uparrow-\text{O}}| \approx 1.5$ pm. Note that in Fig. 3b the chemical contrast between nickel and oxygen atoms, which can be estimated as $h_{\text{Ni-O}} = \frac{1}{2}|h_{\text{Ni}\downarrow-\text{O}} + h_{\text{Ni}\uparrow-\text{O}}| \approx 4.5$ pm, is the same as in Fig. 3a. Furthermore, no significant difference in contrast is observed for oxygen atoms in neighbouring rows.

The dependence of the contrast on the tip-sample distance apparent in the data of Fig. 2 agrees with density functional calculations for the Fe/NiO(001) system, which found that chemical interactions are detectable at relatively large separations, whereas magnetic exchange forces give rise to detectable contrast only for distances below 340 pm (ref. 20). At larger tip-sample distances, such as those used in Fig. 2a, the foremost iron atom at the tip apex mainly interacts with the O(2p) electrons that dominate the total valence charge density and are expected to reach farther into the vacuum region above the surface than the localized Ni(3d) electrons²¹. The latter electrons, which carry the magnetic spin in this system, can be probed by the tip only at relatively small separations as in Fig. 2b. Assuming that the magnetic exchange interaction involves—as predicted²⁰—ferromagnetic

coupling between tip and sample spins, it will add to the chemical interaction such that the total attractive interaction becomes stronger or weaker if the z component of the magnetic moment of the Ni atoms is respectively parallel or antiparallel to that of the Fe atom at the tip apex. Considering that the topography (constant Δf) images represent contour lines of constant interaction strength, such a spin-dependent variation of the tip-sample interaction readily explains the observed apparent height differences between neighbouring nickel rows.

We note that successful detection of an MExFM contrast is accompanied by the observation of a much fainter chemical contrast than was typically seen in previous measurements that observed only chemical contrast. (Compare 4.5 pm in Fig. 2a with reported corrugation amplitudes of 20–40 pm (refs 5–8) for previous force microscopy measurements over NiO(001).) This behaviour agrees with theoretical predictions that strong chemical interactions prevent a close approach¹⁹ because of spontaneous modifications of the tip apex, which precludes reaching the small separations that are necessary to attain a significant overlap between the itinerant d -electrons of the iron tip and the localized d -electrons at the nickel atoms (see Supplementary Information). We found that the magnitude of the observed MExFM contrast varies from tip to tip, ranging between 0.5 and 1.5 pm. Such variations are expected because the magnitude of the magnetic exchange interaction depends on the relative orientation between tip and sample spins.

This study is a first step in establishing MExFM as a versatile technique to probe magnetic moments of surfaces at the atomic scale and independently of the samples' conductivity. We expect that this approach can be used to study systems such as the antiferromagnetic insulating pinning layers in exchange-bias systems²², which are widely used in the development of future magnetic storage and sensor devices, or magnetically active single atoms and molecules that are adsorbed on insulators to avoid hybridization. By performing measurements as a function of tip-sample distance, it should be possible to quantify the magnitude of the interaction force and to distinguish between different spin-coupling mechanisms underlying the exchange interaction. Even dynamic processes such as spin precession or spin wave (magnon) excitation might be accessible, through evaluation of the energy dissipated during scanning.

Received 17 May 2006; accepted 19 January 2007.

- Heinze, S. *et al.* Real-space imaging of two-dimensional antiferromagnetism on the atomic scale. *Science* **288**, 1805–1808 (2000).
- Martin, Y. & Wickramasinghe, H. K. Magnetic imaging by 'force microscopy' with 1000 Å resolution. *Appl. Phys. Lett.* **50**, 1455–1457 (1987).
- Wiesendanger, R. *et al.* Vacuum tunneling of spin-polarized electrons detected by scanning tunnelling microscopy. *J. Vac. Sci. Technol. B* **9**, 519–524 (1990).
- Binnig, G., Quate, C. F. & Gerber, C. Atomic force microscope. *Phys. Rev. Lett.* **56**, 930–933 (1986).
- Hölscher, H., Langkat, S. M., Schwarz, A. & Wiesendanger, R. Measurement of three-dimensional force fields with atomic resolution using dynamic force spectroscopy. *Appl. Phys. Lett.* **81**, 4428–4430 (2002).
- Langkat, S., Hölscher, H., Schwarz, A. & Wiesendanger, R. Determination of site-specific forces between an iron coated tip and the NiO(001) surface by force field spectroscopy. *Surf. Sci.* **527**, 12–20 (2003).
- Hoffmann, R. *et al.* Atomic resolution imaging and frequency versus distance measurements on NiO(001) using low-temperature scanning force microscopy. *Phys. Rev. B* **67**, 085402 (2003).
- Hosoi, H., Sueoka, K. & Mukasa, K. Investigations on the topographical asymmetry of non-contact atomic force microscopy images of NiO(001) surface observed with a ferromagnetic tip. *Nanotechnology* **15**, 506–509 (2004).
- Albrecht, T. R., Grütter, P., Horne, D. & Rugar, D. Frequency modulation detection using high-Q cantilevers for enhanced force microscope sensitivity. *J. Appl. Phys.* **69**, 669–673 (1991).
- Giesibl, F. J. Atomic resolution of the silicon (111)-(7 × 7) surface by atomic force microscopy. *Science* **267**, 68–71 (1995).
- Morita, S., Wiesendanger, R. & Meyer, E. (eds) *Noncontact Atomic Force Microscopy* (Springer, Berlin, 2002).
- Okazawa, T., Yagi, Y. & Kido, Y. Ruffled surface structure and lattice dynamics of NiO(001). *Phys. Rev. B* **67**, 195406 (2003).
- Anderson, P. W. Antiferromagnetism. Theory of superexchange interaction. *Phys. Rev.* **79**, 350–356 (1950).

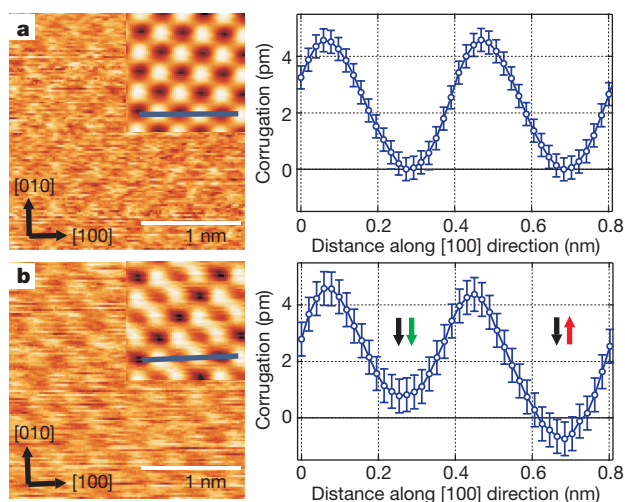


Figure 3 | Quantification of the chemical contrast and the MExFM contrast after unit cell averaging. The raw data are displayed together with an inset tiled from the single chemical (a) and magnetic (b) unit cell, respectively, obtained after averaging over all imaged unit cells of the raw data in Fig. 2. From the line section along the [001] direction the purely chemical apparent height difference between nickel and oxygen in a obtained at a relatively large tip-sample distance can be measured as about 4.5 pm. At a smaller separation the additional apparent height difference between nickel atoms of opposite spin orientations due to the magnetic exchange interaction with the spin of the iron tip is 1.5 pm. The error bars (± 0.2 pm in a, ± 0.3 pm in b) represent the root-mean-square noise after unit cell averaging. Note that the indicated relative spin orientation between iron tip (black arrow) and nickel (green and red arrows, respectively) in b corresponds to a ferromagnetic exchange coupling, as predicted in ref. 20.

14. Hillebrecht, F. U. *et al.* Magnetic moments at the surface of antiferromagnetic NiO(100). *Phys. Rev. Lett.* **86**, 3419–3422 (2001).
15. Liebmann, M., Schwarz, A., Langkat, S. M. & Wiesendanger, R. A low-temperature ultrahigh vacuum scanning force microscope with a split-coil magnet. *Rev. Sci. Instrum.* **73**, 3508–3514 (2002).
16. Kubetzka, A. *et al.* Revealing antiferromagnetic order of the Fe monolayer on W(001): spin-polarized scanning tunneling microscopy and first-principles calculations. *Phys. Rev. Lett.* **94**, 087204 (2005).
17. Castell, M. R., Dudarev, S. L., Briggs, G. A. D. & Sutton, A. P. Unexpected differences in the surface electronic structure of NiO and CoO observed by STM and explained by first-principles theory. *Phys. Rev. B* **59**, 7342–7345 (1999).
18. Regan, T. J. *et al.* Chemical effects at metal/oxide interfaces studied by x-ray-absorption spectroscopy. *Phys. Rev. B* **64**, 214422 (2001).
19. Foster, A. S. & Shluger, A. L. Spin contrast in non-contact SFM on oxide surfaces: Theoretical modelling of NiO(001) surface. *Surf. Sci.* **490**, 211–219 (2001).
20. Momida, H. & Oguchi, T. First-principles study on exchange force image of NiO(001) surface using a ferromagnetic Fe probe. *Surf. Sci.* **590**, 42–50 (2005).
21. Castell, M. R. *et al.* Atomic-resolution STM of a system with strongly correlated electrons: NiO(001) surface structure and defect sites. *Phys. Rev. B* **55**, 7859–7863 (1997).
22. Nogues, J. & Schuller, I. K. Exchange bias. *J. Magn. Magn. Mater.* **192**, 203–232 (1999).

Supplementary Information is linked to the online version of the paper at www.nature.com/nature.

Acknowledgements This work was supported by a grant from the Sonderforschungsbereich Magnetismus vom Einzelatom zur Nanostruktur of the Deutsche Forschungsgemeinschaft.

Author Information Reprints and permissions information is available at www.nature.com/reprints. The authors declare no competing financial interests. Correspondence and requests for materials should be addressed to A.S. (aschwarz@physnet.uni-hamburg.de).

LETTERS

Absolute configuration of chirally deuterated neopentane

J. Haesler¹, I. Schindelholz¹, E. Riguet¹, C. G. Bochet¹ & W. Hug¹

The relationship between macroscopic chirality and chirality on the molecular level was unequivocally established in 1951 through anomalous X-ray scattering¹. Although this technique became the definitive method for determining the absolute configuration of a molecule, one important limitation of the approach is that the molecule must contain 'heavy' atoms (for example, bromine). The direct determination of absolute configurations for a wider range of molecules has recently become possible by measuring a molecule's vibrational optical activity^{2,3}. Here we show that instrumental advances in Raman optical activity^{4,5}, combined with quantum chemical computations^{6–8}, make it possible to determine the absolute configuration of (*R*)-[²H₁, ²H₂, ²H₃]-neopentane⁹. This saturated hydrocarbon represents the archetype of all molecules that are chiral as a result of a dissymmetric mass distribution. It is chemically inert and cannot be derivatized to yield molecules that would reveal the absolute configuration of the parent compound. Diastereomeric interactions with other molecules, optical rotation, and electronic circular dichroism are, in contrast to the well-known case of bromochlorofluoromethane^{10–12}, not expected to be measurable. Vibronic effects in the vacuum ultraviolet circular dichroism might reveal that the molecule is chiral, but the presence of nine rotamers would make it extremely difficult to interpret the spectra, because the spatial arrangement of the rotamers' nuclei resembles that of enantiomers. The unequivocal spectroscopic determination of the absolute configuration of (*R*)-[²H₁, ²H₂, ²H₃]-neopentane therefore presented a major challenge, one that was at the very limit of what is possible.

The synthesis of enantioenriched (*R*)-[²H₁, ²H₂, ²H₃]-neopentane **1** is itself a challenge. It bears a quaternary chiral centre, the substituents of which are differentiated only by their isotopic pattern; it is gaseous at room temperature and pressure, and it is highly flammable. The intuitive retrosynthetic analysis based on the deprotonation/alkylation of an α -CD₃-substituted chiral propionate derivative (see Supplementary Information) fails because the high electronic and steric similarity between the CH₃ and the CD₃ groups prevent the preferential formation of one of the two diastereomeric enolates.

We therefore decided to exploit the difference in shape between a tetrahedral Csp³ and a trigonal Csp² carbon by a γ -deprotonation/ α -alkylation sequence as shown in Fig. 1 (see Supplementary Information for full protocols and characterization). Hence, treatment of the chiral oxazolidinone derivative **4** with sodium hexamethyldisilazide, followed by alkylation with perdeuterated methyl iodide provided the compound **5** with a diastereomeric purity of 95% (the diastereomeric ratio was measured by hydrogen nuclear magnetic resonance, ¹H-NMR); its absolute configuration was assigned by analogy to a closely related alkylation¹³. At this point, the chiral quaternary centre bears no risk of racemization, and the optical purity can be assumed to be 95% enantiomeric ratio (e.r.) throughout the rest of the synthesis. Reductive removal of the chiral auxiliary with lithium aluminium deuteride, followed by ozonolysis and *in situ* reduction with sodium borodeuteride, gave the diol **7**, which was then converted into the stable and non-volatile dimesylate **8**. ¹H-NMR analysis confirmed the expected 1:3 ratio of methylene versus

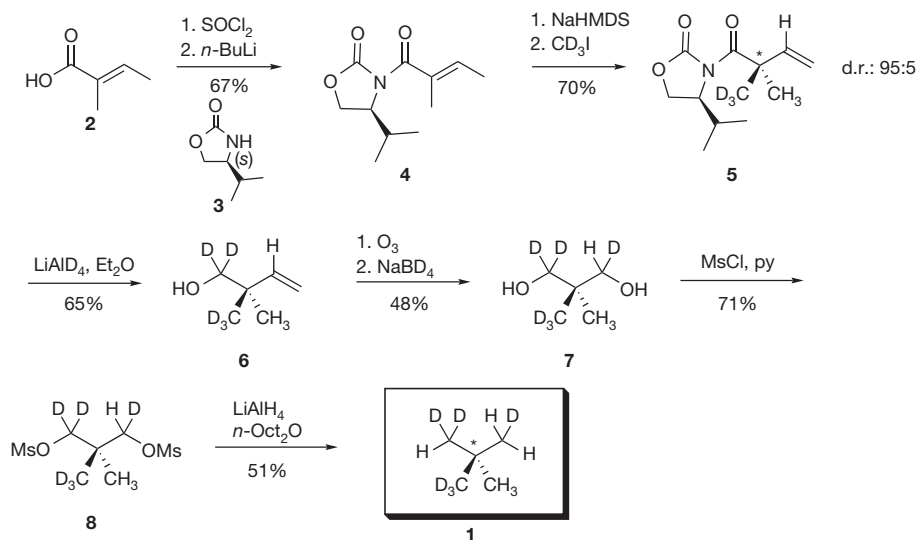


Figure 1 | Synthetic route to chirally deuterated neopentane **1**. Yields are given in percentage. d.r., diastereomeric ratio. NaHMDS, sodium hexamethyldisilazide; Et₂O, diethyl ether; Ms, mesyl; py, pyridine.

¹Department of Chemistry, University of Fribourg, ch. du Musée 9, CH-1700 Fribourg, Switzerland.

methyl resonances, also compatible with the reference mesylate CH_3 groups (see Supplementary Information). Displacement of both mesylates was performed by an excess of lithium aluminium hydride at 50 °C in a sealed tube for 48 h. (*R*)-[$^2\text{H}_1, ^2\text{H}_2, ^2\text{H}_3$]-neopentane **1** was collected by room pressure and room temperature distillation into a NMR tube precooled to 77 K. The tube was then sealed by fusion.

Owing to the procedure used to collect the sample, the yield (30 mg, 51%) was evaluated spectroscopically by proton NMR with an internal standard (25 mg of **1** were collected in the NMR tube and 5.1 mg in a glass capillary for Raman measurements). ^1H -NMR shows three distinct resonances at 0.89, 0.87 and 0.86 p.p.m. with the integral ratios (3:2:1) and multiplicity (singlet, triplet and quintet), expected for the peripheral CH_3 , CH_2D and CHD_2 groups (see Supplementary Information). The ^2H -NMR spectrum shows three broad singlets in the methyl regions. Interestingly, it is in the ^{13}C -NMR (with ^1H broadband decoupling) that all the methyl groups are visible, confirmed by the corresponding DEPT-135 sequence (see Fig. 2).

Noise and deterministic spurious signals are the two biggest problems in Raman optical activity. The criterion for its measurability is less the absolute size than the ratio of Raman optical activity (ROA) to Raman scattering, commonly designated by Δ (ref. 14). From the computed spectra it was estimated that Δ for the mixture of the rotamers of (*R*)-[$^2\text{H}_1, ^2\text{H}_2, ^2\text{H}_3$]-neopentane would be too small for ROA to be measurable except in the 720 to 950 cm^{-1} and the 1,150 to 1,340 cm^{-1} spectral regions⁹. Even for these two spectral regions, the size of the computed Δ values is only a few times 10^{-5} in backscattering, with even smaller values for other scattering geometries. This made the backscattering geometry the one most likely to allow us to confirm spectroscopically the chirality of (*R*)-[$^2\text{H}_1, ^2\text{H}_2, ^2\text{H}_3$]-neopentane.

The physical properties of the compound—its boiling point is expected to be 9.5 °C, the same as for neopentane and perdeuterated neopentane—the long measurement times needed to recover ROA for small Raman bands with tiny Δ values, and the small amount of substance available, made it necessary to perform the measurements in a sealed capillary. Backscattering requires us to orient a capillary's axis perpendicularly to the direction of the exciting laser beam⁵. This arrangement is more prone to spurious signals than the use of cells

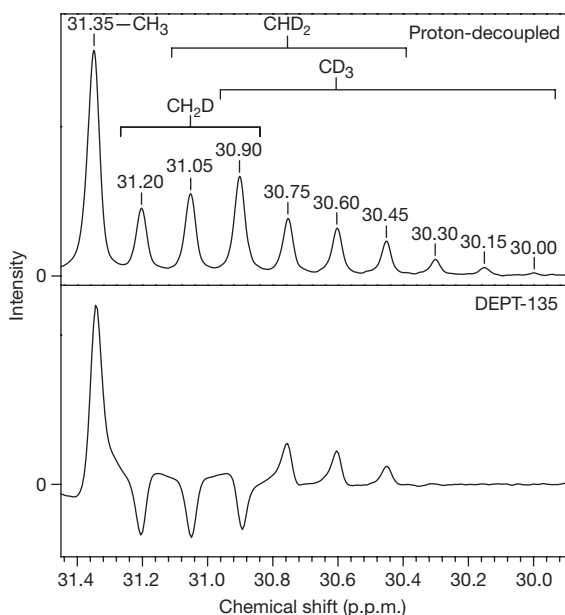


Figure 2 | ^{13}C -NMR characterization of the quaternary centre. Upper panel, broadband proton-decoupled spectrum. Lower panel, DEPT-135 spectrum.

with flat windows. In our scattered circular polarization experiment, in which the amount of right and left circularly polarized scattered light is analysed, the optical properties of the sample cell matter least for Raman bands for which the degree of circularity¹⁵ is zero or slightly positive, which is the case for the 720 to 950 cm^{-1} and the 1,150 to 1,340 cm^{-1} region (see Supplementary Information).

The scattered circular polarization ROA instrument¹⁶ (see Supplementary Information) used in this work is based on the design of an earlier one⁴. A dual-arm light-collection arrangement with fibre optics permits the simultaneous analysis of right and left circularly polarized scattered light, and an error-correction scheme⁵ reduces deterministic spurious signals by creating the chiroptical properties of the enantiomeric sample, through optical means, from the sample physically present. Subtracting the signals makes the technique equivalent to recovering optical activity from a measurement of both enantiomers. Linearly polarized components of light are scrambled throughout all optical paths.

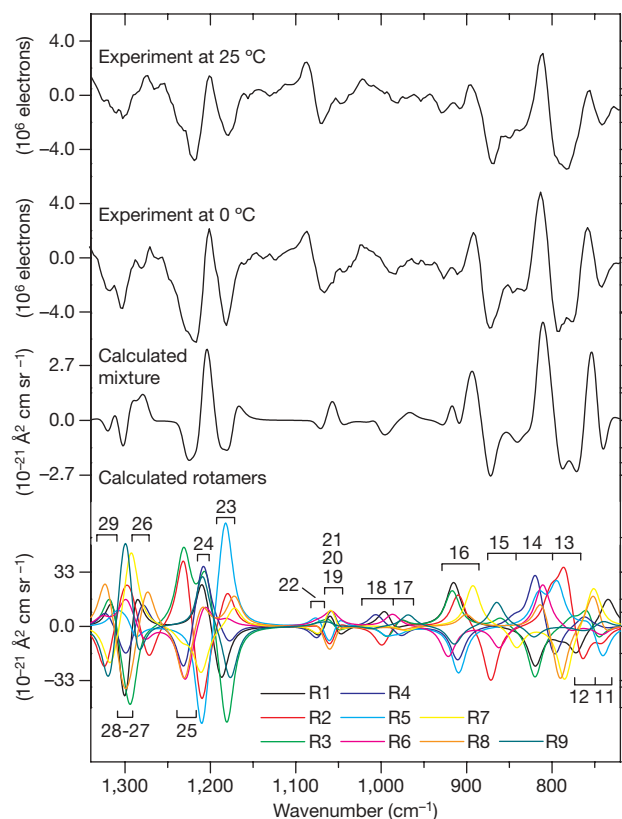


Figure 3 | ROA spectra of (*R*)-[$^2\text{H}_1, ^2\text{H}_2, ^2\text{H}_3$]-neopentane. The upper two traces show measured ROA spectra with temperatures as indicated. The lower traces show computed individual ROA spectra for the nine rotamers R1 to R9 (colours as indicated) and the average ROA spectrum for the mixture of all rotamers. The number of electrons is per column on the charge-coupled device (CCD) detector, which corresponds to 2.4 cm^{-1} . The numbers in the computed spectra refer to the vibrations of the nine rotamers. The measurement parameters are: exposure time, 40 h; laser power at sample, 300 mW; exciting wavelength, 532 nm; resolution, 7 cm^{-1} ; sample size, 5.1 mg. The experimental spectra were smoothed by a third-order seven-point Savitzky–Golay procedure. The computational parameters are: density functional theory with the B3LYP functional and the augmented correlation consistent polarized valence double zeta (aug-cc-pVDZ) basis set for geometry and vibrations as implemented in Gaussian 03 (ref. 28); time-dependent Hartree–Fock with the aug-cc-pVDZ basis set for electronic tensors as implemented in the molecular electronic structure program DALTON (release 1.1 in 2000; <http://www.kjemi.uio.no/software/dalton/dalton.html>). The computed wavenumbers were multiplied by a scaling factor of 0.9875 to account for anharmonicity. See text for band shape parameters.

The ROA and Raman spectra for the mixture of the rotamers are shown in Figs 3 and 4, together with those computed for individual rotamers. This makes it clear that the computed bands do not correspond to individual vibrational modes. Rather, each band is the result of the superposition of the ROA or Raman intensities of many modes of different conformers, a situation which is not uncommon in vibrational optical activity.

That the computed and measured ROA data agree to the extent they do is impressive. The ROA of individual rotamers, often of opposite sign, exceeds the ROA of the mixture by more than an order of magnitude. The relative size, and the relative position, calculated for the ROA bands of different rotamers, must therefore be of a far higher precision than has up to now been judged attainable. The dependence of the theoretical spectra on computational details was carefully checked. We have attributed the stability we found to the T_d site symmetry of the molecule, the close to identical electron distribution of the rotamers, and the observation that normal coordinates of energetically close vibrational modes of different rotamers decompose similarly into valence coordinates.

The choice of band shapes for rendering the theoretical spectra is important in a comparison with measured ones⁹. We assumed the lineshape function of the instrument to be gaussian with a full-width at half-maximum height (FWHM) of 7 cm^{-1} . The lineshape of the instrument was convoluted with lorentzian curves of 10 cm^{-1} and 18 cm^{-1} FWHM for the computed isotropic and anisotropic intensities, respectively. These values, which must be considered averages for different bands, gave the best agreement with the measured data at hand, including the Raman spectra of ordinary and of perdeuterated neopentane. For these compounds the complication of the presence of different conformers does not exist.

In the limited temperature range accessible to our instrument, the anisotropic lineshape was found to vary more than the isotropic one with the sample temperature. The visible sharpening of the Raman

spectrum in Fig. 4 upon lowering the temperature from 25 to 0°C can be attributed to the narrowing of the anisotropic band shape of individual rotamers. Similarly, in Fig. 3, the ROA spectrum measured at 0°C has a higher amplitude than the spectrum measured at 25°C and appears to be, to the extent that noise permits such a conclusion, more structured. We note that ROA measured in backscattering is purely anisotropic.

The internal rotational barrier of the methyl groups of neopentane has been the subject of much interest. Thermodynamic data¹⁷, the frequency of the methyl torsional mode^{18,19}, and cold neutron scattering^{20,21} yield values between 18 and 21 kJ per mole. This amounts to about seven times the value of kT at room temperature. The molecule's different rotamers therefore do not convert rapidly into each other. The amplitude of the hindered rotational motion of the methyl groups was estimated from model potentials to be about 15° at room temperature²². The C–C stretching force constant was found to depend on the torsional angle²³. The stronger variation with temperature of the anisotropic band shape than of the isotropic one makes it unlikely that this is the main cause for the changes in the Raman and ROA spectra we observe. More probably, these changes are due to the temperature dependence of the librational motions of the whole $(R)\text{-}[^2\text{H}_1, ^2\text{H}_2, ^2\text{H}_3]\text{-neopentane}$ molecules in the liquid phase. The substantial size of the changes, despite the modest measured temperature range of only 25°C , is put into perspective by the fact that it is equivalent to the span between the melting and boiling point of neopentane at 1 bar. From the temperature dependence of the entropy we also know that onset of molecular reorientation occurs at -133°C , at the passage to a face-centred cubic crystal structure²¹.

The vibrations in the 720 to 950 cm^{-1} region are dominated by the rocking motions of whole methyl groups⁹. In the $1,150$ to $1,350\text{ cm}^{-1}$ region, C–C bond stretching and the deformation of the methyl groups becomes important. In each of the two spectral regions, the distribution of vibrational energy shifts from the deuterium to the hydrogen nuclei with increasing frequency.

The synthesis of $(R)\text{-}[^2\text{H}_1, ^2\text{H}_2, ^2\text{H}_3]\text{-neopentane}$, the spectroscopic proof of its chiral nature, and the actual determination of the absolute configuration of this chemically inert, pure hydrocarbon molecule with T_d site symmetry, all extend the scope of chiral chemistry and of vibrational optical activity. Although the measurement of optical activity of molecules chiral by isotope substitution has been accomplished in the past, in the ultraviolet²⁴, by Raman spectroscopy^{25,26}, and in the infrared²⁷, none of the molecules measured presented the challenges faced here: a highly symmetric electron distribution, absence of an electronic chromophore, and the presence of multiple, equally weighted conformers with mutually cancelling optical activity. There should remain few, if any, chiral systems the absolute configuration of which is not now spectroscopically accessible, either by anomalous X-ray scattering, by vibrational optical activity, or, under favourable circumstances, by the classical chiroptical methods of electronic rotatory dispersion and circular dichroism.

The reason that vibrational optical activity is so demonstrably more powerful than the methods mentioned above is that any chiral molecule must comprise at least four nuclei in a non-planar arrangement, and it will thus have a minimum of six vibrational modes reflecting its absolute configuration. Their shape is not the only, but is the decisive aspect in the computation of vibrational optical activity. Once a molecule's force field is known, calculating vibrational modes becomes largely a problem of classical mechanics. The calculation of a force field precise enough for determining the absolute configuration of a molecule like $(R)\text{-}[^2\text{H}_1, ^2\text{H}_2, ^2\text{H}_3]\text{-neopentane}$ can be done with little expense, as we have demonstrated here.

METHODS

For the Raman and ROA measurements, Minicaps of length 30 mm with an inner diameter of 1.3 mm and a wall thickness of 0.2 mm were used. A Minicap was fused at one end, evacuated, cooled with liquid nitrogen, and

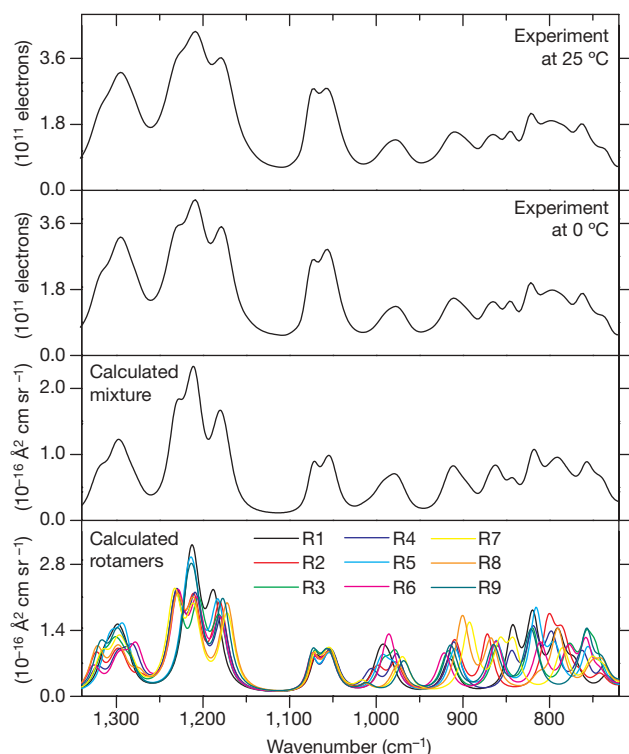


Figure 4 | Raman spectra of $(R)\text{-}[^2\text{H}_1, ^2\text{H}_2, ^2\text{H}_3]\text{-neopentane}$. The upper two traces show measured Raman spectra with temperature as indicated. The lower traces show computed individual Raman spectra for the nine rotamers R1 to R9 (colours as indicated) and the average Raman spectrum for the mixture of all rotamers. Experimental and computational parameters are as in Fig. 3.

5.1 mg (8.5 μ l) of (R)-[$^2\text{H}_1$, $^2\text{H}_2$, $^2\text{H}_3$]-neopentane condensed into it, directly from the Schlenk tube in which the compound had been synthesized. Fusion of the other end yielded a hermetically sealed sample of (R)-[$^2\text{H}_1$, $^2\text{H}_2$, $^2\text{H}_3$]-neopentane, slightly pressurized at room temperature, on which measurements could be performed. The laser power was kept at a relatively low 300 mW at the sample to avoid warming the capillary and distilling neopentane from the scattering zone to cooler parts during the long measurement sessions, typically lasting about 40 h. Measurements below room temperature were done while blowing dried cold air into a cage surrounding the capillary. Neopentane freezes at -16.5°C and the perdeuterated form at -18°C , which suggests a similar lower temperature limit for performing ROA measurements on liquid (R)-[$^2\text{H}_1$, $^2\text{H}_2$, $^2\text{H}_3$]-neopentane. In practice, we had to limit the lowest temperature to 0°C to avoid condensation on the light-collection optics of the instrument.

Received 19 October 2006; accepted 5 February 2007.

1. Bijvoet, J. M., Peerdeman, A. F. & van Bommel, A. J. Determination of the absolute configuration of optically active compounds by means of X-rays. *Nature* **168**, 271–272 (1951).
2. Barron, L. D., Bogaard, M. P. & Buckingham, A. D. Raman scattering of circularly polarized light by optically active molecules. *J. Am. Chem. Soc.* **95**, 603–605 (1973).
3. Holzwarth, G., Hsu, E. C., Mosher, H. S., Faulkaner, T. R. & Moscovitz, A. Infrared circular dichroism of carbon-hydrogen and carbon-deuterium stretching modes. Observations. *J. Am. Chem. Soc.* **96**, 251–252 (1974).
4. Hug, W. & Hangartner, G. A novel high-throughput Raman spectrometer for polarization difference measurements. *J. Raman Spectrosc.* **30**, 841–852 (1999).
5. Hug, W. Virtual enantiomers as the solution of optical activity's deterministic offset problem. *Appl. Spectrosc.* **57**, 1–13 (2003).
6. Helgaker, T., Ruud, K., Bak, K. L., Joergensen, P. & Olsen, J. Vibrational Raman optical activity calculations using London atomic orbitals. *Faraday Discuss.* **99**, 165–180 (1994).
7. Ruud, K., Helgaker, T. & Bouř, P. Gauge-origin independent density-functional theory calculations of vibrational Raman optical activity. *J. Phys. Chem. A* **106**, 7448–7455 (2002).
8. Zuber, G. & Hug, W. Rarefied basis sets for the calculation of optical tensors. 1. The importance of gradients on hydrogen atoms for the Raman scattering tensor. *J. Phys. Chem.* **108**, 2108–2118 (2004).
9. Hug, W. & Haesler, J. Is the vibrational optical activity of (R)-[$^2\text{H}_1$, $^2\text{H}_2$, $^2\text{H}_3$]-neopentane measurable? *Int. J. Quantum Chem.* **104**, 695–715 (2005).
10. Costante, J., Hecht, L., Polavarapu, P. L., Collet, A. & Barron, L. D. Absolute configuration of bromochlorofluoromethane from experimental and *ab initio* theoretical vibrational Raman optical activity. *Angew. Chem. Int. Edn Engl.* **36**, 885–887 (1997).
11. Crassous, J. & Collet, A. The bromochlorofluoromethane saga. *Enantiomer* **5**, 429–438 (2000).
12. Jiang, Z., Crassous, J. & Schurig, V. Gas-chromatographic separation of tri(hetero)halogenomethane enantiomers. *Chirality* **17**, 488–493 (2005).
13. Abe, T., Suzuki, T., Sekiguchi, K., Hosokawa, S. & Kobayashi, S. Stereoselective construction of a quaternary carbon substituted with multifunctional groups: application to the concise synthesis of (+)-ethosuximide. *Tetrahedr. Lett.* **44**, 9303–9305 (2003).
14. Barron, L. D. *Molecular Light Scattering and Optical Activity* 162, Ch. 3 (Cambridge Univ. Press, Cambridge, 2004).
15. Long, D. A. *Raman Spectroscopy* 130 (McGraw-Hill, New York, 1977).
16. Haesler, J. *Construction of a New Forward and Backward Scattering Raman Optical Activity Spectrometer and Graphical Analysis of Measured and Calculated Spectra for (R)-[$^2\text{H}_1$, $^2\text{H}_2$, $^2\text{H}_3$]-neopentane*. PhD thesis (Univ. Fribourg, 2006).
17. Pitzer, K. S. & Kilpatrick, J. E. The entropies and related properties of branched paraffin hydrocarbons. *Chem. Rev.* **39**, 435–447 (1946).
18. Weiss, S. & Leroi, G. E. Infrared spectra and internal rotation in propane, isobutane, and neopentane. *Spectrochim. Acta A* **25**, 1759–1766 (1969).
19. Durig, J. R., Craven, S. M. & Bragin, J. Low-frequency modes in molecular crystals. VI. Methyl torsions and barriers to internal rotation of $\text{C}(\text{CH}_3)_4$, $\text{C}(\text{CD}_3)_4$, $\text{Si}(\text{CH}_3)_4$, $\text{Ge}(\text{CH}_3)_4$, and $\text{Sn}(\text{CH}_3)_4$. *J. Chem. Phys.* **52**, 2046–2052 (1970).
20. Rush, J. J. Cold-neutron study of hindered rotations in solid and liquid methylchloroform, neopentane, and ethane. *J. Chem. Phys.* **46**, 2285–2291 (1967).
21. Grant, D. M., Strong, K. A. & Brugger, R. M. Direct observation of methyl librations in neopentane. *Phys. Rev. Lett.* **20**, 983–986 (1968).
22. Petryk, M. W. P. & Henry, B. R. Through space coupling and fermi resonances in neopentane- d_0 , - d_6 , - d_9 , and tetramethylsilane. *J. Phys. Chem.* **106**, 8599–8608 (2002).
23. Palmo, K., Mirkin, N. G. & Krimm, S. Spectroscopically determined force fields for macromolecules. 2. Saturated hydrocarbon chains. *J. Phys. Chem. A* **102**, 6448–6456 (1998).
24. Barth, G. & Djerassi, C. Circular dichroism of molecules with isotopically engendered chirality. *Tetrahedron* **37**, 4123–4142 (1981).
25. Barron, L. D. Raman optical activity due to isotopic substitution: [α -2H]benzyl alcohol. *J. Chem. Soc. Chem. Commun.* **9**, 305–306 (1977).
26. Hug, W. Instrumental and theoretical advances in Raman optical activity. In *Raman Spectroscopy, Linear and Nonlinear* (eds Lascombe, J. & Huong, P. V.) **3** (John Wiley & Sons, Chichester, 1982).
27. Polavarapu, P. L., Nafie, L. A., Benner, S. A. & Morton, T. H. Optical activity due to isotopic substitution. Vibrational circular dichroism and the absolute configurations of α -deuterated cyclohexanones. *J. Am. Chem. Soc.* **103**, 5349–5359 (1981).
28. Frisch, M. J. et al. *Gaussian 03 Revision C.02* (Gaussian Inc., Wallingford, Connecticut, 2004).

Supplementary Information is linked to the online version of the paper at www.nature.com/nature. A figure summarizing the main result of this paper is also included.

Acknowledgements We thank F. Nydegger and F. Fehr for their analytical work. This work was supported by the Swiss National Science Foundation.

Author Contributions W.H. developed the design of the instrument. J.H. constructed the spectrometer used in this work and performed the ROA measurements. J.H. and I.S. isolated the sample in the capillary. J.H. performed the *ab initio* calculations. I.S. and E.R. performed and optimized the synthesis. C.G.B. designed the synthetic route. W.H. proposed this work. W.H. and C.G.B. wrote the paper. All authors discussed the results and commented on the manuscript.

Author Information Reprints and permissions information is available at www.nature.com/reprints. The authors declare no competing financial interests. Correspondence and requests for materials should be addressed to W.H. (w.hug@gmx.net) or J.H. (jacques.haesler@unifr.ch).

LETTERS

Climate sensitivity constrained by CO₂ concentrations over the past 420 million years

Dana L. Royer¹, Robert A. Berner² & Jeffrey Park²

A firm understanding of the relationship between atmospheric carbon dioxide concentration and temperature is critical for interpreting past climate change and for predicting future climate change¹. A recent synthesis² suggests that the increase in global-mean surface temperature in response to a doubling of the atmospheric carbon dioxide concentration, termed 'climate sensitivity', is between 1.5 and 6.2 °C (5–95 per cent likelihood range), but some evidence is inconsistent with this range^{1–5}. Moreover, most estimates of climate sensitivity are based on records of climate change over the past few decades to thousands of years, when carbon dioxide concentrations and global temperatures were similar to or lower than today^{1,6}, so such calculations tend to underestimate the magnitude of large climate-change events⁷ and may not be applicable to climate change under warmer conditions in the future. Here we estimate long-term equilibrium climate sensitivity by modelling carbon dioxide concentrations over the past 420 million years and comparing our calculations with a proxy record. Our estimates are broadly consistent with estimates based on short-term climate records, and indicate that a weak radiative forcing by carbon dioxide is highly unlikely on multi-million-year timescales. We conclude that a climate sensitivity greater than 1.5 °C has probably been a robust feature of the Earth's climate system over the past 420 million years, regardless of temporal scaling.

In an effort to reduce the uncertainty of climate sensitivity, $\Delta T(2\times)$, we turned to the Phanerozoic record (the past 542 Myr), an interval that includes times when the Earth was both colder and substantially warmer than the present day⁸. Phanerozoic records generally show a positive coupling between CO₂ and temperature^{9,10}, but determining $\Delta T(2\times)$ quantitatively has proved difficult because there are no convenient proxies for global-mean surface temperature. The GEOCARB and GEOCARBSULF long-term carbon cycle models^{11,12} have been used to calculate multi-million-year patterns of Phanerozoic CO₂. Importantly, a critical factor in this approach is the effect of atmospheric CO₂ level on the rate of CO₂ uptake by weathering of calcium and magnesium silicate minerals. A rise in temperature, accompanying a rise in CO₂, increases the rate of silicate weathering, which in turn accelerates atmospheric CO₂ consumption, forming a negative feedback loop.

Here, using the logarithmic relation between temperature change and CO₂, we examine how different values of $\Delta T(2\times)$ affect calculated Phanerozoic CO₂ levels for best estimates, and physically reasonable ranges, of all other factors affecting CO₂ in the long-term carbon cycle. Such factors include solar evolution, changes in palaeogeography, palaeolithology, palaeohydrology, global degassing, organic and carbonate burial rates, and land plant population¹¹. Calculating $\Delta T(2\times)$ in this manner differs from most existing approaches in that it does not involve independent estimates of

temperature, incorporates information from times when the Earth was substantially warmer than today, and reflects an equilibrium sensitivity that integrates over millions of years.

We amended the GEOCARBSULF¹² model to include a well-defined temperature coefficient for the weathering of calcium and magnesium silicates¹³, and held this and all other parameters in GEOCARBSULF fixed except for the CO₂-doubling response, $\Delta T(2\times)$. We then compared model calculations against an independent proxy data set⁹ for atmospheric CO₂ over the Phanerozoic (Fig. 1). The best fit between the standard version of the model and proxies occurs for $\Delta T(2\times) = 2.8$ °C (blue curve in Fig. 2a), which parallels the most probable values suggested by climate models (2.3–3.0 °C)^{2,5} (Fig. 2b). For $\Delta T(2\times) < 1.5$ °C, unreasonably high levels of atmospheric CO₂ are required to maintain the necessary feedback effect. In the opposite extreme, if $\Delta T(2\times)$ is too large (> 6 °C), the silicate weathering feedback prevents atmospheric CO₂ levels from reaching the high past values indicated by proxy data (Fig. 1).

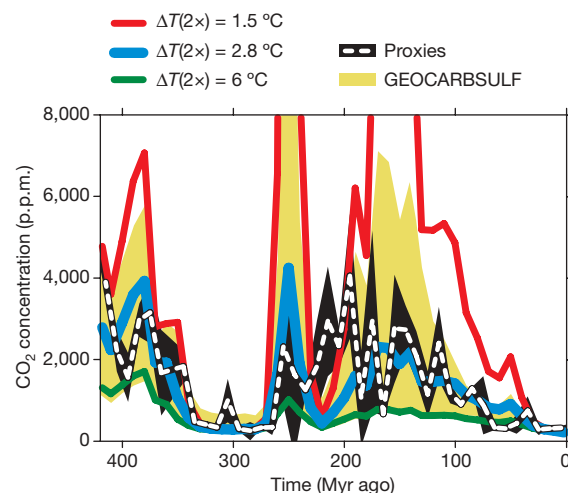


Figure 1 | Comparison of CO₂ calculated by GEOCARBSULF for varying $\Delta T(2\times)$ to an independent CO₂ record from proxies. For the GEOCARBSULF calculations (red, blue and green lines), standard parameters from GEOCARB¹¹ and GEOCARBSULF¹² were used except for an activation energy for Ca and Mg silicate weathering of 42 kJ mol⁻¹ (ref. 13). The proxy record (dashed white line) was compiled from 47 published studies using five independent methods⁹ ($n = 490$ data points). All curves are displayed in 10 Myr time-steps. The proxy error envelope (black) represents ± 1 s.d. of each time-step. The GEOCARBSULF error envelope (yellow) is based on a combined sensitivity analysis (10% and 90% percentile levels) of four factors used in the model (see Methods).

¹Department of Earth and Environmental Sciences, Wesleyan University, Middletown, Connecticut 06459, USA. ²Department of Geology and Geophysics, Yale University, New Haven, Connecticut 06520, USA.

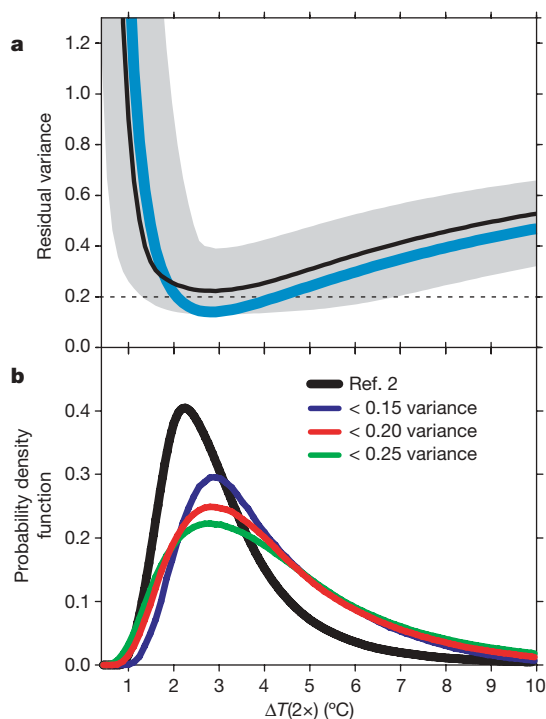


Figure 2 | Calculation of the long-term equilibrium climate sensitivity to CO_2 . **a**, Statistical fit between the proxy and model data sets for varying $\Delta T(2\times)$. The blue curve represents the fit when standard values for all factors^{11,12} are used. The thin black curve corresponds to the median fit when four factors are varied simultaneously in a sensitivity analysis (see Methods); the grey region encompasses the 10–90% percentile levels. The residual variance (y axis) represents the relative misfit of GEOCARBSULF to departures of the 10-Myr-averaged proxy- CO_2 data from present-day values. The dashed line corresponds to a residual variance of 0.2, which is roughly twice the residual variance of the best-fit GEOCARBSULF solution. **b**, Bayesian probability density function for three levels of residual variance from **a**. For comparison, the probability density function of ref. 2, which synthesizes calculations of $\Delta T(2\times)$ from climate models and decadal to millennial observations, is also shown.

Many factors influence the calculations of CO_2 in GEOCARBSULF, as discussed above and elsewhere^{11,12}. It is important, then, to test the sensitivity of CO_2 to variations of $\Delta T(2\times)$ for different values of these other factors (Figs 2 and 3; Supplementary Fig. 1; Methods). Critically, sensitivity analyses demonstrate that physically reasonable variations of the values representing these factors, either singly (Fig. 3; Supplementary Fig. 1) or in combination (Fig. 2), support our overall conclusion that values of $\Delta T(2\times) < 1.5^\circ\text{C}$ lead to a poor fit between the model and the proxies. Owing to trade-offs in the carbon cycle, a handful of extreme parameter choices can combine with $\Delta T(2\times) < 1.5^\circ\text{C}$ to model the proxy data adequately; for example, a small response of weathering rate to a rise in CO_2 , due to an unusually low $\Delta T(2\times)$, can be compensated if increasing CO_2 levels fertilize nearly all terrestrial plant life optimally (no nutrient, water or light limitation) and thereby greatly enhance plant-assisted weathering. If we take a Bayesian assumption that all GEOCARBSULF parameters are equally probable a priori within the specified ranges, a larger parameter range at $\Delta T(2\times) > 1.5^\circ\text{C}$ for successful modelling translates into a higher probability for this case (Fig. 2). Overall, the largest ranges of GEOCARBSULF parameters that fit proxy data well fall within the range of $1.6^\circ\text{C} < \Delta T(2\times) < 5.5^\circ\text{C}$ (Fig. 3; Supplementary Fig. 1), a range that is consistent with most climate model studies^{1–5}. The factor with the lowest best-fit $\Delta T(2\times)$, shown as the curve 'Eros.' in Fig. 3b, is based on the extreme assumption that global physical erosion rates have not changed through time.

Our results pertain most directly to the long-term (multi-million-year) radiative forcing by CO_2 ; this includes, for example, periods of

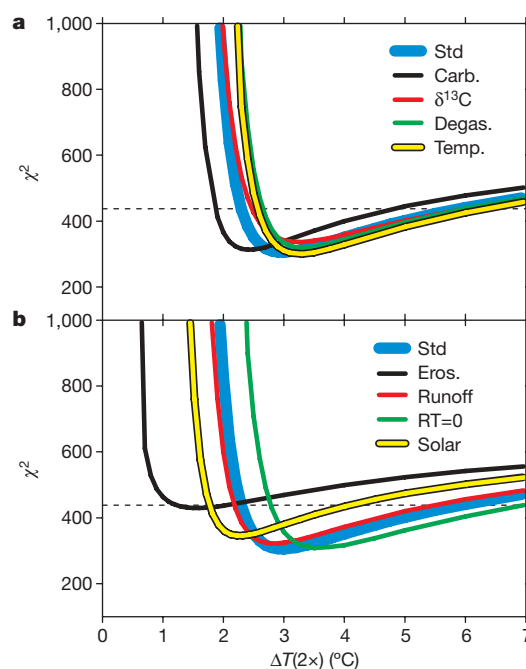


Figure 3 | Sensitivity analysis for the effect of nine additional parameters in the GEOCARBSULF carbon cycle model on the fit between model-derived and proxy CO_2 values for varying $\Delta T(2\times)$. In all cases, the thick blue curve represents the standard formulation (Std; blue curve in Fig. 2a). Values of χ^2 (489 degrees of freedom) below the dashed line correspond to a $>95\%$ likelihood that the model and proxy data sets are statistically indistinguishable. **a**, Effect on $\Delta T(2\times)$ of holding constant and equal to present values: the area of land underlain by carbonates undergoing weathering (Carb.), $\delta^{13}\text{C}$ of carbonates and $\delta^{13}\text{C}$ of organic matter undergoing deposition ($\delta^{13}\text{C}$), rates of CO_2 degassing (Degas.), and land temperature (Temp.). **b**, Effect on $\Delta T(2\times)$ of holding constant and equal to present values: global physical erosion (Eros.), river runoff (Runoff) and solar radiation (Solar), and the effect of ignoring the influence of changing global mean temperature on river runoff (RT = 0).

greatly varying continental ice cover and thus varying ice-albedo feedback, so that our best-fit $\Delta T(2\times)$ gives a mean state for the past 420 Myr. GEOCARBSULF simulations cannot exclude the possibility of a high climate sensitivity (Figs 2, 3) because of the logarithmic behaviour of the forcing and the current error constraints of the modelling¹¹ and proxy⁹ approaches. However, these limitations notwithstanding, our results demonstrate that a weak, long-term radiative forcing by CO_2 ($\Delta T(2\times) < 1.5^\circ\text{C}$) is highly unlikely. This conclusion is consistent with decadal to millennial records from the recent past^{1–5} and with millennial records from the ancient past, such as the Palaeocene–Eocene thermal maximum^{14,15}. Combined, these data suggest that a $\Delta T(2\times)$ of at least 1.5°C has been a robust feature of the Earth's climate system over the past 420 Myr, regardless of temporal scaling.

METHODS

Sensitivity analyses. We tested the combined influence of the following four factors on $\Delta T(2\times)$ (Fig. 2): varying the activation energy for the dissolution of primary calcium and magnesium silicates during continental weathering from 20 to 83 kJ mol^{-1} (refs 11, 13, 16); varying the CO_2 fertilization of plant-assisted weathering from 15% to 75% of plants affected globally by CO_2 fertilization¹¹; varying the weathering rate ratio of early Palaeozoic algal/bryophytic biota to that of modern trees (mainly angiosperms) from 0.125 to 0.5 (refs 11, 17); and varying the weathering rate ratio of gymnosperms to angiosperms from 0.5 to 1.2 (ref. 11). We sampled parameter space at 10 values of each parameter, giving a total of 10,000 GEOCARBSULF simulations for each value of $\Delta T(2\times)$. The success of each simulation was quantified in two ways: with an uncertainty-weighted χ^2 criterion for fitting individual CO_2 -concentration estimates, and by a residual-variance criterion that measures the extent to which a simulation explains past departures of CO_2 concentrations from present-day values (for

example, a residual variance of 0.1 implies that 90% of the logarithmic departure of past CO₂ from present-day values is explained by the model). For the second criterion, we fit GEOCARBSULF simulations to a 10 Myr uncertainty-weighted moving average of CO₂ proxy data. We performed averages and quantified model fits in the logarithmic domain because the greenhouse effect scales with the logarithm of CO₂ concentration, and proxy CO₂ estimates (and their reported uncertainties) range over more than an order of magnitude.

Ranges of values for the remaining factors cannot be simply estimated, so to demonstrate their effects the extreme situation of no change with time in each factor was examined (Fig. 3). This includes the effect on silicate weathering of physical erosion, land temperature, palaeogeography and global mean temperature as they affect river runoff, and the area of land underlain by carbonates versus silicates. Additional consideration was given to the effects on $\Delta T(2\times)$ of holding constant: rates of global CO₂ degassing, solar radiation, and $\delta^{13}\text{C}$ of carbonates and organic matter undergoing deposition.

Received 10 October 2006; accepted 23 February 2007.

- Houghton, J. T., et al. (eds) *Climate Change 2001: The Scientific Basis* (Cambridge Univ. Press, Cambridge, UK, 2001).
- Hegerl, G. C., Crowley, T. J., Hyde, W. T. & Frame, D. J. Climate sensitivity constrained by temperature reconstructions over the past seven centuries. *Nature* **440**, 1029–1032 (2006).
- Forest, C. E., Stone, P. H., Sokolov, A. P., Allen, M. R. & Webster, M. D. Quantifying uncertainties in climate system properties with the use of recent climate observations. *Science* **295**, 113–117 (2002).
- Knutti, R., Stocker, T. F., Joos, F. & Plattner, G.-K. Constraints on radiative forcing and future climate change from observations and climate model ensembles. *Nature* **416**, 719–723 (2002).
- Alley, R. et al. Climate change 2007: The physical science basis. Summary for policymakers. (<http://www.ipcc.ch/SPM2feb07.pdf>) (2007).
- Siegenthaler, U. et al. Stable carbon cycle-climate relationship during the late Pleistocene. *Science* **310**, 1313–1317 (2005).
- Huber, B. T., MacLeod, K. G. & Wing, S. L. (eds) *Warm Climates in Earth History* (Cambridge Univ. Press, Cambridge, UK, 2000).
- Frakes, L. A., Francis, J. E. & Syktus, J. I. *Climate Modes of the Phanerozoic* (Cambridge Univ. Press, Cambridge, UK, 1992).
- Royer, D. L. CO₂-forced climate thresholds during the Phanerozoic. *Geochim. Cosmochim. Acta* **70**, 5665–5675 (2006).
- Montañez, I. P. et al. CO₂-forced climate and vegetation instability during late Paleozoic deglaciation. *Science* **315**, 87–91 (2007).
- Berner, R. A. *The Phanerozoic Carbon Cycle: CO₂ and O₂* (Oxford Univ. Press, New York, 2004).
- Berner, R. A. GEOCARBSULF: A combined model for Phanerozoic atmospheric O₂ and CO₂. *Geochim. Cosmochim. Acta* **70**, 5653–5664 (2006).
- Dessert, C. et al. Erosion of Deccan Traps determined by river geochemistry: impact on the global climate and the ⁸⁷Sr/⁸⁶Sr ratio of seawater. *Earth Planet. Sci. Lett.* **188**, 459–474 (2001).
- Higgins, J. A. & Schrag, D. P. Beyond methane: Towards a theory for the Paleocene-Eocene thermal maximum. *Earth Planet. Sci. Lett.* **245**, 523–537 (2006).
- Pagani, M., Caldeira, K., Archer, D. & Zachos, J. C. An ancient carbon mystery. *Science* **314**, 1556–1557 (2006).
- Riebe, C. S., Kirchner, J. W. & Finkel, R. C. Sharp decrease in long-term chemical weathering rates along an altitudinal transect. *Earth Planet. Sci. Lett.* **218**, 421–434 (2004).
- Moulton, K. L., West, J. & Berner, R. A. Solute flux and mineral mass balance approaches to the quantification of plant effects on silicate weathering. *Am. J. Sci.* **300**, 539–570 (2000).

Supplementary Information is linked to the online version of the paper at www.nature.com/nature.

Acknowledgements We thank L. D. Harvey, E. W. Bolton and T. J. Crowley for discussions, and G. C. Hegerl for data. This work was supported in part by the US Department of Energy (R.A.B.).

Author Contributions D.L.R. and R.A.B. initiated the project, and all authors developed it. R.A.B. performed the carbon cycle calculations and J.P. performed most of the statistical analyses. D.L.R. managed the project and wrote most of the paper.

Author Information Reprints and permissions information is available at www.nature.com/reprints. The authors declare no competing financial interests. Correspondence and requests for materials should be addressed to D.L.R. (droyer@wesleyan.edu).

Seasonal dynamics of recurrent epidemics

Lewi Stone^{1,2*}, Ronen Olinky^{1*} & Amit Huppert^{1,2*}

Seasonality is a driving force that has a major effect on the spatio-temporal dynamics of natural systems and their populations^{1–5}. This is especially true for the transmission of common infectious diseases (such as influenza, measles, chickenpox and pertussis), and is of great relevance for host–parasite relationships in general^{1–23}. Here we gain further insights into the nonlinear dynamics of recurrent diseases through the analysis of the classical seasonally forced SIR (susceptible, infectious or recovered) epidemic model^{6,7}. Our analysis differs from other modelling studies in that the focus is more on post-epidemic dynamics than the outbreak itself. Despite the mathematical intractability of the forced SIR model, we identify a new threshold effect and give clear analytical conditions for predicting the occurrence of either a future epidemic outbreak, or a ‘skip’—a year in which an epidemic fails to initiate. The threshold is determined by the population’s susceptibility measured after the last outbreak and the rate at which new susceptible individuals are recruited into the population. Moreover, the time of occurrence (that is, the phase) of an outbreak proves to be a useful parameter that carries important epidemiological information. In forced systems, seasonal changes can prevent late-peaking diseases (that is, those having high phase) from spreading widely, thereby increasing population susceptibility, and controlling the triggering and intensity of future epidemics. These principles yield forecasting tools that should have relevance for the study of newly emerging and re-emerging diseases controlled by seasonal vectors.

The strong effect of seasonality on population dynamics is no better seen than in the historical long-term data sets of seasonally recurring childhood infectious diseases, such as measles, mumps and chickenpox. These diseases are driven by the seasonally changing contact rate between children which increases sharply at the beginning of each school year, and strongly controls the ensuing disease transmission. Figure 1a, c displays two time series of reported cases of measles in New York (1928–64) and London (1948–68) in the pre-vaccination era^{4–6}. Major epidemics peak close to Spring each year, and on many occasions every second year if the dynamics are biennial and the outbreak ‘skips’ a year. Note there is also a strong erratic and possibly chaotic component, as seen in the variability of peak heights of the epidemics, as well as the intermittent jumps between periods of annual and biennial dynamics^{4–12}. Theoretical studies have shown that seasonal forcing can be responsible for inducing similar complex population dynamics such as higher-order cycles, resonances and deterministic chaos^{6,7,10–26}. These complex responses can easily mask any simple underlying mechanistic processes that might otherwise help in forecasting future epidemics (Fig. 1 legend). The modelling framework used here helps uncover, and gives new insights into, these processes.

The driving force maintaining recurrent epidemic dynamics has long been recognized to be the continuous birth and recruitment of new susceptible individuals into the population^{1,5,6,25}. As an outbreak progresses, susceptibles (*S*) become infected, drop to a minimum level (*S*₀) in the wake of the epidemic, and then grow in number as the birth

process begins to dominate once again. The pattern of epidemics from year to year is controlled by the population’s periodically changing annual contact rate. Our mathematical analysis has shown it useful to focus on *S*₀, defined as the local minimum number of susceptibles left in the wake of an epidemic. *S*₀ controls whether there will be an outbreak in the year ahead or the number of ensuing skips that follow. To a good approximation, we have shown that to generate *k* or more consecutive skips in successive years requires that *S*₀ fall below:

$$S_c(k) = \frac{\gamma + \mu}{\beta_0} - \frac{(k+1)\mu\chi}{2} \quad (1)$$

The critical threshold is defined in terms of classical epidemiological parameters: γ represents the rate at which infected individuals recover;

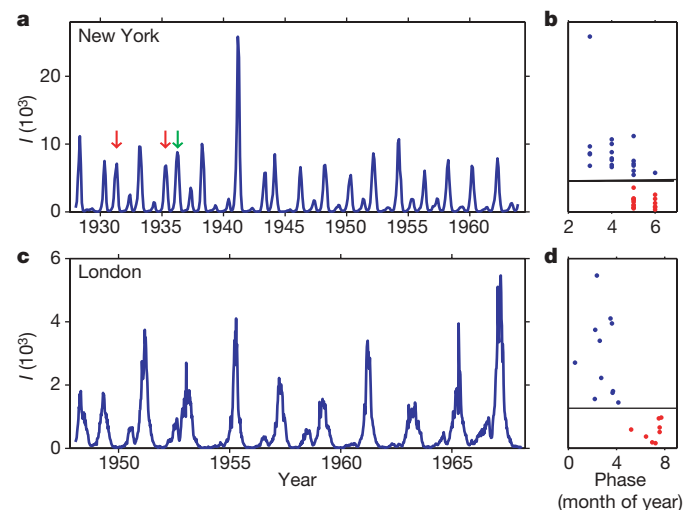


Figure 1 | Epidemic time series together with their associated phase relationship and synchronization effects. **a, c,** Time series of reported measles infective cases (*I*, in thousands) from the largest city in the US (New York, monthly sampling) and in the UK (London, weekly sampling) in the pre-vaccination era (see Methods). **b, d,** The maximum number of infectives of each epidemic is plotted as a function of the time of year (phase in months) at which this maximum occurred. Minor epidemic peaks (skips) have been plotted in red to emphasize that all skips occur at the end of the ‘high’ season, and are thus synchronized (see text). The probability of finding all red points only in the late phase regime is $P < 0.001$, making the synchronization significant. Limitations of conventional prediction schemes are as follows. Consider the New York time-series (**a**) where two similar sized ‘intermediate’ outbreaks occurred in 1931 and 1935 (red arrows). The former was followed by a skip, whereas the latter was followed by another intermediate outbreak in 1936 (green arrow). Given the very different outcomes, peak-to-peak predictions become untenable. The problem intensifies when trying to predict outbreaks that occur after skips. The latter skips can be followed by a variety of different sized peaks, ranging from a successive skip (for example, New York in 1940) to extremely large epidemics (for example, New York in 1941).

¹Biomathematics Unit, Department of Zoology, Faculty of Life Science, ²The Porter School of Environmental Studies, Tel Aviv University, Ramat Aviv 69978, Israel.

*These authors contributed equally to this work.

μ is the per capita rate at which members of the population reproduce and die; and β_0 is the rate of effective contacts between infected and susceptible individuals averaged over the year. The seasonal forcing modulates the contact rate and is taken to be annual with period $\chi = 1$ (χ having time units of years). For example, the commonly used sinusoidally forced contact rate changes annually in time (t) according to the relation $\beta(t) = \beta_0[1 + \delta \sin(2\pi t)]$, with δ setting the strength of the forcing. The mathematical derivation of the threshold is given in Supplementary Information B and C, and is based on an analysis of the model's post-epidemic dynamics in the phase plane (Fig. 2a and Methods). More specifically, for $k = 0$, one obtains:

$$S_0 > S_c = \frac{\gamma + \mu}{\beta_0} - \frac{\mu\chi}{2} \Rightarrow \text{epidemic} \quad (2)$$

whereas if $S_0 < S_c$ there is a skip in the following year.

The above threshold rests on the principle that after a large epidemic the infected population recovers and passes through a period

of long-term immunity. A large epidemic is able to exhaust the susceptible pool (S_0), and should the latter fall below the critical threshold level (S_c), there is a skip—it becomes impossible for a major epidemic to be triggered in the following year. Interestingly, the above criteria (equations (1) and (2)) go beyond the predictions of the classical theory based on the unforced epidemic model^{1,27}, which sometimes proves to be a misleading guide. For instance, during the skip marked in Fig. 2a, there is a period in which infectives begin to increase rapidly owing to favourable seasonal conditions (high disease transmission). This increase is an indicator that the reproductive number R_0 is greater than unity ($R_0 > 1$) and thus, according to the classical theory, suggests a major epidemic is under way. But instead, the growth of infectives is cut short, owing to a change of seasons (diminished disease transmission) which curtails the build-up of the epidemic process, and results in a skip. Whereas predictions based on R_0 prove unhelpful here, the criterion of equation (2) is able to correctly differentiate skips from large-scale outbreaks.

The effectiveness of the threshold prediction may be demonstrated through the study of simulated epidemic time series. The seasonally forced SIR model was integrated in the chaotic regime, which advantageously generates time series with skips and variability similar to real world data. The threshold point (S_c) may thus be easily checked. Figure 3 plots the time τ between two successive large-scale epidemics A and B, as a function of the susceptibles S_0 left after the first outbreak A. For the given model parameters (Fig. 3 legend), the theoretical critical susceptible threshold ($S_c = 0.031$ from equation (2)) corresponds to the number of susceptibles seen in Fig. 3 that separates the annual dynamics ($\tau \approx 1$) from the biennial dynamics ($\tau \approx 2$) in which there is a skip between two outbreaks. Our formalism provides an exact topological distinction that differentiates a skip from an outbreak, even if small. During a skip, susceptibles always increase in time, whereas during an outbreak they must decrease (Fig. 2 legend). Figure 3 shows explicitly how S_0 , which characterizes population susceptibility, gives accurate predictions of future outbreaks.

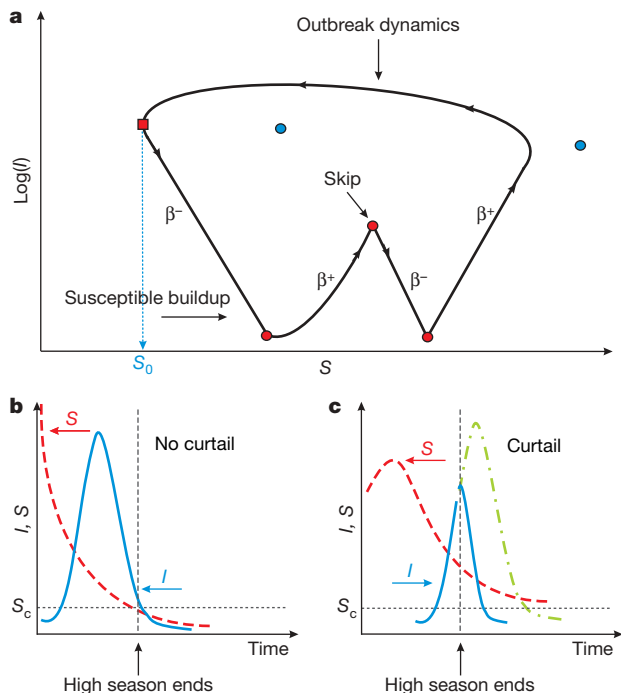


Figure 2 | Effects of seasonality on population dynamics. **a**, Phase plane diagram with the number of infectives $\log(I)$ plotted as a function of susceptible numbers (S) for a typical biennial cycle. The trajectory of the SIR model (equation (3)) rotates anti-clockwise around the phase plane. The trajectory is attracted to the quasi-equilibrium associated with each season (each marked as a filled blue circle). As the seasons (and contact rates β^\pm) change, the trajectory is kicked from one equilibrium to the next. The symbols β^+ and β^- are marked on the curve to indicate those periods of time when the contact rates are associated with high and low seasons respectively. In this biennial cycle, an epidemic occurs in the upper part of phase plane, after which susceptibles pass through a minimum (S_0 , marked by the red square), with a skip occurring in the following year (lower part of phase plane). During a skip, the susceptibles slowly build up, and a small maximum in infective numbers develops one year after the major outbreak. This maximum is prevented from reaching large numbers, as it is curtailed by the change of seasons ($\beta^+ \rightarrow \beta^-$). In contrast to a skip, susceptibles decrease in number during an outbreak. We now consider the relationship between peak outbreak magnitude and initiation time. **b**, An infected individual enters the population early in the high season, and a full scale epidemic develops (solid line). Susceptible numbers fall below the critical level S_c . **c**, An infected individual enters the population very late in the high season. The epidemic (solid line) is cut short at the end of the high season, and prevented from reaching its full potential (dashed-dotted line). Susceptible numbers remain above the critical level S_c . Although the outbreak is curtailed, it should not be viewed as a skip (as susceptible levels decrease over the epidemic).

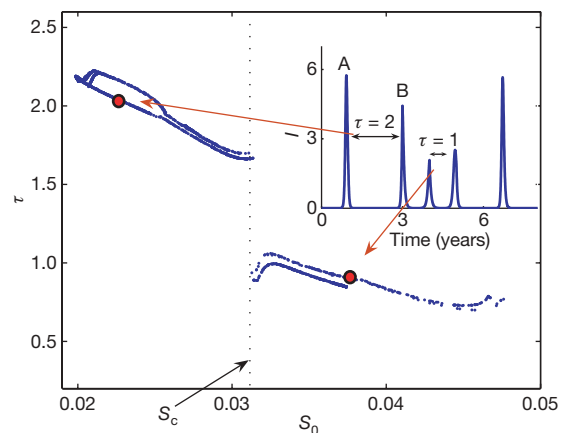


Figure 3 | Testing the threshold prediction, equation (2). The forced SIR epidemic model was integrated in the chaotic regime to generate simulated time series of infectives and susceptibles in the population. A typical chaotic time series is displayed in the inset, where the proportion of infectives I is scaled by a factor of 10^{-3} . Main panel, the time τ between two successive large-scale epidemics A and B is plotted as a function of the proportion of susceptibles S_0 left in the wake of the first epidemic A. To aid visualization, red arrows identify location of specific τ values found in the time series (inset). To calculate S_0 , recall that after the peak of a major epidemic the susceptibles S fall in number and eventually build up again due to births. S_0 is defined as the number of susceptibles at the local minimum. The theoretical susceptible threshold ($S_c = 0.031$ from equation (2)) corresponds to the susceptible numbers seen in the figure separating annual dynamics ($\tau \approx 1$) from biennial dynamics ($\tau \approx 2$). Parameters for the simulated chaotic regime: $\mu = 0.02$, $\gamma = 66$, $\beta_0 = 1,600$, $\delta = 0.18$, $\varepsilon = 10^{-12}$. Forcing is described in Methods, with high and low seasons both half a year in duration.

The relationship between τ and S_0 remains very similar even when the phase and intensity of seasonality undergoes significant random perturbation or for different transmission forms of the function $\beta(t)$ (for example, sinusoidal, step). Similar results are obtained with time series generated by the stochastic TSIR time series model^{8,9,25} (Supplementary Information E).

The above model formulation also gives insights as to what might occur if there are shifts in demographic parameters. For example, it has been argued^{6,8,9} that the shift from annual to biennial measles dynamics in the UK in the 1940s (Fig. 1) is a consequence of a parallel decline in birth-rate, μ . The threshold criterion (equation (2)) indicates that a decrease in μ (and its concomitant decrease in available susceptibles) increases the critical susceptible threshold S_c to a level that can prevent an epidemic occurring in the next year. This confirms the verbal arguments and simulations in refs 6, 8 and 9.

The threshold prediction (equation (2)) corroborates conventional epidemiological wisdom⁴, which suggests that very large outbreaks should be followed by minor outbreaks or even no outbreaks at all (skips) owing to exhaustion of the susceptible pool S_0 . However, as we will show below, conventional wisdom cannot always be relied upon. First though, it is important to identify the key factors that have the greatest influence on S_0 , and thus on the magnitude of the following outbreak. We argue that the phase of the epidemic, or the specific time (for example, month) of the year at which the epidemic achieves a maximum, is an overlooked factor. Our SIR modelling approach provides a natural way to disentangle the complicated relationship between phase and S_0 when there is seasonal forcing. The essence of our theoretical results (Supplementary Information D) may be understood through the following simplified sketch. First, consider the case in which there are only two main seasons each year, a 'high' season (high disease transmission) and a 'low' season (low disease transmission). Suppose an infected individual is introduced into a population of susceptibles during the high season. It makes a crucial difference whether the individual enters the population relatively early or late.

First, consider the scenario in which the infected individual is introduced early in the high season and proceeds to initiate an epidemic. This gives plentiful time for the development of a full-scale epidemic (see Fig. 2b). These large protracted epidemics eventually die out, exhausting the susceptible pool (S_0) in the process. If $S_0 < S_c$, there are too few susceptibles to fuel an epidemic in the following year. Second, in contrast, should an infected individual enter the susceptible population very late in the high season, there may be little time available for the build up of a large-scale outbreak. Being late, the epidemic is more likely to be affected as the season changes from high to low. The smaller contact rate associated with the low season can act to curtail the epidemic, and cut it short (Fig. 2c). As a result, a large susceptible pool S_0 remains. Should $S_0 > S_c$, the number of susceptibles will be enough to trigger an outbreak in the following year. Note that although the epidemic is curtailed, it should not be viewed as a skip (Fig. 2c legend).

The above intuitive argument predicts that for otherwise similar initial conditions the resultant S_0 is positively correlated with the entry time of the infected individual. The same can be shown (Supplementary Information D) for the forced SIR model where the phase of the epidemic is directly related to the entry time of infected individuals, and thus positively correlated with the resultant S_0 . An epidemic that peaks early (low phase) will thus leave small S_0 and vice versa.

When this observation is combined with the above threshold theorem, we can immediately see the consequences. Epidemics that occur very early in the season (that is, having low phase) have the potential to exhaust the susceptible pool to a point where $S_0 < S_c$. These epidemics are followed by a skip. Indeed, this proves to be the case in both model and real data. Figure 4 is a plot of the maximum of the following year's outbreak as a function of the phase of the current year's outbreak for four well known time series of measles in four major cities of England and the United States (see Supplementary

Information F for other cities and diseases). The plot demonstrates that epidemics peaking early in the year (months 0–3) are generally not followed by large-scale epidemics, but are followed by skips instead. Model time series of infectives undergoing chaotic oscillations show the same pattern (Fig. 4 inset; months 4–6.5). A more detailed analysis of the forced SIR model²⁸ shows that the later the phase, the larger the next epidemic, as also seen in the analysis of real data in Fig. 4.

It is now possible to understand why large epidemics are not always followed by skips, as conventional wisdom might suggest. Depending on initial conditions, some outbreaks are able to reach large levels despite the fact that they occur relatively late in the high season. These outbreaks will be curtailed when the season changes from high to low. Outbreaks that are curtailed before attaining their potential maximum have the distinguishing feature of being synchronized to the seasonal cycle, as they are all curtailed at the same time—when the season changes. Furthermore, these synchronized outbreaks will have consumed only a fraction of the available susceptible pool. Thus, in the case of the SIR model, all the late synchronized outbreaks are followed by major epidemics in the next year, as shown (in red) in Fig. 4 inset.

Another intriguing outcome of the model concerns the synchronization dynamics of skips. Fine and Clarkson⁵ noted that all minor outbreaks in England and Wales arrive relatively late in the school year and end at summer, synchronized to the beginning of the school vacation. The seasonally forced SIR model makes clear why skips are synchronized. As shown in Fig. 2a, all skips in the model occur when the seasons change from high to low and as such infectives change sharply from increasing growth rate to a decreasing one. These curtailed skips must peak at exactly the same time of year. Naturally, when the seasonal change is more gradual, as in the real world, the synchronization will be less exact but the tendency will be strongly apparent. Figure 1b and d makes clear that for the New York and London measles data sets, all of the smaller peaks (skips) occur in the last months of the school season (as marked in red), confirming the synchronization effect.

The analysis reported here is not restricted to childhood epidemics. The above seasonally forced epidemic model is used in a

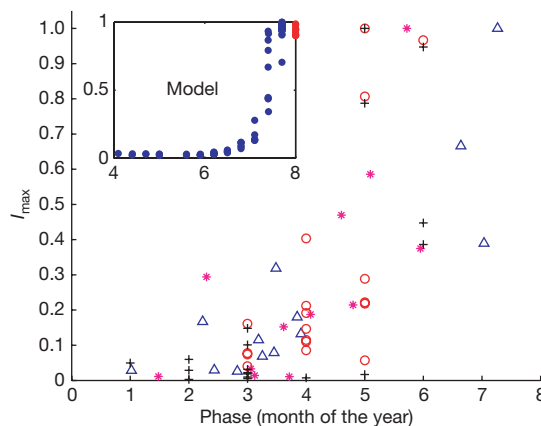


Figure 4 | The relationship between an outbreak's current phase (month of year) and the maximum number of infectives I_{\max} in the following year's outbreak. Outbreaks that occur early (low phase) are followed in the next year by skips (minor epidemics). Late occurring outbreaks give rise to large epidemics in the following year. Phase relationships are shown for New York (circles), London (triangles), Birmingham (stars) and Baltimore (plus signs) measles time series, using data selected as detailed in Methods after normalization. An extended analysis of these and other measles and mumps data sets is given in Supplementary Information F. Inset, the same analysis is repeated for chaotic model time series (Fig. 3 inset); axes as main panel. All curtailed outbreaks (red) peak at $t = 8$. These synchronized outbreaks (which constitute 20% of outbreaks shown) are all followed in the next year by large epidemics.

range of applications from studies of influenza dynamics^{15,16} to models of plant pathogens as agents of bioterrorism²⁹. The threshold identified above should have importance in many of these different contexts. The work goes beyond existing theories on the regular and irregular cycles of recurrent diseases, in that it offers new epidemic predictions derived from a widely studied model otherwise considered analytically intractable. Moreover, because of the complex dynamics induced by seasonality, these predictions can differ from expectations obtained from the unforced model. Further work is required to extend the analysis to the case of variable population size, and for conditions of variable birth rates, both of which are recognized as important processes in previous theory of childhood diseases. Predictions based on phase should have particular relevance for newly emerging and re-emerging diseases³⁰, where time series are too short for rigorous statistical analysis and the epidemiological parameters are extremely difficult to estimate. Yet the theory suggests that useful information can be gained by determining whether an epidemic dies from resource exhaustion or by being curtailed through seasonal change. The latter should be seen as a warning signal for the next year, as population susceptibility and the propensity for an epidemic must both be large. In addition, this work highlights the role of phase as a proxy for population susceptibility. As phase is determined according to the seasonal cycle, the above results imply that monitoring seasonal factors (for example, vector abundance) is imperative in public health management.

METHODS

Models. The classical forced SIR model¹ has the following equations:

$$\dot{S} = \mu - \mu S - \beta(t) S(I + \varepsilon); \quad \dot{I} = \beta(t) S(I + \varepsilon) - \gamma I - \mu I; \quad \dot{R} = \gamma I - \mu R; \quad (3)$$

where the population is composed of susceptible (S), infected (I) and recovered (R) individuals, and are scaled here as proportions. The rate of birth and mortality is μ , infected individuals recover at rate γ , and $\varepsilon = 10^{-12}$ is a small immigration term¹⁸. For the case of two seasons each year, the contact rate $\beta(t)$ may be approximated as $\beta^+ = \beta_0(1 + \delta)$ in the high season and as $\beta^- = \beta_0(1 - \delta)$ in the low season, where $0 < \delta < 1$ represents the strength of the seasonal forcing. Over time, the seasons change sequentially: high \rightarrow low \rightarrow high \rightarrow low \rightarrow

A mathematical analysis of the forced ($\delta > 0$) model's epidemic dynamics is given in Supplementary Information A–C and ref. 28. The simulations in ref. 7 also clarify the effects of forcing, but do not develop a language of skips attempted here. For a given S_0 , it is possible to derive mathematical expressions for the model's orbit in the lower part of phase plane in Fig. 2a, and calculate the resulting number of skips. The analysis uncovers the threshold point separating annual and biennial (or higher-order) dynamics. An intuitive understanding may be gained by removing seasonal forcing ($\delta = 0$) altogether. Let $w = \log(I)$, and consider the model's trajectory in the lower part of the S – w phase plane. Beginning in the wake of a large epidemic, with $(S, w) = (S_0, w_0)$, equations (3) may be approximated as: $\dot{w} = \beta_0 S - \gamma - \mu$ and $\dot{S} \approx \mu$. Susceptibles build up linearly, $S(t) \approx S_0 + \mu t$, and $w(t)$ follows a simple parabola (Supplementary Information C), first descending to very low numbers, and later increasing when the turning point is reached. The recovery time between major epidemics is approximately $t_r = 2(\gamma + \mu - \beta_0 S_0)/(\beta_0 \mu)$, the time needed for $w(t)$ to return to $w = w_0$. The number of skips is $k \approx t_r/\chi - 1$, where $\chi = 1 - \text{year}$. Rearranging the last equation for t_r gives the maximum level of S_0 susceptibles required to generate k consecutive skips, namely $S_c(k) = (\gamma + \mu)/\beta_0 - (k + 1)\mu\chi/2$. We have shown that the above results hold when forcing ($\delta > 0$) is fully taken into account (Supplementary Information B; ref. 28).

Data analysis. Measles time series for the US (1928–63, sampled monthly) and the UK (1948–68, sampled weekly) were obtained from ref. 4 and <http://www.zoo.ufl.edu/bolker/>. In preparing Fig. 4, UK time series were first smoothed using a gaussian kernel as an aid in peak-detection. When testing the effect of the phase of a major epidemic on the following year's peak height, only years having major epidemics are relevant for the analysis. Those years with skips (~50% of US and ~30% of UK data) were omitted. Likewise, owing to the action of the threshold, the very largest peaks (independent of their phase) were always followed by skips, and hence were also removed from the analysis, although the results obtained were robust to inclusion of these latter points. The final data sets are given in Supplementary Information F. A more refined method for checking the effects of phase would require removing the interaction of peak height altogether. With plentiful data, this could be achieved by examining only a subset of epidemic peaks of a specific height, say h , from which a graph of phase versus

the next peak's height could be compiled. However, given the limited number of data points, this was impractical for the measles time series, but data-rich model simulations yielded the expected phase relationship, shown in Fig. 4 inset.

Received 25 July 2006; accepted 10 January 2007.

- Anderson, R. M. & May, R. M. *Infectious Diseases of Humans: Dynamics and Control* (Oxford Univ. Press, New York, 1991).
- Pascual, M. & Dobson, A. Seasonal patterns of infectious diseases. *PLoS Med.* **2**, 18–19 (2005).
- Altizer, S. *et al.* Seasonality and the dynamics of infectious diseases. *Ecol. Lett.* **9**, 467–484 (2006).
- London, W. P. & Yorke, J. A. Recurrent outbreaks of measles, chickenpox and mumps. 1. Seasonal variation in contact rates. *Am. J. Epidemiol.* **98**, 453–468 (1973).
- Fine, P. E. M. & Clarkson, J. A. Measles in England and Wales-I: An analysis of factors underlying seasonal patterns. *Int. J. Epidemiol.* **11**, 5–14 (1982).
- Earn, D. J. D., Rohani, P., Bolker, B. M. & Grenfell, B. T. A simple model for complex dynamical transitions in epidemics. *Science* **287**, 667–670 (2000).
- Keeling, M., Rohani, P. & Grenfell, B. T. Seasonally forced disease dynamics explored as switching between attractors. *Physica D* **148**, 317–335 (2001).
- Bjornstad, O. N., Finkenstadt, B. F. & Grenfell, B. T. Dynamics of measles epidemics: estimating scaling of transmission rates using a time series SIR model. *Ecol. Monogr.* **72**, 169–184 (2002).
- Finkenstadt, B. F. & Grenfell, B. T. Time series modelling of childhood diseases: a dynamical system approach. *Appl. Stat.* **49**, 187–205 (2000).
- Olsen, L. F., Truty, G. L. & Schaffer, W. M. Oscillations and chaos in epidemics: a nonlinear dynamic study of six childhood diseases in Copenhagen, Denmark. *Theor. Pop. Biol.* **33**, 344–370 (1988).
- Schwartz, I. B. & Smith, H. L. Infinite subharmonic bifurcation in an SEIR epidemic model. *J. Math. Biol.* **18**, 233–253 (1983).
- Aron, J. L. & Schwartz, I. B. Seasonality and period-doubling bifurcations in an epidemic model. *J. Theor. Biol.* **110**, 665–679 (1984).
- Bolker, B. M. & Grenfell, B. T. Chaos and biological complexity in measles dynamics. *Proc. R. Soc. Lond. B* **251**, 75–81 (1993).
- Billings, L. & Schwartz, I. B. Exciting chaos with noise: unexpected dynamics in epidemic outbreaks. *J. Math. Biol.* **44**, 31–48 (2002).
- Andreasen, V. Dynamics of annual influenza A epidemics with immuno-selection. *J. Math. Biol.* **46**, 504–536 (2003).
- Casagrandi, R., Bolzoni, L., Levin, S. A. & Andreasen, V. The SIRC model and influenza A. *Math. Biosci.* **200**, 152–169 (2006).
- Dietz, K. The incidence of infectious diseases under the influence of seasonal fluctuations. *Lect. Notes Biomath.* **11**, 1–15 (1976).
- Engbert, R. & Drepper, F. R. Chance and chaos in population biology – models of recurrent epidemics and food chain dynamics. *Chaos Solitons Fractals* **4**, 1147–1169 (1994).
- Olsen, L. F. & Schaffer, W. M. Chaos versus noisy periodicity: alternative hypotheses for childhood epidemics. *Science* **249**, 499–504 (1990).
- Rand, D. A. & Wilson, H. B. Chaotic stochasticity: a ubiquitous source of unpredictability in epidemics. *Proc. R. Soc. Lond. B* **246**, 179–184 (1991).
- Schaffer, W. M. & Kot, M. Nearly one dimensional dynamics in an epidemic. *J. Theor. Biol.* **112**, 403–427 (1985).
- Dushoff, J., Plotkin, J. B., Levin, S. A. & Earn, D. J. D. Dynamical resonance can account for seasonality of influenza epidemics. *Proc. Natl Acad. Sci. USA* **48**, 16915–16916 (2004).
- Shulgin, B., Stone, L. & Agur, Z. Pulse vaccination strategy in the SIR epidemic model. *Bull. Math. Biol.* **60**, 1123–1148 (1998).
- Huppert, A., Blasius, B., Olinky, R. & Stone, L. A model for seasonal phytoplankton blooms. *J. Theor. Biol.* **236**, 276–290 (2005).
- Finkenstadt, B. F. & Grenfell, B. T. Empirical determinants of measles metapopulation dynamics in England and Wales. *Proc. R. Soc. Lond. B* **265**, 211–220 (1998).
- Sugihara, G. & May, R. M. Nonlinear forecasting as a way of distinguishing chaos from measurement error in time-series. *Nature* **344**, 734–741 (1990).
- Murray, J. D. *Mathematical Biology* 2nd edn (Springer, Berlin, 1989).
- Olinky, R., Huppert, A. & Stone, L. Thresholds in seasonally forced epidemiological models. *Proc. Natl Acad. Sci. USA* (submitted).
- Madden, L. V. & Van den Bosch, F. A population-dynamics approach to assess the threat of plant pathogens as biological weapons against annual crops. *Bioscience* **52**, 65–74 (2002).
- Morens, D. M., Folker, G. K. & Fauci, A. S. The challenge of emerging and re-emerging infectious diseases. *Nature* **430**, 242–249 (2004).

Supplementary Information is linked to the online version of the paper at www.nature.com/nature.

Acknowledgements We are grateful for the support of the James S. McDonnell Foundation. A.H. was partly supported by the Porter School of Environmental Studies at Tel Aviv University.

Author Information Reprints and permissions information is available at www.nature.com/reprints. The authors declare no competing financial interests. Correspondence and requests for materials should be addressed to L.S. (lewi@post.tau.ac.il).

Strain-resolved community proteomics reveals recombining genomes of acidophilic bacteria

Ian Lo¹, Vincent J. Denef¹, Nathan C. VerBerkmoes², Manesh B. Shah², Daniela Goltsman¹, Genevieve DiBartolo¹, Gene W. Tyson¹, Eric E. Allen¹, Rachna J. Ram¹, J. Chris Detter³, Paul Richardson³, Michael P. Thelen⁴, Robert L. Hettich² & Jillian F. Banfield¹

Microbes comprise the majority of extant organisms, yet much remains to be learned about the nature and driving forces of microbial diversification. Our understanding of how microorganisms adapt and evolve can be advanced by genome-wide documentation of the patterns of genetic exchange, particularly if analyses target coexisting members of natural communities. Here we use community genomic data sets to identify, with strain specificity, expressed proteins from the dominant member of a genomically uncharacterized, natural, acidophilic biofilm. Proteomics results reveal a genome shaped by recombination involving chromosomal regions of tens to hundreds of kilobases long that are derived from two closely related bacterial populations. Inter-population genetic exchange was confirmed by multilocus sequence typing of isolates and of uncultivated natural consortia. The findings suggest that exchange of large blocks of gene variants is crucial for the adaptation to specific ecological niches within the very acidic, metal-rich environment. Mass-spectrometry-based discrimination of expressed protein products that differ by as little as a single amino acid enables us to distinguish the behaviour of closely related coexisting organisms. This is important, given that microorganisms grouped together as a single species may have quite distinct roles in natural systems^{1–3} and their interactions might be key to ecosystem optimization. Because proteomic data simultaneously convey information about genome type and activity, strain-resolved community proteomics is an important complement to cultivation-independent genomic (metagenomic) analysis^{4–6} of microorganisms in the natural environment.

Biofilms from the Richmond mine (Supplementary Fig. 1) are ideally suited to cultivation-independent genomic⁴ and proteomic analysis⁷ owing to their low species richness and abundant biomass. In this study, a community genomic data set was generated from a pink biofilm from the UBA location (UBA genomic data set). Like the community from the 5-way location (5-way CG genomic data set), the biofilm was dominated by bacteria belonging to *Leptospirillum* group II^{4,8,9}, and contains lower abundances of *Leptospirillum* group III¹⁰ and several archaea. *Leptospirillum* species are chemoautotrophs that obtain their metabolic energy by aerobic oxidation of ferrous iron. The ferric iron byproduct subsequently reacts with the surfaces of metal sulphide minerals present in ore deposits, promoting sulphur oxidation and metal release and generating very acidic, metal-rich solutions¹¹.

The genome of *Leptospirillum* group II from the UBA genomic data set was assembled independently of that from the 5-way CG genomic data set and both were aligned (Supplementary Table 1). The 2,160 genes in the UBA composite genome with orthologues in the 5-way CG genome almost all have the same genomic context (that

is, the genomes are largely syntenous). Orthologues share an average of 95.24% amino acid sequence identity (median = 96.69%). However, this value includes blocks of 10s to 100s of kilobase pairs (kbs; comprising a total of 421 genes) with nucleotide sequence that is essentially identical to that of the 5-way CG composite genome; after exclusion of identical proteins, orthologues share an average identity of 94.11% (median = 95.53%). In some cases, integrase genes and the high numbers of transposase and hypothetical genes suggest that shared sequence is due to insertion of plasmid- or phage-like DNA (for example, see scaffold 8049 in Supplementary Table 1). However, other blocks encode primarily core metabolic genes. For example, one region contains 54 genes (63% of protein products detected) with ~100% nucleotide-level sequence identity, spans a transfer RNA, lacks integrases and transposases, and is unlikely to be phage-derived (Fig. 1). Regions such as this may arise when recombination between two genome types is followed by a selection event that removes from the population (or reduces to low abundance) blocks of one sequence type¹².

Tandem mass spectra were collected from peptides generated by enzymatic digestion of proteins extracted from a third biofilm obtained from the genomically uncharacterized ABend location within the Richmond Mine (Supplementary Fig. 1). This proteomic

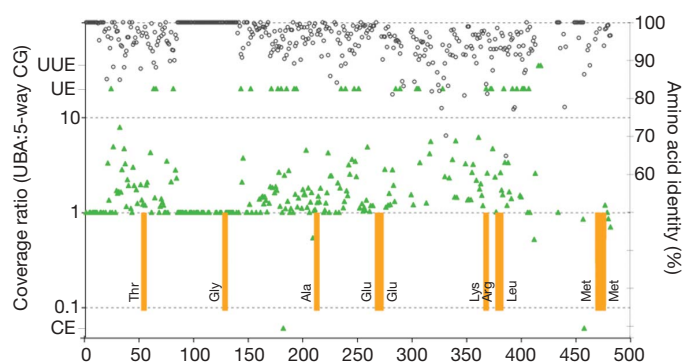


Figure 1 | Protein coverage ratios across scaffold 7931. Ratio of protein coverage by peptides using the UBA versus 5-way CG *Leptospirillum* group II protein sequences (green triangles) across scaffold 7931 of the UBA composite genome (and corresponding genome regions in the composite 5-way CG genome). The percentage amino acid identity is plotted for all orthologue pairs (black circles) and tRNA genes are marked (orange). UUE, expressed gene, unique to the UBA genome; UE, expressed gene, present in both genomes, only detected using UBA protein sequence; CE, expressed gene, present in both genomes, only detected using 5-way CG protein sequence.

¹University of California, Berkeley, California 94720, USA. ²Oak Ridge National Laboratory, Oak Ridge, Tennessee 37831, USA. ³Joint Genome Institute, Walnut Creek, California 94598, USA. ⁴Lawrence Livermore National Laboratory, Livermore, California 94550, USA.

data set was previously analysed by searching with only the 5-way CG genomic data⁷. Mass spectra were re-analysed using a single database containing 16,170 protein entries, including all predicted proteins from both the UBA and 5-way CG type *Leptospirillum* group II, the *Leptospirillum* group III, and archaeal genomes (Supplementary Information). Because tandem mass spectral identification depends on a high quality match between the masses of predicted and measured peptide fragments, most peptides predicted to differ in their amino acid composition and mass can be distinguished. For *Leptospirillum* group II proteins, we detected 7,526 peptides matching the 5-way CG but not the UBA protein variants, and 23,787 peptides matching the UBA but not the 5-way CG protein variants. A total of 74,483 non-unique (matching both variants) peptides were identified (counts are cumulative over replicate fractions). This result suggested that proteins of both the UBA- and the 5-way CG-type were present in the ABend sample, and that UBA-type proteins dominate (~69%).

We used sequence coverage (fraction of a protein sequence matched by identified peptides) to determine which genome type encodes the proteins in the ABend biofilm. When the sequence coverage obtained using UBA protein sequences exceeds that achieved using the 5-way CG sequences, the protein is more similar to the UBA than the 5-way CG-type protein. When the ratio of protein coverage achieved using the UBA versus 5-way CG sequences is plotted as a function of genomic location across region 7931 (Fig. 1, green triangles), it is apparent that the entire genomic block encodes proteins of the UBA type.

Figure 2a illustrates a 698 kb genomic fragment (~27% of the genome, containing the origin of replication; Supplementary Fig. 2) across which regions with coverage ratios of > 1 (UBA:5-way CG) alternate with regions with ratios < 1. We also plotted the number of unique peptides identified for each protein across the same region (Fig. 2b). Only one protein variant was detected at each locus, indicating only one *Leptospirillum* group II genome type was present in the ABend sample. It is inferred that this genome comprises alternating blocks of genes encoding UBA and 5-way CG protein variants. The average number of unique peptides per protein and the total number of peptides per protein (Fig. 3), is approximately the same

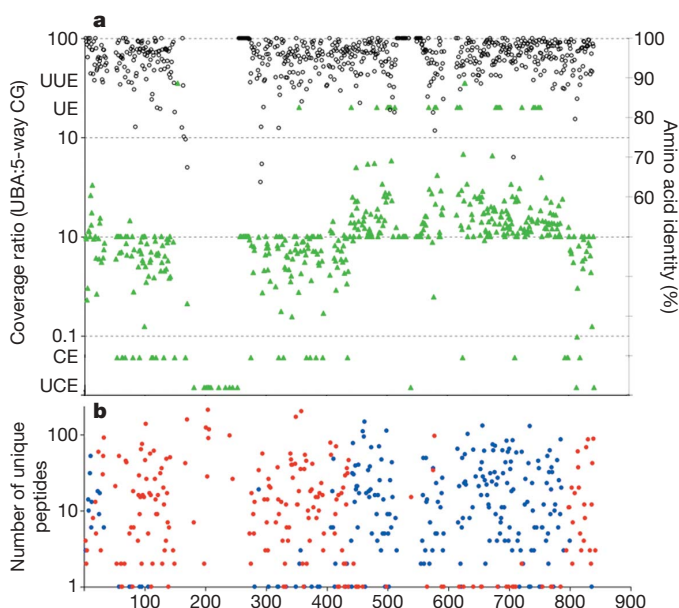


Figure 2 | Protein coverage ratios and unique peptide counts across scaffold 8241. a, Ratio of the protein detection coverage (see Fig. 1 legend) and percentage amino acid identity between orthologues across the region equivalent to scaffold 8241 of the UBA genome. **b**, Number of 5-way CG (red circles) and UBA (blue circles) protein variant-specific peptides detected (unique peptides). UCE, expressed gene, unique to 5-way CG genome.

across UBA and 5-way CG blocks, as expected for proteins encoded by a single genome type (Supplementary Information). The UBA and 5-way CG *Leptospirillum* group II populations are deeply sampled and near clonal, and the resulting genome sequences are not strain composites (Supplementary Information). Therefore, the proteomic plots showing transition from UBA- to 5-way CG-type sequence shadow the recombined genome structure of the *Leptospirillum* group II population in the ABend biofilm. Plots for the other large genome fragments (Supplementary Fig. 3) were used to infer the genome-wide recombination pattern (Fig. 3).

We mapped peptides onto protein alignments (Fig. 4a, b) across the recombination point in Fig. 2 to verify the accuracy of peptide identifications for detection of a recombination point. Notably, proteins that differ by only a single amino acid can be distinguished if peptides are recovered in the relevant regions. We manually verified 226 unique peptides in this region (Supplementary Table 2); 206 were found to be true positives. Most 5-way CG-type peptides in otherwise UBA proteins (and vice versa) were false positives found at the edge of the scoring threshold. Filtering levels that are too stringent will result in loss of real information, limiting the view of the genome, whereas filtering levels that are too liberal will generate false positives and blur the view of recombination. As in the previous study⁷, we used a filtering level which, on the basis of reverse database searching, results in a false positive detection rate of <1% at the peptide level (Supplementary Information; Supplementary Table 3). The recombination pattern is also observable with ultraliberal or ultraconservative filters (Supplementary Fig. 3).

Throughout the genome there were 129 instances where two or more unique peptides were detected for a single locus. After removing from consideration those cases due to mass discrimination limitations and false positives (Supplementary Materials), there were only 24 (18.6%) loci with two or more unique peptides for both protein variants. Proteins with two or more unique peptides are distributed throughout the genome. Generally the cumulative number of unique peptides detected for one variant is far greater than the other, suggesting that the second protein variant is present in a minor fraction of the population (either associated with a distinct genome type or the dominant genome type into which this gene has recombined). At least one of the three cases where we detected a high number of unique peptides for both variants is clearly a recombinant protein (a putative Rubisco-like protein; Fig. 5a).

Because this is the first mapping of genome-wide recombination structure using proteomic analysis, we analysed *Leptospirillum* group II isolates using PCR-based multilocus sequence typing (MLST)¹³. Three isolates share most of their gene sequences with the 5-way CG population and one isolate shares most, but not all, gene sequences with the UBA population (Table 1b). Given that the two population genomic data sets are near clonal (Supplementary Information), they can be used to evaluate linkage patterns in the same way that isolate genomes would be employed. The MLST data for the UBA-like isolate (strain CF-1) compared to the genomic data sets and other isolate MLST data prove the occurrence of recombination. MLST analysis of the ABend biofilm confirms the genome structure inferred from proteomic data (Table 1; Fig. 3; and Supplementary Information).

The combination of MLST and proteomics results suggests that the CF-1 isolate is similar to the ABend population (see Table 1). Interestingly, the PCR amplified nucleotide sequence of the Rubisco-like gene from the CF-1 isolate is a recombinant version of the genes in the UBA and 5-way CG data sets (Fig. 5b), as inferred by proteomics for the ABend sample (Fig. 5a). Overall, results confirm the inferred recombinant genome structure deduced from proteomic analysis.

The UBA genomic data set contains a few (~0.04%) sequencing reads with ~92% identity to the UBA genome type. Almost all of these had very high (typically 100%) nucleotide sequence identity to the *Leptospirillum* group II detected in the 5-way CG genomic data set. In essentially all cases analysed, both sequenced ends (mate pairs)

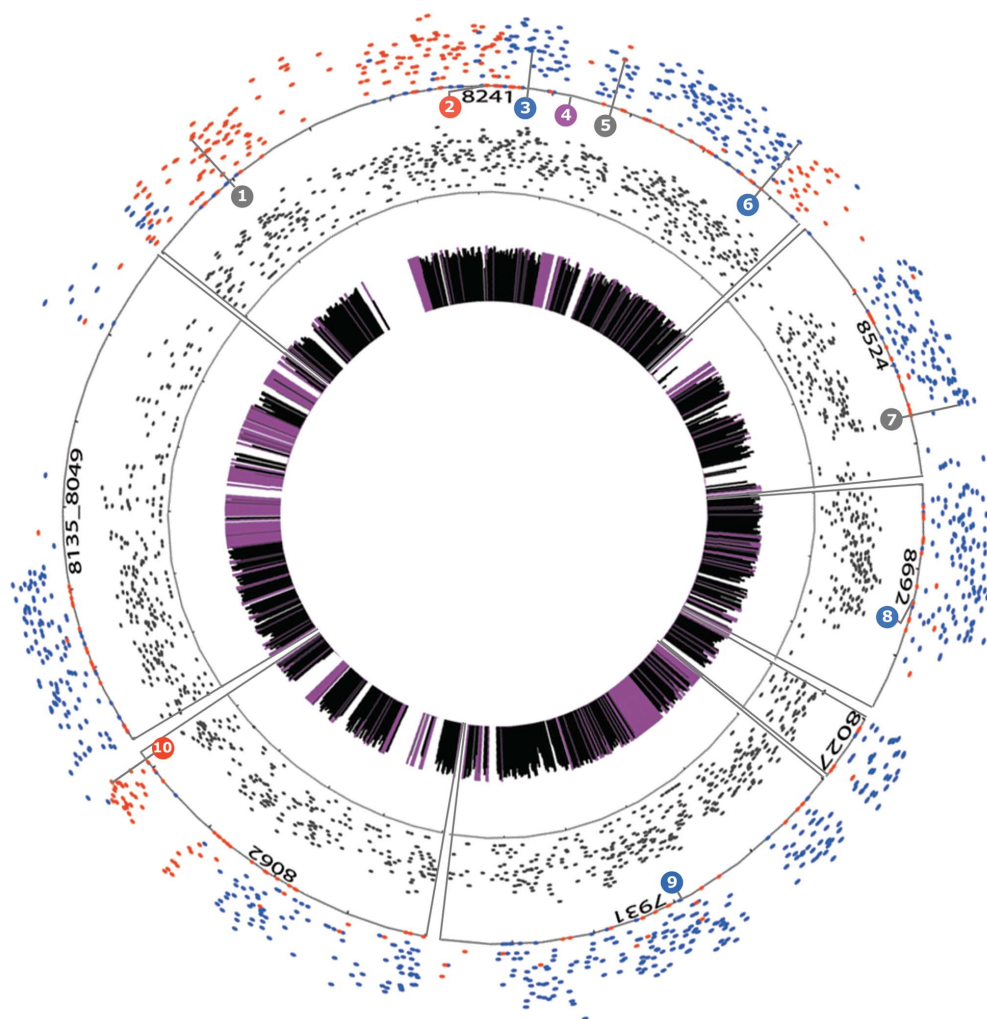


Figure 3 | Inferred recombinant AbEnd *Leptospirillum* group II genome structure. Recombination structure inferred on the basis of unique 5-way CG (red) and UBA (blue) peptide counts (arbitrary order genomic fragments; Supplementary Fig. 3). Inner ring displays amino acid identity between UBA and 5-way CG orthologues, scaled with height from 50–100% (purple, 100% identity; gap, no orthologue). Middle and outer rings display

total (grey) and unique (red/blue) peptide count (height above solid line indicates number; average protein coverage is ~45%) for detected proteins. As in Figs 1, 2, all peptide counts are cumulative over all liquid-chromatography–mass-spectrometry runs. Numbered circles identify genes analysed by MLST and are coloured by nucleotide sequence type (Table 1); other numbers refer to scaffold names.

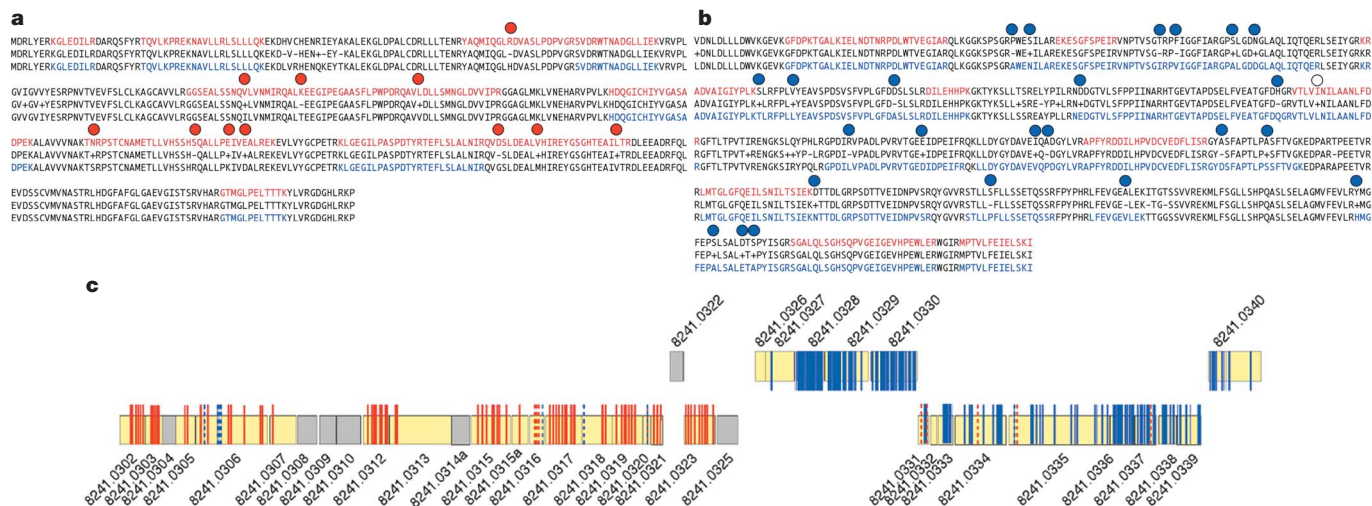


Figure 4 | Peptide-resolved analysis of two *Leptospirillum* group II orthologous protein pairs (scaffold 8241 genes 317 (a) and 330 (b) from the region in c (also see Fig. 2). Top sequence, 5-way CG sequence; bottom sequence, UBA sequence; middle sequence, consensus). Coloured letters represent sequence covered by detected peptides matching the 5-way CG (red) or UBA sequence (blue). Coloured circles

represent amino acid substitutions within detected peptides, distinguishing protein variants (open circle, indistinguishable isoleucine–leucine substitution). c, Region equivalent to UBA scaffold 8241 genes 302 to 340 (sense- and antisense-coded genes are distinguished). Genes (boxes) marked yellow for detected proteins, with discriminating amino acid substitutions marked as coloured bars. Dashed lines, peptides detected with low confidence (Supplementary Table 2).

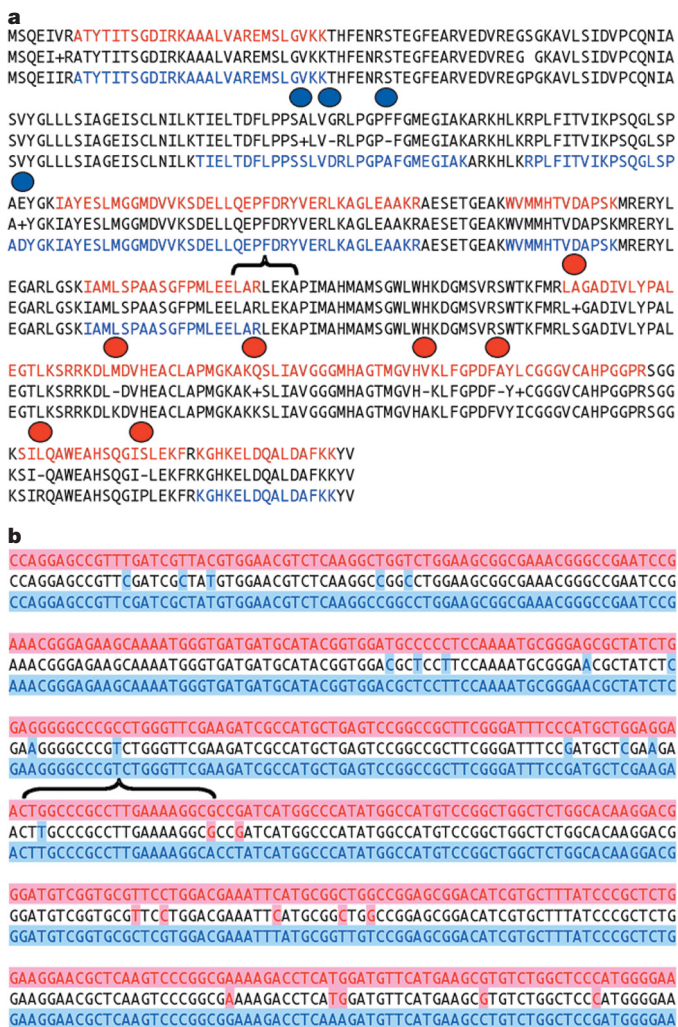


Figure 5 | Evidence for the recombinant nature of a Rubisco-like protein.

a, The inferred sequence of the Rubisco-like protein (gene number 5 in Table 1) based on unique peptide detection (as per Fig. 4a, b) in the ABend biofilm. **b**, The nucleotide sequence for the central region of the corresponding CF-1 isolate gene (for full sequence see Supplementary Table 4). The CF-1 genome is inferred to be similar to ABend *Leptospirillum* group II. Highlights in the middle row indicate single nucleotide polymorphisms distinguishing the UBA (blue) and 5-way CG (pink) sequence types. The recombination point (bracket in **b**) falls within the region inferred by proteomics (bracket in **a**).

Table 1 | Multi-locus sequence typing

Gene number	1	2	3	4	5	6	7	8	9	10
5-way CG gene number	21-51	3-15	3-65	26-6	80-24	13-13	8-70	137-1	2-52	174-2
UBA gene number	8241.0077	8241.0307	8241.0357	8241.0430	8241.0467	8241.0652	8524.0247	8692.0126	7931.0189	8062.0371
Genomic data										
UBA genome	17	52	53	0	74	11	23	54	55	47
5-way CG genome	0	0	0	0	0	0	0	0	0	0
Environmental MLST										
ABend sample	-	0	53	0	-	11	-	54	55	0
Isolates MLST										
CF-1	0	52	53	0	37	11	23	54	51 s	0
5w02LII-1	0	0	1	-	0	0	0	-	0	-
UBABS05-4	0	0	0 s	0	0	0	0	0	0	0
ABM05-7	0	0	0 s	0	0	2	0	0	0	0

MLST data for 10 genes from the ABend biofilm sample (Environmental MLST) and *Leptospirillum* group II isolates from the Richmond Mine, California (Isolates MLST; for gene annotations see Supplementary Table 1; s, indicates incomplete sequence). A single sequence type, UBA (blue) or 5-way CG (red) was recovered from the ABend sample, consistent with a single dominant genome type. Purple numbers indicate that 5-way CG and UBA genes are identical; '-' indicates cases for which sequence data are not available. The numbers in boxes indicate the number of nucleotide substitutions distinguishing genes from the 5-way CG data set.

of these DNA fragments are 5-way CG type over their entire length. This is consistent either with a low abundance of the 5-way CG population type in the UBA community or recombinants with large recombination fragment size. However, in at least one case, a 5-way-CG-type gene fragment has recombined into about half of the UBA-type genomes sampled (Supplementary Table 7). Given that 9 of the 15 nucleotide substitutions in this gene correspond to amino acid differences, we infer that the recombination event probably resulted in heterogeneity in the function of this permease within the population. In combination with the example of the Rubisco-like protein, this observation indicates that modular creation of new protein types is an important source of new functionality in these acidophiles. This is similar to earlier observations in, for example, *Escherichia coli*¹⁴.

Previously, evidence for extensive recombination was documented in archaeal populations from the Richmond mine biofilms⁴ and in other archaea and bacteria¹⁵⁻¹⁸. The current study indicates a recombination block size in *Leptospirillum* group II that is unusually large (10s to 100s of kb) compared with typical values (~100 bp to 10 kb, summarized in ref. 18). Whether this is due to an unusual recombination makeup of *Leptospirillum* group II is not yet clear. The genomes have many genes required for DNA uptake (competence) and secretion, homologous pairing and recombination. Of principal interest are RecA (homologous pairing), RuvA and B (branch migration) and RuvC (resolvase), proteins that were all confidently detected with high per cent coverage by the proteomics measurements. Notably, we did not detect the RecB protein of RecBCD pre-synaptic nuclease, or the antirecombinant genes SbcB, C and D. In comparison with many prokaryote genomes, the overall recombination gene composition is most similar to that of *Geobacter sulfurreducens*¹⁹. Recombination events are apparently infrequent between *Leptospirillum* group II types, as might be expected on the basis of a log-linear dependence of recombination on sequence identity²⁰. Less frequent recombination in *Leptospirillum* group II compared with archaea probably accounts for the lower population-level diversity (that is, near-clonality within populations) compared with the archaea²¹.

Mass-spectrometry-based characterization of amino acid substitutions has been demonstrated previously for haemoglobin variants related to human disease²²⁻²⁴. These studies have relied on the wealth of previous information on haemoglobin variation in human populations, which provided a known starting point for the protein identification. The key methodological advance of our study is the finding that it is possible to partially or completely deduce the sequences of gene variants, genome wide, in an uncultivated organism from a sample lacking prior genomic characterization, so long as genomic data from relatively closely related organisms are available. Similarly, proteomic analysis of communities containing micro-organisms for which multiple proteomic data sets are now available (for example, *Shewanella*, *Prochlorococcus* and *Burkholderia*) could be used to identify peptide sequences shared with sequenced organisms

and to simultaneously constrain the biochemical function at the time of sampling. In addition to detailed exploration of the microbial ecology of natural consortia, high-resolution proteogenomic approaches may find application in strain typing of pathogens, discrimination between closely related proteins involved in disease, and protein biomarker identification.

METHODS

Proteogenomics. Approximately 100 Mb of genomic sequence was obtained from a small insert shotgun library constructed using DNA extracted from a biofilm collected in June, 2005. Sequence data were assembled to generate genome fragments that were assigned to *Leptospirillum* group II^{8,9}, *Leptospirillum* group III¹⁰, and archaeal organisms on the basis of per cent G+C content, sequence depth, and ultimately by assembly. All *Leptospirillum* group II sequence fragments of >~2 kb were manually assembled into seven scaffolds (7931, 8027, 8135_8049, 8062, 8241, 8524 and 8692), yielding a near complete composite 2.64 Mb genome with 2,601 genes (Supplementary Table 1). The 16S rRNA gene of the UBA and 5-way CG type *Leptospirillum* group II share 99.7% sequence identity. Both genomic data sets were manually curated to avoid unsubstantiated differences in gene length and reading frame. Shotgun proteomics was performed as previously described⁷ by digestion of biofilm proteins into peptides and subsequent analysis by multidimensional chromatography coupled to a linear ion trap operating in data-dependent mode. Details are provided in the Supplementary Information.

Isolation and MLST. *Leptospirillum* group II strains were isolated for MLST analysis (Supplementary Table 6) using a plate overlay method²⁵ (Supplementary Information and Supplementary Table 5).

Received 16 November 2006; accepted 26 January 2007.

Published online 7 March 2007.

1. Acinas, S. G. *et al.* Fine-scale phylogenetic architecture of a complex bacterial community. *Nature* **430**, 551–554 (2004).
2. Johnson, Z. I. *et al.* Niche partitioning among *Prochlorococcus* ecotypes along ocean-scale environmental gradients. *Science* **311**, 1737–1740 (2006).
3. DeLong, E. F. Microbial community genomics in the ocean. *Nature Rev. Microbiol.* **3**, 459–469 (2005).
4. Tyson, G. W. *et al.* Community structure and metabolism through reconstruction of microbial genomes from the environment. *Nature* **428**, 37–43 (2004).
5. Venter, J. C. *et al.* Environmental genome shotgun sequencing of the Sargasso Sea. *Science* **304**, 66–74 (2004).
6. DeLong, E. F. *et al.* Community genomics among stratified microbial assemblages in the ocean's interior. *Science* **311**, 496–503 (2006).
7. Ram, R. J. *et al.* Community proteomics of a natural microbial biofilm. *Science* **308**, 1915–1920 (2005).
8. Bond, P. L., Smruga, S. P. & Banfield, J. F. Phylogeny of microorganisms populating a thick, subaerial, predominantly lithotrophic biofilm at an extreme acid mine drainage site. *Appl. Environ. Microbiol.* **66**, 3842–3849 (2000).
9. Coram, N. J. & Rawlings, D. E. Molecular relationship between two groups of the genus *Leptospirillum* and the finding that *Leptospirillum ferriphilum* sp. nov. dominates South African commercial biooxidation tanks that operate at 40 °C. *Appl. Environ. Microbiol.* **68**, 838–845 (2002).
10. Tyson, G. W. *et al.* Genome-directed isolation of the key nitrogen fixer *Leptospirillum ferrodiazotrophum* sp. nov. from an acidophilic microbial community. *Appl. Environ. Microbiol.* **71**, 6319–6324 (2005).
11. Johnson, D. B. & Hallberg, K. B. The microbiology of acidic mine waters. *Res. Microbiol.* **154**, 466–473 (2003).
12. Cohan, F. M. What are bacterial species? *Annu. Rev. Microbiol.* **56**, 457–487 (2002).
13. Maiden, M. C. *et al.* Multilocus sequence typing: a portable approach to the identification of clones within populations of pathogenic microorganisms. *Proc. Natl Acad. Sci. USA* **95**, 3140–3145 (1998).

14. Mau, B., Glasner, J. D., Darling, A. E. & Perna, N. T. Genome-wide detection and analysis of homologous recombination among sequenced strains of *Escherichia coli*. *Genome Biol.* **7**, R44 (2006).
15. Whitaker, R. J., Grogan, D. W. & Taylor, J. W. Recombination shapes the natural population structure of the hyperthermophilic archaeon *Sulfolobus islandicus*. *Mol. Biol. Evol.* **22**, 2354–2361 (2005).
16. Papke, R. T., Koenig, J. E., Rodriguez-Valera, F. & Doolittle, W. F. Frequent recombination in a saltern population of *Halorubrum*. *Science* **306**, 1928–1929 (2004).
17. Nesbo, C. L., Dlutek, M. & Doolittle, W. F. Recombination in *Thermotoga*: implications for species concepts and biogeography. *Genetics* **172**, 759–769 (2006).
18. Falush, D. *et al.* Recombination and mutation during long-term gastric colonization by *Helicobacter pylori*: estimates of clock rates, recombination size, and minimal age. *Proc. Natl Acad. Sci. USA* **98**, 15056–15061 (2001).
19. Rocha, E., Cornet, E. & Michel, B. Comparative and evolutionary analysis of the bacterial homologous recombination systems. *PLoS Genet.* **1**, 247–259 (2005).
20. Majewski, J. & Cohan, F. M. DNA sequence similarity requirements for interspecific recombination in *Bacillus*. *Genetics* **153**, 1525–1533 (1999).
21. Majewski, J. & Cohan, F. M. Adapt globally, act locally: the effect of selective sweeps on bacterial sequence diversity. *Genetics* **152**, 1459–1474 (1999).
22. Syvanen, A. C. Accessing genetic variation: genotyping single nucleotide polymorphisms. *Nature Rev. Genet.* **2**, 930–942 (2001).
23. Manabe, T. Capillary electrophoresis of proteins for proteomic studies. *Electrophoresis* **20**, 3116–3121 (1999).
24. Dalluge, J. J. Mass spectrometry: an emerging alternative to traditional methods for measurement of diagnostic proteins, peptides and amino acids. *Curr. Protein Pept. Sci.* **3**, 181–190 (2002).
25. Johnson, D. B. Selective solid media for isolating and enumerating acidophilic bacteria. *J. Microbiol. Methods* **23**, 205–218 (1995).

Supplementary Information is linked to the online version of the paper at www.nature.com/nature.

Acknowledgements We thank T. W. Arman, President, Iron Mountain Mines and R. Sugarek, EPA, for site access, and R. Carver for on-site assistance. We thank D. B. Johnson, University of Wales, Bangor, for assistance with culturing; and F. Larimer and M. Land of the ORNL Genome Analysis and System Modeling Group for computational resources for proteomic analysis. DNA sequencing was carried out at the DOE Joint Genome Institute. Funding was provided by the DOE Genomics:GTL Program (Office of Science), the NSF Biocomplexity Program and the NASA Astrobiology Institute.

Author Contributions I.L. isolated the *Leptospirillum* group II strains; I.L., V.J.D., G.D. and R.J.R. performed MLST; J.C.D. and P.R. made clone libraries and produced the sequencing reads; G.W.T., E.E.A. and J.F.B. assembled and binned the sequencing reads and produced the automatic annotation; D.G., G.D., V.J.D., G.W.T. and J.F.B. manually curated the *Leptospirillum* group II genome assemblies and annotation; N.C.V. optimized and performed proteomic experiments; M.B.S. created the proteomic analytical pipeline; V.J.D., N.C.V. and J.F.B. analysed the data; J.F.B. designed the research; and I.L., V.J.D., N.C.V., M.P.T., R.L.H. and J.F.B. wrote the paper.

Author Information The UBA community Whole Genome Shotgun project has been deposited at DDBJ/EMBL/GenBank under the project accession AAWO00000000. The version described in this paper, containing the assembled and annotated *Leptospirillum* group II UBA genome, is the first version, AAWO1000000. Sequencing reads were deposited in the NCBI trace archive. All proteomics datasets were submitted to PRIDE (<http://www.ebi.ac.uk/pride/>; experiment accession numbers 1854–1867). All proteomic datasets, databases and supplementary files can also be found at http://compbio.ornl.gov/biofilm_and_recombination. Reprints and permissions information is available at www.nature.com/reprints. The authors declare no competing financial interests. Correspondence and requests for materials should be addressed to J.F.B. (jbanfield@berkeley.edu).

LETTERS

A single class of olfactory neurons mediates behavioural responses to a *Drosophila* sex pheromone

Amina Kurtovic^{1*}, Alexandre Widmer^{1*} & Barry J. Dickson¹

Insects, like many other animals, use sex pheromones to coordinate their reproductive behaviours¹. Volatile pheromones are detected by odorant receptors expressed in olfactory receptor neurons (ORNs). Whereas fruit odours typically activate multiple ORN classes², pheromones are thought to act through single dedicated classes of ORN³. This model predicts that activation of such an ORN class should be sufficient to trigger the appropriate behavioural response. Here we show that the *Drosophila melanogaster* male-specific pheromone 11-*cis*-vacccenyl acetate (cVA) acts through the receptor Or67d to regulate both male and female mating behaviour. Mutant males that lack Or67d inappropriately court other males, whereas mutant females are less receptive to courting males. These data suggest that cVA has opposite effects in the two sexes: inhibiting mating behaviour in males but promoting mating behaviour in females. Replacing Or67d with moth pheromone receptors renders these ORNs sensitive to the corresponding moth pheromones. In such flies, moth pheromones elicit behavioural responses that mimic the normal response to cVA. Thus, activation of a single ORN class is both necessary and sufficient to mediate behavioural responses to the *Drosophila* sex pheromone cVA.

Several lines of evidence initially suggested that *Drosophila* mating behaviours might be guided in part by pheromones detected by the class of ORNs that expresses the odorant receptor Or67d. First, the Or67d ORNs innervate a sexually dimorphic glomerulus (DA1) in the antennal lobe^{4,5}. Second, these neurons constitute one of only three ORN classes that express the sex-specific transcripts of the behavioural sex determination gene *fruitless* (*fru*)^{6,7}. Third, blocking the activity of all three classes of *fru*-positive ORNs impairs male courtship activity⁵.

To assess the role of Or67d and the Or67d ORNs in *Drosophila* mating behaviour, we generated mutant alleles in which the open reading frame of Or67d was replaced with that of the yeast transcriptional activator GAL4 (Fig. 1a). These mutant knock-in alleles allowed us to assess the function of Or67d itself, and also to use GAL4-responsive transgenes to study the function of the Or67d ORNs. We initially used ends-in homologous recombination⁸ to produce a tandem duplication at the Or67d locus, consisting of one copy of the wild-type locus and one copy with the GAL4 replacement (Supplementary Fig. S1). By resolving this duplication, we recovered two independent mutant alleles that carried only the GAL4 replacement (Or67d^{GAL4[1]} and Or67d^{GAL4[2]}), and two independent control alleles in which the original intact locus was restored (Or67d⁺[1] and Or67d⁺[2]).

Using a UAS-*mCD8-GFP* reporter to label these cells with green fluorescent protein (GFP), we confirmed that the Or67d^{GAL4} knock-in drives transgene expression exclusively in the ORNs that also express Or67d (Fig. 1b). Previous studies using an Or67d promoter

fragment to drive GAL4 expression did not fully clarify whether Or67d ORNs project to DA1 exclusively⁶ or to both the DA1 and VA6 glomeruli⁷. Using the Or67d^{GAL4} knock-in, we confirmed that the DA1 glomerulus alone is targeted by Or67d ORNs, in both males (Fig. 1c) and females. We did not detect reporter expression anywhere else in adults, nor in embryos or larvae.

The Or67d receptor is thought to mediate the detection of the male pheromone cVA ([Z]-11-octadecenyl acetate): cVA activates the T1 class of trichoid sensilla⁹ in which the Or67d neurons alone are housed⁶, and ectopic expression of Or67d in other trichoid ORNs confers sensitivity to cVA¹⁰. Indeed, using single-sensillum recordings, we found that cVA elicits a rapid and robust firing response in the T1 sensilla of control Or67d⁺ males but not in those of Or67d^{GAL4} mutants (Fig. 1d). Spontaneous activity was also greatly reduced in these mutants. Restoring Or67d function with a UAS-Or67d transgene fully rescued both the spontaneous and evoked responses (Fig. 1d). The responses to cVA were quantitatively indistinguishable in males and females (Fig. 1e) across a 1,000-fold range of concentrations (Fig. 1f). To assess whether odorant receptors in other ORNs might also detect cVA, we used electroantennograms to simultaneously measure the responses of a large number of ORNs on the third antennal segment. Neither Or67d^{GAL4} males nor females produced a detectable response to cVA, although both responded normally to ethanol (Fig. 1g, h). These genetic data confirm that Or67d mediates physiological responses to cVA, and show further that males and females respond equally to cVA and that Or67d is likely to be the only receptor for cVA.

If cVA acts as a sex pheromone and Or67d is its sole receptor, then Or67d^{GAL4} males or females should be impaired in their performance of one or more mating behaviours. To test this, we first monitored male courtship behaviour in single-pair courtship assays, using the courtship index (CI, the percentage of time for which the male courts during a 10-min assay) as a simple measure of overall courtship activity. Typically, wild-type males court with a CI of about 80% when paired with a virgin female (Fig. 2a), but only about 10% when paired with another male (Fig. 2b). When paired with virgin females, Or67d^{GAL4} mutant males courted at levels comparable to those of the control Or67d⁺ males (Fig. 2a). In contrast, when paired with wild-type males, Or67d^{GAL4} mutant males displayed a roughly threefold higher courtship activity than the Or67d⁺ controls ($P < 0.0001$, permutation test; Fig. 2b and Supplementary Fig. S2). To confirm that this increased male-male courtship was indeed due to the loss of Or67d function, we introduced independent UAS-Or67d transgene insertions into each of the two Or67d^{GAL4} lines. For both alleles, restoring Or67d function in this way suppressed male-male courtship back to its normal low levels (Fig. 2b).

To assess whether Or67d also functions in female mating behaviour, we paired individual mutant or control virgin females with

¹Research Institute of Molecular Pathology (IMP), Dr Bohr-gasse 7, A-1030 Vienna, Austria.

*These authors contributed equally to this work.

naive wild-type males in a series of small chambers and measured their latency to copulation. About 50% of the control *Or67d*⁺ females copulated within 18 min, and about 60% within 30 min (Fig. 2c). In contrast, only about 20% of the *Or67d*^{GAL4} females copulated within 18 min, and about 30% within 30 min ($P < 0.0001$ at both time points, χ^2 test; Fig. 2c and Supplementary Fig. S2). When *Or67d* expression was restored with the *UAS-Or67d* transgenes, the mutant females copulated as rapidly as the control females (Fig. 2c). The reduced receptivity of *Or67d*^{GAL4} females was evidently not due to a lower attractiveness of these females to males, because they were courted as vigorously as *Or67d*⁺ females (Fig. 2d).

These behavioural data imply that cVA is a dual-purpose sex pheromone, acting in males to inhibit mating¹¹ (Fig. 2b) and in females to promote mating (Fig. 2c). To test directly whether cVA inhibits male courtship behaviour, and if so whether this requires *Or67d*, we applied cVA to the abdomens of virgin females and offered these females to mutant or control males in single-pair courtship assays. Indeed, application of cVA suppressed courtship by *Or67d*⁺ control males but not by *Or67d*^{GAL4} mutant males ($P < 0.0001$, permutation test; Fig. 3). cVA also suppressed courtship by *Or67d*^{GAL4} males carrying the *UAS-Or67d* transgene (Fig. 3). Thus, cVA acts through *Or67d* to inhibit male courtship behaviour. However, it should be noted that cVA is not the sole mediator of sex discrimination

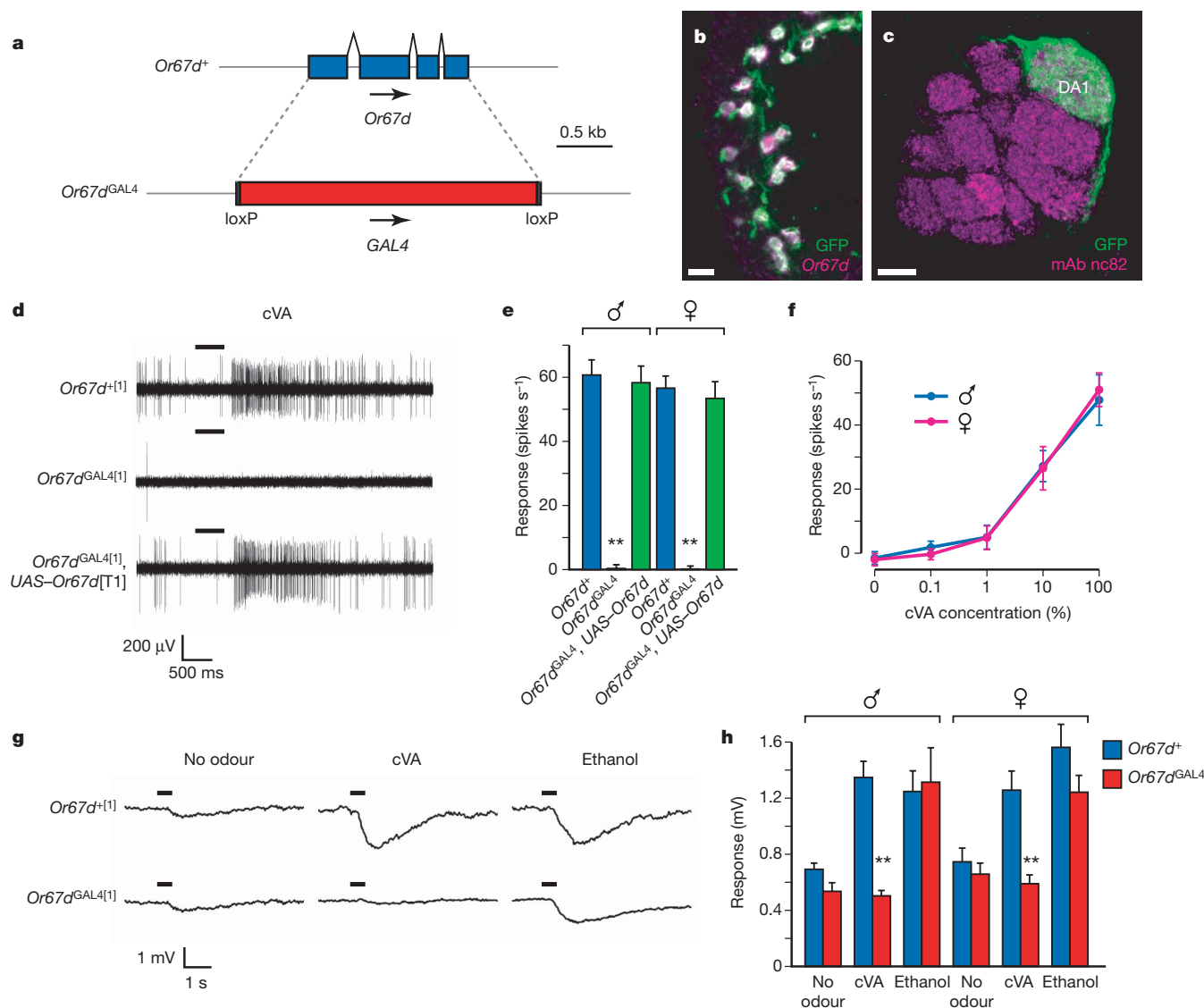


Figure 1 | *Or67d* mediates physiological responses to cVA. **a**, Diagram showing the organization of the *Or67d* locus in the wild-type control (*Or67d*⁺) and GAL4 knock-in (*Or67d*^{GAL4}) alleles. kb, kilobase. **b**, Expression of mCD8–GFP (anti-GFP, green) and *Or67d* mRNA (magenta) in the third antennal segment of an *Or67d*^{GAL4}/UAS-mCD8–GFP male. Scale bar, 10 μ m. **c**, Confocal section of the antennal lobe of a *Or67d*^{GAL4}/UAS-mCD8–GFP male, stained with anti-GFP (green) to visualize the projections of the *Or67d* ORNs and the synaptic marker mAb nc82 (magenta) to visualize the glomerular organization. Scale bar, 10 μ m. **d**, Recordings from T1 sensilla in *Or67d*⁺ control, mutant, and rescue males stimulated with cVA. The horizontal bar indicates the duration of stimulus delivery. The delay in the response is consistent with the time required for the odour to reach the antenna. **e**, Summary of single-sensillum recording data, plotted as means and s.e.m.; $n = 10$ for each control and rescue, and

$n = 6$ for mutants. No significant difference was observed between the two independent alleles for each genotype; data for each genotype were therefore pooled. Two asterisks, $P < 0.0001$ compared with controls; Kruskal–Wallis analysis of variance (ANOVA) test. **f**, Dose–response curve for T1 sensilla from *Or67d*⁺ males and females, plotted as means \pm s.e.m.; $n = 6$ for each data point. cVA was serially diluted in paraffin oil. **g**, Electrophysiological plots from control and mutant males, stimulated with cVA, ethanol or an empty odour cartridge. The horizontal bar indicates the duration of stimulus delivery. **h**, Summary of electrophysiological data, plotted as means and s.e.m.; $n = 16$ and 13 for *Or67d*⁺ and *Or67d*^{GAL4} males, respectively, and $n = 10$ for females for both genotypes. Data from the two independent alleles were pooled. Two asterisks, $P < 0.002$ for *Or67d*^{GAL4} compared with corresponding *Or67d*⁺ control; Kruskal–Wallis ANOVA test.

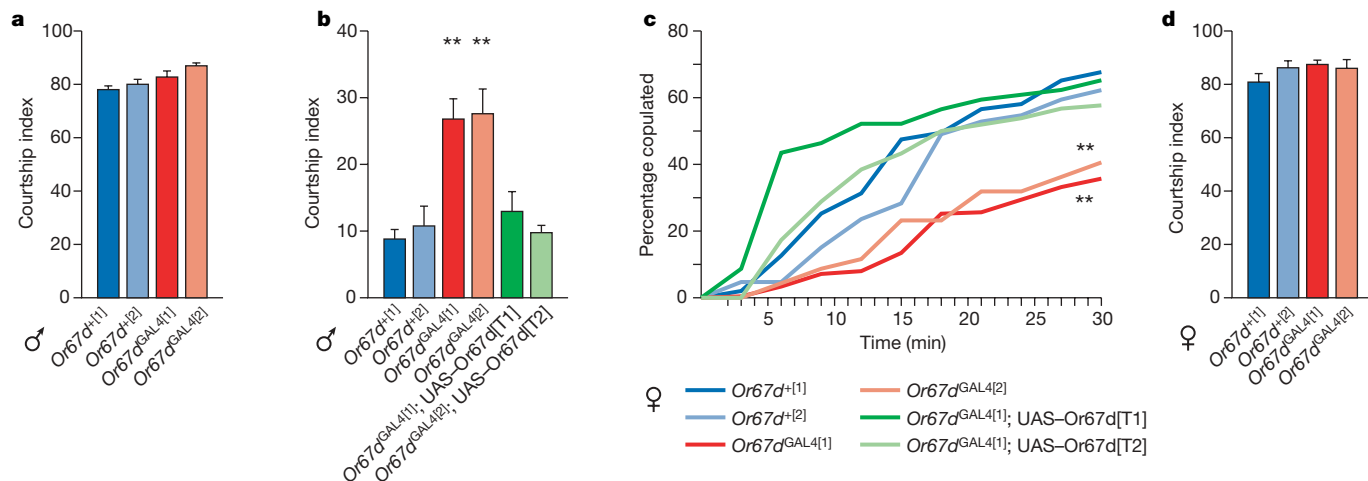


Figure 2 | *Or67d* functions in male and female mating behaviours.

a, Courtship indices for males of the indicated genotypes paired with wild-type virgin females. $n = 37, 57, 47$ and 61 , respectively. **b**, Courtship indices for males of the indicated genotypes paired with wild-type males. $n = 103, 42, 92, 60, 30$ and 57 , respectively. Two asterisks, $P < 0.0001$ compared with both *Or67d⁺* controls; permutation test. **c**, Copulation latency for females of

the indicated genotypes paired with wild-type males. $n = 198, 106, 238, 69, 69$ and 104 , respectively. Two asterisks, $P < 0.0001$ compared with both *Or67d⁺* controls at both the 18-min and 30-min time points; χ^2 test. **d**, Courtship indices for wild-type males paired with virgin females of the indicated genotypes. $n = 28, 18, 35$ and 24 , respectively. Error bars indicate s.e.m. throughout.

in *Drosophila*, because *Or67d* mutant males still courted females much more avidly than they courted other males (Fig. 2a, b). This implies the existence of either additional inhibitory cues from the male, stimulatory cues from the female, or both.

General odorants are thought to activate many different receptors, with odour identity encoded by the specific combination of receptors that are activated^{2,12}. In this model, no single ORN class encodes a specific odour, and odour perception is thought to arise through spatial¹³ and temporal¹⁴ integration of ORN signals in higher-order olfactory circuits. In contrast, odours of particular biological significance, such as pheromones, may activate only a single class of ORN, such that this ORN class alone communicates an unambiguous signal to the brain through a dedicated 'labelled line'¹³. We have shown that *Or67d* is required for physiological and behavioural responses to cVA, but this does not distinguish between the combinatorial and labelled-line models for signal processing. For this, we required a method of activating the *Or67d* ORNs artificially. In a combinatorial model, stimulation of *Or67d* ORNs alone is not predicted to induce a behavioural response, but in the labelled-line model it should.

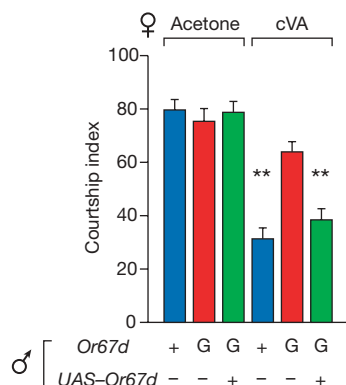


Figure 3 | *Or67d* mediates cVA-induced courtship suppression. Courtship indices for homozygous males of the indicated genotypes paired with wild-type virgin females treated either with acetone solvent alone or with cVA. Error bars indicate s.e.m.; $n = 14, 15, 23, 62, 58$ and 55 , respectively. Two asterisks, $P < 0.0001$ compared with the corresponding solvent control; permutation test. For the male genotypes, '+' and 'G' indicate the *Or67d⁺* and *Or67d^{GAL4}* alleles, respectively, and '+' and '-' the presence and absence of the *UAS-Or67d* transgene.

We sought to stimulate *Or67d* ORNs artificially with a heterologous ligand–receptor pair. For this, we turned to the sex pheromones of moths. The female silkworm *Bombyx mori* emits the pheromone bombykol ([E,Z]-10,12-hexadecadien-1-ol) to attract and stimulate the male¹⁵. To the same effect, the female tobacco budworm *Heliothis virescens* produces a sex pheromone blend, one component of which is (Z)-11-hexadecenal¹⁶. The receptor BmOR1 has recently been identified as a receptor for bombykol, on the basis of its ability to confer cellular responses to bombykol in *Xenopus* oocytes and *Drosophila* ORNs^{17–20}. Similarly, using single-sensillum recordings we found that replacing *Or67d* with BmOR1 conferred a new response to bombykol in the *Or67d* ORNs (Fig. 4a, b). The *Heliothis* receptors HR13–16 have been identified as candidate pheromone receptors²¹, and by the same strategy we found that HR13 conferred sensitivity to (Z)-11-hexadecenal in the *Or67d* ORNs (Fig. 4a, b). Thus, despite more than 300 million years of evolutionary divergence, these moth pheromone receptors are fully functional when expressed in *Drosophila* ORNs.

To test whether artificial activation of the *Or67d* ORNs suppressed courtship, we applied bombykol or hexadecenal to virgin females and offered these females to naive males expressing either BmOR1 or HR13, respectively, in the *Or67d* ORNs. Courtship activity of these males was suppressed to a similar degree to that observed when cVA-treated females were offered to wild-type males (Figs 3 and 4c). In contrast, both *Or67d⁺* and *Or67d^{GAL4}* males vigorously courted the bombykol-treated or hexadecenal-treated females, and the receptor replacement males vigorously courted females treated with solvent alone (Fig. 4c). Thus, courtship suppression is strictly dependent on both the presence of the moth pheromone on the female and the corresponding pheromone receptor in the *Or67d* ORNs in the males. We infer that the activation of the *Or67d* ORNs alone is sufficient to inhibit male courtship behaviour, in accordance with the labelled-line hypothesis for pheromone detection.

Tracing this labelled line into higher olfactory centres should help to reveal how the activation of *Or67d* ORNs suppresses male mating behaviour, and perhaps also how the same signal might have the opposite effect in females. These neurons connect in the DA1 glomerulus to two distinct classes of second-order projection neurons (PNs): GABAergic vPNs and cholinergic iPNs^{22–27}. Both the DA1 vPNs and iPNs project their axons to a putative sex-pheromone processing centre in the lateral horn of the protocerebrum, specifically targeting two sexually dimorphic regions, one enlarged in males

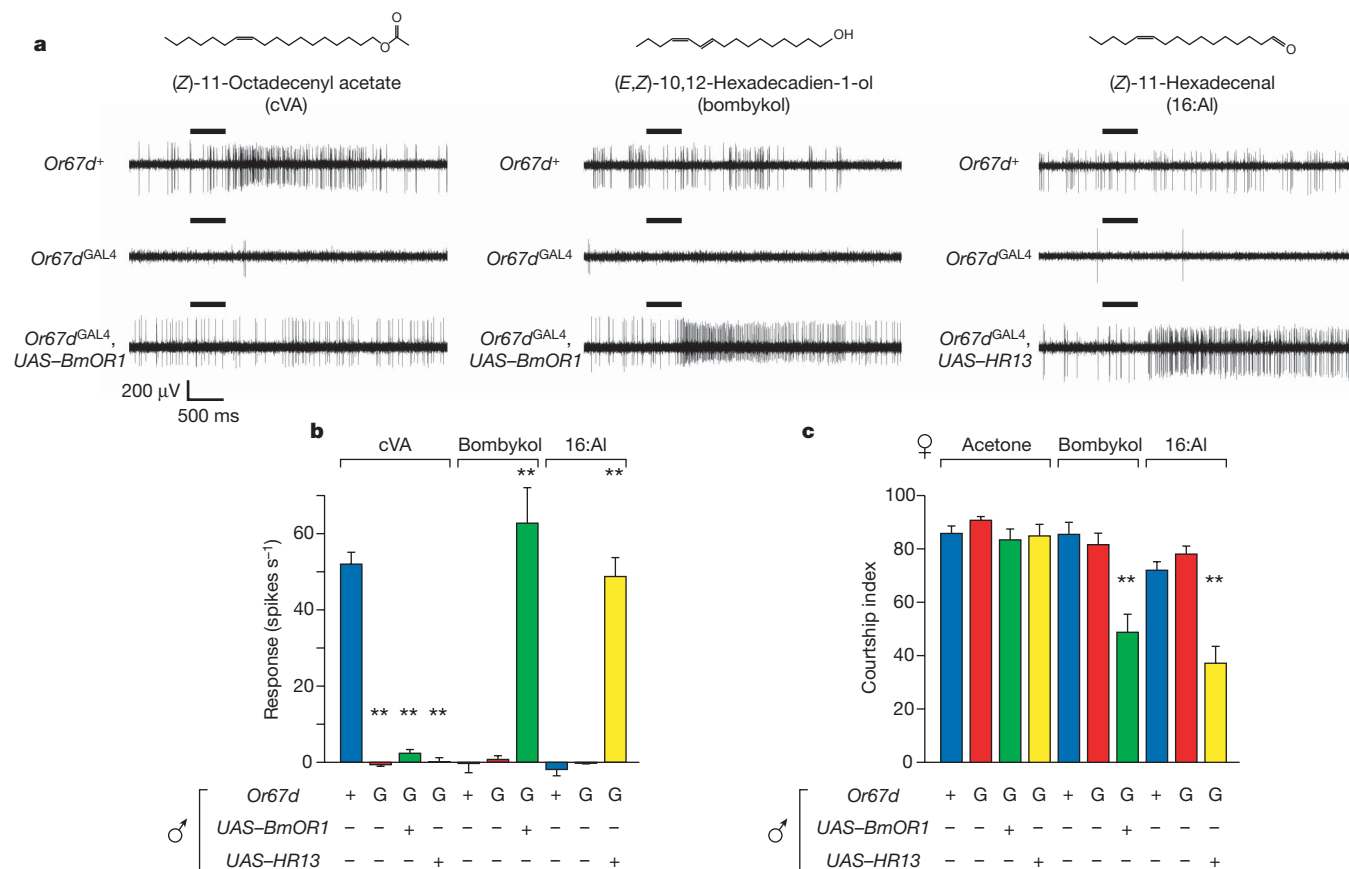


Figure 4 | Artificial activation of Or67d ORNs mimics cVA responses. **a**, Recordings from T1 sensilla in Or67d⁺, Or67d^{GAL4}, and Or67d^{GAL4} UAS-BmOR1 or Or67d^{GAL4} UAS-HR13 males stimulated with either cVA, bombykol or (Z)-11-hexadecenal (16:Al). The horizontal bar indicates the duration of stimulus delivery. The variation in the response latency most probably reflects slight variations in the settings of the stimulus controller and the position of the preparation. **b**, Summary of single-sensillum recording data, plotted as mean and s.e.m.; $n = 8$ –18 for each experiment.

and the other enlarged in females²⁴. It will be interesting to test whether the DA1 PN makes sexually dimorphic patterns of inhibitory or excitatory connections in these regions, and if so, to what extent such dimorphic circuitry might shape distinct male and female responses to the cVA signal.

METHODS

Genetic manipulations. Targeting of the *Or67d* locus was performed essentially according to the ends-in method of homologous recombination⁸ and is illustrated in Supplementary Fig. S1. Each of the two final Or67d^{GAL4} and Or67d⁺ lines was verified by polymerase chain reaction (PCR) amplification and sequencing of the entire *GAL4* or *Or67d* coding region. These lines were then backcrossed into an endogenous *white*⁺ background for behavioural and physiological studies.

UAS-Or67d was prepared by PCR amplification of the *Or67d* coding region from *Drosophila melanogaster* genomic DNA. UAS-BmOR1 was prepared by amplifying each of the six coding exons of *BmOR1* from genomic DNA from the *B. mori* Daizo strain, and then using overlap-extension PCR to combine all six fragments into a single intronless product. UAS-HR13 was prepared by subcloning an *HR13* cDNA.

Electrophysiology. Single-sensillum recordings²⁸ and electroantennograms²⁹ were performed as described previously and in Supplementary Methods. cVA (99% purity), bombykol (95% purity) and (Z)-11-hexadecenal (93% purity) were obtained from Pherobank. Ethanol, of the highest purity available, was obtained from Sigma-Aldrich.

Behavioural assays and histochemistry. Behavioural assays³⁰, *in situ* hybridization⁶ and immunohistochemistry⁵ were performed as described previously. For the application of cVA, bombykol or (Z)-11-hexadecenal, the pheromones were diluted 1:10, 1:100 or 1:50, respectively, in acetone, and 0.2 μ l was applied to the

dorsal abdomen of flies lightly anaesthetized with CO₂. Flies were allowed to recover for 1 h in food vials before behavioural assays were performed. All behavioural assays were scored blind to the genotype. For permutation tests, CIs for control and experimental animals were pooled and then randomly assorted into simulated data sets of the same size as in the original data. The *P* value was determined as the fraction of 10,000 such randomly permuted data sets that produced a CI difference at least as large as that observed in the actual data.

Two asterisks, $P < 0.0001$ compared with Or67d⁺ controls stimulated with the same pheromone; Kruskal–Wallis ANOVA test. **c**, Courtship indices for males of the indicated genotypes paired with wild-type virgin females treated either with acetone solvent alone, with bombykol or with 16-al. Error bars indicate s.e.m.; $n = 30, 40, 24, 12, 17, 21, 18, 34, 28$ and 32, respectively. Two asterisks, $P < 0.0001$ compared with the corresponding Or67d⁺ control; permutation test.

Received 9 October 2006; accepted 8 February 2007.

- Howard, R. W. & Blomquist, G. J. Ecological, behavioral, and biochemical aspects of insect hydrocarbons. *Annu. Rev. Entomol.* **50**, 371–393 (2005).
- Hallem, E. A., Ho, M. G. & Carlson, J. R. The molecular basis of odor coding in the *Drosophila* antenna. *Cell* **117**, 965–979 (2004).
- Hildebrand, J. G. & Shepherd, G. M. Mechanisms of olfactory discrimination: converging evidence for common principles across phyla. *Annu. Rev. Neurosci.* **20**, 595–631 (1997).
- Kondoh, Y., Kaneshiro, K. Y., Kimura, K. & Yamamoto, D. Evolution of sexual dimorphism in the olfactory brain of Hawaiian *Drosophila*. *Proc. R. Soc. Lond. B* **270**, 1005–1013 (2003).
- Stockinger, P., Kvitsiani, D., Rotkopf, S., Tirian, L. & Dickson, B. J. Neural circuitry that governs *Drosophila* male courtship behavior. *Cell* **121**, 795–807 (2005).
- Couto, A., Alenius, M. & Dickson, B. J. Molecular, anatomical, and functional organization of the *Drosophila* olfactory system. *Curr. Biol.* **15**, 1535–1547 (2005).
- Fishilevich, E. & Vosshall, L. B. Genetic and functional subdivision of the *Drosophila* antennal lobe. *Curr. Biol.* **15**, 1548–1553 (2005).
- Rong, Y. S. et al. Targeted mutagenesis by homologous recombination in *D. melanogaster*. *Genes Dev.* **16**, 1568–1581 (2002).
- Clyne, P., Grant, A., O'Connell, R. & Carlson, J. R. Odorant response of individual sensilla on the *Drosophila* antenna. *Invertebr. Neurosci.* **3**, 127–135 (1997).
- Ha, T. S. & Smith, D. P. A pheromone receptor mediates 11-cis-vaccenyl acetate-induced responses in *Drosophila*. *J. Neurosci.* **26**, 8727–8733 (2006).

11. Mane, S. D., Tompkins, L. & Richmond, R. C. Male esterase 6 catalyzes the synthesis of a sex pheromone in *Drosophila melanogaster* females. *Science* **222**, 419–421 (1983).
12. Malnic, B., Hirono, J., Sato, T. & Buck, L. B. Combinatorial receptor codes for odors. *Cell* **96**, 713–723 (1999).
13. Zou, Z. & Buck, L. B. Combinatorial effects of odorant mixes in olfactory cortex. *Science* **311**, 1477–1481 (2006).
14. Broome, B. M., Jayaraman, V. & Laurent, G. Encoding and decoding of overlapping odor sequences. *Neuron* **51**, 467–482 (2006).
15. Butenandt, A., Beckmann, R., Stamm, D. & Hecker, E. Über den Sexuallockstoff des Seidenspinners *Bombyx mori*. Reindarstellung und Konstitution. *Z. Naturforsch.* **14b**, 283–284 (1959).
16. Roelofs, W. L., Hill, A. S., Carde, R. T. & Baker, T. C. Two sex pheromone components of the tobacco budworm moth, *Heliothis virescens*. *Life Sci.* **14**, 1555–1562 (1974).
17. Sakurai, T. *et al.* Identification and functional characterization of a sex pheromone receptor in the silkworm *Bombyx mori*. *Proc. Natl Acad. Sci. USA* **101**, 16653–16658 (2004).
18. Nakagawa, T., Sakurai, T., Nishioka, T. & Touhara, K. Insect sex-pheromone signals mediated by specific combinations of olfactory receptors. *Science* **307**, 1638–1642 (2005).
19. Krieger, J., Grosse-Wilde, E., Gohl, T. & Breer, H. Candidate pheromone receptors of the silkworm *Bombyx mori*. *Eur. J. Neurosci.* **21**, 2167–2176 (2005).
20. Syed, Z., Ishida, Y., Taylor, K., Kimbrell, D. A. & Leal, W. S. Pheromone reception in fruit flies expressing a moth's odorant receptor. *Proc. Natl Acad. Sci. USA* **103**, 16538–16543 (2006).
21. Krieger, J. *et al.* Genes encoding candidate pheromone receptors in a moth (*Heliothis virescens*). *Proc. Natl Acad. Sci. USA* **101**, 11845–11850 (2004).
22. Marin, E. C., Jefferis, G. S., Komiyama, T., Zhu, H. & Luo, L. Representation of the glomerular olfactory map in the *Drosophila* brain. *Cell* **109**, 243–255 (2002).
23. Wong, A. M., Wang, J. W. & Axel, R. Spatial representation of the glomerular map in the *Drosophila* protocerebrum. *Cell* **109**, 229–241 (2002).
24. Jefferis, G. S. X. E. *et al.* Comprehensive maps of *Drosophila* higher olfactory centres: spatially segregated fruit and pheromone representation. *Cell* (in the press) (2007).
25. Schürmann, F. W. Acetylcholine, GABA, glutamate and NO as putative transmitters indicated by immunocytochemistry in the olfactory mushroom body system of the insect brain. *Acta Biol. Hung.* **51**, 355–362 (2000).
26. Yasuyama, K., Meinertzhagen, I. A. & Schürmann, F. W. Synaptic connections of cholinergic antennal lobe relay neurons innervating the lateral horn neuropile in the brain of *Drosophila melanogaster*. *J. Comp. Neurol.* **466**, 299–315 (2003).
27. Wilson, R. I. & Laurent, G. Role of GABAergic inhibition in shaping odor-evoked spatiotemporal patterns in the *Drosophila* antennal lobe. *J. Neurosci.* **25**, 9069–9079 (2005).
28. de Bruyne, M., Foster, K. & Carlson, J. R. Odor coding in the *Drosophila* antenna. *Neuron* **30**, 537–552 (2001).
29. Rollmann, S. M., Mackay, T. F. & Anholt, R. R. Pinocchio, a novel protein expressed in the antenna, contributes to olfactory behavior in *Drosophila melanogaster*. *J. Neurobiol.* **63**, 146–158 (2005).
30. Demir, E. & Dickson, B. J. *fruitless* splicing specifies male courtship behavior in *Drosophila*. *Cell* **121**, 785–794 (2005).

Supplementary Information is linked to the online version of the paper at www.nature.com/nature.

Acknowledgements We thank A. Couto and M. Alenius for the initial identification of *Or67d* expression in the T1 ORNs and for the images in Fig. 1b, c; K. Golic for targeting stocks; Y. Banno for the *Bombyx mori* genomic DNA; J. Krieger for the *HR13* cDNA and the supply of bombykol used in our initial experiments; R. Fuchs and Azra Kurtovic for technical assistance; G. Jefferis, A. Keene and M. Leyssen for comments on the manuscript; and G. Jefferis and L. Luo for communicating unpublished data. A.W. was supported in part by a postdoctoral fellowship from the Swiss National Science Foundation. This work was funded by Boehringer Ingelheim GmbH.

Author Contributions A.K. and B.J.D. generated the *Or67d* knock-in alleles. A.K. performed the behavioural analysis with assistance from A.W., who also carried out all the electrophysiological experiments. All three authors contributed to the experimental design and preparation of the manuscript.

Author Information Reprints and permissions information is available at www.nature.com/reprints. The authors declare no competing financial interests. Correspondence and requests for materials should be addressed to B.J.D. (dickson@imp.ac.at).

Tyrosine kinase receptor RET is a key regulator of Peyer's Patch organogenesis

Henrique Veiga-Fernandes¹, Mark C. Coles¹, Katie E. Foster¹, Amisha Patel¹, Adam Williams¹, Dipa Natarajan², Amanda Barlow², Vassilis Pachnis² & Dimitris Kioussis¹

Normal organogenesis requires co-ordinate development and interaction of multiple cell types, and is seemingly governed by tissue specific factors. Lymphoid organogenesis during embryonic life is dependent on molecules the temporal expression of which is tightly regulated. During this process, haematopoietic 'inducer' cells interact with stromal 'organizer' cells, giving rise to the lymphoid organ primordia¹. Here we show that the haematopoietic cells in the gut exhibit a random pattern of motility before aggregation into the primordia of Peyer's patches, a major component of the gut-associated lymphoid tissue. We further show that a $CD45^{+}CD4^{-}CD3^{-}IL7R\alpha^{-}c\text{-Kit}^{+}CD11c^{+}$ haematopoietic population expressing lymphotoxin has an important role in the formation of Peyer's patches. A subset of these cells expresses the receptor tyrosine kinase RET, which is essential for mammalian enteric nervous system formation². We demonstrate that RET signalling is also crucial for Peyer's patch formation. Functional genetic analysis revealed that *Gfra3*-deficiency results in impairment of Peyer's patch development, suggesting that the signalling axis RET/GFR α 3/ARTN is involved in this process. To support this hypothesis, we show that the RET ligand ARTN is a strong attractant of gut haematopoietic cells, inducing the formation of ectopic Peyer's patch-like structures. Our work strongly suggests that the RET signalling pathway, by regulating the development of both the nervous and lymphoid system in the gut, has a key role in the molecular mechanisms that orchestrate intestine organogenesis.

The formation of Peyer's patches is dependent on the colonization of the gut wall during embryogenesis by haematopoietic lymphoid tissue inducer (LTi) cells which, following interactions with resident stroma lymphoid tissue organizer (LT α) cells, aggregate on embryonic day E16.5 to generate the Peyer's patch primordia^{1,3–5}. Deficiency in Ikaros⁶, ROR γ (ref. 7), Id2 (ref. 8), TRANCE/TRANCER^{9–11} and CXCL13–CXCR5 (refs 12, 13) result in developmental or functional deficits of LTi cells and an impairment in Peyer's patch formation, whereas lymphotoxin β receptor (LT β r)-deficient mice fail to form Peyer's patches owing to impaired LT α stroma cell function^{14–17}. IL7–IL7R α interactions have also been implicated in Peyer's patch formation^{4,5,18,19}.

Human CD2–GFP transgenic mice express green fluorescent protein (GFP) in a population of haematopoietic cells aggregating in embryonic sites that develop lymph nodes in the adult²⁰. Such cells were also detected in the gut by fluorescence microscopy from day E12.5 (Fig. 1a). Fluorescent cells were initially restricted to the pyloric/duodenum region and the caecum, but were found evenly distributed throughout the gut by stage E15.5 (Fig. 1b). Within the next 24 h these cells aggregate to form Peyer's patch primordia (Fig. 1b). To examine whether the final number of haematopoietic cells within the gut is achieved by the expansion of an early precursor pool or the continuous influx of new cells, we analysed the cell cycle profile of the enteric GFP⁺ cells. Virtually all $CD45^{+}GFP^{+}$ cells from E15.5 or

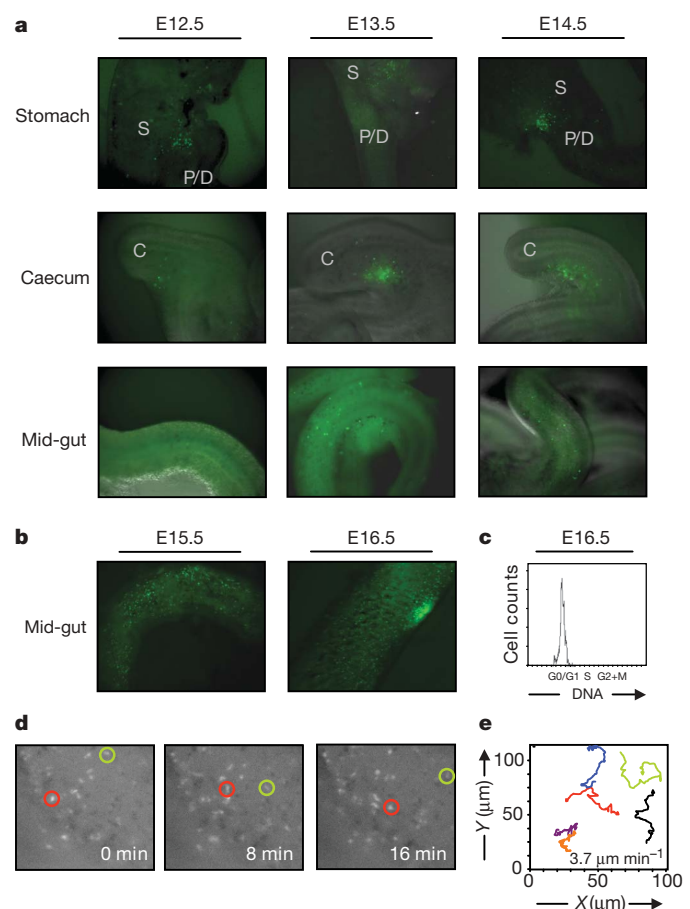


Figure 1 | Colonization of the embryonic intestine by GFP⁺ haematopoietic cells. **a**, Human CD2–GFP⁺ embryos were dissected and the intestines analysed by stereo fluorescence microscopy ($\times 1.6$ objective). Results show the distribution of GFP⁺ cells from E12.5 to E14.5 in the stomach (S), pylorus/duodenum junction (P/D), caecum (C) and mid-gut. **b**, GFP⁺ cells in the mid-gut from E15.5 to E16.5 are depicted showing Peyer's patch primordium formation by E16.5. **c**, E16.5 GFP⁺ Peyer's patch primordia were micro-dissected and digested with collagenase. Cell suspensions were sorted by flow cytometry for GFP⁺ cells and their cell cycle status analysed by propidium iodide incorporation. GFP⁺ cell counts (2,063) are shown in the histogram. Similar results were obtained at E15.5. **d**, E15.5 GFP⁺ intestines were immobilized in a collagen matrix and time-lapse stereo microscopy analysis was performed. Results show detail of time-lapse analysis showing different time points and relative positions of two different cells during the analysis. **e**, Cell tracks are shown for six different cells analysed over 25 min in the same conditions as in **d**. Average cell speed is indicated ($3.7 \pm 0.6 \mu\text{m min}^{-1}$; error is s.d.). For the time-lapse sequence please see Supplementary Video 1 and 2.

¹Division of Molecular Immunology, ²Division of Molecular Neurobiology, MRC National Institute for Medical Research, The Ridgeway Mill Hill, London NW7 1AA, UK.

E16.5 were arrested at the G0/G1 stage of the cell cycle (Fig. 1c), consistent with the idea that proliferation does not have a major role in the increase of the enteric $CD45^+GFP^+$ pool during embryogenesis. However, these cells exhibit a remarkable and seemingly random motility, often reaching $6\mu m\ min^{-1}$ (average speed $3.7\mu m\ min^{-1}$; Fig. 1d, e; Supplementary Video 1 and 2), suggesting that new influx and migration are the main factors for their dissemination within the gut wall.

Phenotypic analysis of cells from days E15.5 and E16.5 revealed that the $CD45^+GFP^+$ population included the $CD4^+CD3^-IL7R\alpha^+c-Kit^+$ LTi cells described previously¹. In addition, we detected a phenotypically distinct population of $CD4^+CD3^-IL7R\alpha^+c-Kit^+CD11c^+$ cells, which followed a pattern of distribution and aggregation like that of the LTi cells and are probably similar to the $CD11c^+$ cells previously described in E17.5 intestine^{3,21} (Fig. 2a, b; Supplementary Fig. 1a–d; Supplementary Video 3).

Phenotypic analysis revealed differences and similarities between the $CD4^+CD3^-IL7R\alpha^+c-Kit^+CD11c^+$ cells from the embryonic gut and dendritic cells isolated from adult spleens. Thus, $CD4^+CD3^-IL7R\alpha^+c-Kit^+CD11c^+$ cells express major histocompatibility complex class II and CD11b similar to the splenic dendritic cells, but lack the DEC205 marker and are positive for the surface markers GR-1 and NK1.1, which are not expressed by the adult dendritic cells (Supplementary Fig. 1b). Furthermore, we found that compared with $CD4^+CD3^-IL7R\alpha^+c-Kit^+$ LTi cells, $CD4^+CD3^-IL7R\alpha^+c-Kit^+CD11c^+$ cells express higher levels of lymphotoxin β (Fig. 2b; Supplementary Fig. 3d), a molecule known to be crucial for Peyer's patch organogenesis^{1,14–17,22,23}.

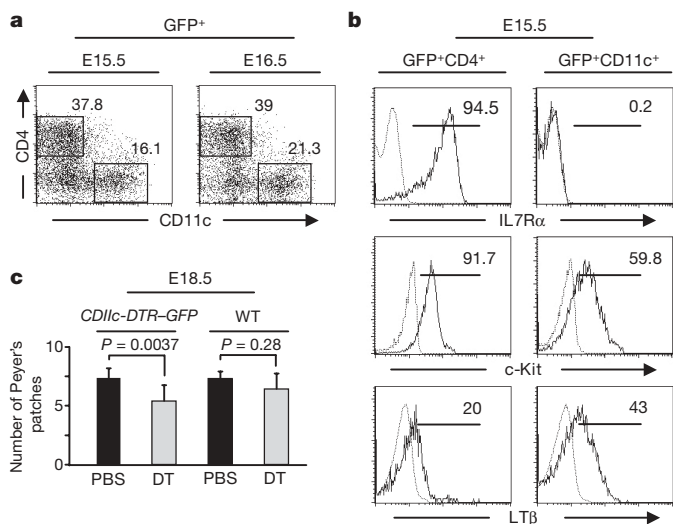


Figure 2 | Phenotype of embryonic GFP^+ haematopoietic cells in the intestine. **a**, GFP^+ haematopoietic cells from E15.5 and E16.5 intestines were purified after collagenase treatment. Cell suspensions were analysed by flow cytometry analysis and dot plots depicted. Numbers represent cell percentages in the respective gates. **b**, E15.5 intestines were analysed as above. Left panels, expression profiles on GFP^+CD4^+ cells; right panels, expression profiles on GFP^+CD11c^+ cells. Dotted lines show negative control staining. GFP^+ cells are also $CD3^-CD19^-CD8\alpha^-$ (Supplementary Fig. 1a). **c**, $CD11c-DTR-GFP$ transgenic mice were crossed with human $CD2-DsRed$ transgenic mice (Supplementary Fig. 2c) and were treated daily (intraperitoneal injection) from E14.5 to E17.5 with 4 nanograms of diphtheria toxin (DT; Sigma) per gram of mouse. At E18.5 Peyer's patches were counted by stereo fluorescent microscopy (Supplementary Fig. 2c). Results show Peyer's patch numbers in $CD11c-DTR-GFP$ and wild-type (WT) mice treated with phosphate-buffered saline (PBS) or DT. $CD11c-DTR-GFP$ PBS-treated, $n = 6$; $CD11c-DTR-GFP$ DT-treated, $n = 22$; wild type PBS-treated, $n = 3$; wild type DT-treated, $n = 14$; two-tailed t -test P values were $CD11c-DTR-GFP$ PBS-treated versus $CD11c-DTR-GFP$ DT-treated, $P = 0.0037$; wild-type PBS-treated versus wild type DT-treated, $P = 0.279$; $CD11c-DTR-GFP$ DT-treated versus wild type DT-treated, $P = 0.043$. Error bars show s.d.

To determine whether these cells have a role in the formation of Peyer's patches, we examined transgenic mice that express the diphtheria toxin receptor (DTR) and GFP under the control of the $CD11c$ promoter ($CD11c-GFP-DTR$ mice)²⁴. These mice express DTR and GFP in approximately 20–30% of the $CD11c$ cells in E14.5 to E17.5 gut (Supplementary Fig. 2a). Administration of diphtheria toxin to $CD11c-GFP-DTR$ transgenic embryos resulted in a significant reduction (25%) in the number of Peyer's patches (Fig. 2c). Taken together, these experiments suggest that the formation of normal numbers of Peyer's patches during gut organogenesis requires the full complement of $CD4^+CD3^-IL7R\alpha^+c-Kit^+CD11c^+$ cells.

The colonization of the embryonic gut by lymphoid cells and their aggregation to form Peyer's patches is reminiscent of the invasion of the gut mesenchyme by neuroectodermal cells that colonize the gut

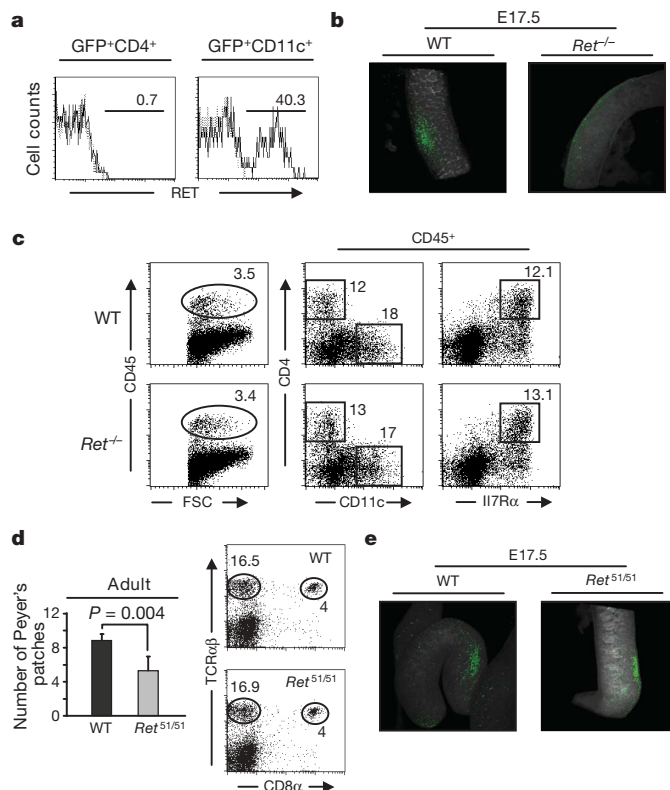


Figure 3 | Peyer's patch development in tyrosine kinase RET mutants.

a, Expression of tyrosine kinase RET in the intestine by E14.5. Results show RET expression on GFP^+CD4^+ (left) and GFP^+CD11c^+ (right) cells. Dotted lines show negative control staining. No other RET^+ cells were detected among GFP^+ cells (Supplementary Fig. 3b); $CD11c^+RET^+$ positive cells do not express *Sox10* or *Mash1*, which are highly expressed in neural crest cells (not shown). **b**, E16.5 and E17.5 intestines from RET -deficient embryos ($Ret^{-/-}$) and wild-type (WT) littermate controls were fixed and whole-mount stained with monoclonal CD4 antibodies. Whole-mount stainings were analysed by stereo and confocal microscopy ($\times 10$ objective) for Peyer's patch development. Confocal images of mid-gut from wild-type and $Ret^{-/-}$ embryos are shown. Grey, intestine structure; green, CD4. The same patterns were obtained in six independent experiments. Number of analysed embryos were: wild type and $Ret^{+/+}$, $n = 18$; $Ret^{-/-}$, $n = 10$. Error bars show s.d. **c**, E15.5 intestines from $Ret^{-/-}$ and wild-type littermate controls were purified as in Fig. 2a and cell suspensions analysed by flow cytometry analysis. $CD4$, $CD11c$ and $IL7R\alpha$ expression is shown on $CD45^+$ haematopoietic gated cells. **d**, Intestines from $Ret^{51/51}$ adults and wild-type littermate controls were analysed by stereo microscopy and Peyer's patches counted. Left panels, number of Peyer's patches in $Ret^{51/51}$ and wild-type mice. Wild type, $n = 5$; $Ret^{51/51}$, $n = 5$; two-tailed t -test $P = 0.004$. Error bars show s.d. Right panels, flow cytometry analysis of Peyer's patches from $Ret^{51/51}$ and wild-type adult mice. **e**, E17.5 intestines from $Ret^{51/51}$ embryos and wild-type littermate controls were analysed as in Fig. 3b. Grey, intestine structure; green, CD4.

and coalesce to form enteric ganglia. Because the receptor tyrosine kinase RET has a key role in the formation of the mammalian enteric nervous system², we examined whether CD45⁺GFP⁺ cells in the gut lymphoid tissue primordia also express this receptor. Using a monoclonal antibody against RET we show that ~40% of the CD4⁺CD3⁺IL7R α ⁺c-Kit⁺CD11c⁺ cells found in the embryonic gut are also positive for this receptor (Fig. 3a). These results were further confirmed by indirect immunofluorescence of whole-mount gut preparations and RNA expression (Supplementary Figs 1d and 3a).

To assess the functional role of RET expressed in CD4⁺CD3⁺IL7R α ⁺c-Kit⁺CD11c⁺ cells of the gut, we examined formation of Peyer's patches primordia in the intestines of E16.5 and E17.5 embryos homozygous for a severe loss-of-function mutation in *Ret* (*Ret*^{-/-})². Compared with wild-type or heterozygous (*Ret*^{+/-}) littermates, E17.5 *Ret*^{-/-} embryos show an absence of Peyer's patch primordia (Fig. 3b). Despite the absence of Peyer's patches, CD4⁺LTi cells were detectable in the gut wall of *Ret*^{-/-} embryos at this stage (Fig. 3b). Moreover, fluorescence-activated cell sorting (FACS) analysis of haematopoietic cells from the gut of E15.5 *Ret*^{-/-} and wild-type littermates revealed no differences in the relative frequency or phenotype of the recovered cells (Fig. 3c), indicating that *Ret*^{-/-} mice have a full complement of gut LTi cells. We therefore suggest that the primary defect in Peyer's patch primordia formation in *Ret*^{-/-} mice is not due to the absence of haematopoietic subpopulations, but rather to their failure to aggregate.

To examine whether the absence of Peyer's patches in *Ret*^{-/-} mutants is secondary to the failure of enteric nervous system formation in these embryos, we analysed mice homozygous for a hypomorphic allele of *Ret* (*Ret*^{51/51}), which results in distal colonic aganglionosis, but an apparently normoganglionic small intestine (where Peyer's patches are located)²⁵. Despite the presence of a normal complement of enteric ganglia in the small intestine, the number of Peyer's patches in adult *Ret*^{51/51} animals is significantly reduced compared with wild-type or heterozygous (*Ret*^{+51/51}) littermates (Fig. 3d), suggesting that the Peyer's patches phenotype observed in *Ret*^{-/-} animals is not secondary to enteric nervous system deficits. Peyer's patches in *Ret*^{51/51} animals formed at approximately the right time during embryogenesis (Fig. 3e) and had normal size, their overall organization and cell type content was similar to that in control animals (Fig. 3d; Supplementary Fig. 4). These results argue against the idea that the absence of Peyer's patches in *Ret*^{-/-} mice is due to a delay in the timing of Peyer's patch primordia formation and suggest that RET signalling has a crucial role in the early events of nucleation of the Peyer's patch primordium rather than controlling later events related to the organization and maintenance of the structure.

Previous studies have established that neural crest proliferation and migration within the gut wall depends on the cell autonomous activation of RET by stroma-derived glial-cell-line-derived neurotrophic factor (GDNF) and its co-receptor GFR α 1 (refs 26–28). Perinatal mice homozygous for null alleles of *Gdnf* (*Gdnf*^{-/-}) and *Gfra1* (*Gfra1*^{-/-}) showed that neither GDNF nor GFR α 1 are implicated in Peyer's patch formation, because mice deficient in these molecules develop a normal complement of Peyer's patches (Supplementary Fig. 5). In addition, these studies provide further evidence that RET signalling is independently required within the neural crest and lymphoid lineages. Expression analysis of the genes encoding the other RET ligands revealed that both *Artn* and *Nrtn* (but not *Pspn*) were expressed by non-haematopoietic stroma cells within the gut wall (Fig. 4a; Supplementary Fig. 3a). Importantly, *Artn* was expressed in VCAM1⁺ gut stromal cells, which include the LTi and blood vessel endothelial cells (Fig. 4a). Because it has been previously shown that ARTN is not produced by endothelial cells²⁹, this finding indicates that the VCAM1⁺ LTi cells may be the main source of the ligand that is responsible for RET signalling in gut lymphoid tissue. Assessing Peyer's patch formation in mice homozygous for a null mutation in *Gfra3* (*Gfra3*^{-/-}), the locus encoding the main co-receptor for ARTN, showed that *Gfra3*^{-/-} animals have significantly fewer, albeit well-formed, Peyer's patches

(Fig. 4b, c; Supplementary Fig. 4), suggesting that the ARTN/GFR α 3/RET signalling axis is involved in gut lymphoid organogenesis. However, because the phenotype observed in *Gfra3*^{-/-} mice is partial, it is likely that in the absence of GFR α 3, other ligands (NRTN) and co-receptors (GFR α 2) that are expressed in the microenvironment of CD4⁺CD3⁺IL7R α ⁺c-Kit⁺CD11c⁺RET⁺ cells, may also contribute to Peyer's patch primordia formation.

Further evidence that ARTN/RET interactions have a role in the mobility and aggregation of GFP haematopoietic cells was provided by *in vitro* organ culture experiments. When whole embryonic gut was incubated with agarose beads soaked in ARTN, large aggregates of GFP⁺ cells were formed in the vicinity of the beads (Fig. 4d, e). Remarkably, immunohistochemical staining of these aggregates revealed that, in addition to the expected CD11c⁺ cells, a large number of CD4⁺LTi cells were also found within these aggregates (Fig. 4e). Furthermore, upregulation of VCAM1 was also observed in presumably sessile mesenchymal cells in the vicinity of the cellular aggregates (Fig. 4e), altogether giving rise to an ectopic Peyer's patch primordium structure. Importantly, these ectopic structures were likely to be the exclusive product of GFP⁺ cell migration, because

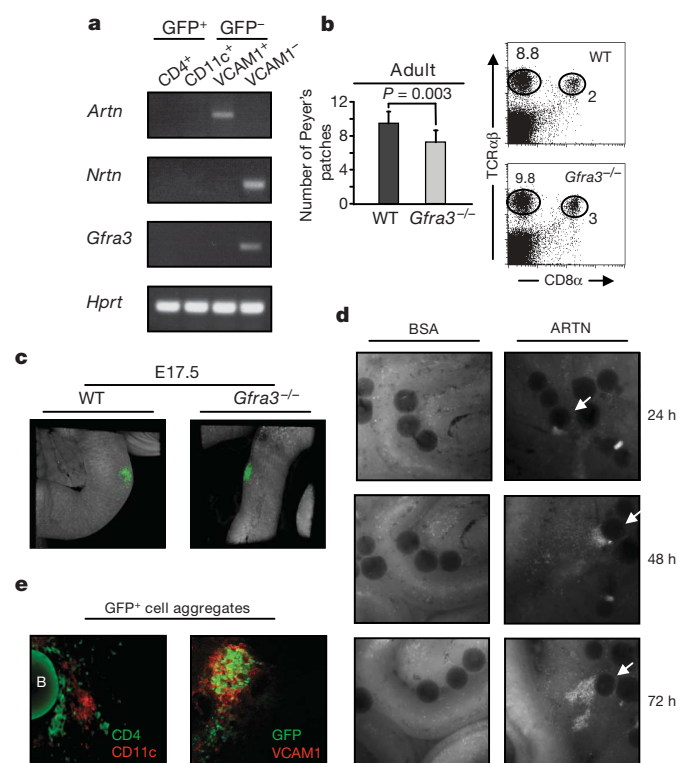


Figure 4 | RET/GFR α 3/ARTN signalling axis and Peyer's patch development. **a**, Cells from E15.5 intestines were purified as in Fig. 2a. Cell suspensions were sorted by flow cytometry for different cell populations and expression analysis carried out by RT-PCR. **b**, Intestines from *Gfra3*^{-/-} adults and wild-type littermate controls were analysed by stereo microscopy and Peyer's patches counted. Left panel, number of Peyer's patches in *Gfra3*^{-/-} and wild-type mice. Wild type, $n = 10$; *Gfra3*^{-/-}, $n = 8$; two-tailed t -test, $P = 0.003$. Error bars show s.d. Right panels, flow cytometry analysis of Peyer's patch cells from *Gfra3*^{-/-} and wild-type adult mice. **c**, E17.5 intestines from *Gfra3*^{-/-} embryos and wild-type littermate controls were analysed as in Fig. 3b. Grey, intestine structure; green, CD4. **d**, E15.5 GFP⁺ intestines were cultured *in vitro* with agarose beads impregnated with BSA (left) or ARTN recombinant protein (right). Analysis was performed over 72 h by stereo microscopy ($\times 1.6$ objective). Arrows show the same individual bead over time. Similar results were obtained in more than five independent experiments. **e**, GFP⁺ cell aggregates were obtained as described in Fig. 4d. Images were obtained using confocal microscopy ($\times 40$ objective). Left panel, CD4 (green) and CD11c (red) staining. B, agarose bead. Right panel, GFP (green) and VCAM1 (red).

no GFP⁺BrdU⁺ cells were detected in this assay (Supplementary Fig. 6).

Our data demonstrate that RET signalling is required during embryogenesis for the development of secondary lymphoid structures of the gut and provide evidence that ARTN/GFR α 3 is at least one of the critical regulators of RET-dependent Peyer's patch primordia formation. Our data also suggest that RET is required for the proper migratory behaviour of haematopoietic cells during embryogenesis. This suggestion is based on the observed motility of enteric GFP⁺ cells and the ability of ARTN to promote the formation of large ectopic aggregates of GFP⁺ expressing cells in gut explants.

It is possible that RET activation in CD4⁺CD3⁺IL7R α ⁺c-Kit⁺CD11c⁺RET⁺ cells may result in direct or indirect lymphotoxin β production (Fig. 2b) leading to the stimulation of LT α cells through their LT β R. Likewise, the ability to produce and respond to chemokines might also be modulated by RET signalling. The results presented here are consistent with the hypothesis that signalling via RET activates a gene expression programme empowering the haematopoietic cells to respond to and affect the rest of the cells required for Peyer's patch development, including other LT α and LT α cells. Interestingly, B and T lymphocytes have been also reported to express RET³⁰, but the functional significance of this expression is unclear.

We propose that RET/ligand interactions are part of the initiating event that leads to the subsequent formation of the Peyer's patch primordium. In this context, the aggregation is the result of a cascade of events triggered by the chance interaction of the randomly moving CD4⁺CD3⁺IL7R α ⁺c-Kit⁺CD11c⁺RET⁺ cells with stroma elements leading to the attraction of CD4⁺CD3⁺IL7R α ⁺c-Kit⁺ LT α cells and subsequent organization into secondary lymphoid organ primordia. The frequency of such an event occurring would be dependent on the numbers of the different cellular participants and their motility, as well as on the concentration of the different soluble factors. Such a model is consistent with the fact that Peyer's patches do not form in fixed sites along the gut, whereas their number is fairly constant in normal mice. Because the aggregation of the cells is taking place within 24 h (between E15.5 and E16.5), it is very likely that the onset of expression of a particular receptor or ligand, or the appearance (or maturation) of a cellular component during that period is the rate-limiting step. Our results indicate that CD4⁺CD3⁺IL7R α ⁺c-Kit⁺CD11c⁺ cells may have a decisive role in this rate-limiting step, because their partial ablation results in a reduction of Peyer's patch formation and deficiency in RET (expressed by these cells) results in absence of Peyer's patches.

The findings presented in this paper provide evidence that molecular mechanisms that have been historically ascribed to one specific tissue development may be used more generally to orchestrate the global development of organs containing structures derived from diverse germ layers. In the present case, the RET signalling pathway thought to be essential for the development of the enteric nervous system is now revealed also to be critical for the formation of an enteric haematopoietic organ such as Peyer's patches. Thus, by regulating both developmental processes RET emerges as a key molecule in the orchestration of intestine organogenesis.

METHODS

Mice. Human CD2–GFP transgenic mice³¹, CD11c–DTR–GFP transgenic mice²⁴, Ret^{−/−} B10 (ref. 2), Ret^{31/51} (ref. 2), Gfra1^{−/−} (ref. 28), Gdnf^{−/−} (ref. 27) and Gfra3^{−/−} (ref. 32) mice were previously described. All mice were bred at NIMR animal facilities.

Stereo and time-lapse microscopy. Stereo microscopy was performed using a Zeiss M2Bio (Carl Zeiss) stereo-fluorescent microscope. Pictures were taken using an Orca ER (Hamamatsu) camera and Openlab software (Improvision). Peyer's patches of adult mice were counted using a 1.6 \times objective because the size of these structures, around 2 mm, allows a clear identification at such low magnifications. Analysis of GFP expression was done using a green filter cube (emission, 525 nm) (Krammer scientific). Time-lapse microscopy was performed using the above specified stereo fluorescence microscope. Still

pictures were taken every 30 s for 25 min. Movie sequences and cell tracking was done using Velocity software (Improvision).

Confocal microscopy and whole-mount staining. Embryonic intestines were micro dissected at different developmental stages using a stereo microscope. Intestines were fixed in 4% PFA at room temperature for 20 min and then stained using antibodies listed in Supplementary Methods 1. Samples were optically cleared in BABB (Sigma) and acquired on a Leica SP2 microscope (Leica microsystems) using a 10 \times /0.4 numerical aperture objective lens. Serial optical sections from whole-mount stained small intestines were taken. Three-dimensional reconstruction of images was achieved using Velocity software (Improvision) and snapshot pictures were obtained from the three-dimensional images.

Cellular analysis, flow cytometry and RT–PCR analysis. Embryonic intestines were micro-dissected at different developmental stages using a stereo microscope and further digested with collagenase H (Roche). Reverse transcription and PCR (RT–PCR) reactions were carried out using reagents described elsewhere³³. Detailed information on protocols and reagents can be found in Supplementary Methods 1 and 2.

In vitro aggregation assays. E15.5 intestines were micro-dissected from human CD2–GFP mice. Whole intestines were cultured *in vitro* at 37 °C and incubated with agarose beads impregnated overnight with 200 ng μ l^{−1} of recombinant ARTN (PreproTech EC) or BSA (Sigma). Pictures were taken using the stereo microscope described above.

Received 26 October 2006; accepted 15 January 2007.

Published online 25 February 2007.

- Mebius, R. E. Organogenesis of lymphoid tissues. *Nature Rev. Immunol.* **3**, 292–303 (2003).
- Schuchardt, A., D'Agati, V., Larsson-Blomberg, L., Costantini, F. & Pachnis, V. Defects in the kidney and enteric nervous system of mice lacking the tyrosine kinase receptor Ret. *Nature* **367**, 380–383 (1994).
- Adachi, S., Yoshida, H., Kataoka, H. & Nishikawa, S. Three distinctive steps in Peyer's patch formation of murine embryo. *Int. Immunol.* **9**, 507–514 (1997).
- Adachi, S. *et al.* Essential role of IL-7 receptor α in the formation of Peyer's patch anlage. *Int. Immunol.* **10**, 1–6 (1998).
- Yoshida, H. *et al.* IL-7 receptor α ⁺ CD3[−] cells in the embryonic intestine induces the organizing center of Peyer's patches. *Int. Immunol.* **11**, 643–655 (1999).
- Wang, J. H. *et al.* Selective defects in the development of the fetal and adult lymphoid system in mice with an Ikaros null mutation. *Immunity* **5**, 537–549 (1996).
- Kurebayashi, S. *et al.* Retinoid-related orphan receptor γ (ROR γ) is essential for lymphoid organogenesis and controls apoptosis during thymopoiesis. *Proc. Natl Acad. Sci. USA* **97**, 10132–10137 (2000).
- Yokota, Y. *et al.* Development of peripheral lymphoid organs and natural killer cells depend on the helix–loop–helix inhibitor Id2. *Nature* **397**, 702–706 (1999).
- Kim, D. *et al.* Regulation of peripheral lymph node genesis by the tumor necrosis factor family member TRANCE. *J. Exp. Med.* **192**, 1467–1478 (2000).
- Kong, Y. Y. *et al.* OPGL is a key regulator of osteoclastogenesis, lymphocyte development and lymph-node organogenesis. *Nature* **397**, 315–323 (1999).
- Dougall, W. C. *et al.* RANK is essential for osteoclast and lymph node development. *Genes Dev.* **13**, 2412–2424 (1999).
- Forster, R. *et al.* A putative chemokine receptor, BLR1, directs B cell migration to defined lymphoid organs and specific anatomic compartments of the spleen. *Cell* **87**, 1037–1047 (1996).
- Ansel, K. M. *et al.* A chemokine-driven positive feedback loop organizes lymphoid follicles. *Nature* **406**, 309–314 (2000).
- Banks, T. A. *et al.* Lymphotoxin- α -deficient mice. Effects on secondary lymphoid organ development and humoral immune responsiveness. *J. Immunol.* **155**, 1685–1693 (1995).
- De Togni, P. *et al.* Abnormal development of peripheral lymphoid organs in mice deficient in lymphotoxin. *Science* **264**, 703–707 (1994).
- Futterer, A., Mink, K., Luz, A., Kosco-Vilbois, M. H. & Pfeffer, K. The lymphotoxin β receptor controls organogenesis and affinity maturation in peripheral lymphoid tissues. *Immunity* **9**, 59–70 (1998).
- Koni, P. A. *et al.* Distinct roles in lymphoid organogenesis for lymphotoxins α and β revealed in lymphotoxin β -deficient mice. *Immunity* **6**, 491–500 (1997).
- Park, S. Y. *et al.* Developmental defects of lymphoid cells in Jak3 kinase-deficient mice. *Immunity* **3**, 771–782 (1995).
- Cao, X. *et al.* Defective lymphoid development in mice lacking expression of the common cytokine receptor gamma chain. *Immunity* **2**, 223–238 (1995).
- Coles, M. C. *et al.* Role of T and NK cells and IL7/IL7r interactions during neonatal maturation of lymph nodes. *Proc. Natl Acad. Sci. USA* **103**, 13457–13462 (2006).
- Hashi, H. *et al.* Compartmentalization of Peyer's patch anlagen before lymphocyte entry. *J. Immunol.* **166**, 3702–3709 (2001).
- Rennett, P. D., Browning, J. L., Mebius, R., Mackay, F. & Hochman, P. S. Surface lymphotoxin α / β complex is required for the development of peripheral lymphoid organs. *J. Exp. Med.* **184**, 1999–2006 (1996).

23. Alimzhanov, M. B. *et al.* Abnormal development of secondary lymphoid tissues in lymphotoxin β -deficient mice. *Proc. Natl Acad. Sci. USA* **94**, 9302–9307 (1997).
24. Jung, S. *et al.* *In vivo* depletion of CD11c⁺ dendritic cells abrogates priming of CD8⁺ T cells by exogenous cell-associated antigens. *Immunity* **17**, 211–220 (2002).
25. de Graaff, E. *et al.* Differential activities of the RET tyrosine kinase receptor isoforms during mammalian embryogenesis. *Genes Dev.* **15**, 2433–2444 (2001).
26. Pichel, J. G. *et al.* Defects in enteric innervation and kidney development in mice lacking GDNF. *Nature* **382**, 73–76 (1996).
27. Moore, M. W. *et al.* Renal and neuronal abnormalities in mice lacking GDNF. *Nature* **382**, 76–79 (1996).
28. Cacalano, G. *et al.* GFR α 1 is an essential receptor component for GDNF in the developing nervous system and kidney. *Neuron* **21**, 53–62 (1998).
29. Honma, Y. *et al.* Artemin is a vascular-derived neurotropic factor for developing sympathetic neurons. *Neuron* **35**, 267–282 (2002).
30. Vargas-Leal, V. *et al.* Expression and function of glial cell line-derived neurotrophic factor family ligands and their receptors on human immune cells. *J. Immunol.* **175**, 2301–2308 (2005).
31. de Boer, J. *et al.* Transgenic mice with hematopoietic and lymphoid specific expression of Cre. *Eur. J. Immunol.* **33**, 314–325 (2003).
32. Nishino, J. *et al.* GFR α 3, a component of the artemin receptor, is required for migration and survival of the superior cervical ganglion. *Neuron* **23**, 725–736 (1999).
33. Peixoto, A., Monteiro, M., Rocha, B. & Veiga-Fernandes, H. Quantification of multiple gene expression in individual cells. *Genome Res.* **14**, 1938–1947 (2004).

Supplementary Information is linked to the online version of the paper at www.nature.com/nature.

Acknowledgements The work described in this paper was funded by the Medical Research Council (MRC), UK. We thank C. Atkins and G. Preece for cell sorting; S. Pagakis, M. Tolaini, T. Norton and K. Williams for technical assistance. We also thank H. Hamada and J. Nishino for the GFR α 3 knockout mice. H.V.-F. and K.E.F. were supported by a grant from the European Union.

Author Information Reprints and permissions information is available at www.nature.com/reprints. The authors declare no competing financial interests. Correspondence and requests for materials should be addressed to D.K. (dkiouss@nimr.mrc.ac.uk).

LETTERS

Epithelial-cell-intrinsic IKK- β expression regulates intestinal immune homeostasis

Colby Zaph¹, Amy E. Troy¹, Betsy C. Taylor¹, Lisa D. Berman-Booty¹, Katherine J. Guild¹, Yurong Du¹, Evan A. Yost¹, Achim D. Gruber³, Michael J. May², Florian R. Greten⁴†, Lars Eckmann⁵, Michael Karin⁴ & David Artis¹

Intestinal epithelial cells (IECs) provide a primary physical barrier against commensal and pathogenic microorganisms in the gastro-intestinal (GI) tract, but the influence of IECs on the development and regulation of immunity to infection is unknown¹. Here we show that IEC-intrinsic I κ B kinase (IKK)- β -dependent gene expression is a critical regulator of responses of dendritic cells and CD4⁺ T cells in the GI tract. Mice with an IEC-specific deletion of IKK- β show a reduced expression of the epithelial-cell-restricted cytokine thymic stromal lymphopoietin in the intestine and, after infection with the gut-dwelling parasite *Trichuris*, fail to develop a pathogen-specific CD4⁺ T helper type 2 (T_H2) response and are unable to eradicate infection. Further, these animals show exacerbated production of dendritic-cell-derived interleukin-12/23p40 and tumour necrosis factor- α , increased levels of CD4⁺ T-cell-derived interferon- γ and interleukin-17, and develop severe intestinal inflammation. Blockade of proinflammatory cytokines during *Trichuris* infection ablates the requirement for IKK- β in IECs to promote CD4⁺ T_H2 cell-dependent immunity, identifying an essential function for IECs in tissue-specific conditioning of dendritic cells and limiting type 1 cytokine production in the GI tract. These results indicate that the balance of IKK- β -dependent gene expression in the intestinal epithelium is crucial in intestinal immune homeostasis by promoting mucosal immunity and limiting chronic inflammation.

The mucosal surface of the GI tract is a major site of pathogen entry, but the immune cells associated with the gut must remain hyporesponsive to food antigens and commensal bacteria or risk chronic inflammation. Despite this need for balance, the processes that orchestrate immune responses in the intestinal tract are still poorly defined. Previous studies *in vitro* have implicated IECs in the regulation of innate immunity and chronic inflammation, but a direct role for these cells in immunity to enteric pathogens has never been tested *in vivo*^{2–5}. We employed the *Trichuris muris* infection model to investigate the role of IECs in regulating CD4⁺ T-cell-mediated immunity and inflammation in the GI tract. *Trichuris* is a natural GI pathogen of mice and provides a model for human intestinal nematode infections that affect an estimated 1,000 million people worldwide⁶. *Trichuris*-specific CD4⁺ T_H2 cells that produce the cytokines interleukin (IL)-4, IL-5 and IL-13 are required to mediate resistance to infection, whereas interferon (IFN)- γ -producing T_H1 cells are associated with chronic infection and, in some circumstances, severe intestinal inflammation^{7–10}.

Trichuris lives in close association with the intestinal epithelium¹¹ and induces nuclear factor (NF)- κ B activation as measured by DNA-binding activity in IECs of the large intestine of genetically resistant mice (Fig. 1a). To determine whether IEC-intrinsic NF- κ B activation

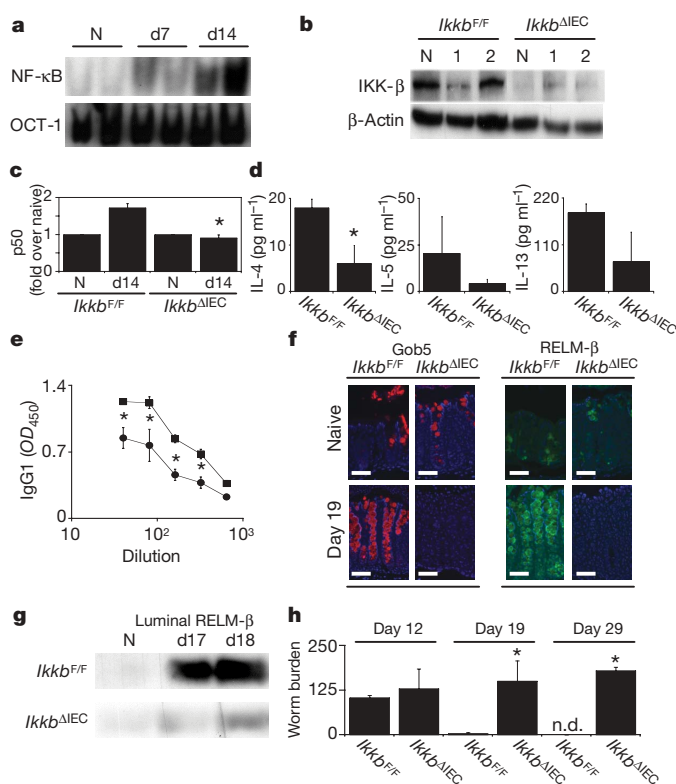


Figure 1 | IKK- β -dependent NF- κ B activation in IECs is required for adaptive immunity to *Trichuris*. **a**, Infection-induced NF- κ B activation in wild-type IECs from naive (N) and infected (days 7 and 14) animals. Assays were performed with either a consensus NF- κ B-binding site probe or an octamer binding protein-1 OCT-1 probe as a loading control. **b**, IKK- β expression in IECs from naive (N) and infected (1 and 2) control *Ikkb*^{F/F} or *Ikkb*^{ΔIEC} mice. **c**, NF- κ B activation in IECs from naive (N) or infected control *Ikkb*^{F/F} or *Ikkb*^{ΔIEC} mice determined by DNA capture ELISA. Data in **a–c** are representative of four to six individual animals from three independent experiments. **d**, *Trichuris*-specific cytokine responses after restimulation of mLN cells isolated from infected *Ikkb*^{F/F} and *Ikkb*^{ΔIEC} mice. **e**, *Trichuris*-specific serum IgG1 levels (squares, *Ikkb*^{F/F}; circles, *Ikkb*^{ΔIEC}). **f**, Gob5 and RELM- β expression in the caecum of naive or infected (day 19) *Ikkb*^{F/F} or *Ikkb*^{ΔIEC} mice. Scale bar, 50 μ m. **g**, Levels of secreted RELM- β isolated from faecal pellets of naive (N) and infected (days 17 and 18) *Ikkb*^{F/F} or *Ikkb*^{ΔIEC} mice. **h**, Worm burdens at days 12, 19 and 29 after infection. n.d., not detected. Asterisk, $P < 0.05$. Error bars indicate s.e.m. ($n = 4–6$).

¹Department of Pathobiology and ²Department of Animal Biology, University of Pennsylvania, Philadelphia, Pennsylvania 19104, USA. ³Department of Veterinary Pathology, Free University Berlin, 14163 Berlin, Germany. ⁴Laboratory of Gene Regulation and Signal Transduction, Department of Pharmacology, and ⁵Department of Medicine, University of California San Diego, La Jolla, California 92093, USA. †Present address: Second Department of Medicine, Technical University Munich, 81675 Munich, Germany.

influences immune responses in the GI tract, we examined the development of protective immunity in mice with an IEC-specific deletion of IKK- β (IKK- β /IKK-2). IKK- β is the catalytic subunit of the IKK complex responsible for NF- κ B activation through the canonical pathway¹². Mice in which the third exon of the *Ikkb* gene was flanked with *loxP* sites¹³ ('floxed' *Ikkb*; *Ikkb*^{F/F}) were crossed with mice expressing the Cre recombinase from the IEC-specific *villin* promoter to generate mice in which IKK- β was specifically deleted in IECs (*Ikkb* ^{Δ IEC} mice; Fig. 1b and refs 14–16). As a result, IECs isolated from *Ikkb* ^{Δ IEC} mice fail to exhibit NF- κ B activation after *Trichuris* infection (Fig. 1c). Analysis of the adaptive immune response revealed that, after infection, control *Ikkb*^{F/F} mice developed polarized *Trichuris*-specific CD4⁺ T_H2 responses characterized by increased production of IL-4, IL-5 and IL-13 after restimulation of draining mesenteric lymph node (mLN) cells with antigen (Fig. 1d). However, mLN cells isolated from infected *Ikkb* ^{Δ IEC} mice showed decreased expression of protective CD4⁺ T-cell-derived T_H2 cytokines (Fig. 1d and Supplementary Fig. 1a). Other parameters of type 2 immunity, including antibody isotype switching to IgG1 (Fig. 1e) and goblet cell responses, including hyperplasia (Supplementary Fig. 1b) and expression of Gob5 and RELM- β ^{17,18} (Fig. 1f, g), were impaired in the absence of IKK- β -dependent gene expression in IECs. Consistent with defective type 2 immune responses, *Ikkb* ^{Δ IEC} mice were susceptible to infection, failing to clear parasites from the GI tract (Fig. 1h). IEC-intrinsic expression of IKK- β -dependent genes is therefore a crucial component in the development of CD4⁺ T-cell-dependent protective immunity in the GI tract.

Results of studies *in vitro* have implicated cross-talk between IECs and intestinal dendritic cells (DCs) in influencing responses of DCs in the GI tract^{3,19,20}. To determine whether the dysregulated CD4⁺ T-cell response in infected *Ikkb* ^{Δ IEC} mice was due to aberrant IEC–DC interactions, the composition and function of DC subsets in the gut-associated lymphoid tissue of *Ikkb*^{F/F} or *Ikkb* ^{Δ IEC} mice was examined

after infection^{21,22}. Similar frequencies of CD11c⁺CD11b[−]CD8 α [−] (double-negative, DN), CD11c⁺CD11b[−]CD8 α ⁺ (CD8 α ⁺) and CD11c⁺CD11b⁺CD8 α [−] (CD11b⁺) DC subsets were observed in mLN of *Ikkb*^{F/F} and *Ikkb* ^{Δ IEC} mice before and after infection (Fig. 2a). Consistent with development of a protective type 2 response, no significant expression of the proinflammatory cytokines IL-12/23p40 or tumour necrosis factor (TNF)- α was observed by any DC subset isolated from infected *Ikkb*^{F/F} mice (Fig. 2b, and data not shown). In contrast, there was an increased frequency of DN and CD11b⁺ DCs expressing IL-12/23p40 and TNF- α in infected *Ikkb* ^{Δ IEC} mice (Fig. 2b). The increased proinflammatory cytokine production could have been due to a loss of epithelial barrier function, because NF- κ B controls the survival of IECs after exposure to sublethal doses of radiation or chemical inducers of colitis^{14,15}. However, there was no evidence for defective barrier integrity in naive or infected *Ikkb* ^{Δ IEC} mice (Supplementary Figs 2 and 3). These results therefore indicate that IEC-intrinsic IKK- β expression might have a crucial role in tissue-specific conditioning of DCs, specifically influencing the expression of proinflammatory cytokines independently of regulating barrier function.

To investigate which IKK- β -dependent genes within IECs could be responsible for dysregulated DC responses, we isolated RNA from the large intestine of naive *Ikkb*^{F/F} or *Ikkb* ^{Δ IEC} mice and analysed the expression of a panel of IEC-specific genes. Although we could not detect any significant differences in expression of the chemokines CCL6, CCL20 or CCL28 between naive and infected *Ikkb*^{F/F} or *Ikkb* ^{Δ IEC} mice (Supplementary Fig. 4), we observed significantly lower expression of the IEC-derived cytokine thymic stromal lymphopoietin (TSLP) in *Ikkb* ^{Δ IEC} mice both before and after infection with *Trichuris* (Fig. 2c, d). The murine *Tslp* promoter contains two NF- κ B-binding sites, which is consistent with a role for IKK- β in TSLP production²³. To address whether *Tslp* messenger RNA expression in IECs is dependent on NF- κ B activation, the murine

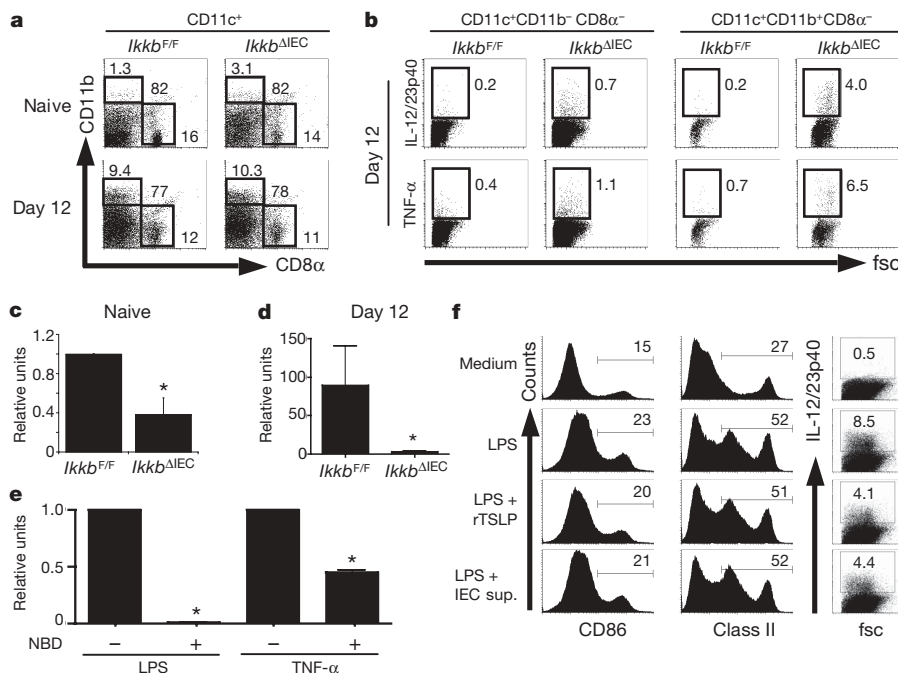


Figure 2 | Dysregulated dendritic cell responses in *Ikkb* ^{Δ IEC} mice after infection with *Trichuris* are associated with defective TSLP expression. **a**, Composition of the dendritic cell compartment in the mLN of naive and infected (day 12) *Ikkb*^{F/F} or *Ikkb* ^{Δ IEC} mice. **b**, IL-12/IL-23p40 and TNF- α production by CD11c⁺CD11b[−]CD8 α [−] or CD11c⁺CD11b⁺CD8 α [−] cells from the draining mLN of infected (day 12) *Ikkb*^{F/F} or *Ikkb* ^{Δ IEC} mice. **c**, **d**, *Tslp* mRNA levels in the intestine of naive (**c**) and infected (**d**) *Ikkb*^{F/F} or *Ikkb* ^{Δ IEC} mice. Results in **c** represent fold induction over naive *Ikkb*^{F/F} animals; results in **d** represent fold induction of infected *Ikkb*^{F/F} or *Ikkb* ^{Δ IEC} mice relative to

respective naive *Ikkb*^{F/F} or *Ikkb* ^{Δ IEC} controls. **e**, *Tslp* mRNA levels in CMT-93 cells after treatment with IKK inhibitor peptide (NBD) or vehicle (dimethylsulphoxide) before stimulation with LPS or TNF- α . **f**, Bone-marrow-derived DCs were stimulated with LPS in the presence or absence of supernatants (sup.) from the IEC line CMT-93 or rTSLP and analysed for expression of surface markers and production of IL-12/23p40. Fsc, forward scatter. Asterisk, $P < 0.05$. Error bars indicate s.e.m. Data are representative of four independent experiments.

IEC line CMT-93 was stimulated with lipopolysaccharide (LPS) or TNF- α in the presence or absence of a peptide inhibitor of the IKK complex²⁴. Stimulation of CMT-93 cells with LPS or TNF- α resulted in a fivefold and eightfold upregulation of *Tslp* mRNA by 24 h, respectively (data not shown). Treatment with the IKK inhibitor peptide NEMO-binding domain (NBD) resulted in a significant decrease in both LPS-induced and TNF- α -induced *Tslp* mRNA expression at 24 h after stimulation (Fig. 2e), indicating that IEC-intrinsic expression of TSLP might be regulated by IKK- β -dependent NF- κ B activation.

Interactions between TSLP and its receptor (TSLPR) have been implicated in driving type 2 responses, either by providing a positive signal to DCs that governs their ability to promote T_H2 cell differentiation or by limiting the production of proinflammatory cytokines that promote T_H1 or T_H17 cell differentiation²⁵. To determine whether IEC-derived products, including TSLP, could directly affect DC maturation and function, bone-marrow-derived DCs were activated with LPS in the presence or absence of either conditioned supernatants from a murine IEC line (CMT-93) or recombinant TSLP (rTSLP). The presence of IEC-conditioned supernatant or rTSLP had no effect on LPS-induced expression of CD86 or major histocompatibility complex class II (Fig. 2f, histograms). However, both IEC supernatant and rTSLP inhibited the production of LPS-induced IL-12/23p40 (Fig. 2f, dot plots). These data support the hypothesis that dysregulated IEC-intrinsic TSLP expression in *Ikkb*^{ΔIEC} mice contributes to heightened production of DC-derived proinflammatory cytokines.

Associated with decreased TSLP levels and enhanced expression of proinflammatory cytokines was a heightened expression of *Trichuris*-specific CD4⁺ T-cell-derived IFN- γ in infected *Ikkb*^{ΔIEC} mice (Fig. 3a). Single-cell analysis revealed that the increased IFN- γ secretion in culture supernatants was due to both a heightened frequency of IFN- γ ⁺ CD4⁺ T cells (Fig. 3a; *Ikkb*^{F/F}, 2.6%; *Ikkb*^{ΔIEC}, 6.1%) and increased IFN- γ production per cell (Fig. 3a; mean fluorescence intensity: *Ikkb*^{F/F}, 314; *Ikkb*^{ΔIEC}, 679). Increased production of IL-17, a cytokine implicated in the pathogenesis of several inflammatory conditions including chronic intestinal inflammation²⁶, was also detected in supernatants of antigen-restimulated mLN cells isolated from infected *Ikkb*^{ΔIEC} mice (Fig. 3b). Enhanced expression of proinflammatory cytokines in infected *Ikkb*^{ΔIEC} mice was accompanied by increased migration of B220⁺ and CD3⁺ lymphocytes into the intestine at day 19 after infection (Fig. 3c). Flow cytometric analysis of lamina propria cell populations showed increased frequencies of CD4⁺ and CD8⁺ T cells as well as CD19⁺ B cells in infected *Ikkb*^{ΔIEC} mice compared with infected *Ikkb*^{F/F} mice (Fig. 3d). The increased infiltration of lymphocytes into the lamina propria of infected *Ikkb*^{ΔIEC} mice at day 29 after infection was correlated with severe intestinal inflammation, disrupted crypt architecture, areas of focal ulceration and increased frequency of apoptotic IECs (Fig. 3e, and data not shown), which resulted in septicaemia (Fig. 3f). Thus, IEC IKK- β is critical for the delivery of signals that condition DCs in the gut to allow the development of CD4⁺ T_H2 responses and prevent intestinal inflammation.

The ability of TSLP to limit the expression of proinflammatory cytokines by DCs, and its reduced expression in *Ikkb*^{ΔIEC} mice, led to the hypothesis that IEC-intrinsic IKK- β -dependent expression of TSLP is necessary to limit the production of cytokines that drive non-protective type 1 responses rather than to promote the expression of T_H2 cytokines directly. To test this, we used monoclonal antibodies to block the proinflammatory cytokines IL-12, IL-23 and IFN- γ in *Trichuris*-infected *Ikkb*^{ΔIEC} mice. This resulted in a decreased expression of antigen-specific IL-12-dependent IFN- γ and IL-23-dependent IL-17, and a concomitant increase in *Trichuris*-specific IL-13 after restimulation of cells isolated from mLN of treated *Ikkb*^{ΔIEC} mice (Fig. 4a, compare Ctrl with Tx). Consistent with increased type 2 and decreased type 1 cytokines, levels of *Trichuris*-specific IgG2a, an IFN- γ -dependent antibody isotype, were decreased in infected *Ikkb*^{ΔIEC} mice after treatment with monoclonal antibodies (Fig. 4b).

In addition, blockade of IL-12, IL-23 and IFN- γ recovered goblet cell responses (Supplementary Fig. 5a), increased the expression of Gob5 and RELM- β (Fig. 4c and Supplementary Fig. 5b) and resulted in resistance to infection (Fig. 4d). The recovery of immunity in *Ikkb*^{ΔIEC} mice after blockade of proinflammatory cytokines shows that IEC-intrinsic IKK- β expression is not absolutely required for the promotion of type 2 immunity. Rather, IKK- β -dependent genes—including *Tslp*—seem to be a critical component of homeostatic processes that limit type 1 cytokine responses in the GI micro-environment. To test this hypothesis, DCs were isolated from the GI tract of mice deficient in TSLPR (*Tpte2*^{-/-} mice). Consistent with a role for TSLP–TSLPR interactions in limiting DC proinflammatory cytokine production, there was an increased frequency (Fig. 4e) and absolute number (Fig. 4f) of DN and CD11b⁺ DCs that expressed IL-12/23p40 in *Tpte2*^{-/-} mice compared with controls. Similarly to results observed in *Trichuris*-infected *Ikkb*^{ΔIEC} mice, mLN cells isolated from infected *Tpte2*^{-/-} mice produced significantly higher levels of antigen-specific IFN- γ (Fig. 4g). Other parameters of type 2 immunity, including *Trichuris*-specific serum IgG1 levels (Fig. 4h) and goblet cell hyperplasia (Fig. 4i), were also defective in *Tpte2*^{-/-} mice. In addition,

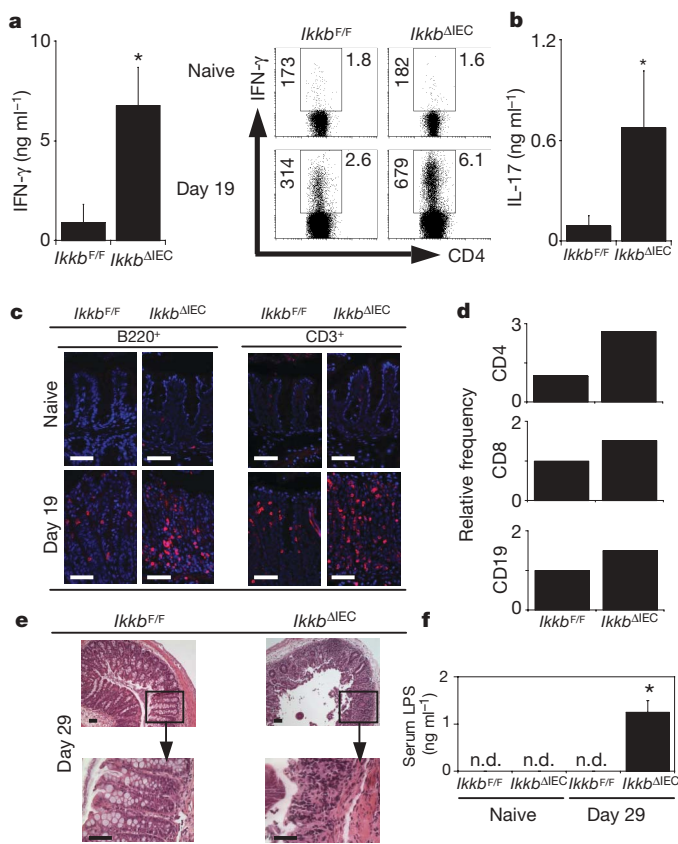


Figure 3 | *Ikkb*^{ΔIEC} mice show exacerbated pathogen-specific IFN- γ and IL-17 responses and severe intestinal inflammation after infection with *Trichuris*. **a, b**, *Trichuris*-specific IFN- γ (**a**) and IL-17 (**b**) responses after restimulation of cells isolated from mLN of naive and infected (day 19) *Ikkb*^{F/F} or *Ikkb*^{ΔIEC} mice. **c, d**, Cell infiltration in the caecal mucosa of naive and infected *Ikkb*^{F/F} or *Ikkb*^{ΔIEC} mice determined by immunofluorescent staining for B220 or CD3 (**c**) and by flow cytometry of isolated lamina propria cells (**d**). Scale bar, 50 μ m. Data in **d** represent the relative increase in frequency of CD4⁺, CD8⁺ and CD19⁺ cells in infected *Ikkb*^{ΔIEC} mice by comparison with infected *Ikkb*^{F/F} mice. **e**, Intestinal inflammation detected by haematoxylin/eosin staining of caecal sections isolated from infected *Ikkb*^{F/F} or *Ikkb*^{ΔIEC} mice on day 29 after infection. Scale bar, 50 μ m. **f**, Serum LPS levels were determined by *Limulus* amoebocyte lysis (LAL) assay on samples from naive and infected *Ikkb*^{F/F} and *Ikkb*^{ΔIEC} mice on day 29 after infection. n.d., not detected. Asterisk, $P < 0.05$. Error bars indicate s.e.m. Data are representative of two to four independent experiments ($n = 4-6$).

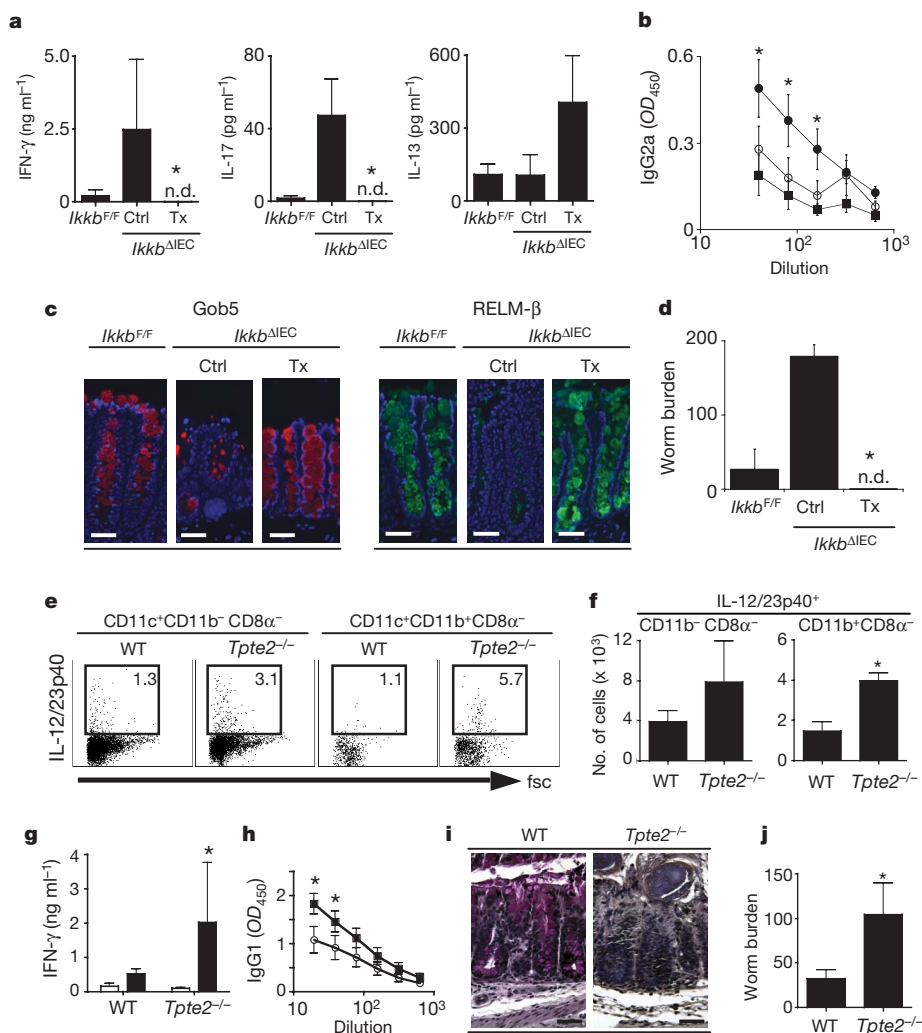


Figure 4 | IEC-intrinsic IKK-β is required for limiting proinflammatory cytokine responses in the GI tract. **a**, *Trichuris*-specific cytokine responses after restimulation of cells isolated from mLN of *Trichuris*-infected *Ikkb*^{F/F} mice, infected *Ikkb*^{ΔIEC} mice treated with control immunoglobulin (Ctrl), and infected *Ikkb*^{ΔIEC} mice treated with monoclonal antibodies against IL-12/IL-23p40 and IFN-γ (Tx) mice. **b**, *Trichuris*-specific serum IgG2a (filled squares, infected *Ikkb*^{F/F} mice; filled circles, infected *Ikkb*^{ΔIEC} mice; open circles, infected *Ikkb*^{ΔIEC} Tx mice). **c**, Gob5 or RELM-β expression in the caecum of infected *Ikkb*^{F/F}, *Ikkb*^{ΔIEC} and *Ikkb*^{ΔIEC} Tx mice on day 19 after infection. **d**, Worm burdens at day 19 after infection. n.d., not detected.

Tpte2^{-/-} mice were susceptible to infection with *Trichuris*, failing to expel worms as rapidly as wild-type mice (Fig. 4j). Thus, TSLP–TSLPR interactions are crucial for the development of protective type 2 immunity against *Trichuris*.

Taken together, these studies reveal a previously unrecognized role of IEC-derived factors in the regulation of intestinal immune homeostasis after exposure to a pathogen of the GI tract. Specifically, in addition to established pathways involved in pathogen recognition and the initiation of immune responses in the GI tract, which include M cells and specialized DC subsets that directly sample the luminal environment^{27,28}, results presented here support a role for IECs in directly influencing innate and adaptive immunity in the gut. Harnessing IKK-β-dependent functions of IECs will be an important consideration in the design and delivery of both anti-inflammatory agents and vaccines that target mucosal sites.

METHODS

Mice, parasites, antigens and infections. Animals were maintained in a specific-pathogen-free environment and tested negative for pathogens in routine

e, DC responses in the caecal patch of wild-type (WT) and *Tpte2*^{-/-} mice. **f**, Absolute number of IL-12/23p40⁺ DC subsets in the mLN of naive WT and *Tpte2*^{-/-} mice. **g**, *Trichuris*-specific cytokine responses from infected WT and *Tpte2*^{-/-} mice. Open bars, medium; filled bars, antigen. **h**, *Trichuris*-specific serum IgG1 levels (squares, WT; circles, *Tpte2*^{-/-}). **i**, Goblet cell hyperplasia in the caecum of infected WT and *Tpte2*^{-/-} mice. Bar, 50 μm. **j**, Worm burdens at day 21 after infection. Asterisk, *P* < 0.05. Error bars indicate s.e.m. Data are representative of two experiments (*n* = 4–8).

screening. All experiments were performed at the University of Pennsylvania and University of California at San Diego in accordance with institutional guidelines. Mice were infected with 150–200 *Trichuris* eggs.

Cell culture, cytokine analysis and flow cytometry. Cells from naive or infected mice were plated in medium alone or in the presence of *T. muris* ES Ag (50 μg ml⁻¹), caecal bacterial antigen (100 μg ml⁻¹), LPS (10 ng ml⁻¹) or anti-CD3/CD28 (1 μg ml⁻¹; eBioscience). In some cases mLN cells were labelled with carboxyfluorescein succinimidyl ester (Molecular Probes) before stimulation. Cell-free supernatants were harvested and analysed for cytokine secretion by sandwich enzyme-linked immunosorbent assay (ELISA) or for intracellular cytokines by flow cytometry. Bone-marrow-derived DCs were conditioned for 16 h in the presence or absence of IEC-conditioned medium (CMT-93 cells) or TSLP (100 ng ml⁻¹; R&D Systems), before stimulation. IECs and LPLs were isolated and analysed *ex vivo* by flow cytometry. Gene expression was analysed by real-time polymerase chain reaction with the use of SYBR Green chemistry.

Analysis of IKK-β expression and NF-κB activation. Whole-cell extracts from IECs of naive or infected mice were analysed by SDS–polyacrylamide gel electrophoresis (PAGE) followed by immunoblotting with anti-IKK-β antibody (Cell Signalling). Extracts were analysed for DNA binding by ELISA (Pierce) or electrophoretic mobility-shift assay.

Serum immunoglobulin and LPS analysis. Serum was analysed for *Trichuris*-specific IgG1 and IgG2a by ELISA and for LPS by *Limulus* amoebocyte lysis assay (Sigma).

Goblet cell and RELM- β responses. For the detection of intestinal goblet cells, paraffin-embedded sections were stained with Alcian blue–periodic acid Schiff's reagent. Equal amounts of protein isolated from faecal pellets (20 μ g) were analysed by SDS–PAGE and immunoblotted for RELM- β with a polyclonal rabbit anti-murine RELM- β antibody (Peprotech).

Statistical analysis. Results are shown as means \pm s.e.m. for individual animals or conditions. Statistical significance was determined by Student's *t*-test (when comparing two groups) or analysis of variance with a post hoc test (when comparing more than two groups). Results were considered significant at $P < 0.05$.

Received 16 November 2006; accepted 11 January 2007.

Published online 25 February 2007.

- Nagler-Anderson, C. Man the barrier! Strategic defences in the intestinal mucosa. *Nature Rev. Immunol.* **1**, 59–67 (2001).
- Neish, A. S. *et al.* Prokaryotic regulation of epithelial responses by inhibition of I κ B α ubiquitination. *Science* **289**, 1560–1563 (2000).
- Rimoldi, M. *et al.* Intestinal immune homeostasis is regulated by the crosstalk between epithelial cells and dendritic cells. *Nature Immunol.* **6**, 507–514 (2005).
- Karin, M., Lawrence, T. & Nizet, V. Innate immunity gone awry: linking microbial infections to chronic inflammation and cancer. *Cell* **124**, 823–835 (2006).
- Rakoff-Nahoum, S., Paglino, J., Eslami-Varzaneh, F., Edberg, S. & Medzhitov, R. Recognition of commensal microflora by Toll-like receptors is required for intestinal homeostasis. *Cell* **118**, 229–241 (2004).
- Bethony, J. *et al.* Soil-transmitted helminth infections: ascariasis, trichuriasis, and hookworm. *Lancet* **367**, 1521–1532 (2006).
- Cliffe, L. J. & Grencis, R. K. The *Trichuris muris* system: a paradigm of resistance and susceptibility to intestinal nematode infection. *Adv. Parasitol.* **57**, 255–307 (2004).
- Owyang, A. M. *et al.* Interleukin 25 regulates type 2 cytokine-dependent immunity and limits chronic inflammation in the gastrointestinal tract. *J. Exp. Med.* **203**, 843–849 (2006).
- Schopf, L. R., Hoffmann, K. F., Cheever, A. W., Urban, J. F. Jr & Wynn, T. A. IL-10 is critical for host resistance and survival during gastrointestinal helminth infection. *J. Immunol.* **168**, 2383–2392 (2002).
- Artis, D. *et al.* Differential requirement for NF- κ B family members in control of helminth infection and intestinal inflammation. *J. Immunol.* **169**, 4481–4487 (2002).
- Tilney, L. G., Connelly, P. S., Guild, G. M., Vranich, K. A. & Artis, D. Adaptation of a nematode parasite to living within the mammalian epithelium. *J. Exp. Zool. A Comp. Exp. Biol.* **303**, 927–945 (2005).
- Ghosh, S. & Karin, M. Missing pieces in the NF- κ B puzzle. *Cell* **109** (Suppl.) S81–S96 (2002).
- Li, Z. W., Omori, S. A., Labuda, T., Karin, M. & Rickert, R. C. IKK β is required for peripheral B cell survival and proliferation. *J. Immunol.* **170**, 4630–4637 (2003).
- Egan, L. J. *et al.* I κ B-kinase β -dependent NF- κ B activation provides radioprotection to the intestinal epithelium. *Proc. Natl Acad. Sci. USA* **101**, 2452–2457 (2004).
- Greten, F. R. *et al.* IKK β links inflammation and tumorigenesis in a mouse model of colitis-associated cancer. *Cell* **118**, 285–296 (2004).
- Chen, L. W. *et al.* The two faces of IKK and NF- κ B inhibition: prevention of systemic inflammation but increased local injury following intestinal ischemia-reperfusion. *Nature Med.* **9**, 575–581 (2003).
- Artis, D. *et al.* RELM β /FIZZ2 is a goblet cell-specific immune-effector molecule in the gastrointestinal tract. *Proc. Natl Acad. Sci. USA* **101**, 13596–13600 (2004).
- Zhou, Y. *et al.* Characterization of a calcium-activated chloride channel as a shared target of Th2 cytokine pathways and its potential involvement in asthma. *Am. J. Respir. Cell Mol. Biol.* **25**, 486–491 (2001).
- Kelsall, B. L. & Leon, F. Involvement of intestinal dendritic cells in oral tolerance, immunity to pathogens, and inflammatory bowel disease. *Immunol. Rev.* **206**, 132–148 (2005).
- Rescigno, M. *et al.* Dendritic cells express tight junction proteins and penetrate gut epithelial monolayers to sample bacteria. *Nature Immunol.* **2**, 361–367 (2001).
- Iwasaki, A. & Kelsall, B. L. Localization of distinct Peyer's patch dendritic cell subsets and their recruitment by chemokines macrophage inflammatory protein (MIP)-3 α , MIP-3 β , and secondary lymphoid organ chemokine. *J. Exp. Med.* **191**, 1381–1394 (2000).
- Iwasaki, A. & Kelsall, B. L. Unique functions of CD11b $^{+}$, CD8 α^{+} , and double-negative Peyer's patch dendritic cells. *J. Immunol.* **166**, 4884–4890 (2001).
- Li, M. *et al.* Topical vitamin D3 and low-calcemic analogs induce thymic stromal lymphopoietin in mouse keratinocytes and trigger an atopic dermatitis. *Proc. Natl Acad. Sci. USA* **103**, 11736–11741 (2006).
- May, M. J. *et al.* Selective inhibition of NF- κ B activation by a peptide that blocks the interaction of NEMO with the I κ B kinase complex. *Science* **289**, 1550–1554 (2000).
- Ziegler, S. F. & Liu, Y. J. Thymic stromal lymphopoietin in normal and pathogenic T cell development and function. *Nature Immunol.* **7**, 709–714 (2006).
- Weaver, C. T., Harrington, L. E., Mangan, P. R., Gavrieli, M. & Murphy, K. M. Th17: an effector CD4 T cell lineage with regulatory T cell ties. *Immunity* **24**, 677–688 (2006).
- Niess, J. H. *et al.* CX3CR1-mediated dendritic cell access to the intestinal lumen and bacterial clearance. *Science* **307**, 254–258 (2005).
- Jang, M. H. *et al.* Intestinal villous M cells: an antigen entry site in the mucosal epithelium. *Proc. Natl Acad. Sci. USA* **101**, 6110–6115 (2004).

Supplementary Information is linked to the online version of the paper at www.nature.com/nature.

Acknowledgements We thank C. A. Hunter, E. J. Pearce and E. H. Wilson for critical reading of the manuscript, and J. N. Ihle for the *Tpte2 $^{-/-}$* mice. This work was supported by the NIH (D.A., L.E. and M.K.), the pilot feasibility program of the NIDDK Diseases Centre (D.A.), and NIAID (A.E.T.) and NCRR (L.D.B.-B.) NIH training grants. M.K. is an American Cancer Society Research Professor. C.Z. is a recipient of a fellowship from the Irvington Institute for Immunological Research. D.A. is the recipient of the Crohn's and Colitis Foundation of America's William and Shelby Modell Family Foundation Research Award.

Author Contributions C.Z., A.E.T., B.C.T., F.R.G., L.E., M.K. and D.A. designed the research. C.Z., A.E.T., B.C.T., L.D.B.-B., K.J.G., Y.D., E.A.Y. and D.A. performed the research. F.R.G., L.E., A.D.G., M.J.M. and M.K. contributed new reagents. C.Z., A.E.T., B.C.T., F.R.G., L.E., M.J.M., M.K. and D.A. analysed the data. C.Z. and D.A. wrote the paper.

Author Information Reprints and permissions information is available at www.nature.com/reprints. The authors declare no competing financial interests. Correspondence and requests for materials should be addressed to D.A. (dartis@vet.upenn.edu).

Epithelial NEMO links innate immunity to chronic intestinal inflammation

Arianna Nenci^{1,2*}, Christoph Becker^{3*}, Andy Wullaert¹, Ralph Gareus¹, Geert van Loo², Silvio Danese⁴, Marion Huth², Alexei Nikolaev³, Clemens Neufert³, Blair Madison⁵, Deborah Gumucio⁵, Markus F. Neurath^{3*} & Manolis Pasparakis^{1,2}

Deregulation of intestinal immune responses seems to have a principal function in the pathogenesis of inflammatory bowel disease^{1–4}. The gut epithelium is critically involved in the maintenance of intestinal immune homeostasis—acting as a physical barrier separating luminal bacteria and immune cells, and also expressing antimicrobial peptides^{3,5,6}. However, the molecular mechanisms that control this function of gut epithelial cells are poorly understood. Here we show that the transcription factor NF- κ B, a master regulator of pro-inflammatory responses^{7,8}, functions in gut epithelial cells to control epithelial integrity and the interaction between the mucosal immune system and gut microflora. Intestinal epithelial-cell-specific inhibition of NF- κ B through conditional ablation of NEMO (also called I κ B kinase- γ (IKK γ)) or both IKK1 (IKK α) and IKK2 (IKK β)—IKK subunits essential for NF- κ B activation^{7–9}—spontaneously caused severe chronic intestinal inflammation in mice. NF- κ B deficiency led to apoptosis of colonic epithelial cells, impaired expression of antimicrobial peptides and translocation of bacteria into the mucosa. Concurrently, this epithelial defect triggered a chronic inflammatory response in the colon, initially dominated by innate immune cells but later also involving T lymphocytes. Deficiency of the gene encoding the adaptor protein MyD88 prevented the development of intestinal inflammation, demonstrating that Toll-like receptor activation by intestinal bacteria is essential for disease pathogenesis in this mouse model. Furthermore, NEMO deficiency sensitized epithelial cells to tumour-necrosis factor (TNF)-induced apoptosis, whereas TNF receptor-1 inactivation inhibited intestinal inflammation, demonstrating that TNF receptor-1 signalling is crucial for disease induction. These findings demonstrate that a primary NF- κ B signalling defect in intestinal epithelial cells disrupts immune homeostasis in the gastrointestinal tract, causing an inflammatory-bowel-disease-like phenotype. Our results identify NF- κ B signalling in the gut epithelium as a critical regulator of epithelial integrity and intestinal immune homeostasis, and have important implications for understanding the mechanisms controlling the pathogenesis of human inflammatory bowel disease.

To investigate the function of NF- κ B signalling in the gut epithelium *in vivo*, we generated mice lacking NEMO specifically in intestinal epithelial cells (NEMO^{IEC-KO} mice) by crossing mice carrying *loxP*-flanked (floxed, FL) *NEMO* (*Ikkbg*) alleles¹⁰ with *villin-Cre* transgenics¹¹. Southern blot DNA analysis showed *NEMO* deletion specifically in the small intestine and colon of NEMO^{IEC-KO} mice (Fig. 1b). Furthermore, immunostaining showed lack of NEMO expression in most epithelial cells from the small intestine and colon

(Fig. 1a), indicating efficient NEMO ablation in intestinal epithelial cells.

NEMO^{IEC-KO} mice were born at the expected mendelian ratio; however, at a young age they showed runting, diarrhoea and rectal bleeding, indicating intestinal pathology. High-resolution mini-endoscopy¹² revealed signs of severe colitis with thickening of the bowel wall, a granular and bleeding mucosa, loss of regular vessel architecture and diarrhoea in NEMO^{IEC-KO} mice (Fig. 1c). Furthermore, macroscopic examination showed severe pancolitis affecting all parts of the colon distal from the caecum but sparing the small intestine (Fig. 1d). The colitis phenotype was observed in all NEMO^{IEC-KO} mice examined older than 3 weeks, irrespective of whether they were maintained in a specific pathogen-free or a conventional animal facility. Macroscopic and histological examination of 6-week-old NEMO^{IEC-KO} mice did not reveal any pathological findings in the small intestine, whereas the colon was heavily inflamed (Supplementary Fig. 1 and data not shown). Colitis in NEMO^{IEC-KO} mice was characterized by thickening of the mucosa, enlarged crypts with loss of goblet cells, and a marked infiltration of mononuclear cells into the mucosa and submucosa, similar to the histopathology seen in patients with inflammatory bowel diseases (Fig. 1e and Supplementary Fig. 2). Analysis of pro-inflammatory gene expression showed upregulation of *Il1b*, *Il6*, *Tnf* and *Ccl2* (also called *MCP-1*) in the colon of NEMO^{IEC-KO} mice already at 2 weeks after birth (Fig. 2a), which was even more pronounced in 6-week-old animals, when *Ccl5* (*RANTES*) was also induced. To investigate which cells were responsible for the inflammatory response in the colon of NEMO^{IEC-KO} mice, we examined the cellular infiltrate within the mucosa. In 2-week-old mice, inflammatory infiltrates were dominated by large numbers of dendritic cells and granulocytes, and to a much lesser extent by CD4⁺ T cells (Fig. 2b). However, at 12 and 36 weeks, colonic tissue from NEMO^{IEC-KO} mice showed numerous lymphoid follicles and a massive infiltration with dendritic cells, CD4⁺ T cells and granulocytes (Fig. 2b). Thus, intestinal epithelial-cell-specific NEMO ablation causes the spontaneous development of severe chronic colitis associated with increased expression of inflammatory cytokines and chemokines, an early accumulation of innate immune cells, and the presence of T-cell infiltrates at later time points.

NEMO-deficient cells lack the ability to activate NF- κ B and are sensitive to apoptosis induced by cytokines such as TNF^{10,13,14}. Indeed, TdT-mediated dUTP nick end labelling (TUNEL) staining of colon cross-sections from 2-week-old mice revealed extensive epithelial cell apoptosis in a few scattered areas in NEMO^{IEC-KO} mice but

¹Institute for Genetics, University of Cologne, Zùlpicher Strasse 47, 50674 Cologne, Germany. ²EMBL Mouse Biology Unit, I-00016 Monterotondo, Italy. ³Laboratory of Clinical Immunology, I. Department of Medicine, University of Mainz, Obere Zahlbacher Strasse 63, 55131 Mainz, Germany. ⁴Division of Gastroenterology, Istituto Clinico Humanitas-IRCCS in Gastroenterology, Viale Manzoni 56, 20089 Rozzano, Milan, Italy. ⁵Department of Cell & Developmental Biology, Center for Organogenesis, The University of Michigan, Ann Arbor, Michigan 48109-0616, USA.

*These authors contributed equally to this work.

not in controls (Fig. 3a). Furthermore, histological analysis of colon sections from these mice revealed the presence of crypts showing extensive epithelial destruction with loss of epithelial cells in such areas (Fig. 3b). Therefore, a localized disruption of epithelial integrity occurs in young $NEMO^{IEC-KO}$ mice, which probably allows for the translocation of bacteria from the lumen into the mucosa. Consistently, fluorescence *in situ* hybridization (FISH) using a probe specific for the ribosomal RNA of all eubacteria showed the presence of bacteria within the lamina propria of $NEMO^{IEC-KO}$ mice, in close proximity to areas displaying defects in epithelial integrity (Fig. 3c). High-power microscopic examination showed that in addition to the presence of free bacterial rods in the mucosa, cells in these areas also stained positive for bacterial rRNA, indicating phagocytosis of bacteria by immune cells (Fig. 3d). Immunofluorescence analysis revealed an accumulation of $CD11c^+$ dendritic cells, neutrophils and a few $CD4^+$ T cells around areas showing local disruption to

epithelial integrity, suggesting that bacterial translocation into the mucosa leads to immune cell recruitment and activation (Fig. 3e). Quantification of apoptotic cells ($TUNEL^+$), cells showing bacterial phagocytosis ($FISH^+$) and of neutrophils (MPO^+) in colon sections from newborn, 1-, 2- and 3-week-old mice showed that disruption of epithelial integrity, bacterial translocation into the mucosa and recruitment of neutrophils are first observed in 1-week-old mice and the pathology develops progressively over time (Supplementary Fig. 3). Taken together, our data are consistent with a model in which intestinal epithelial-cell-specific $NEMO$ deficiency compromises colonic epithelial integrity, resulting in translocation of luminal bacteria into the mucosa. Concomitantly with bacterial translocation, an inflammatory response is initiated, characterized initially by activation of innate immune cells such as dendritic cells and neutrophils.

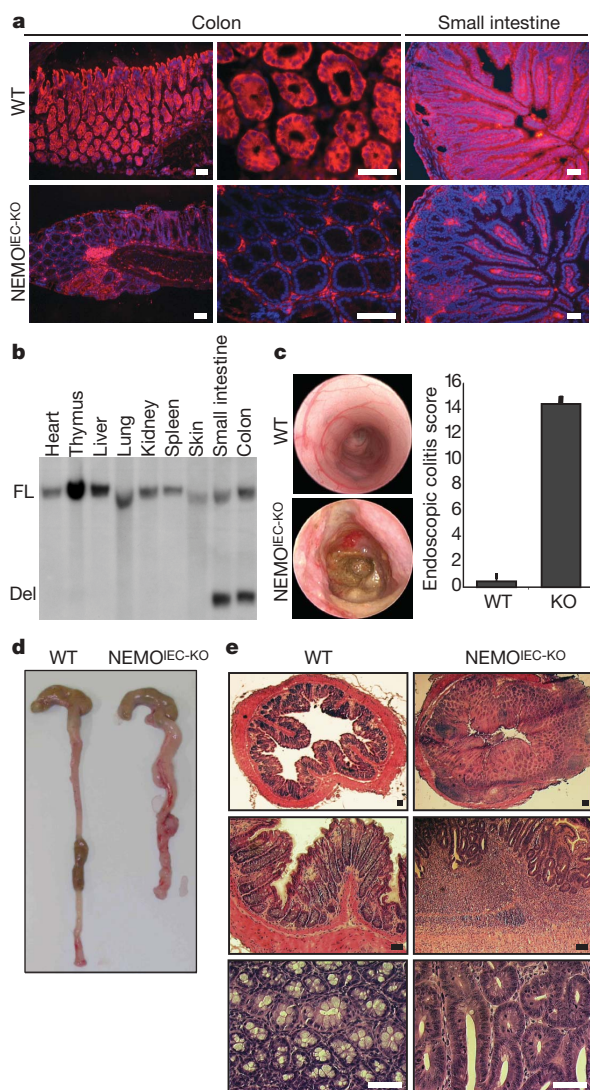


Figure 1 | Intestinal epithelium-specific $NEMO$ ablation causes severe spontaneous colitis. **a**, Immunofluorescence with anti- $NEMO$ antibodies shows efficient $NEMO$ ablation in the intestinal epithelium of $NEMO^{IEC-KO}$ mice. WT, wild type. **b**, Southern blot DNA analysis shows $NEMO$ deletion (Del) specifically in the intestines of $NEMO^{IEC-KO}$ mice. **c**, $NEMO^{IEC-KO}$ ($n = 3$) and wild-type ($n = 5$) mice were examined at the age of 32–36 weeks using mini-endoscopy. Murine endoscopic index of colitis severity (MEICS)²⁹ scores are shown (mean \pm s.d.). **d**, The colon of $NEMO^{IEC-KO}$ mice is thickened and shortened, indicating severe colitis. **e**, Haematoxylin-and-eosin-stained colon cross-sections show severe inflammation and loss of goblet cells in $NEMO^{IEC-KO}$ mice. All scale bars, 50 μ m.

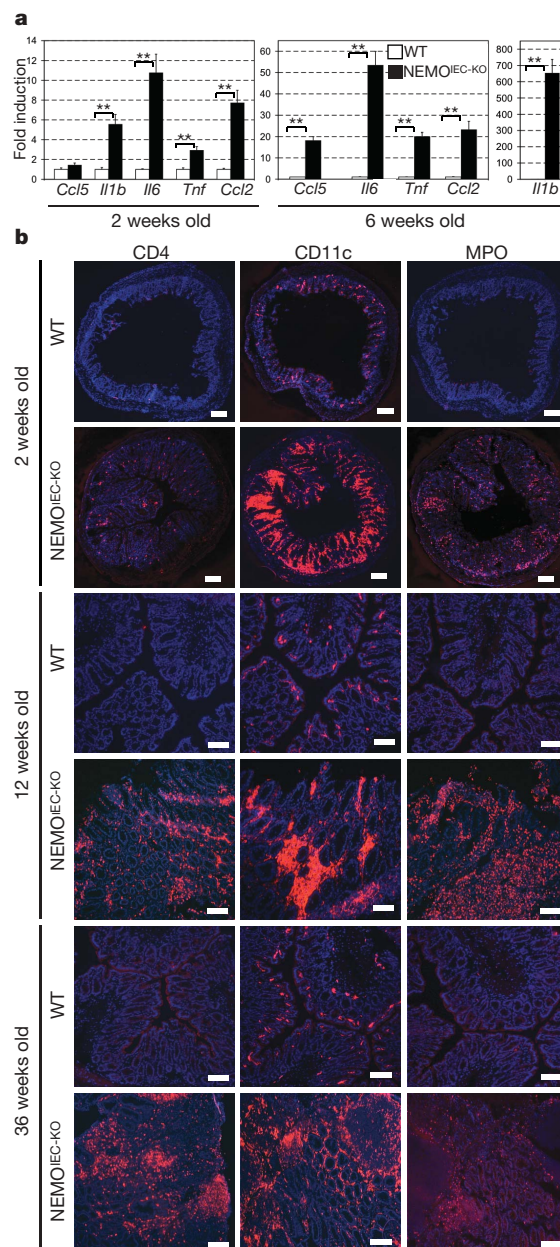


Figure 2 | Inflammation in the colon of $NEMO^{IEC-KO}$ mice. **a**, Expression of pro-inflammatory cytokines and chemokines in the colons of $NEMO^{IEC-KO}$ and wild-type mice ($n = 4$ –6 mice per group). Data shown are mean values relative to ubiquitin (\pm s.e.m.); double asterisk, $P < 0.01$. **b**, Colon cross-sections from $NEMO^{IEC-KO}$ and wild-type mice were immunostained with antibodies for CD4, CD11c or myeloperoxidase (MPO) (red). Nuclei were counterstained with Hoechst 3342 (blue). Scale bars, 100 μ m.

This pathology starts in a localized fashion in scattered areas of the colon in young NEMO^{IEC-KO} mice between 1 and 2 weeks after birth. At later time points, the inflammation affects the entire colon and also involves T lymphocytes. In mice with advanced-stage colitis, we could detect lymphoid follicles surrounded by dendritic cells, whereas CD11c/FISH double staining revealed bacterial rRNA signals co-localized with dendritic cells in these areas (Fig. 3f),

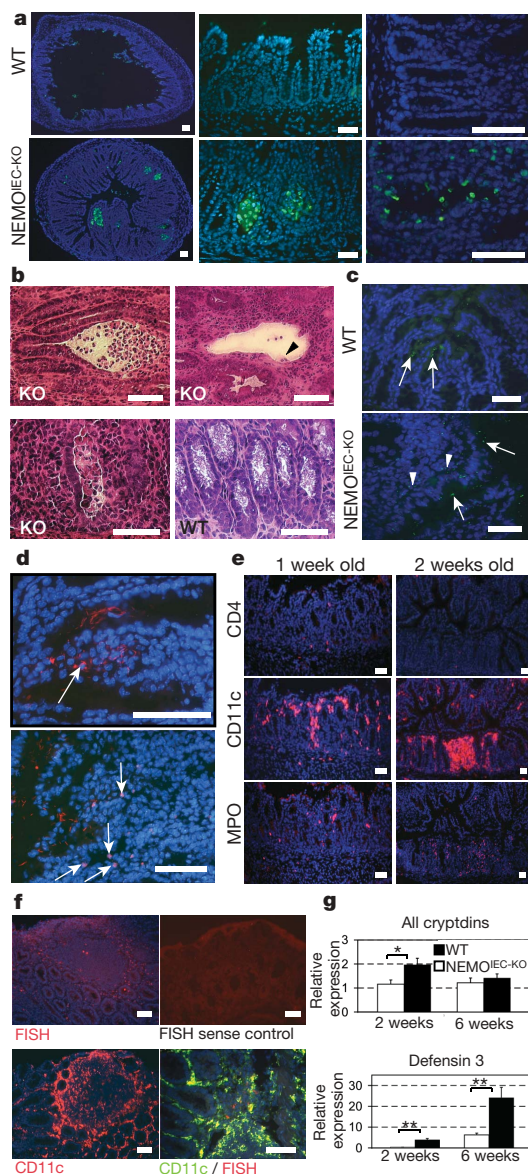


Figure 3 | Compromised epithelial integrity and bacterial translocation in the colon of NEMO^{IEC-KO} mice. **a**, TUNEL staining (green) on colon cross-sections from 2-week-old NEMO^{IEC-KO} and wild-type mice. **b**, Haematoxylin-and-eosin-stained colon cross-sections from 3-week-old NEMO^{IEC-KO} (KO) and wild-type mice. Note the epithelial disintegration in several crypts. The arrowhead depicts two remaining epithelial cells in a crypt showing nearly complete loss of epithelium. **c**, Bacterial FISH staining (green) was detected in the lamina propria of NEMO^{IEC-KO} colon (arrowheads), but was restricted to the lumen in wild-type mice (arrows). **d**, Bacterial FISH staining (red) co-localizes with cells in two representative NEMO^{IEC-KO} colon sections (see arrows). **e**, Focal infiltration of neutrophils and dendritic cells in the lamina propria of young NEMO^{IEC-KO} mice. **f**, Double FISH/CD11c staining on colon cross-sections from 36-week-old NEMO^{IEC-KO} mice shows co-localization of dendritic cells with bacteria around a lymphoid follicle. **g**, Expression of cryptdins and of defensin-3 in the colons of NEMO^{IEC-KO} and wild-type mice (4–5 mice per group). Results are shown as mean values relative to ubiquitin (\pm s.e.m.); asterisk, $P < 0.05$; double asterisk, $P < 0.01$. All scale bars, 50 μ m.

indicating that the presence of bacteria drives the immune response also at later stages.

Antimicrobial peptide expression by the intestinal epithelium is believed to have an important function in controlling the number of bacteria around epithelial cells, and has recently been suggested to have a principal role in the pathogenesis of inflammatory bowel disease⁶. Because the NF- κ B signalling pathway regulates antimicrobial peptide expression⁶, we investigated whether NEMO deficiency affected antimicrobial peptide expression from the colonic epithelium. Using a primer set that detects simultaneously all 17 mouse cryptdin genes¹⁵, we found that collective expression of cryptdins was only mildly reduced in 2-week-old NEMO^{IEC-KO} mice compared to controls, and was unaffected at 6 weeks of age (Fig. 3g). However, beta-defensin-3, the expression of which is induced in mouse primary colonic epithelial cells by bacteria¹⁶, was significantly downregulated in 2- and 6-week-old NEMO^{IEC-KO} mice compared with littermate controls (Fig. 3g and Supplementary Fig. 4). A recent study reported that reduced expression of human beta-defensin-2, which is homologous to mouse beta-defensin-3, predisposes to colonic Crohn's disease in humans¹⁷. Thus, reduced expression of defensin-3 may lead to impaired antibacterial defence in the colon, and might be implicated in the translocation of commensal bacteria into the gut mucosa and consecutive colitis development in NEMO^{IEC-KO} mice.

Consistent with a previous report¹⁸, mice with intestinal epithelial-cell-specific IKK2 ablation (IKK2^{IEC-KO}), generated by crossing villin-Cre transgenic mice with mice carrying loxP-flanked IKK2 (*ikkbk*) alleles¹⁹, did not develop spontaneous intestinal inflammation (Supplementary Fig. 5). The differential effect of NEMO versus IKK2 ablation in the gut epithelium is probably due to the fact that pro-inflammatory-signal-induced NF- κ B activity is completely blocked in NEMO-deficient cells but only partially affected in IKK2-deficient cells^{10,20}. Indeed, NEMO-deficient intestinal epithelial cells displayed a complete lack of NF- κ B activation, whereas IKK2-deficient intestinal epithelial cells displayed low levels of residual NF- κ B activity (Fig. 4a and Supplementary Fig. 6). Furthermore, NEMO-deficient intestinal epithelial cells failed to upregulate NF- κ B-dependent genes, such as *Ikbz* (also called *Nfkbia*) and *IP10* (*Cxcl10*), upon *in vivo* lipopolysaccharide stimulation, whereas IKK2-deficient intestinal epithelial cells showed intermediate levels of induction compared to wild-type cells (Fig. 4b). Thus, NEMO deficiency completely blocks canonical NF- κ B activity in intestinal epithelial cells, whereas IKK2-deficient cells show residual NF- κ B activation, presumably through compensatory signalling by means of IKK1. To test whether IKK1 signalling protects the colon of IKK2^{IEC-KO} mice from intestinal inflammation, we generated mice lacking both IKK1 and IKK2 in intestinal epithelial cells (IKK1/2^{IEC-KO}) by crossing the IKK2^{IEC-KO} mice with mice carrying *IKK1* (*Chuk*) loxP-flanked alleles²¹. Whereas intestinal epithelial-cell-specific IKK1-deficient mice (IKK1^{IEC-KO}) did not develop colitis, double IKK1/2^{IEC-KO} mice displayed diarrhoea and rectal bleeding, as well as macroscopic, endoscopic and histological evidence of colitis (Fig. 4c–e and Supplementary Fig. 7). Thus, although neither IKK1^{IEC-KO} nor IKK2^{IEC-KO} mice show spontaneous intestinal inflammation, IKK1/2^{IEC-KO} mice develop severe colitis, similarly to NEMO^{IEC-KO} mice. These results demonstrate that complete inhibition of canonical NF- κ B activity in intestinal epithelial cells—achieved by ablation of either NEMO or both IKK1 and IKK2—results in severe inflammatory colitis, and reveal that canonical IKK/NF- κ B signalling in intestinal epithelial cells has an essential function in maintaining epithelial integrity and immune homeostasis in the colon. Moreover, our findings uncover a redundancy between the two I κ B kinases in mediating this function.

The presence of bacteria within the lamina propria may trigger the development of chronic inflammatory colitis in NEMO^{IEC-KO} mice by means of Toll-like receptor (TLR) stimulation⁵. To investigate whether TLR activation contributes to the development of colitis

in $NEMO^{IEC-KO}$ mice, we crossed them with mice lacking MyD88, an adaptor molecule required for signalling by most members of the interleukin (IL)-1R/TLR family²². Macroscopic and immunohistological analysis of colons from $NEMO^{IEC-KO}$ /MyD88-deficient mice revealed no sign of colitis (13 mice were analysed between 6–20 weeks of age) (Fig. 4f), demonstrating that MyD88-dependent signals are essential for disease pathogenesis in this model. These results suggest that TLR-mediated bacterial recognition has a critical role in inducing intestinal inflammation in $NEMO^{IEC-KO}$ mice; however, IL-1-mediated signals that also depend on MyD88 might also be involved in the pathogenesis of colitis.

TNF blockade is an effective therapy for inflammatory bowel disease patients²³. To investigate whether TNF signalling contributes to the development of colitis in $NEMO^{IEC-KO}$ mice, we crossed them onto a TNF receptor-1 (TNFRI)-deficient background. Double $NEMO^{IEC-KO}$ /TNFRI-deficient mice did not show macroscopic or histological signs of colitis (10 mice were analysed between 6–10 weeks of age), demonstrating that TNFRI signalling is crucial for disease

pathogenesis in this model (Fig. 4g). Because cells lacking NEMO are more sensitive to TNF-induced apoptosis than cells lacking IKK2 (refs 10, 24), TNF-mediated killing of NEMO-deficient intestinal epithelial cells probably contributes to the induction of colon inflammation by compromising epithelial integrity in $NEMO^{IEC-KO}$ mice. Indeed, TNF administration caused increased apoptosis of colon epithelial cells in $NEMO^{IEC-KO}$ /TNF-deficient mice—generated by crossing with TNF-deficient mice²⁵ and used here to facilitate assessment of apoptosis in a disease-free colon—compared with TNF-deficient, $IKK2^{IEC-KO}$ and wild-type mice (Supplementary Fig. 8), demonstrating that NEMO-deficient intestinal epithelial cells are more sensitive to TNF-induced killing *in vivo* than IKK2-deficient intestinal epithelial cells. These results suggest that one key mechanism by which TNF signalling induces colon inflammation in $NEMO^{IEC-KO}$ mice is by killing the NF- κ B-deficient intestinal epithelial cells, resulting in disruption of epithelial integrity. However, TNF may also have a critical role in coordinating the mucosal inflammatory response by inducing the recruitment and activation of immune cells.

Taken together, our findings support a model (Fig. 5) in which impaired NF- κ B signalling in the colonic epithelium results in TNF-mediated epithelial cell apoptosis and diminished expression of antimicrobial peptides, thus compromising epithelial integrity and allowing bacterial translocation into the mucosa of $NEMO^{IEC-KO}$ mice. The presence of bacteria within the colonic mucosa activates innate immune cells through MyD88-dependent TLR signalling, triggering the expression of pro-inflammatory cytokines such as TNF and IL-1 β , which cause further destruction of the NF- κ B-deficient colonic epithelium and induce the recruitment of additional immune cells including T-lymphocytes, finally resulting in chronic inflammation and severe transmural pancolitis in $NEMO^{IEC-KO}$ mice.

Impairment of intestinal epithelial integrity and reduced cryptdin expression in humans have been suggested as important causative factors for the development of intestinal inflammation in patients with inflammatory bowel disease^{5,6}. Our results with the $NEMO^{IEC-KO}$ mice demonstrate that a primary epithelial defect resulting in impairment of both the integrity and antimicrobial defence of the gut epithelium can give rise to chronic intestinal inflammation. The rapid onset and high penetrance of the colitis phenotype in $NEMO^{IEC-KO}$ mice suggest that a defect in epithelial NF- κ B signalling may be an important proximal event in the pathogenesis of inflammatory bowel disease. Thus, epithelial NF- κ B deficiency may provide a new paradigm for the development of an inflammatory-bowel-disease-like disease. Furthermore, NF- κ B signalling in intestinal epithelial cells emerges as a crucial factor for

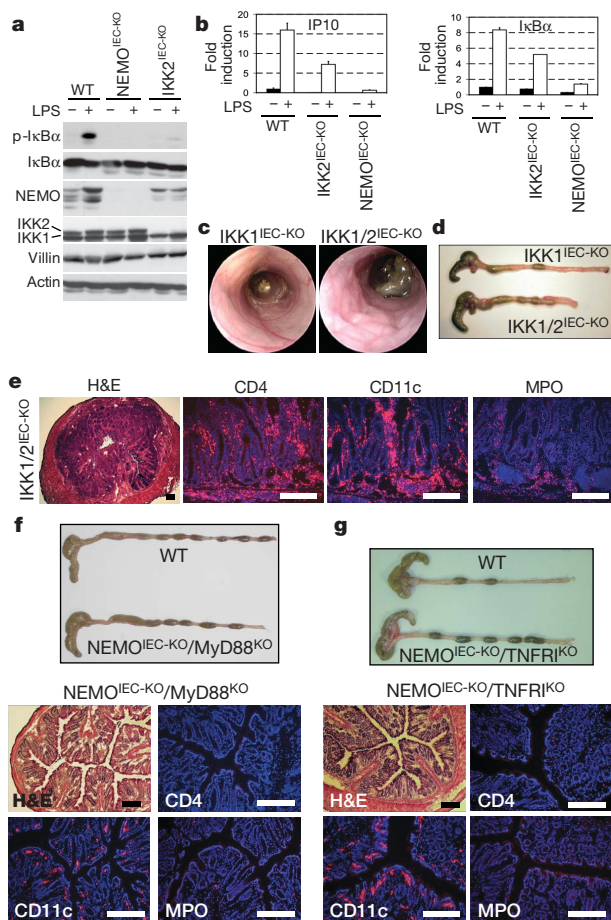


Figure 4 | NF- κ B inhibition in intestinal epithelial cells causes inflammatory colitis that depends on TNFRI and MyD88 signalling. **a**, **b**, Intestinal epithelial cells were isolated from mice with the indicated genotypes 90 min after administration of lipopolysaccharide (LPS; 25 μ g per 10 g body weight) or PBS. **a**, Immunoblot analysis of I κ B α phosphorylation and degradation, and NEMO, IKK2, villin and actin expression. **b**, Quantitative RT-PCR analysis of I κ B α and IP10 expression. Mean values (\pm s.e.m.) are shown. **c**, **d**, Mini-endoscopy (**c**) and macroscopic colon examination (**d**) reveal severe colitis in 11-week-old double $IKK1/2^{IEC-KO}$ mice but not in $IKK1^{IEC-KO}$ mice. **e**, Colon cross-sections from 11-week-old $IKK1/2^{IEC-KO}$ mice were stained with haematoxylin and eosin or with antibodies for CD4, CD11c or MPO (red). Nuclei were counterstained with Hoechst 3342 (blue). **f**, **g**, Macroscopic and histological examination of colons from 8-week-old $NEMO^{IEC-KO}$ /MyD88^{KO} (**f**) and $NEMO^{IEC-KO}$ /TNFRI^{KO} (**g**) mice reveal lack of colon inflammation in both double mutant strains. All scale bars, 200 μ m.

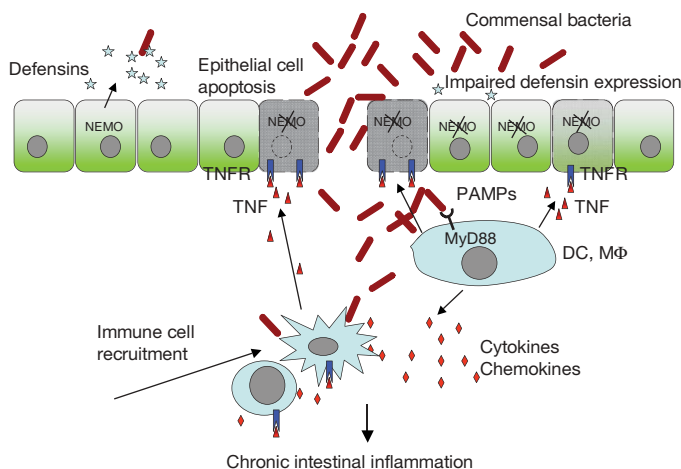


Figure 5 | NEMO-mediated NF- κ B activation in intestinal epithelial cells is essential for the maintenance of epithelial barrier integrity and immune homeostasis in the colon. DC, dendritic cell; M Φ , macrophage; PAMPs, pathogen-associated molecular patterns.

maintaining homeostasis between commensal microflora and host immunity in the gastrointestinal tract, and represents a critical determinant for prevention of gut inflammation.

METHODS

Mice. The mouse lines used in this study have been described previously: *NEMO*^{FL} (ref. 10), *IKK2*^{FL} (ref. 19), *villin-Cre*¹¹, TNFRI-deficient²⁶, MyD88-deficient²⁷, TNF-deficient²⁵, *IKK1*^{FL} (ref. 21). The experiments were performed on mice backcrossed into the C57BL/6 genetic background for at least five generations. In all experiments, littermates carrying the *loxP*-flanked alleles but not expressing Cre recombinase were used as wild-type controls. The mice used in this study were housed in individually ventilated cage systems at the EMBL Mouse Biology Unit or at the Institute for Genetics of the University of Cologne, in either specific pathogen-free or conventional animal facilities.

Immunohistochemistry, FISH and apoptosis. Immunofluorescence of cryosections was performed using the TSA Cy3 system (Perkin Elmer) and a fluorescence microscope (Olympus fluorescence microscope) as described²⁸. *In situ* hybridization of bacterial rRNA on glass slides was performed as previously described²⁸. Apoptosis was analysed using the *in situ* cell death detection kit (Roche).

Endoscopic procedures. For endoscopic colitis monitoring, a high-resolution mouse video endoscope, denoted Coloview, was used, as previously described²⁹.

Southern blot analysis. Southern blot analysis was performed as described previously¹⁰.

Isolation of intestinal epithelial cells. Intestinal epithelial cells were isolated from small intestines or colons (see Supplementary Information).

Immunoblot analysis. Total cell extracts were electrophoresed by SDS-polyacrylamide gel electrophoresis (10%) and transferred to Immobilon P membranes (Millipore). Membranes were probed with the antibodies listed in the Supplementary Information.

Quantitative real-time PCR. Total RNA from colon, small intestine and intestinal epithelial cells was isolated using Trizol (Invitrogen) and analysed by real-time PCR with SyBr Green (Finnzymes) or by TaqMan gene expression (Applied Biosystems). Individual primer sequences are listed in the Supplementary Information. All values were normalized to the level of ubiquitin messenger RNA.

Received 8 December 2006; accepted 23 February 2007.

Published online 14 March 2007.

1. Bouma, G. & Strober, W. The immunological and genetic basis of inflammatory bowel disease. *Nature Rev. Immunol.* **3**, 521–533 (2003).
2. Hanauer, S. B. Inflammatory bowel disease: epidemiology, pathogenesis, and therapeutic opportunities. *Inflamm. Bowel Dis.* **12** (suppl. 1), S3–S9 (2006).
3. Macdonald, T. T. & Monteleone, G. Immunity, inflammation, and allergy in the gut. *Science* **307**, 1920–1925 (2005).
4. Neurath, M. F., Finotto, S. & Glimcher, L. H. The role of Th1/Th2 polarization in mucosal immunity. *Nature Med.* **8**, 567–573 (2002).
5. Abreu, M. T., Fukata, M. & Arditi, M. TLR signaling in the gut in health and disease. *J. Immunol.* **174**, 4453–4460 (2005).
6. Wehkamp, J., Fellermann, K., Herrlinger, K. R., Bevins, C. L. & Stange, E. F. Mechanisms of disease: defensins in gastrointestinal diseases. *Nature Clin. Pract. Gastroenterol. Hepatol.* **2**, 406–415 (2005).
7. Karin, M. & Greten, F. R. NF- κ B: linking inflammation and immunity to cancer development and progression. *Nature Rev. Immunol.* **5**, 749–759 (2005).
8. Li, Q. & Verma, I. M. NF- κ B regulation in the immune system. *Nature Rev. Immunol.* **2**, 725–734 (2002).
9. Ghosh, S. & Karin, M. Missing pieces in the NF- κ B puzzle. *Cell* **109** (suppl.) S81–S96 (2002).
10. Schmidt-Suppran, M. et al. NEMO/IKK γ -deficient mice model incontinentia pigmenti. *Mol. Cell* **5**, 981–992 (2000).

11. Madison, B. B. et al. Cis elements of the villin gene control expression in restricted domains of the vertical (crypt) and horizontal (duodenum, cecum) axes of the intestine. *J. Biol. Chem.* **277**, 33275–33283 (2002).
12. Becker, C. et al. TGF- β suppresses tumor progression in colon cancer by inhibition of IL-6 trans-signaling. *Immunity* **21**, 491–501 (2004).
13. Rudolph, D. et al. Severe liver degeneration and lack of NF- κ B activation in NEMO/IKK γ -deficient mice. *Genes Dev.* **14**, 854–862 (2000).
14. Makris, C. et al. Female mice heterozygous for IKK γ /NEMO deficiencies develop a dermatopathy similar to the human X-linked disorder incontinentia pigmenti. *Mol. Cell* **5**, 969–979 (2000).
15. Darmoul, D. & Ouellette, A. J. Positional specificity of defensin gene expression reveals Paneth cell heterogeneity in mouse small intestine. *Am. J. Physiol.* **271**, G68–G74 (1996).
16. Lan, J. G. et al. Different cytokine response of primary colonic epithelial cells to commensal bacteria. *World J. Gastroenterol.* **11**, 3375–3384 (2005).
17. Fellermann, K. et al. A chromosome 8 gene-cluster polymorphism with low human β -defensin 2 gene copy number predisposes to Crohn disease of the colon. *Am. J. Hum. Genet.* **79**, 439–448 (2006).
18. Greten, F. R. et al. IKK β links inflammation and tumorigenesis in a mouse model of colitis-associated cancer. *Cell* **118**, 285–296 (2004).
19. Pasparakis, M. et al. TNF-mediated inflammatory skin disease in mice with epidermis-specific deletion of IKK2. *Nature* **417**, 861–866 (2002).
20. Li, Q., Estepa, G., Memet, S., Israel, A. & Verma, I. M. Complete lack of NF- κ B activity in IKK1 and IKK2 double-deficient mice: additional defect in neurulation. *Genes Dev.* **14**, 1729–1733 (2000).
21. Gareus, R. et al. Normal epidermal differentiation but impaired skin barrier formation upon keratinocyte-restricted IKK1 ablation. *Nature Cell Biol.* doi:10.1038/ncb1560 (in the press).
22. Kawai, T. & Akira, S. TLR signaling. *Cell Death Differ.* **13**, 816–825 (2006).
23. Targan, S. R. et al. A short-term study of chimeric monoclonal antibody cA2 to tumor necrosis factor α for Crohn's disease. Crohn's Disease cA2 Study Group. *N. Engl. J. Med.* **337**, 1029–1035 (1997).
24. Luedde, T. et al. Deletion of NEMO/IKK γ in liver parenchymal cells causes steatohepatitis and hepatocellular carcinoma. *Cancer Cell* **11**, 119–132 (2007).
25. Pasparakis, M., Alexopoulou, L., Episkopou, V. & Kollias, G. Immune and inflammatory responses in TNF α -deficient mice: a critical requirement for TNF α in the formation of primary B cell follicles, follicular dendritic cell networks and germinal centers, and in the maturation of the humoral immune response. *J. Exp. Med.* **184**, 1397–1411 (1996).
26. Pfeffer, K. et al. Mice deficient for the 55 kd tumor necrosis factor receptor are resistant to endotoxin shock, yet succumb to *L. monocytogenes* infection. *Cell* **73**, 457–467 (1993).
27. Kawai, T., Adachi, O., Ogawa, T., Takeda, K. & Akira, S. Unresponsiveness of MyD88-deficient mice to endotoxin. *Immunity* **11**, 115–122 (1999).
28. Becker, C. et al. Constitutive p40 promoter activation and IL-23 production in the terminal ileum mediated by dendritic cells. *J. Clin. Invest.* **112**, 693–706 (2003).
29. Becker, C. et al. *In vivo* imaging of colitis and colon cancer development in mice using high resolution chromoendoscopy. *Gut* **54**, 950–954 (2005).

Supplementary Information is linked to the online version of the paper at www.nature.com/nature.

Acknowledgements We thank K. Pfeffer and S. Akira for providing TNFRI-deficient and MyD88-deficient mice, respectively. This work was supported by grants from the German Research Council to C.B. and M.F.N., and by EU-FP6 grants MUGEN and IMDEMI to M.P.; A.W. received a research fellowship from the Alexander von Humboldt Foundation.

Author Contributions A. Nenci, C.B., A.W., R.G., G.v.L., M.F.N. and M.P. designed the research. A. Nenci, C.B., A.W., R.G., G.v.L., S.D., M.H., A. Nikolaev and C.N. performed the research. B.M. and D.G. contributed new reagents. A. Nenci, C.B., A.W., R.G., M.F.N. and M.P. analysed the data and wrote the paper. M.F.N. and M.P. share senior authorship.

Author Information Reprints and permissions information is available at www.nature.com/reprints. The authors declare no competing financial interests. Correspondence and requests for materials should be addressed to M.P. (pasparakis@uni-koeln.de).

LETTERS

Dioxin receptor is a ligand-dependent E3 ubiquitin ligase

Fumiaki Ohtake^{1,2}, Atsushi Baba², Ichiro Takada², Maiko Okada², Kei Iwasaki¹, Hiromi Miki², Sayuri Takahashi^{2,3}, Alexander Kouzmenko^{1,2}, Keiko Nohara⁴, Tomoki Chiba⁵, Yoshiaki Fujii-Kuriyama^{6,7} & Shigeaki Kato^{1,2}

Fat-soluble ligands, including sex steroid hormones and environmental toxins, activate ligand-dependent DNA-sequence-specific transcriptional factors that transduce signals through target-gene-selective transcriptional regulation¹. However, the mechanisms of cellular perception of fat-soluble ligand signals through other target-selective systems remain unclear. The ubiquitin–proteasome system regulates selective protein degradation, in which the E3 ubiquitin ligases determine target specificity^{2–4}. Here we characterize a fat-soluble ligand-dependent ubiquitin ligase complex in human cell lines, in which dioxin receptor (AhR)^{5–9} is integrated as a component of a novel cullin 4B ubiquitin ligase complex, CUL4B^{AhR}. Complex assembly and ubiquitin ligase activity of CUL4B^{AhR} *in vitro* and *in vivo* are dependent on the AhR ligand. In the CUL4B^{AhR} complex, ligand-activated AhR acts as a substrate-specific adaptor component that targets sex steroid receptors for degradation. Thus, our findings uncover a function for AhR as an atypical component of the ubiquitin ligase complex and demonstrate a non-genomic signalling pathway in which fat-soluble ligands regulate target-protein-selective degradation through a ubiquitin ligase complex.

The transcriptional regulatory system and the ubiquitin–proteasome system are two major target-selective systems that control intracellular protein levels. This target selectivity depends on the recognition of specific DNA elements by sequence-specific transcription factors¹ and the recognition of degradation substrates by E3 ubiquitin ligases^{2–4}. These transcription factors and ligases serve primarily as specific adaptors that subsequently recruit transcriptional co-regulators and E2 ubiquitin-conjugating enzymes, respectively, to appropriate targets. The selective biological effects of fat-soluble ligands have been reported to be mediated by two classes of sequence-specific transcription factors, nuclear receptors¹ and arylhydrocarbon receptor (AhR) belonging to the basic helix–loop–helix (bHLH)/Per-Arnt-Sim (PAS) family^{5–9}.

AhR ligands modulate oestrogen and sex hormone, signalling both positively and negatively^{8,10–13}. Functional impairments of male and female reproductive organs in AhR-deficient mice indicate the possible importance of AhR in sex hormone signalling^{10,14}. Different AhR agonists⁹, including 3-methylcholanthrene (3MC) and 2,3,7,8-tetrachlorodibenzo-*p*-dioxin (TCDD), modulate oestrogen-dependent oestrogen receptor (ER)- α transactivation through the association of activated AhR/Arnt with ER- α ¹⁵. Similarly, the transcriptional activity of nuclear androgen receptor (AR) was modulated by association with activated AhR (Supplementary Fig. S2a). However, ligand-bound AhR did not block oestrogen-induced co-activator recruitment on the oestrogen-responsive promoter (Supplementary Fig. S2b). This implies another mode of function for ligand-activated AhR beyond transcriptional regulation.

On activation of AhR by 3MC, we observed that protein levels of endogenous ER- α (in mammary tumour MCF-7 cells), ER- β (in ovarian tumour KGN cells) and AR (in prostate cancer LNCaP cells) were drastically decreased (Fig. 1a–c, and Supplementary Fig. 3a) without a change in messenger RNA levels (data not shown), irrespective of the presence of their cognate hormones. Other AhR agonists⁹ (namely β -naphthoflavone (β -NF), environmental toxins such as TCDD and benzo[a]pyrene, and the endogenous metabolite indirubin) were similarly effective in protein degradation for ER- α (Fig. 1b) and ER- β /AR (data not shown), in agreement with a previous report on downregulated levels of uterine ER- α protein in rats treated with TCDD¹⁶. An AhR partial agonist/antagonist α -naphthoflavone (α -NF) was unable to accelerate the degradation of either AhR or ER- α (Fig. 1b, and Supplementary Fig. S3b).

AhR ligand-induced degradation (Fig. 1a–c) and functional repression (Supplementary Fig. S2c, d) of sex steroid receptors were abrogated in the presence of a proteasome inhibitor MG132. Consistently, poly-ubiquitination of ER- α was promoted by the activated AhR regardless of the presence of oestrogen (Fig. 1d, and Supplementary Fig. S3c). Pulse-chase kinetic analysis indicated that 3MC-induced degradation of ER- α was coupled to that of AhR^{8,17,18} (Supplementary Fig. S3d). Moreover, the self-ubiquitination activity of the ligand-bound AhR immunocomplex was detected in an E1/E2-dependent manner (Supplementary Fig. S3e). Together with 3MC-dependent recognition of sex steroid receptors by AhR^{8,12,13,15}, these properties of AhR resemble those of classical adaptor components of the E3 ubiquitin ligase complexes, such as F-box proteins³ or von Hippel–Lindau protein¹⁹. We therefore reasoned that activated AhR might act as an E3 ubiquitin ligase complex component.

To address this idea, AhR-containing complexes were purified from HeLa cells expressing Flag–AhR treated with 3MC or α -NF^{15,20}. AhR formed large complexes in the presence of 3MC (Supplementary Fig. S4a–c). Further purification revealed five major 3MC-dependent complexes containing AhR (Fig. 1e). Complexes A and C contained well-known co-activators TRAP220/DRIP205/Med220 and p300 (ref. 1) (Supplementary Fig. S4d, e). Endogenous ER- α was detected in complexes B and C; however, ubiquitinated components were seen only in complex B (Fig. 1f, g).

Complex B was composed of the ubiquitin ligase core components cullin 4B (CUL4B)^{3,21,22}, damaged-DNA-binding protein 1 (DDB1)^{23–27} and Rbx1 (Roc1)³, together with subunits of the proteasomal 19S regulatory particle (19S RP), Arnt and transducin- β -like 3 (TBL3) (Fig. 1h). These components eluted with AhR in the presence of 3MC but not in the presence of α -NF (Fig. 1i, and Supplementary Fig. S4f). Neither CUL4A nor known substrate-specific adaptor components of CUL4A, such as DDB2, CSA and DET1^{23,24}, were present

¹ERATO, Japan Science and Technology Agency, 4-1-8 Honcho, Kawaguchi, Saitama 332-0012, Japan. ²Institute of Molecular and Cellular Biosciences, University of Tokyo, 1-1-1 Yayoi, Bunkyo-ku, Tokyo 113-0032, Japan. ³Department of Urology, Faculty of Medicine, University of Tokyo, 7-3-1 Hongo, Bunkyo-ku, 113-8655, Japan. ⁴National Institute for Environmental Studies, Tsukuba, Ibaraki 305-8506, Japan. ⁵Graduate School of Life and Environmental Sciences, and ⁶TARA Center, University of Tsukuba, 1-1-1 Tennodai Tsukuba, 305-8577, Japan. ⁷SORST, Japan Science and Technology Agency, 4-1-8 Honcho, Kawaguchi, Saitama 332-0012, Japan.

in the AhR–CUL4B complex. As the cullin amino terminus binds adaptor components and the carboxy terminus interacts with an E2 enzyme-binding subunit Rbx1 (ref. 3), we performed tandem purification of the AhR–CUL4B complex with glutathione *S*-transferase (GST)-tagged CUL4B-N (N-terminal domain of CUL4B) and Flag–AhR. This led to the identification of a core complex consisting of five components: DDB1, AhR, Arnt, TBL3 and CUL4B (Fig. 1j). Together with Rbx1, this complex is denoted by CUL4B^{AhR}.

Immunoprecipitation of AhR together with endogenous CUL4B from MCF-7 and LNCaP cells was observed only in the presence of 3MC (Fig. 2a, b). Consistently, ligand-dependent co-localization of AhR with CUL4B was seen in MCF-7 cells (Fig. 2c). Whereas CUL4B seemed to act as a scaffold mediating DDB1–TBL3 and AhR–DDB1

interactions in CUL4B^{AhR} (Fig. 2d, lane 4), ligand-activated AhR induced the assembly of complex components (Fig. 2d, lanes 1–3). DDB1 did not bridge CUL4B association with TBL3 or AhR, apparently because of the absence of the signature WDXR/DWD box^{22,25–27} of either TBL3 or AhR, which is essential for DDB1 binding (Fig. 2d, lane 5, and Supplementary Fig. S5a). Consistently, specific and 3MC-dependent interaction of the conserved C-terminal acidic domain of AhR with the N-terminal region of CUL4B, but not with DDB1, was observed in a GST pulldown assay (Supplementary Figs S5b and S6). Because a constitutively active AhR mutant (AhR Δ PASB)⁹ interacted with CUL4B in the absence of ligand (Supplementary Fig. S5b), ligand-dependent structural alteration presumably induces AhR–CUL4B interaction. An AhR mutant lacking the CUL4B-binding

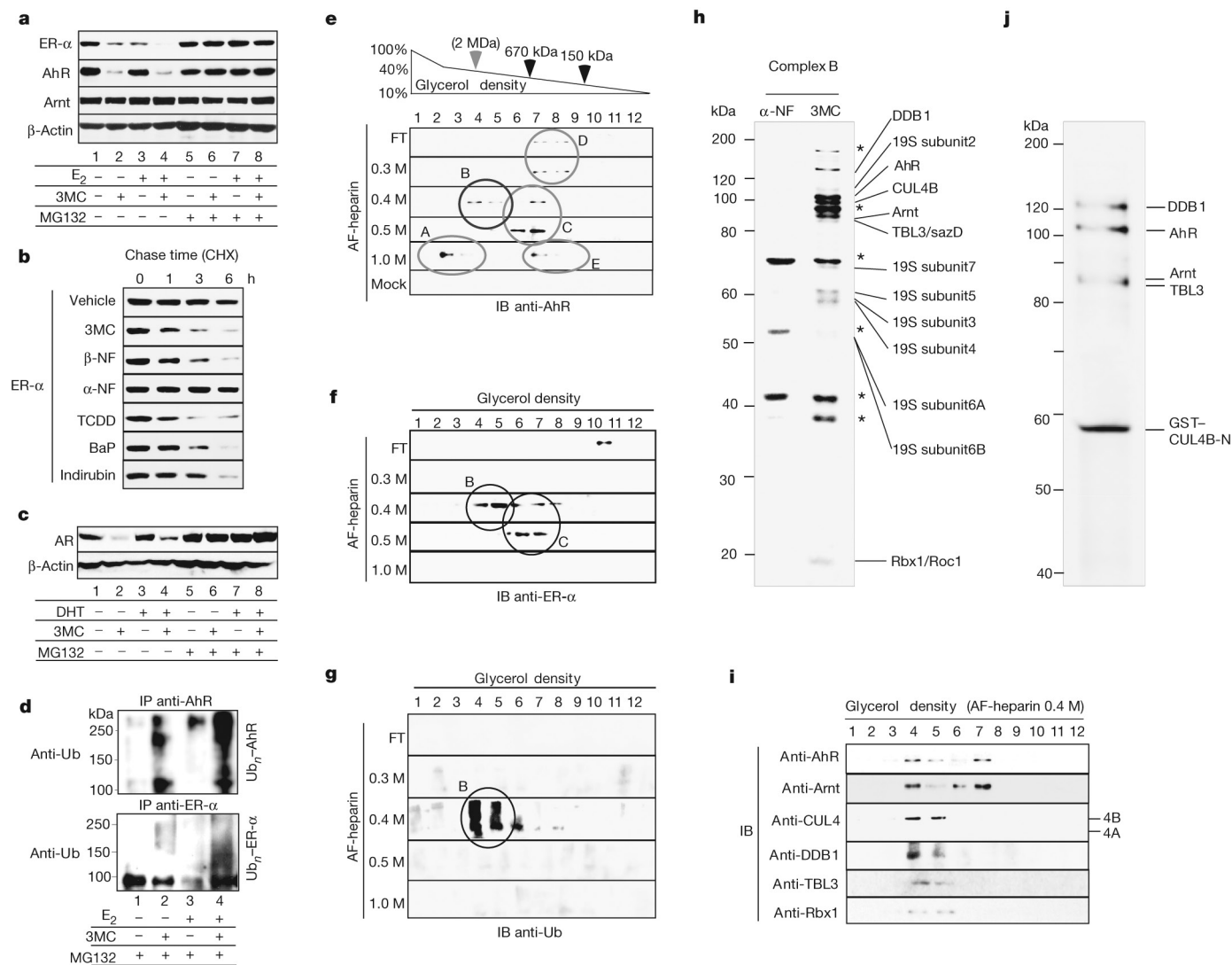


Figure 1 | Activated AhR acts as an E3 ubiquitin ligase. **a–c**, AhR-ligand-induced proteasomal degradation of ER-α (**a**, **b**) and AR (**c**). MCF-7 cells (**a**, **b**) and LNCaP cells (**c**) were incubated as indicated with E₂ (10 nM), DHT (10 nM) and/or 3MC (1 μM), β-NF (1 μM), benzo[a]pyrene (BaP; 100 nM), TCDD (10 nM), indirubin (10 nM) and α-NF (1 μM) in the presence or absence of MG132 (10 μM) and cycloheximide (CHX; 5 μM) for 3 h (**a**, **c**) or the indicated durations (**b**). Cell lysates were subjected to western blotting with specified antibodies. **d**, AhR-ligand-induced ubiquitination of ER-α. MCF-7 cells were incubated with the indicated ligands for 6 h. Western blots were subjected to dark exposure to detect poly-ubiquitinated forms of the receptors. IP, immunoprecipitation; Ub, ubiquitin. **e**, **f**, Biochemical separation and identification of AhR-associated complexes. Flag–AhR-associated proteins in the presence of 3MC or α-NF from HeLa cells stably expressing Flag–AhR were first fractionated by glycerol-density-gradient centrifugation (top, fractions 1–12), and then separated by Toyopearl AF-

heparin column chromatography with the indicated KCl concentrations (FT, 1.0 M KCl). Samples from the 3MC-treated cells were resolved into five distinct complexes. IB, immunoblotting. **g**, Components of an AhR-associated complex are highly ubiquitinated. Western blots with anti-ubiquitin antibody. **h**, Identification of AhR-associated CUL4B ubiquitin ligase complex components. Components of complex B in **e** (fractions 4 and 5 from the glycerol-density-gradient centrifugation, eluted from an AF-heparin column at 0.4 M KCl) were resolved by SDS-PAGE, silver-stained and identified by matrix-assisted laser desorption/ionization–time-of-flight MS analysis. **i**, Co-elution of the complex B components as a large complex. **j**, Association of activated AhR with the CUL4B complex. The CUL4B^{AhR} complex from Flag–AhR-expressing HeLa cells treated with 3MC was affinity purified with GST-tagged N-terminal domain of CUL4B followed by anti-Flag antibody column fractionation.

acidic domain (AhR Δ acid; Supplementary Fig. S6a) was indeed unable to promote ER- α ubiquitination *in vivo*, although the mutant retained 3MC-dependent transactivation function (Supplementary Fig. S5c). This indicates that the ubiquitin ligase function of AhR is independent of its transactivation function.

With two separately prepared components of recombinant AhR and CUL4B/DDB1/Rbx1 purified from *Spodoptera frugiperda* (Sf9) cells (Supplementary Fig. S7a), complex assembly *in vitro* was also

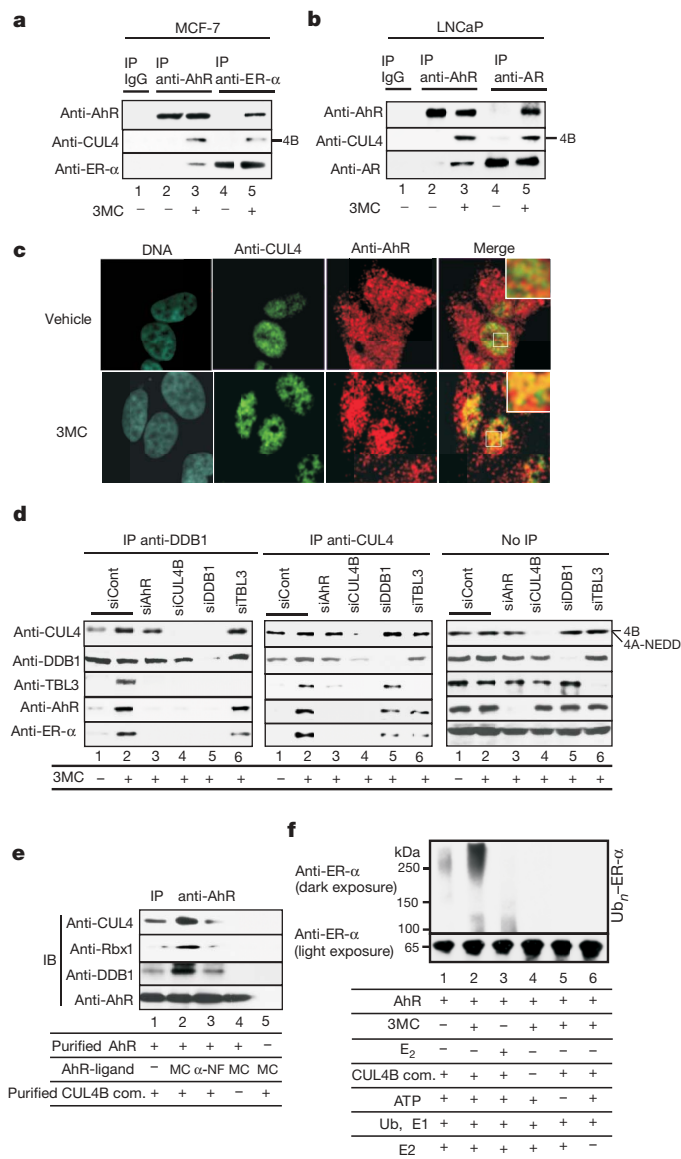


Figure 2 | AhR ligand-dependent assembly and ubiquitin ligase activity of CUL4B^{AhR}. **a, b**, 3MC-dependent association of endogenous CUL4B and AhR with ER- α and AR. Co-immunoprecipitation analyses from MCF-7 (**a**) and LNCaP (**b**) cells incubated with ligand and MG132 for 2 h. IP, immunoprecipitation. **c**, 3MC-dependent co-localization of AhR with CUL4B. MCF-7 cells incubated with 3MC and MG132 for 2 h were immunostained with the indicated antibodies. **d**, Formation of the CUL4B^{AhR} complex. MCF-7 cells were transfected with specified short interfering RNAs (siRNAs) for 48 h, treated with 3MC and MG132 for 2 h, and immunoprecipitated with the indicated antibodies. **e**, Assembly of the CUL4B complex components with AhR is dependent on 3MC *in vitro*. Immunoprecipitation with anti-AhR antibodies of the indicated recombinant CUL4B complex components (CUL4B com.) was observed only in the presence of 3MC. IB, immunoblotting. **f**, CUL4B^{AhR} ubiquitinates ER- α *in vitro*. ER- α protein was incubated with and without recombinant CUL4B^{AhR} E3 complex components, ubiquitin (Ub), ATP, E1 and E2 enzymes as indicated, then subjected to western blotting.

dependent on 3MC (Fig. 2e). Furthermore, by *in vitro* ubiquitination assay (Supplementary Fig. S7b), the E3 ubiquitin ligase activity of CUL4B^{AhR} for ER- α was dependent on 3MC but not on 17 β -oestradiol (E₂) (Fig. 2f). These data indicate that both the complex assembly and the ubiquitin ligase activity of CUL4B^{AhR} may be dependent on AhR agonists.

We then examined whether the recognition of sex steroid receptors for 3MC-dependent ubiquitination is indeed mediated by AhR. Co-immunoprecipitation analyses indicated that ligand-activated AhR was required for the recruitment of ER- α (Fig. 2a, d) or AR (Fig. 2b, and data not shown) to CUL4B^{AhR}. TBL3 and DDB1 did not seem essential for ER- α recruitment but stabilized the association of ER- α with CUL4B^{AhR} (Fig. 2d). Moreover, knockdown of CUL4B^{AhR} components (Supplementary Fig. S8) impaired the 3MC-induced ubiquitination and degradation of ER- α (Fig. 3a–d, and Supplementary Fig. S9a, b) and AR (Fig. 3e, Supplementary Fig. S9c and data not shown), and abolished the AhR-ligand-induced repression of ER- α transactivation (Supplementary Fig. S10a). Recognition of ER- α by activated AhR was retained, but ubiquitination of AhR-bound ER- α was abrogated, by knockdown of the other CUL4B^{AhR} components (Fig. 3d). An ER- α Δ A/B mutant¹⁵ that lacks interaction with AhR, and an ER- α K7R mutant in which seven lysine residues had been replaced with arginine (Supplementary Fig. S6b), were resistant to AhR-dependent ubiquitination and transrepression (Fig. 3f, and Supplementary Fig. S10b). Taken together, these data suggest that ligand-activated AhR functions as a substrate-specific adaptor component of CUL4B^{AhR}. AhR is therefore a unique and atypical substrate-specific component of a cullin-based E3 complex, because AhR bears no known interaction motif with cullin complexes yet associates directly with CUL4B. Ubiquitination of ER- α -associated AhR was similarly abolished by the knockdown, and the overall ubiquitination and degradation of AhR^{8,17,18} were partly affected (Supplementary Fig. S11a, b). This implies the existence of CUL4B^{AhR}-dependent (self-ubiquitination³) and CUL4B^{AhR}-independent pathways for AhR degradation.

Human ER- α (hER- α) degradation is reportedly accelerated by the binding of E₂ (ref. 1) or the phosphorylation of Ser 118 (ref. 28), whereas a partial antagonist, tamoxifen, has been shown to stabilize ER- α ¹. Nevertheless, 3MC-activated AhR efficiently induced the ubiquitination and subsequent degradation of tamoxifen-bound ER- α and ER- α -S118A mutant (Fig. 3f). Reciprocally, AhR was dispensable for E₂-dependent ER- α degradation (Supplementary Fig. S11c). These results indicate that the CUL4B^{AhR} system may act independently of innate protein degradation system(s) for ER- α . XAP2/ARA9/AIP^{7,8,17}, a chaperone that modulates the stability of unliganded AhR, seemed unlikely to mediate the accelerated degradation of ER- α by activated AhR (Supplementary Fig. S11d).

Last, we addressed the physiological significance of CUL4B^{AhR} for sex hormone signalling in intact animals. Injection with either 3MC (Fig. 4a) or β -NF (Fig. 4c) did not affect the expression of ER- α or AR mRNA (data not shown) but caused a decrease in protein levels of uterine ER- α in ovariectomized female wild-type mice and of prostate AR in castrated male wild-type mice (Fig. 4b) regardless of their treatment with cognate sex hormones. However, AhR deficiency (AhR^{-/-} mice)^{9,14} abolished such effects of AhR ligands but did not affect the modulation of stability of sex steroid receptors by their respective hormones (Fig. 4a, b). As a result of reduced sex steroid receptor levels after pretreatment with 3MC, E₂-dependent induction of *c-fos* in the uterus¹⁵ and dihydrotestosterone (DHT)-dependent induction of *Probasin* in the prostate¹⁰ were severely impaired (Fig. 4a, b). Cellular proliferation and gene induction in response to sex hormones in primary cultured epithelial cells from normal mouse uterus and prostate were consistently suppressed by 3MC (Supplementary Fig. S12a, b) and β -NF (Supplementary Fig. S12c), but no effect was detected in AhR^{-/-} cells (Supplementary Fig. S12a, b). The significance of CUL4B^{AhR} complex components in the AhR-mediated suppression of sex hormone effects

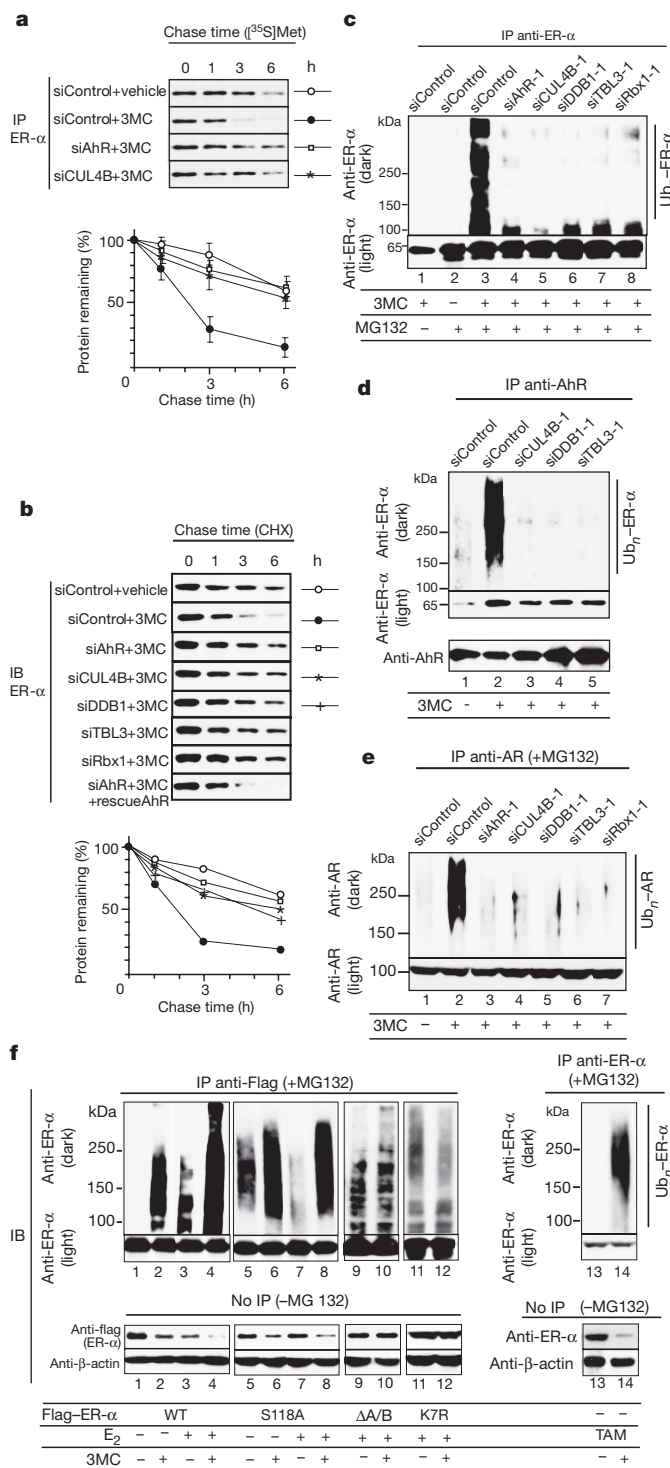


Figure 3 | Activated AhR is a substrate-specific adaptor component of the CUL4B^{AhR} complex. **a–c**, Components of CUL4B^{AhR} are required for 3MC-dependent ubiquitination and degradation of ER- α . MCF-7 cells were transfected with indicated siRNAs for 48 h, then used in pulse-chase analysis as in Supplementary Fig. S3d (**a**), in cycloheximide (CHX) chasing (**b**) and in the *in vivo* ubiquitination assay with ligand incubation for 6 h (**c**). All values are shown as means \pm s.d. ($n = 3$) (**a**) or as means ($n = 3$) (**b**). The knockdown efficiency in the same lysates was confirmed in Supplementary Fig. S9a. IB, immunoblotting; IP, immunoprecipitation. **d**, AhR is the substrate-specific adaptor in the targeting of ER- α by CUL4B^{AhR}. MCF-7 cells transfected with the indicated siRNAs were lysed in TNE buffer and immunoprecipitated with anti-AhR antibody in the presence of MG132. Ubiquitination of the ER- α co-immunoprecipitated with AhR was detected by western blotting. **e**, LNCaP cells were subjected to the same analysis as in **a–c**. **f**, AhR-ligand-induced ER- α ubiquitination requires intact lysine

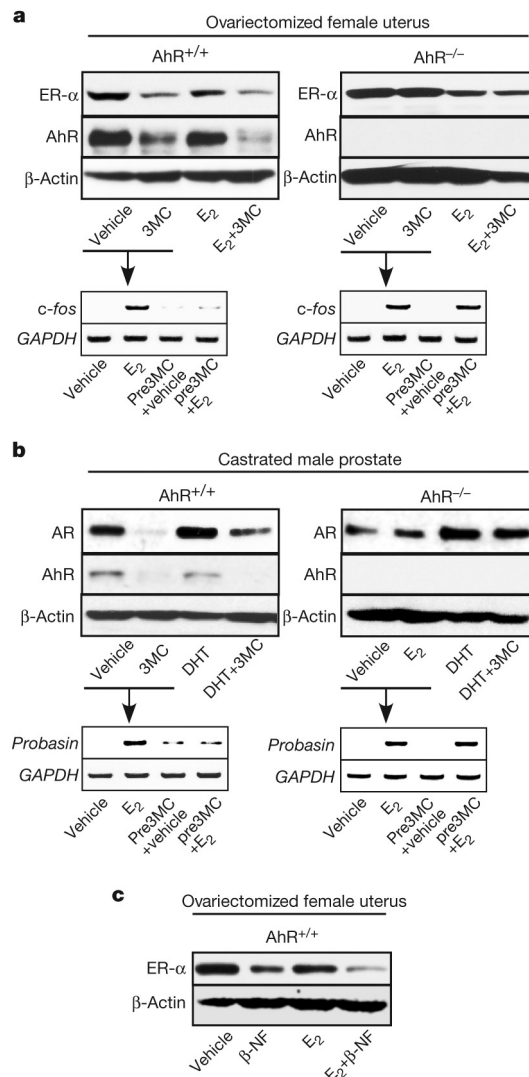


Figure 4 | Ligand-dependent ubiquitin ligase function of AhR *in vivo*. **a, b**, AhR activation enhances the degradation of ER- α and AR *in vivo*. Top: nine-week-old ovariectomized female mice (**a**) or castrated male mice (**b**) of the indicated genotypes were injected with vehicle or indicated ligands. After 4 h, uterus (**a**) or ventral prostate (**b**) was isolated and subjected to western blotting. Bottom: mice pretreated with vehicle or 3MC for 8 h were injected with either vehicle or E₂ (**a**), or DHT (**b**). After 4 h, the uterus or prostate was isolated for reverse transcriptase PCR. GAPDH, glyceraldehyde-3-phosphate dehydrogenase. **c**, Other AhR agonists produce a similar effect on oestrogen signalling to that of 3MC.

(Supplementary Fig. S12a, b) and the promotion of ER- α degradation in uterine cells (Supplementary Fig. S12d) was verified by knock-down of the components.

Here we have shown that a known sequence-specific transcription factor AhR acts as a ligand-dependent CUL4B-based E3 ubiquitin ligase for selectively targeting sex steroid receptors to bring about accelerated protein degradation. The transcription and ubiquitination functions of AhR seem to be responsible for a distinct set of biological events caused by endogenous and exogenous AhR ligands. In ubiquitin ligase complexes, substrate recognition by known

residues and is independent of oestrogen binding or S118 phosphorylation of hER- α . Intact MCF-7 cells (right) or cells transfected with Flag-hER- α , AhR and their derivatives (left) were treated with the indicated ligands in the presence (top) or absence (bottom) of MG132 for 6 h, then subjected to western blotting. TAM, tamoxifen; WT, wild type.

substrate-specific components is generally evoked by substrate modifications^{2–4}. However, the recognition and subsequent ubiquitination of sex steroid receptors by AhR requires dioxin-type compounds as ligands but does not require the phosphorylation or ligand binding of sex steroid receptors. We have therefore shown that fat-soluble ligands directly control the function of a ubiquitin ligase complex for targeted protein destruction in animals (see Supplementary Fig. S1). In plants, auxin was recently found to control protein destruction through the auxin receptor SCF^{TIR1} (refs 29, 30). However, whereas SCF^{TIR1} is regulated by ligand-dependent substrate recognition by TIR1, CUL4B^{AhR} is primarily regulated by the assembly of a ligand-dependent complex as well as substrate recognition. Considered together, ubiquitin-ligase-based perception mechanisms of fat-soluble ligands may be diverse in different species. It is possible that other nuclear receptors and binding proteins for fat-soluble ligands also serve as key components of ubiquitin ligases to mediate a non-genomic pathway of fat-soluble ligands to regulate target-protein-selective destruction.

METHODS

More detailed descriptions of all materials and methods are supplied in the Supplementary Information.

Biochemical purification and separation of AhR-associated complexes. The nuclear extracts preparation, anti-Flag affinity purification and mass spectrometry were performed as described previously^{15,20}. For purification of the core CUL4B^{AhR} complex, the nuclear extracts were first bound to the GST–CUL4B–N (amino acid residues 1–318) columns before being loaded on anti-Flag columns²⁰.

In vitro ubiquitination assay. The *in vitro* ubiquitination assay was performed as described previously²³. Purified Flag–AhR (0.2 µg) was incubated either with 3MC (10 µM) or vehicle (dimethylsulphoxide) for 30 min at 25 °C, then mixed with Flag–CUL4B/DDB1/Rbx1 complex (0.2 µg), and after further incubation for 30 min at 25 °C the substrate, ER-α (Calbiochem), was added.

Plasmids, antibodies, immunoprecipitation, in vivo ubiquitination, pulse-chasing, ligand responses in mice, and RNA-mediated interference experiments. Detailed methods used in this study can be found in the Supplementary Information.

Received 13 December 2006; accepted 16 February 2007.

- McKenna, N. J. & O'Malley, B. W. Combinatorial control of gene expression by nuclear receptors and coregulators. *Cell* **108**, 465–474 (2002).
- Hershko, A. & Ciechanover, A. The ubiquitin system. *Annu. Rev. Biochem.* **67**, 425–479 (1998).
- Deshais, R. J. SCF and Cullin/Ring H2-based ubiquitin ligases. *Annu. Rev. Cell Dev. Biol.* **15**, 435–467 (1999).
- Harper, J. W. A phosphorylation-driven ubiquitination switch for cell-cycle control. *Trends Cell Biol.* **12**, 104–107 (2002).
- Poellinger, L. Mechanistic aspects—the dioxin (aryl hydrocarbon) receptor. *Food Addit. Contam.* **17**, 261–266 (2000).
- Hankinson, O. The aryl hydrocarbon receptor complex. *Annu. Rev. Pharmacol. Toxicol.* **35**, 307–340 (1995).
- Swanson, H. I. & Bradfield, C. A. The AH-receptor: genetics, structure and function. *Pharmacogenetics* **3**, 213–230 (1993).
- Carlson, D. B. & Perdew, G. H. A dynamic role for the Ah receptor in cell signaling? Insights from a diverse group of Ah receptor interacting proteins. *J. Biochem. Mol. Toxicol.* **16**, 317–325 (2002).
- Mimura, J. & Fujii-Kuriyama, Y. Functional role of AhR in the expression of toxic effects by TCDD. *Biochim. Biophys. Acta* **1619**, 263–268 (2003).
- Lin, T. M. *et al.* Effects of aryl hydrocarbon receptor null mutation and in utero and lactational 2,3,7,8-tetrachlorodibenzo-*p*-dioxin exposure on prostate and seminal vesicle development in C57BL/6 mice. *Toxicol. Sci.* **68**, 479–487 (2002).
- Brunnberg, S. *et al.* The basic helix–loop–helix–PAS protein ARNT functions as a potent coactivator of estrogen receptor-dependent transcription. *Proc. Natl Acad. Sci. USA* **100**, 6517–6522 (2003).

- Matthews, J., Wihlen, B., Thomsen, J. & Gustafsson, J. A. Aryl hydrocarbon receptor-mediated transcription: ligand-dependent recruitment of estrogen receptor α to 2,3,7,8-tetrachlorodibenzo-*p*-dioxin-responsive promoters. *Mol. Cell. Biol.* **25**, 5317–5328 (2005).
- Beischlag, T. V. & Perdew, G. H. ER α -AHR-ARNT protein–protein interactions mediate estradiol-dependent transrepression of dioxin-inducible gene transcription. *J. Biol. Chem.* **280**, 21607–21611 (2005).
- Baba, T. *et al.* Intrinsic function of the aryl hydrocarbon (dioxin) receptor as a key factor in female reproduction. *Mol. Cell. Biol.* **25**, 10040–10051 (2005).
- Ohtake, F. *et al.* Modulation of oestrogen receptor signalling by association with the activated dioxin receptor. *Nature* **423**, 545–550 (2003).
- Romkes, M., Piskorska-Pliszczynska, J. & Safe, S. Effects of 2,3,7,8-tetrachlorodibenzo-*p*-dioxin on hepatic and uterine estrogen receptor levels in rats. *Toxicol. Appl. Pharmacol.* **87**, 306–314 (1987).
- Davarinos, N. A. & Pollenz, R. S. Aryl hydrocarbon receptor imported into the nucleus following ligand binding is rapidly degraded via the cytoplasmic proteasome following nuclear export. *J. Biol. Chem.* **274**, 28708–28715 (1999).
- Roberts, B. J. & Whitelaw, M. L. Degradation of the basic helix–loop–helix/Per-ARNT-Sim homology domain dioxin receptor via the ubiquitin/proteasome pathway. *J. Biol. Chem.* **274**, 36351–36356 (1999).
- Maxwell, P. H. *et al.* The tumour suppressor protein VHL targets hypoxia-inducible factors for oxygen-dependent proteolysis. *Nature* **399**, 271–275 (1999).
- Kitagawa, H. *et al.* The chromatin-remodeling complex WINAC targets a nuclear receptor to promoters and is impaired in Williams syndrome. *Cell* **113**, 905–917 (2003).
- Zhong, W., Feng, H., Santiago, F. E. & Kipreos, E. T. CUL-4 ubiquitin ligase maintains genome stability by restraining DNA-replication licensing. *Nature* **423**, 885–889 (2003).
- Higa, L. A. *et al.* CUL4–DDB1 ubiquitin ligase interacts with multiple WD40-repeat proteins and regulates histone methylation. *Nature Cell Biol.* **8**, 1277–1283 (2006).
- Groisman, R. *et al.* The ubiquitin ligase activity in the DDB2 and CSA complexes is differentially regulated by the COP9 signalosome in response to DNA damage. *Cell* **113**, 357–367 (2003).
- Wertz, I. E. *et al.* Human De-etiolated-1 regulates c-Jun by assembling a CUL4A ubiquitin ligase. *Science* **303**, 1371–1374 (2004).
- Jin, J., Arias, E. E., Chen, J., Harper, J. W. & Walter, J. C. A family of diverse Cul4–Ddb1-interacting proteins includes Cdt2, which is required for S phase destruction of the replication factor Cdt1. *Mol. Cell* **23**, 709–721 (2006).
- Angers, S. *et al.* Molecular architecture and assembly of the DDB1–CUL4A ubiquitin ligase machinery. *Nature* **443**, 590–593 (2006).
- He, Y. J., McCall, C. M., Hu, J., Zeng, Y. & Xiong, Y. DDB1 functions as a linker to recruit receptor WD40 proteins to CUL4–ROC1 ubiquitin ligases. *Genes Dev.* **20**, 2949–2954 (2006).
- Valley, C. C. *et al.* Differential regulation of estrogen-inducible proteolysis and transcription by the estrogen receptor alpha N terminus. *Mol. Cell. Biol.* **25**, 5417–5428 (2005).
- Dharmasiri, N., Dharmasiri, S. & Estelle, M. The F-box protein TIR1 is an auxin receptor. *Nature* **435**, 441–445 (2005).
- Kepinski, S. & Leyser, O. The *Arabidopsis* F-box protein TIR1 is an auxin receptor. *Nature* **435**, 446–451 (2005).

Supplementary Information is linked to the online version of the paper at www.nature.com/nature.

Acknowledgements We thank K. Tanaka, C. K. Glass, J. Yanagisawa, Y. Gotoh and J. Mimura for comments; S. Murata, T. Matsuda, T. Suzuki and Y. Tateishi for providing materials; T. Matsumoto, M. Igarashi and S. Fujiyama for technical assistance; and H. Higuchi for manuscript preparation. This work was supported in part by the Program for Promotion of Basic Research Activities for Innovative Biosciences (PROBRAIN) and priority areas from the Ministry of Education, Culture, Sports, Science and Technology (to Y.F.-K. and S.K.).

Author Contributions F.O., T.C., Y.F.-K. and S.K. designed the experiments. F.O., A.B., M.O., K.I., H.M., S.T. and I.T. performed the experiments. F.O., A.K. and S.K. wrote the paper.

Author Information Reprints and permissions information is available at www.nature.com/reprints. The authors declare no competing financial interests. Correspondence and requests for materials should be addressed to S.K. (uskato@mail.ecc.u-tokyo.ac.jp).

Structure of the yeast polarity protein Sro7 reveals a SNARE regulatory mechanism

Douglas A. Hattendorf¹, Anna Andreeva², Akanksha Gangar², Patrick J. Brennwald² & William I. Weis¹

Polarized exocytosis requires coordination between the actin cytoskeleton and the exocytic machinery responsible for fusion of secretory vesicles at specific sites on the plasma membrane¹. Fusion requires formation of a complex between a vesicle-bound R-SNARE and plasma membrane Qa, Qb and Qc SNARE proteins². Proteins in the lethal giant larvae protein family, including lethal giant larvae and tomosyn in metazoans and Sro7 in yeast, interact with Q-SNAREs and are emerging as key regulators of polarized exocytosis³. The crystal structure of Sro7 reveals two seven-bladed WD40 β -propellers followed by a 60-residue-long 'tail', which is bound to the surface of the amino-terminal propeller. Deletion of the Sro7 tail enables binding to the Qbc SNARE region of Sec9 and this interaction inhibits SNARE complex assembly. The N-terminal domain of Sec9 provides a second, high-affinity Sro7 interaction that is unaffected by the tail. The results suggest that Sro7 acts as an allosteric regulator of exocytosis through interactions with factors that control the tail. Sequence alignments indicate that lethal giant larvae and tomosyn have a two- β -propeller fold similar to that of Sro7, but only tomosyn appears to retain the regulatory tail.

Growth of the bud during cell division in *Saccharomyces cerevisiae* requires polarized vesicle fusion at the bud tip¹. Sro7, a 1,033-residue protein, is part of the cellular machinery that facilitates this process⁴. Physical and genetic interactions exist between Sro7 and other exocytic proteins, including SNAREs, exocyst subunits and the Rab GTPase Sec4 (refs 4–6). In addition, Sro7 suppresses mutations in Rho3 and Cdc42, two Rho GTPases necessary for exocytosis and polarization of the actin cytoskeleton, and in Myo2, a myosin involved in vesicle transport^{7–9}. Genetic analysis places Sro7 function downstream of the GTPases and the exocyst⁵. However, the molecular mechanism of Sro7 in polarized bud growth remains unclear.

Like Sro7, lethal giant larvae (LGL) and tomosyn regulate targeted delivery of secretory vesicles. LGL acts during establishment of polarity in epithelial cells and asymmetric neuroblast division^{3,10}, and tomosyn functions in the presynaptic nerve terminal to inhibit priming of synaptic vesicles^{11,12}. Sro7, LGL and tomosyn each physically interact with Q-SNARE proteins, but with different specificities. Sro7 binds to Sec9 (ref. 4), which has both Qb and Qc SNARE motifs, whereas LGL binds to syntaxin 4, a Qa-SNARE¹³. Tomosyn has an R-SNARE motif at its carboxy terminus that substitutes for synaptobrevin in the neuronal SNARE complex^{14,15}. Sro7 and LGL lack this R-SNARE motif, although ~40 amino acids at the extreme C terminus of Sro7 are predicted to form an α -helix of unknown function¹⁵.

We determined the crystal structure of a proteolytic fragment of *S. cerevisiae* Sro7, spanning residues 61–962, at 2.4 Å resolution. The final model includes residues 62–582 and 598–951. The sequence containing the predicted α -helix at the C terminus was protease-sensitive and is absent from the crystallized fragment. The structure

consists of 14 WD40 repeats distributed throughout almost the entire sequence, followed by a 60-residue tail (Fig. 1a–d). The WD40 repeats fold into two seven-bladed β -propeller domains with a topology similar to Aip1 (refs 16, 17). Blades 1–7 form the N-terminal domain, and blades 8–14 form the C-terminal domain. Each blade is an antiparallel β -sheet, typically comprising four β -strands labelled A to D. The bottom surface of each propeller is formed by the A–B and C–D loops, and the top surfaces are formed by the B–C and D–A loops.

The β -propeller domains are arranged to resemble a twisted, open clamshell. A notable feature of the domain interface is the amphipathic 7C–8A loop, which is buried between the two domains (Fig. 1c). Its hydrophobic face packs against the N-terminal β -propeller (Supplementary Fig. 1a), and its hydrophilic face interacts with the C-terminal β -propeller through an extensive network of direct and water-mediated hydrogen bonds (Supplementary Fig. 1b). Another feature of the interface is the 8AB loop, which is anchored by a hydrophobic α -helix that binds to the C-terminal β -propeller and which contains an extended 23-residue region that wraps around the 1AB and 8CD loops at the bottom side of the domain interface (Supplementary Fig. 1c). Leu 490 and Leu 491 in the extended region act as a second anchor by packing into a hydrophobic pocket formed by residues in the N-terminal β -propeller and the 7C–8A loop (Supplementary Fig. 1a).

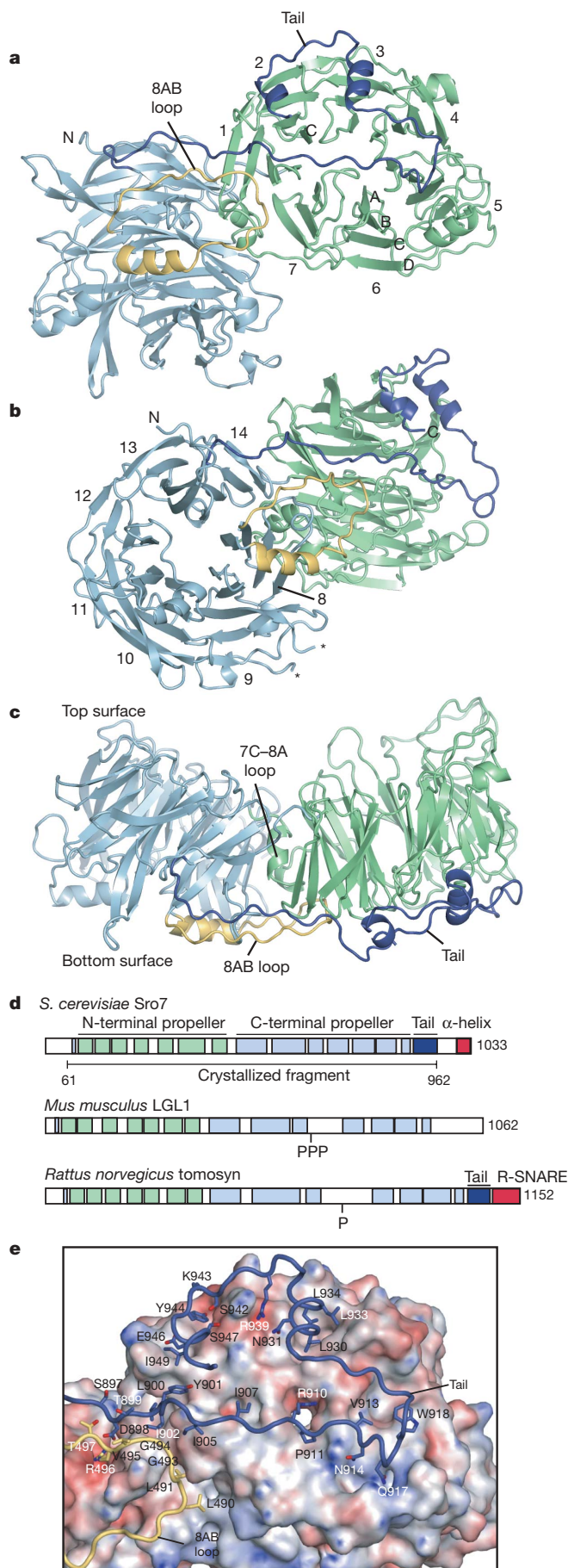
The Sro7 tail (residues 892–951) is bound to the bottom surface of the N-terminal β -propeller (Fig. 1e). The binding interface is extensive, with 4,356 Å² of buried surface area. The base of the tail (residues 898–901) binds to a pocket with one side formed by residues 492–497 of the 8AB loop, which links the tail to the domain interface. The tail spans the entire propeller once in an extended conformation, then again as two short α -helices separated by a 10-residue linker. The second α -helix (residues 945–949) forms the other side of the binding pocket for tail residues 898–901.

Sequence alignment of Sro7 with tomosyn and LGL shows significant conservation in the 14 WD40 repeats and in many elements of the domain interface (Fig. 1d and Supplementary Fig. 2). The metazoan proteins have insertions in the 10D–11A loop that contain phosphorylation sites implicated in their regulation^{18,19}. Notably, many residues in the Sro7 tail that interact with the N-terminal propeller (Fig. 1e) are conserved in tomosyn, but not in LGL. This divergence is also reflected in residues that form the binding site for the tail: they are conserved in the yeast (Fig. 2a) and tomosyn subfamilies, but vary among the LGL proteins (Supplementary Fig. 2). In certain positions, co-variation of residues in the tail and its binding site in tomosyn seem to preserve the contacts observed in Sro7.

The binding site for the tail on Sro7 is largely hydrophilic (Fig. 1e), suggesting that the tail serves a regulatory rather than a structural role. The effect of deleting the Sro7 tail on binding of Sec9 was

¹Departments of Structural Biology and of Molecular and Cellular Physiology, Stanford University School of Medicine, 299 Campus Drive West, Stanford, California 94305-5126, USA.

²Department of Cell and Developmental Biology, University of North Carolina, 538 Taylor Hall, Chapel Hill, North Carolina, 27599-7090, USA.



measured by isothermal titration calorimetry (ITC; Supplementary Fig. 3 and Supplementary Table 2). An Sro7 variant lacking the tail, Sro7(61–891), binds to Sec9 with 3.3-fold higher affinity ($K_d = 800$ nM) and with a 2.3-fold more favourable enthalpy change than either wild-type Sro7 or the crystallization construct Sro7(61–962), which contains the tail. Thus, the tail has an autoinhibitory effect on Sro7 binding to Sec9.

To understand this effect of the tail, we first defined the regions of Sec9 that bind to Sro7 using a yeast two-hybrid assay. Sec9 has a 413-residue N-terminal domain that is not required for growth²⁰, followed by the essential C-terminal region that contains the Qb and Qc SNARE motifs, designated the Qbc-SNARE domain (Supplementary Fig. 4a). The N-terminal domain interacts strongly with Sro7, whereas the Qbc-SNARE domain shows a weaker interaction (Supplementary Fig. 4a). Residues 255–343 in the N-terminal domain were necessary for the high-affinity interaction, because their deletion reduced binding to the level of the isolated Qbc domain. The region of Sec9 necessary for suppression of the *sec4-P48* mutation²⁰ (residues 3–82; Supplementary Fig. 4a) is distinct from the high-affinity Sro7 binding site. The two-hybrid results were confirmed by co-immunoprecipitation (Supplementary Fig. 4b). Deletion of residues 255–343 of Sec9 reduced the amount of Sro7 precipitated with Sec9, but a significant fraction of Sro7 was still associated with the Sec9 mutant.

On the basis of the results of the two-hybrid assay and additional mapping experiments (see Supplementary Methods), a fragment of the Sec9 N-terminal domain was purified to measure its binding to Sro7 *in vitro*. Sec9(250–372) bound to Sro7(61–962) with a K_d of 3 μ M, identical to that of full-length Sec9 (Supplementary Fig. 3 and Supplementary Table 2). Significantly, deletion of the Sro7 tail had no effect on binding of Sec9(250–372) (Supplementary Fig. 3 and Supplementary Table 2). To locate the binding site for the Sec9 N-terminal domain fragment, we examined the conservation of Sro7 surface residues. In addition to the highly conserved tail-binding site (Fig. 2a), there is a second cluster of conserved residues in a shallow groove formed by the A–B and C–D loops of blades 9–12 (Fig. 2b). Of six mutations in the second cluster, two (Y700A and P721A) abolished binding to Sec9(250–372), and three others (E562A, R664A and M764A) each caused a nearly tenfold reduction of the binding affinity (Supplementary Fig. 5 and Supplementary Table 2).

Next, binding of the Sec9 Qbc domain to Sro7 was assessed *in vitro*. In this case, binding was only observed if the Sro7 tail was deleted (Fig. 3a). This interaction was detectable by ITC (Supplementary Fig. 3), but the low affinity and small enthalpy change prevented a precise determination of the binding thermodynamics. Nonetheless, two independent titrations indicated a K_d of approximately 50 μ M. These results indicate that in wild-type Sro7, the tail masks the

Figure 1 | Overview of the Sro7 structure. **a–c**, The N-terminal β -propeller is light green, the C-terminal β -propeller is light blue, the 8AB loop is yellow, and the tail is dark blue. **a**, View of the bottom surface of Sro7, along the axis of the N-terminal β -propeller. WD40 blades 1–7, β -strands A–D of blade 6, the 8AB loop and the tail are labelled. **b**, View along the axis of the C-terminal β -propeller. WD40 blades 8–14 are labelled. Asterisks mark the loop of blade 9 that is not visible in the structure (residues 583–597). **c**, Side-view of the structure; the interface loops and the tail are labelled. **d**, Schematic of the structure-based sequence alignment of the LGL family. Structural elements are coloured as in **a–c**. The predicted C-terminal α -helix in Sro7 and the R-SNARE of tomosyn are shown in red. Light green and light blue boxes correspond to the WD40 blades as observed structurally, rather than the standard definition of a WD40 repeat; that is, strand D of one blade and strands A–C of the next blade. Note that strand 14D is located near the N-terminus of Sro7, before strand 1A, and is indicated by a narrow blue box. Phosphorylation sites in tomosyn and LGL are marked by 'P'. **e**, The Sro7 tail-binding site, with the structure oriented as in panel **a**. The β -propeller domains are shown in surface representation and coloured by electrostatic potential²⁵ in the range of $-10kT/e$ (red) to $10kT/e$ (blue). The tail and the 8AB loop are shown as ribbons. Side chains in the tail that interact with the N-terminal domain are shown as sticks. Side chains in the 8AB loop that form part of the tail-binding site are also shown.

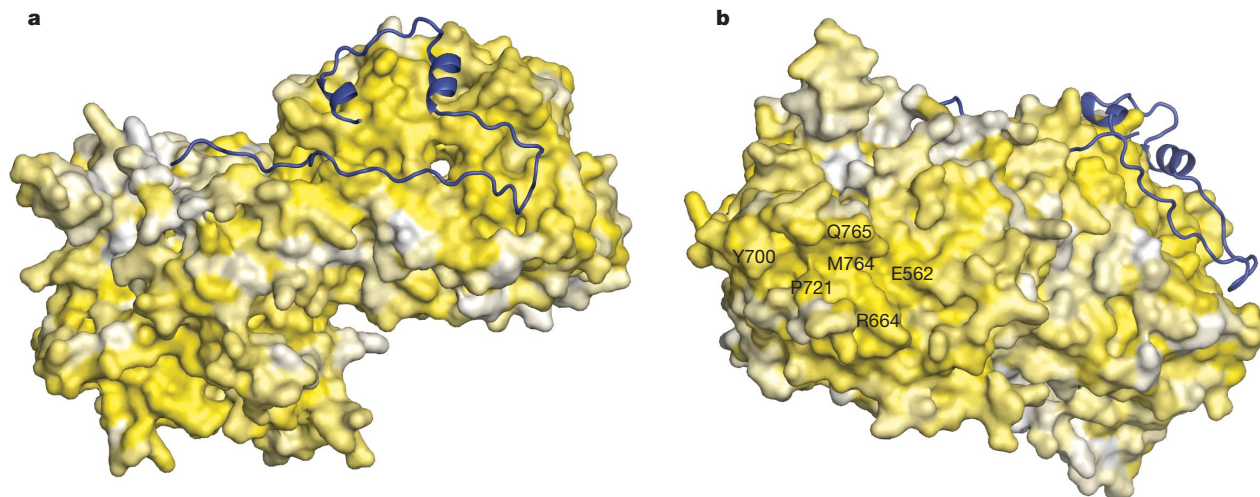


Figure 2 | Surface representation of Sro7, with residues coloured from white to yellow by increasing conservation. The brightest yellow represents 100% identity. Because the Sec9 N-terminal domain is unique to the *Saccharomycotina* subphylum of fungi, the sequences used were limited to species in this subphylum (*S. cerevisiae*, *Candida glabrata*, *Cluyveromyces lactis*, *Ashbya gossypii*, *Yarrowia lipolytica*, *Candida albicans* and

Debaryomyces hansenii). The tail is shown as a dark blue ribbon. Conservation scores were calculated with ConSurf²⁶. **a**, View along the axis of the N-terminal β -propeller, as in Fig. 1a, showing the conservation of the tail-binding site. **b**, Structure rotated from **a** to show the second conserved site on the C-terminal β -propeller. Residues that were mutated to alanine are labelled on the surface.

Qbc-SNARE binding site, either by direct competition or through an allosteric mechanism. This interaction is not entirely specific to Sec9, because the SNARE domain of the Qa-SNARE Sso1 (residues 193–265) also binds Sro7(61–891), albeit more weakly (Supplementary Fig. 6a).

Sro7(61–891) did not bind to the pre-assembled SNARE complex of GST–Sec9 Qbc-SNARE, the Qa-SNARE Sso1 and the R-SNARE Snc2 (Fig. 3a). In a kinetic assay, Sro7(61–891) slowed SNARE

complex assembly fourfold relative to assembly reactions lacking Sro7 or containing Sro7(61–962) (Fig. 3b and Supplementary Fig. 6b). Thus, Sro7(61–891) binds to the Sec9 Qbc-SNARE domain in a manner that competes with SNARE complex formation. At the concentrations used in the kinetic assay, approximately 60% of the Sro7 and full-length Sec9 are expected to be in a complex, whereas almost no complex would exist in the absence of the Sec9 N-terminal domain. The Sec9 N-terminal domain may act as a high-affinity

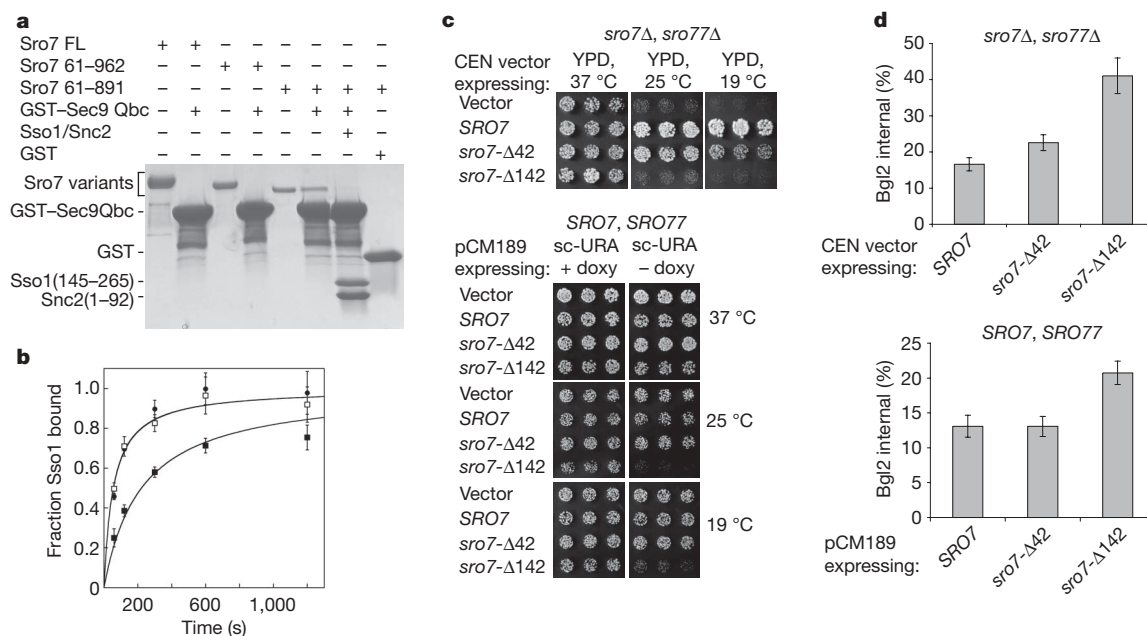


Figure 3 | Interaction of Sec9 with Sro7. **a**, GST pull-down assays of binding of Sro7 variants to the GST–Sec9 Qbc-SNARE domain. A gel stained with Coomassie blue is shown. **b**, Fraction of Sso1(145–265) pulled down by GST–Sec9 as a function of time in the absence of Sro7 (filled circles), or presence of Sro7(61–962) (open squares) or Sro7(61–891) (filled squares). Error bars, s.d.; $n = 3$. Data were fitted to a second-order rate equation (see Supplementary Information). In the absence of Sro7, the rate constant is $7,300 \pm 1,200 \text{ M}^{-1} \text{ s}^{-1}$, which is very similar to that previously determined using a circular dichroism assay for assembly²⁷. Sro7(61–962) had no effect on assembly (rate constant of $7,200 \pm 700 \text{ M}^{-1} \text{ s}^{-1}$, whereas Sro7(61–891)

reduced the rate constant to $1,800 \pm 200 \text{ M}^{-1} \text{ s}^{-1}$. **c**, The effect of *SRO7* tail-deletion mutants on growth. The top panel shows the ability of *SRO7* alleles to complement the cold-sensitive growth phenotype of the *sro7Δ, sro77Δ* strain. The bottom panel examines dominant-negative effects of the *SRO7* alleles in wild-type yeast. In each panel, growth of three independent colonies at the permissive (37 °C) and restrictive temperatures (25 °C and 19 °C) is shown. **d**, The effect of *SRO7* alleles on secretion. Graphs show the per cent of the secreted Bgl2 enzyme that remained inside spheroplasted cells in either the *sro7Δ, sro77Δ* strain (top panel) or wild-type strain (bottom panel). Error bars, s.d.; $n = 3$.

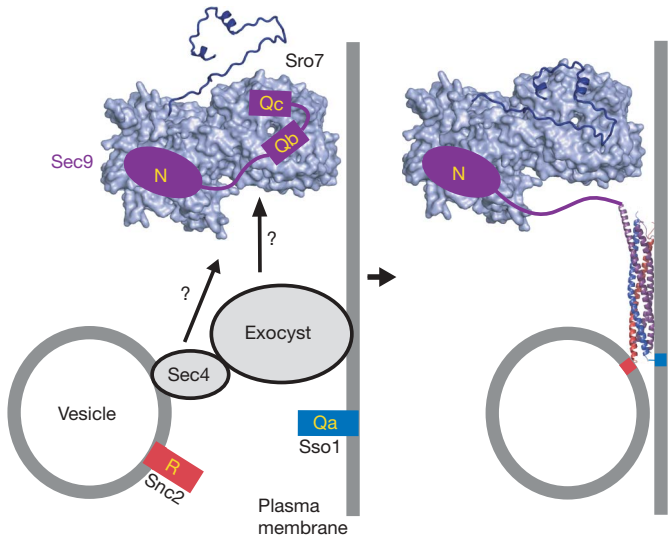


Figure 4 | Proposed model for how Sro7 coordinates release of Sec9 with arrival of a secretory vesicle. The N-terminal and SNARE domains of Sec9 are indicated by N, Qb, and Qc. Although the figure depicts direct binding of the Sec9 Qbc-SNARE domain to the tail-binding site, in the absence of direct structural data it is equally plausible that rebinding of the tail causes a conformational change that displaces the Sec9 Qbc-SNARE domain from a different site. See text for details.

tether for the Qbc-SNARE domain, such that the regulatory interaction between Sro7 and the Qbc domain occurs at a biologically significant concentration. Given the sequence homology among Q-SNAREs²¹, a second, related role may be to increase the specificity of Sro7 for the Qbc-SNARE over Sso1.

The Sro7 mutants that are defective in binding to the Sec9 N-terminal domain had no observable phenotype when expressed in yeast (data not shown), consistent with the fact that this domain is nonessential²⁰. In contrast, deletion of residues 892–1033 (*sro7*-Δ142), which removes the tail, caused a loss-of-function phenotype in a *sro7*Δ,*sro77*Δ strain and a dominant-negative phenotype in the wild-type strain (Fig. 3c). In the complementation assay, the *sro7*-Δ142 mutant was expressed at only 20% of wild-type Sro7 level (Supplementary Fig. 7). However, the mutant does not complement *sro7*Δ,*sro77*Δ even when expressed at a level higher than wild-type

Sro7, from the stronger tetracycline-repressible promoter (data not shown). These phenotypes were specifically associated with removal of the tail that is observed in the structure, because a smaller deletion of the predicted α-helix at the C terminus (residues 987–1,028; *sro7*-Δ42) was a much weaker loss-of-function allele with no dominant-negative effect on growth (Fig. 3c). The growth phenotypes correlated with defects in secretion, monitored by examining the accumulation of internal pools of the secreted enzyme Bgl2 (Fig. 3d). Taken together with the biochemical data, this suggests that the tail is an essential component of Sro7 function during SNARE-mediated exocytosis.

The interaction of wild-type Sro7 with the Sec9 Qbc-SNARE domain *in vivo* suggests that Sro7 exists in two conformational states with different affinities for the tail. The equilibrium between these states may be affected by other factors that regulate Sro7 activity. Such factors could bind the tail directly, or they could bind to a distant site on Sro7 and regulate the tail through an allosteric mechanism. The architecture of Sro7 is suggestive of an allosteric mechanism whereby rearrangements in the β-propeller domain interface that are associated with ligand binding are propagated to the tail through interaction between the tail and the 8AB loop (Fig. 1e and Supplementary Fig. 2).

Unlike other Qb and Qc SNARE proteins, Sec9 does not have a transmembrane domain or palmitoylation sites to tether it to the plasma membrane². Sro7 is associated with the membrane at the bud site⁴, so one role of Sro7 may be to localize Sec9 to the plasma membrane. The mechanism of Sro7 membrane association is unknown, but we suggest that it is coupled to displacement of the tail from its binding site (Fig. 4). In this state, Sro7 could both recruit Sec9 to the eventual site of membrane fusion and inhibit binding to Sso1 and Snc2. A factor that stimulates rebinding of the tail would release the Sec9 Qbc-SNARE domain, allowing SNARE complex assembly to proceed. Sec4 and Exo84 are candidates for such a factor, because they each bind to Sro7 (refs 5, 6) and are both at least partially localized to the vesicle^{22,23}. In this manner, release of Sec9 for SNARE complex formation could be coupled to the arrival of a secretory vesicle at the site of exocytosis.

METHODS

Crystallization and structure determination. Crystals of Sro7 purified from an *S. cerevisiae* overexpression strain were grown at 22 °C in 12% PEG3350, 40 mM MES pH 6.5 and 200 mM NH₄F. During crystallization, Sro7 was cleaved after residues Asn 60, Asn 587, Asn 604 and Asn 962 by a contaminating protease. Phases were determined by single isomorphous replacement with anomalous scattering from a thimerosal derivative of Sro7(61–962). The final model has *R*_{work} and *R*_{free} values of 21.1% and 26.1% at 2.4 Å (Table 1). Details of the crystallographic analysis and statistics are presented as Supplementary Information.

Sro7–Sec9 interaction. Yeast two-hybrid assays, immunoprecipitations and secretion assays were performed essentially as described^{4,7}. For phenotypic analysis, Sro7 constructs were expressed from the *Sro7* promoter on a *CEN-HIS3* plasmid (complementation assay) or from a tetracycline-repressible promoter²⁴ (dominant-negative assay). For pull-down and ITC experiments, Sro7 constructs were purified from *S. cerevisiae* and Sec9 constructs were purified from *Escherichia coli*. ITC was performed at 25 °C by injecting Sec9 at 80 to 200 μM into the ITC cell containing Sro7 at 4 to 10 μM. N-terminal GST fusion proteins immobilized on glutathione-agarose were used for pull-down assays. The rate of SNARE complex assembly was measured in a pull-down assay by incubating 2.5 μM each of GST–Sec9, Sso1(145–265) and Snc2(1–92), in the presence or absence of 2.5 μM of Sro7(61–962) or Sro7(61–891), then quenching the reaction at given time points by tenfold dilution into buffer. Detailed procedures are presented in Supplementary Information.

Received 13 December 2006; accepted 29 January 2007.

1. Pruyne, D., Legesse-Miller, A., Gao, L., Dong, Y. & Bretscher, A. Mechanisms of polarized growth and organelle segregation in yeast. *Annu. Rev. Cell Dev. Biol.* **20**, 559–591 (2004).
2. Jahn, R. & Scheller, R. H. SNARE—engines for membrane fusion. *Nature Rev. Mol. Cell Biol.* **7**, 631–643 (2006).
3. Wirtz-Peitz, F. & Knoblich, J. A. Lethal giant larvae take on a life of their own. *Trends Cell Biol.* **16**, 234–241 (2006).

Table 1 | X-ray data collection and refinement statistics

Data collection	
Space group	<i>P4₂1₂</i>
Cell dimensions	
<i>a</i> , <i>b</i> , <i>c</i> (Å)	130.5, 130.5, 116.0
α , β , γ (°)	90, 90, 90
Resolution (Å)	56.9–2.40 (2.53–2.40)*
<i>R</i> _{merge}	0.108 (0.431)*
<i>I</i> / σ (<i>I</i>)	13.7 (3.6)*
Completeness (%)	99.8 (100)*
Redundancy	4.7 (4.8)*
Refinement	
Resolution (Å)	56.9–2.40
Number of reflections (work/free)	35,772/3,825
<i>R</i> _{work} / <i>R</i> _{free}	0.211/0.261
Number of atoms	
Protein	6,831
Ligand or ion	2
Water	287
B-factors	
Protein	27.4
Ligand or ion	32.9
Water	25.5
Root-mean-square deviations	
Bond lengths (Å)	0.006
Bond angles (°)	1.32

* The highest-resolution shell is shown in parentheses.

4. Lehman, K., Rossi, G., Adamo, J. E. & Brennwald, P. Yeast homologues of tomosyn and lethal giant larvae function in exocytosis and are associated with the plasma membrane SNARE, Sec9. *J. Cell Biol.* **146**, 125–140 (1999).
5. Zhang, X. *et al.* Lethal giant larvae proteins interact with the exocyst complex and are involved in polarized exocytosis. *J. Cell Biol.* **170**, 273–283 (2005).
6. Grosshans, B. L. *et al.* The yeast Igl family member Sro7p is an effector of the secretory Rab GTPase Sec4p. *J. Cell Biol.* **172**, 55–66 (2006).
7. Adamo, J. E., Rossi, G. & Brennwald, P. The Rho GTPase Rho3 has a direct role in exocytosis that is distinct from its role in actin polarity. *Mol. Biol. Cell* **10**, 4121–4133 (1999).
8. Adamo, J. E. *et al.* Yeast Cdc42 functions at a late step in exocytosis, specifically during polarized growth of the emerging bud. *J. Cell Biol.* **155**, 581–592 (2001).
9. Kagami, M., Toh-e, A. & Matsui, Y. Sro7p, a *Saccharomyces cerevisiae* counterpart of the tumor suppressor I(2)gl protein, is related to myosins in function. *Genetics* **149**, 1717–1727 (1998).
10. Vasioukhin, V. Lethal giant puzzle of Lgl. *Dev. Neurosci.* **28**, 13–24 (2006).
11. Gracheva, E. O. *et al.* Tomosyn inhibits synaptic vesicle priming in *Caenorhabditis elegans*. *PLoS Biol.* **4**, e261 (2006).
12. McEwen, J. M., Madison, J. M., Dybbs, M. & Kaplan, J. M. Antagonistic regulation of synaptic vesicle priming by Tomosyn and UNC-13. *Neuron* **51**, 303–315 (2006).
13. Musch, A. *et al.* Mammalian homolog of *Drosophila* tumor suppressor lethal (2) giant larvae interacts with basolateral exocytic machinery in Madin-Darby canine kidney cells. *Mol. Biol. Cell* **13**, 158–168 (2002).
14. Hatsuzawa, K., Lang, T., Fasshauer, D., Bruns, D. & Jahn, R. The R-SNARE motif of tomosyn forms SNARE core complexes with syntaxin 1 and SNAP-25 and down-regulates exocytosis. *J. Biol. Chem.* **278**, 31159–31166 (2003).
15. Pobbati, A. V., Razeto, A., Boddener, M., Becker, S. & Fasshauer, D. Structural basis for the inhibitory role of tomosyn in exocytosis. *J. Biol. Chem.* **279**, 47192–47200 (2004).
16. Mohri, K., Vorobiev, S., Fedorov, A. A., Almo, S. C. & Ono, S. Identification of functional residues on *Caenorhabditis elegans* actin-interacting protein 1 (UNC-78) for disassembly of actin depolymerizing factor/cofilin-bound actin filaments. *J. Biol. Chem.* **279**, 31697–31707 (2004).
17. Voegtli, W. C., Madrona, A. Y. & Wilson, D. K. The structure of Aip1p, a WD repeat protein that regulates cofilin-mediated actin depolymerization. *J. Biol. Chem.* **278**, 34373–34379 (2003).
18. Betschinger, J., Eisenhaber, F. & Knoblich, J. A. Phosphorylation-induced autoinhibition regulates the cytoskeletal protein Lethal (2) giant larvae. *Curr. Biol.* **15**, 276–282 (2005).
19. Baba, T., Sakisaka, T., Mochida, S. & Takai, Y. PKA-catalyzed phosphorylation of tomosyn and its implication in Ca^{2+} -dependent exocytosis of neurotransmitter. *J. Cell Biol.* **170**, 1113–1125 (2005).
20. Brennwald, P. *et al.* Sec9 is a SNAP-25-like component of a yeast SNARE complex that may be the effector of Sec4 function in exocytosis. *Cell* **79**, 245–258 (1994).
21. Fasshauer, D., Sutton, R. B., Brunger, A. T. & Jahn, R. Conserved structural features of the synaptic fusion complex: SNARE proteins reclassified as Q- and R-SNAREs. *Proc. Natl Acad. Sci. USA* **95**, 15781–15786 (1998).
22. Goud, B., Salminen, A., Walworth, N. C. & Novick, P. J. A GTP-binding protein required for secretion rapidly associates with secretory vesicles and the plasma membrane in yeast. *Cell* **53**, 753–768 (1988).
23. Boyd, C., Hughes, T., Pypaert, M. & Novick, P. Vesicles carry most exocyst subunits to exocytic sites marked by the remaining two subunits, Sec3p and Exo70p. *J. Cell Biol.* **167**, 889–901 (2004).
24. Gari, E., Piedrafitra, L., Aldea, M. & Herrero, E. A set of vectors with a tetracycline-regulatable promoter system for modulated gene expression in *Saccharomyces cerevisiae*. *Yeast* **13**, 837–848 (1997).
25. Baker, N. A., Sept, D., Joseph, S., Holst, M. J. & McCammon, J. A. Electrostatics of nanosystems: application to microtubules and the ribosome. *Proc. Natl Acad. Sci. USA* **98**, 10037–10041 (2001).
26. Landau, M. *et al.* ConSurf 2005: the projection of evolutionary conservation scores of residues on protein structures. *Nucleic Acids Res.* **33**, W299–W302 (2005).
27. Nicholson, K. L. *et al.* Regulation of SNARE complex assembly by an N-terminal domain of the t-SNARE Sso1p. *Nature Struct. Biol.* **5**, 793–802 (1998).

Supplementary Information is linked to the online version of the paper at www.nature.com/nature.

Acknowledgements We thank L. Katz for help with the yeast two-hybrid analysis, and S. Kaiser for assistance with mass spectrometry. Diffraction data were measured at the Advanced Light Source and the Stanford Synchrotron Radiation Laboratory. D.A.H. was supported by a fellowship from the American Cancer Society. This work was supported by NIH grants to P.J.B. and W.I.W. and a grant from the G. Harold and Leila Y. Mathers Foundation to P.J.B.

Author Contributions Crystallographic and biochemical experiments were designed by D.A.H. and W.I.W. and performed by D.A.H. Plasmid and strain construction were designed and performed by D.A.H. and P.J.B. Yeast two-hybrid analysis, secretion assays and analysis of mutant phenotypes were designed by P.J.B. and performed by A.A. and A.G. D.A.H. and W.I.W. wrote the paper and all authors made editorial comments.

Author Information Coordinates and structure factors have been deposited in the Protein Data Bank under accession number 2OAJ. Reprints and permissions information is available at www.nature.com/reprints. The authors declare no competing financial interests. Correspondence and requests for materials should be addressed to W.I.W. (bill.weis@stanford.edu) or P.J.B. (pjbrennw@med.unc.edu).

LETTERS

Translational and rotational settings of H2A.Z nucleosomes across the *Saccharomyces cerevisiae* genome

Istvan Albert¹, Travis N. Mavrich^{1,2}, Lynn P. Tomsho¹, Ji Qi¹, Sara J. Zanton^{1,2}, Stephan C. Schuster¹ & B. Franklin Pugh^{1,2}

The nucleosome is the fundamental building block of eukaryotic chromosomes. Access to genetic information encoded in chromosomes is dependent on the position of nucleosomes along the DNA. Alternative locations just a few nucleotides apart can have profound effects on gene expression¹. Yet the nucleosomal context in which chromosomal and gene regulatory elements reside remains ill-defined on a genomic scale. Here we sequence the DNA of 322,000 individual *Saccharomyces cerevisiae* nucleosomes, containing the histone variant H2A.Z, to provide a comprehensive map of H2A.Z nucleosomes in functionally important regions. With a median 4-base-pair resolution, we identify new and established signatures of nucleosome positioning. A single predominant rotational setting and multiple translational settings are evident. Chromosomal elements, ranging from telomeres to centromeres and transcriptional units, are found to possess characteristic nucleosomal architecture that may be important for their function. Promoter regulatory elements, including transcription factor binding sites and transcriptional start sites, show topological relationships with nucleosomes, such that transcription factor binding sites tend to be rotationally exposed on the nucleosome surface near its border. Transcriptional start sites tended to reside about one helical turn inside the nucleosome border. These findings reveal an intimate relationship between chromatin architecture and the underlying DNA sequence it regulates.

Chromatin is composed of repeating units of nucleosomes in which ~147 base pairs (bp) of DNA is wrapped ~1.7 times around the

exterior of a histone protein complex². A nucleosome has two fundamental relationships with its DNA³. A translational setting defines a nucleosomal midpoint relative to a given DNA locus. A rotational setting defines the orientation of DNA helix on the histone surface. Thus, DNA regulatory elements may reside in linker regions between nucleosomes or along the nucleosome surface, where they may face inward (potentially inaccessible) or outward (potentially accessible). Recent discoveries of nucleosome positioning sequences throughout the *S. cerevisiae* (yeast) genome suggest that nucleosome locations are partly defined by the underlying DNA sequence^{4,5}. Indeed, a tendency of AA/TT dinucleotides to recur in 10-bp intervals and in counter-phase with GC dinucleotides generates a curved DNA structure that favours nucleosome formation³. Genome-wide maps of nucleosome locations have been generated^{6,7}, but not at a resolution that would define translational and rotational settings. To acquire a better understanding of how genes are regulated by nucleosome positioning, we isolated and sequenced H2A.Z-containing nucleosomes from *S. cerevisiae*. Such nucleosomes are enriched at promoter regions^{8–11}, and thus maximum coverage of relevant regions can be achieved with fewer sequencing runs. With this high resolution map we sought to address the following questions: (1) what are the DNA signatures of nucleosome positioning *in vivo*? (2) How many translational and rotational settings do nucleosomes occupy? (3) Do chromosomal elements possess specific chromatin architecture? (4) What is the topological relationship between the location of promoter elements and the rotational and translational setting of nucleosomes?

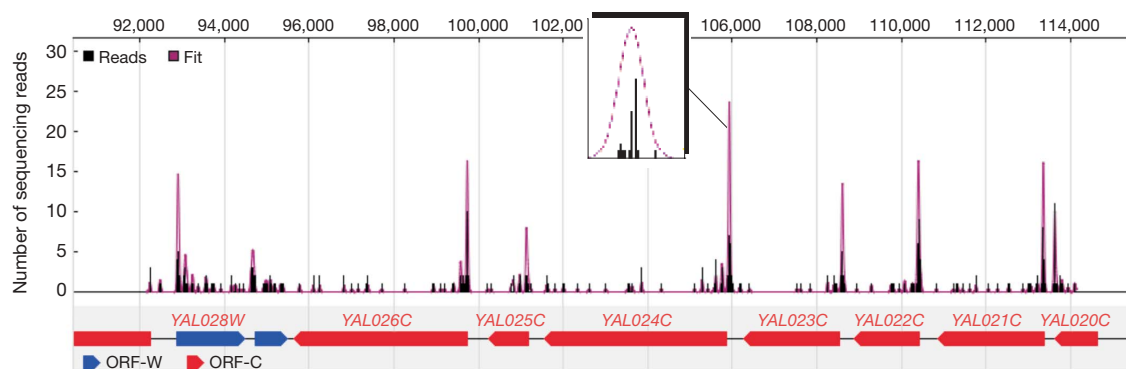


Figure 1 | Distribution of H2A.Z nucleosomal DNA at an arbitrary region of the yeast genome. Any region of the genome can be viewed in this way at <http://nucleosomes.sysbio.bx.psu.edu>. An enlarged view of a peak is shown in the inset, where each vertical bar corresponds to the number of

sequencing reads located at individual chromosomal coordinates. The locations of ORFs are shown below the peaks. Additional browser shots are shown in Supplementary Fig. 1.

¹Center for Comparative Genomics and Bioinformatics, ²Center for Gene Regulation, Department of Biochemistry and Molecular Biology, The Pennsylvania State University, University Park, Pennsylvania 16802, USA.

Nucleosome positions were trapped in yeast by formaldehyde crosslinking. H2A.Z nucleosome core particles were immunoprecipitated from micrococcal nuclease (MNase)-digested chromatin and gel purified (Supplementary Figs 1 and 2); core particles (322,000) were individually sequenced in parallel by pyrosequencing. Most sequencing reads had highly clustered locations throughout the genome and were strongly biased towards the 5' end of genes (Fig. 1), as expected. In generating the map, we made adjustments for sequence bias inherent in MNase cutting (Supplementary Fig. 3). The distribution of sequencing reads was then smoothed at two levels: fine and coarse (see Fig. 2b), corresponding to individual translational settings and the average setting, respectively (provided in Supplementary Table 1). Independent determinations made on the Watson and Crick strands (left and right borders) concurred, producing a median error of 4 bp (Supplementary Fig. 4a). Comparisons with other experimentally and computationally derived maps^{4,5,9,11} are presented in Supplementary Fig. 4b–f.

On average, 25 sequencing reads per nucleosome were used to assign the genomic location of ~10,000 H2A.Z nucleosomes. Another 30,000 nucleosomes, containing low levels of H2A.Z, were assigned with an average of 3–4 reads. Even nucleosomes identified by a single read had comparatively low error (Supplementary Fig. 4d), reflecting widespread incorporation of low H2A.Z levels. This was further examined at the highly repetitive ribosomal DNA locus, which should amplify this noise by a factor of 150–200, corresponding to the number of rDNA repeats. Indeed, reads at the rDNA locus

clustered into nucleosome-sized arrays (Supplementary Fig. 5). When normalized to the number of repeats present, the read count was similar to the low level observed throughout the genome. This low genome-wide level of H2A.Z might represent biological noise (that is, real but not necessarily meaningful).

Nucleosome positioning sequences have been largely defined by dinucleotide patterns present in a relatively small number of sequenced nucleosomes. Positioning sequences have not been defined by nucleosomes trapped at their *in vivo* location, which could differ from thermodynamically favoured positions. We examined >8,000 well-defined nucleosome positions, and found an AA/TT and GC dinucleotide pattern remarkably similar to the thermodynamically favoured pattern (Fig. 2a and Supplementary Fig. 6)^{3,4}. Strikingly, a relatively strong enrichment of GC dinucleotides and a deficiency of AT dinucleotides was detected 3–4 bp from the nucleosome border; this is where the highly regulated histone H3 tails emerge from the DNA gyres¹², which might indicate a histone–DNA regulatory interaction. The deficiency of AT was not evident 1 bp in from the border, suggesting that the intrinsic MNase specificity for AT was not artificially depleting the region of AT.

Coarse-grain and fine-grain smoothing of the read distributions allowed several nucleosomal parameters to be assessed (Fig. 2b). First we investigated the basis of multiple fine-grain peaks within each coarse-grain peak. Multiple peaks might reflect nucleosome delocalization over a rather narrow range. Indeed, the fine-grain positions

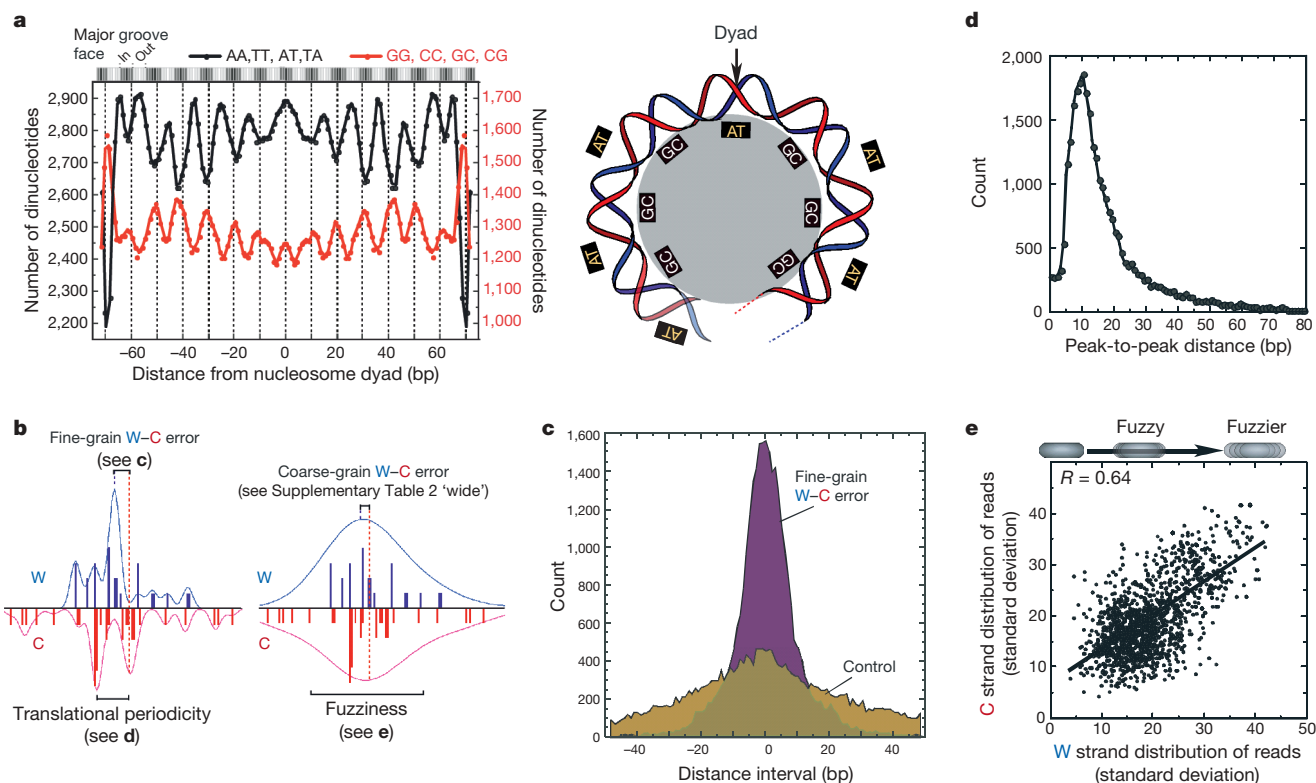


Figure 2 | Rotational and translational settings of H2A.Z nucleosomes. **a**, Smoothed frequency distribution of the combined number of AA, TT, AT, TA or GG, CC, GC, CG dinucleotides at each base pair along the 147 bp of nucleosomal DNA. The schematic shows the rotational setting of the two sets of dinucleotides. **b**, Bar graph depicting the number of reads mapped to each coordinate on the Watson (W, in blue) and Crick (C, in red) strands for an arbitrary nucleosome. Bars are separated in 1-bp increments. Fine-grain (left panel) and coarse-grain smoothing (right panel) are shown for the same data. **c**, Each coarse-grain peak was centred midway between its matched W–C pairs. Closest W–C fine-grain peaks were paired, and their base pair separation calculated. Shown in purple is a smoothed frequency distribution (bin size, 1 bp; 'count', number of fine-grain nucleosome positions) of their distances (error).

As a control, the entire distribution of fine-grain C peaks within a single coarse-grain peak was rotated 180° around the centre of its coarse-grain peak, then paired off with nearest fine-grain W peaks (yellow distribution). The relatively short distance between paired W–C peaks compared with the control indicates that MNase heterogeneity, which would be non-identical on the W and C strands, cannot account for the distribution of fine-grain peaks. **d**, Peak-to-peak distances for peaks located on the same strand were measured, using the highest six peaks within each coarse-grain peak. The number of measurements at the indicated distance intervals is plotted as a smoothed frequency distribution. **e**, Scatter plot of the standard deviation of read coordinates located under a single coarse-grain peak, comparing Watson and Crick matched pairs. A total read count was required to exceed 35, to be included.

determined independently on the Watson and Crick strands were highly co-incident compared to a control set (Fig. 2c), suggesting that these peaks largely represent alternative overlapping translational settings.

The 10-bp periodicity of dinucleotides inherent in nucleosome positioning sequences theoretically restricts DNA to a single rotational setting on the histone surface. In the absence of mitigating factors, this limits nucleosomes to quantum translational settings of 10 bp. To test this prediction, we measured peak-to-peak distances between adjacent translational settings, and found the most frequent positioning interval to be 10 bp (Fig. 2d). Thus, on a genomic scale nucleosomes tend towards a primary rotational setting, resulting in discrete translational settings having 10-bp intervals.

The standard deviation of read locations within each coarse-grain nucleosome provides another metric of delocalization or 'fuzziness'. Figure 2d shows that fuzzier nucleosomes measured on the Watson strand were verifiable when examined on the Crick strand. Approximately 10% of all major H2A.Z nucleosomes were 'very fuzzy', tending towards 3–4 predominant translational settings. Most others had 1–3 predominant settings.

We next explored the biological significance of multiple translational settings by examining the properties of genes having very fuzzy H2A.Z nucleosomes (Supplementary Tables 2 and 3). Indeed,

these genes tended to be TATA-containing and positively regulated by chromatin remodelling factors including SAGA, SWI/SNF and SWR-C, the latter being H2A.Z-specific. They tended to be negatively regulated by histone modifying factors such as Hda1 deacetylase and Set1 methylase, and by the SSN6–TUP1 chromatin repressor complex. Thus, we find a strong link between chromatin regulation and multiple translational settings, suggesting that nucleosome repositioning by chromatin regulators may have important global roles in regulating gene expression, particularly at TATA-containing promoters.

We also examined 'very wide' nucleosomes, which have coarse-grain Watson positions that are farther away from their matching Crick positions than expected by chance (typically >20 bp). Interestingly, genes having very wide nucleosomes also tended to be controlled by chromatin regulators, with the SSN6–TUP1 complex being particularly involved (Supplementary Table 2). SSN6–TUP1 binds to nucleosomes and forms a repressive chromatin domain¹³. Conceivably, its presence might provide additional MNase protection to nucleosomes, creating an appearance of unusually wide nucleosomes.

The geographical landscape of H2A.Z nucleosomes in the vicinity of chromosomal elements is presented in Fig. 3. With the exception of TATA-containing promoters, a characteristic H2A.Z chromosomal architecture was found to encompass distinct classes of

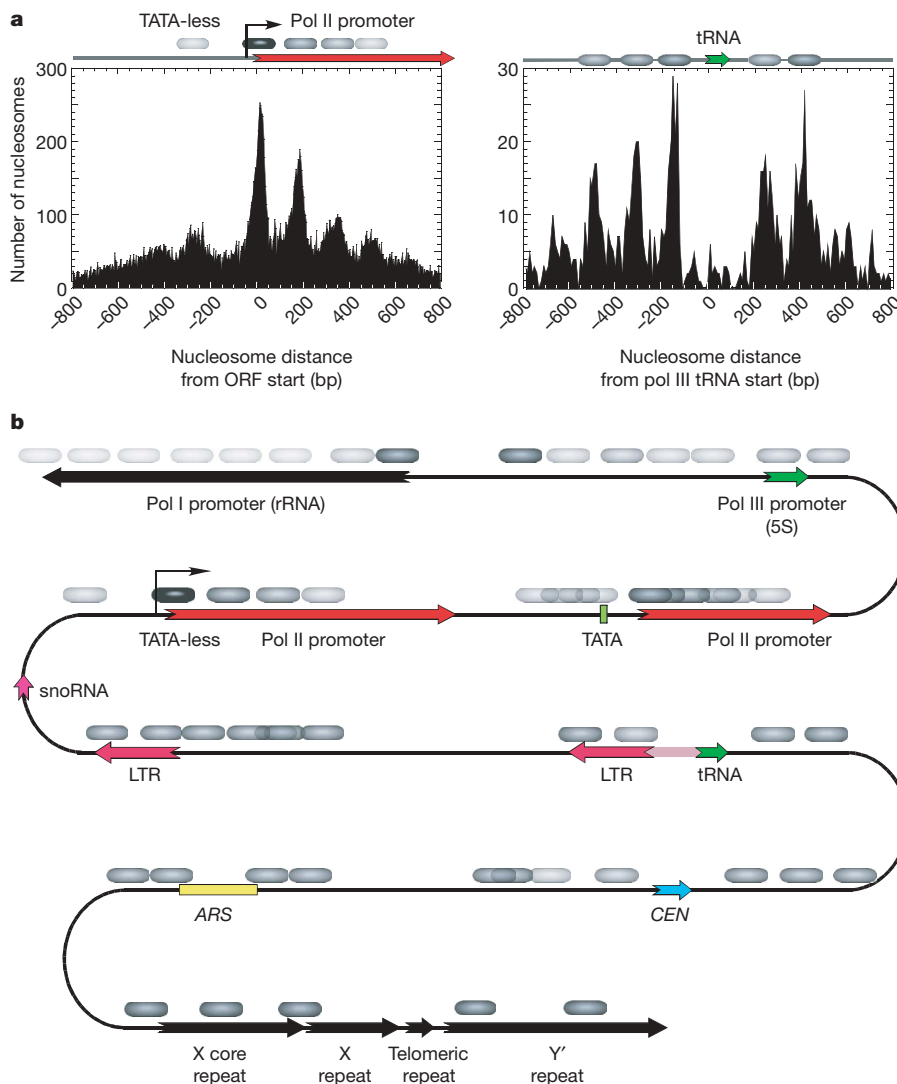


Figure 3 | Distribution of H2A.Z nucleosomes in and around chromosomal elements. **a**, Number of nucleosomes located at varying distances from either an ORF start site (left panel) or a tRNA start site (right panel) were binned in 10-bp intervals, then plotted as a smoothed frequency

distribution. Plots for additional chromosomal elements are shown in Supplementary Figs 5 and 8a–m. **b**, Generalized schematic of nucleosome positions in and around chromosomal elements. The darkness of the ovals represents the relative level of H2A.Z.

chromosomal elements. Telomeric repeats and centromeric regions contained H2A.Z nucleosomes in fixed locations and spaced in ~200 bp intervals rather than the canonical 165 bp. Spacing on parts of the Y' telomeric elements is consistent with an alternating array of standard and H2A.Z-containing nucleosomes. The specialized centromeric nucleosome was devoid of H2A.Z, presumably containing H2A instead. Thus, both H2A and H2A.Z may have geographically distinct roles in centromere function^{14,15}. Origins of replication (ARs) lacked H2A.Z, which is consistent with studies on individual ARs^{16,17}. However, H2A.Z nucleosomes were positioned on flanking genomic DNA, suggesting that the AR, or its cognate factors, establishes an H2A.Z-containing chromatin architecture surrounding the AR, perhaps functionally analogous to the chromatin architecture found at promoter regions.

Ribosomal RNA is transcribed by RNA polymerase (pol) I from a single type of promoter. Two H2A.Z nucleosomes were present at the pol I promoter (Fig. 3b), at +13 and -415, establishing a 268-bp nucleosome-free region akin to that at pol II promoters⁶. An H2A.Z nucleosome was also positioned over the start of the 18S rRNA. Because 18S rRNA is generated by RNA cleavage rather than transcription initiation, the significance of this H2A.Z positioning is unclear. H2A.Z nucleosomes may have an important role at pol I promoters, possibly through their established function in counteracting silent information regulator (SIR)-mediated silencing.

The arrangement of nucleosomes at pol II promoters is now established^{4-6,9} as H2A.Z nucleosomes flanking a nucleosome-free promoter region⁸⁻¹¹. Computational modelling predicts that TATA-containing and TATA-less promoters have distinct nucleosomal architecture⁵. Indeed, TATA-less promoters, which constitute the vast majority of the genome¹⁸, showed the canonical architecture including 165-bp inter-nucleosomal spacing (Fig. 3). In contrast, TATA-containing promoters lacked a canonical architecture (Supplementary Fig. 8f). This scattered distribution was not due to a complete delocalization of individual nucleosomes because nucleosomes were positioned at individual promoters, albeit fuzzy. Rather, each TATA-containing promoter has a tailored chromatin architecture, which may explain their greater dependency on chromatin remodelling^{5,18}.

Highly transcribed genes tend to be depleted of nucleosomes¹⁹⁻²¹. We examined whether this might be due to loss of nucleosomes at specific locations in the promoter region, or whether there was a general depletion. Three groups of genes were examined, including the highly transcribed ribosomal protein genes, the less-transcribed ribosome biogenesis genes, and all highly transcribed genes (Supplementary Fig. 8h-j)²². In all cases, the translational positioning of nucleosomes was unperturbed over the open reading frame (ORF) start region as was the case with most genes and individual genes²³. Instead, H2A.Z levels were reduced, reflecting nucleosome depletion. Transcription of the ORF start region might remove the intervening nucleosome. But, once pol II has passed, the nucleosome returns to its original unperturbed location, perhaps guided by strong positioning sequences.

Pol III-transcribed transfer RNA genes tended to reside in the midst of ~250 bp H2A.Z-free regions, which were flanked by several uniformly positioned nucleosomes with a low H2A.Z content (Fig. 3). Typically two of these flanking nucleosomes housed a long terminal repeat (LTR) from a Ty retrotransposon (Supplementary Fig. 8m), which is often physically linked to tRNA genes²⁴. Thus, H2A.Z might have undiscovered roles in transposition.

We mapped the location of promoter elements relative to the nearest nucleosome, the orientation of which is defined by the nearest ORF. As shown in Fig. 4a, TATA boxes were scattered across the downstream border of the first upstream nucleosome, which is consistent with the heterogeneous chromatin architecture of TATA-containing promoters⁵ and their dependence on chromatin modifying and remodelling factors¹⁸. In contrast, transcriptional start sites were concentrated ~13 bp inside the upstream border of the +1

nucleosome, which tended to be less fuzzy than other nucleosomes (Fig. 4b). This location places the histone H3 amino-terminal tail just upstream of the transcriptional start site, where it could regulate transcription initiation (see Fig. 4e). Indeed, the highly regulated H3 K36 site resides just outside of the DNA gyre, placing it near the start site.

Evolutionarily conserved binding sites for over 100 gene-specific transcription factors have been identified in promoter regions throughout the yeast genome^{25,26}. Only a small fraction of these sites have been reported to bind transcription factors^{27,28}, which brings into question the physiological significance of the vast majority of unbound sites. Irrelevant sites should be randomly distributed without regard to chromatin structure. However, we find that conserved but unbound transcription factor binding sites tend to have a topological relationship with their nucleosome neighbour (Fig. 4c). These sites tended to reside near nucleosome borders, and were concentrated in 10-bp periodicities that aligned with the rotationally exposed DNA major groove on the histone surface. This pattern suggests that many transcription factors recognize their cognate sites on the nucleosome surface. Their placement near nucleosome borders positions them to control the translational setting of nucleosomes. Consistent with this finding, sites that were bound by

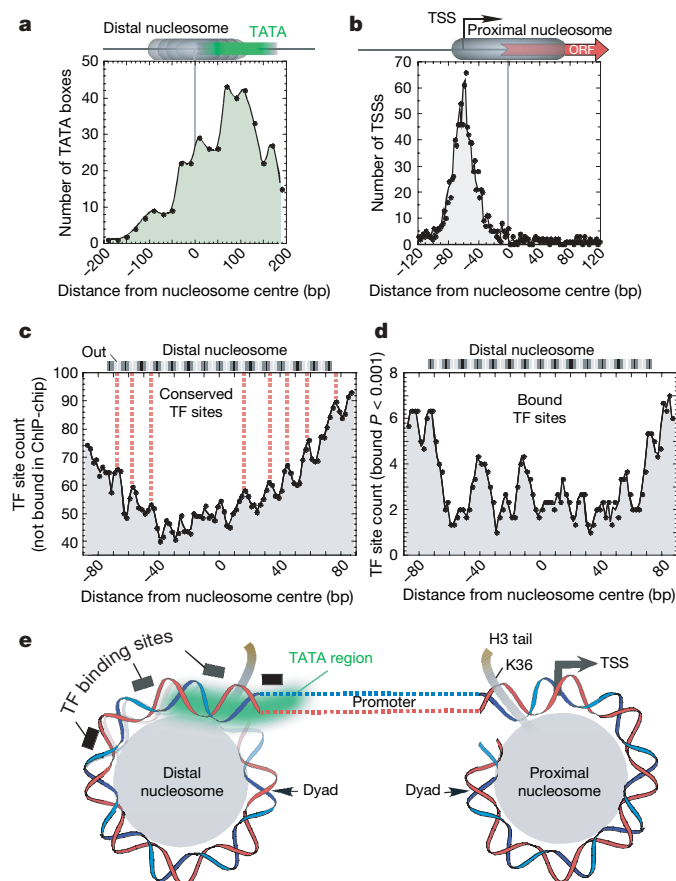


Figure 4 | Distribution of transcriptional regulatory elements along the nucleosome surface. **a–d**, The distance from each element to its nearest nucleosome centre was measured, binned, and plotted as a smooth distribution. Locations of TATA boxes, transcriptional start sites (TSSs) and transcription factor (TF) binding sites are published^{18,29,30}. The topological relationships of individual unbound TF sites with nucleosomes are presented in Supplementary Fig. 9. ChIP-chip, chromatin immunoprecipitation performed on a genome-wide scale. The data sources in panels **c** and **d** were files 'nobind_c3.gff' (stringent conservation and no binding P -value cutoff) and 'p001_c3.gff' (stringent conservation and binding $P < 0.001$), respectively, downloaded from http://fraenkel.mit.edu/improved_map/latest_maps.html. **e**, Representation of the rotational setting of TF binding sites and TSSs on the nucleosome surface.

sequence-specific regulators^{27–29} tended to reside just outside of the nucleosome border (Fig. 4d). Thus, a potential consequence of transcription factors binding to nucleosomal DNA is the translational displacement of the nucleosome, which might be important for gene activation (Fig. 4e). The H2A.Z nucleosome map presented here reveals a tight regulatory relationship between promoter elements and the topology of nucleosome borders.

METHODS

S. cerevisiae (BY4741 *HTZ1-TAP*) was grown to mid-log phase in rich media, then subjected to formaldehyde crosslinking⁶. *HTZ1-TAP* encodes carboxy-terminally TAP-tagged H2A.Z. Collected cells were disrupted, and non-nucleosomal DNA eliminated with MNase. H2A.Z-TAP nucleosomes were immunopurified with immunoglobulin G-sepharose and eluted with the Tobacco Etch Virus (TEV) protease. The resulting 125–170-bp DNA was gel-purified and sequenced with the Genome Sequencer 20. Sequencing reads were mapped to the reference *S. cerevisiae* genome at <http://www.yeastgenome.org>. Additional details can be found in Supplementary Information.

Received 20 October 2006; accepted 26 January 2007.

- Martinez-Campa, C. *et al.* Precise nucleosome positioning and the TATA box dictate requirements for the histone H4 tail and the bromodomain factor Bdf1. *Mol. Cell* **15**, 69–81 (2004).
- Richmond, T. J. & Davey, C. A. The structure of DNA in the nucleosome core. *Nature* **423**, 145–150 (2003).
- Satchwell, S. C., Drew, H. R. & Travers, A. A. Sequence periodicities in chicken nucleosome core DNA. *J. Mol. Biol.* **191**, 659–675 (1986).
- Segal, E. *et al.* A genomic code for nucleosome positioning. *Nature* **442**, 772–778 (2006).
- Ioshikhes, I. P., Albert, I., Zanton, S. J. & Pugh, B. F. Nucleosome positions predicted through comparative genomics. *Nature Genet.* **38**, 1210–1215 (2006).
- Yuan, G. C. *et al.* Genome-scale identification of nucleosome positions in *S. cerevisiae*. *Science* **309**, 626–630 (2005).
- Pokholok, D. K. *et al.* Genome-wide map of nucleosome acetylation and methylation in yeast. *Cell* **122**, 517–527 (2005).
- Li, B. *et al.* Preferential occupancy of histone variant H2A.Z at inactive promoters influences local histone modifications and chromatin remodeling. *Proc. Natl Acad. Sci. USA* **102**, 18385–18390 (2005).
- Raisner, R. M. *et al.* Histone variant H2A.Z marks the 5' ends of both active and inactive genes in euchromatin. *Cell* **123**, 233–248 (2005).
- Zhang, H., Roberts, D. N. & Cairns, B. R. Genome-wide dynamics of Htz1, a histone H2A variant that poises repressed/basal promoters for activation through histone loss. *Cell* **123**, 219–231 (2005).
- Guillemette, B. *et al.* Variant histone H2A.Z is globally localized to the promoters of inactive yeast genes and regulates nucleosome positioning. *PLoS Biol.* **3**, e384 (2005).
- Luger, K., Mäder, A. W., Richmond, R. K., Sargent, D. F. & Richmond, T. J. Crystal structure of the nucleosome core particle at 2.8 Å resolution. *Nature* **389**, 251–260 (1997).
- Malave, T. M. & Dent, S. Y. Transcriptional repression by Tup1–Ssn6. *Biochem. Cell Biol.* **84**, 437–443 (2006).
- Pinto, I. & Winston, F. Histone H2A is required for normal centromere function in *Saccharomyces cerevisiae*. *EMBO J.* **19**, 1598–1612 (2000).
- Krogan, N. J. *et al.* Regulation of chromosome stability by the histone H2A variant Htz1, the Swr1 chromatin remodeling complex, and the histone acetyltransferase NuA4. *Proc. Natl Acad. Sci. USA* **101**, 13513–13518 (2004).
- Lipford, J. R. & Bell, S. P. Nucleosomes positioned by ORC facilitate the initiation of DNA replication. *Mol. Cell* **7**, 21–30 (2001).
- Nieduszynski, C. A., Knox, Y. & Donaldson, A. D. Genome-wide identification of replication origins in yeast by comparative genomics. *Genes Dev.* **20**, 1874–1879 (2006).
- Basehoar, A. D., Zanton, S. J. & Pugh, B. F. Identification and distinct regulation of yeast TATA box-containing genes. *Cell* **116**, 699–709 (2004).
- Bernstein, B. E., Liu, C. L., Humphrey, E. L., Perlstein, E. O. & Schreiber, S. L. Global nucleosome occupancy in yeast. *Genome Biol.* **5**, R62 (2004).
- Boeger, H., Griesenbeck, J., Strattan, J. S. & Kornberg, R. D. Removal of promoter nucleosomes by disassembly rather than sliding *in vivo*. *Mol. Cell* **14**, 667–673 (2004).
- Lee, C. K., Shibata, Y., Rao, B., Strahl, B. D. & Lieb, J. D. Evidence for nucleosome depletion at active regulatory regions genome-wide. *Nature Genet.* **36**, 900–905 (2004).
- Holstege, F. C. *et al.* Dissecting the regulatory circuitry of a eukaryotic genome. *Cell* **95**, 717–728 (1998).
- Gavin, I. M. & Simpson, R. T. Interplay of yeast global transcriptional regulators Ssn6p–Tup1p and Swi–Snf and their effect on chromatin structure. *EMBO J.* **16**, 6263–6271 (1997).
- Kim, J. M., Vanguri, S., Boeke, J. D., Gabriel, A. & Voytas, D. F. Transposable elements and genome organization: a comprehensive survey of retrotransposons revealed by the complete *Saccharomyces cerevisiae* genome sequence. *Genome Res.* **8**, 464–478 (1998).
- Kellis, M., Patterson, N., Endrizzi, M., Birren, B. & Lander, E. S. Sequencing and comparison of yeast species to identify genes and regulatory elements. *Nature* **423**, 241–254 (2003).
- Cliften, P. *et al.* Finding functional features in *Saccharomyces* genomes by phylogenetic footprinting. *Science* **301**, 71–76 (2003).
- Harbison, C. T. *et al.* Transcriptional regulatory code of a eukaryotic genome. *Nature* **431**, 99–104 (2004).
- Lee, T. I. *et al.* Transcriptional regulatory networks in *Saccharomyces cerevisiae*. *Science* **298**, 799–804 (2002).
- MacIsaac, K. D. *et al.* An improved map of conserved regulatory sites for *Saccharomyces cerevisiae*. *BMC Bioinformatics* **7**, 113 (2006).
- David, L. *et al.* A high-resolution map of transcription in the yeast genome. *Proc. Natl Acad. Sci. USA* **103**, 5320–5325 (2006).

Supplementary Information is linked to the online version of the paper at www.nature.com/nature.

Acknowledgements We thank R. Albert for computational support, and S. Tan, J. Reese, D. Gilmour, and Y. Wang for many helpful discussions. This work was supported by a grant from NIH.

Author Contributions I.A. developed computational approaches to derive nucleosome maps from the read locations and developed the associated browser; T.N.M. prepared and purified the nucleosomes; L.P.T. constructed libraries and sequenced nucleosomal DNA; J.Q. mapped sequencing reads to the yeast genome; S.J.Z. produced Supplementary Tables 2 and 3; S.C.S. managed and directed the DNA sequencing phase, and analysed the sequencing data; and B.F.P. directed the project, analysed the processed data, and wrote the paper.

Author Information Reprints and permissions information is available at www.nature.com/reprints. The authors declare no competing financial interests. Correspondence and requests for materials should be addressed to B.F.P. (bfp2@psu.edu).

naturejobs

**THE CAREERS
MAGAZINE FOR
SCIENTISTS**

Sometimes it's hard to be a pioneer. When you're among the first to enter a new research field or a non-traditional career, there's always uncertainty and no well trodden path forward.

That's the impression I got from 12 fellows on a postdoc programme in drug research and regulatory review, launched jointly by the US National Cancer Institute and the US Food and Drug Administration in February 2005 to provide professionals in the emerging field of 'biological' cancer drugs. The first class finishes the programme this spring and only one of the people I visited knows definitely what they want to do when it ends. They all have some idea of the opportunities in this field, of course; that's what made them choose this specialized training programme.

So what can they and others in similarly specialized and novel career paths do? The answer is easy — do their homework. Scientists exploring their career options should fire up their search engines and aim their browsers at some answers. Look for professional associations, trade journals and regional hubs in particular.

For regulatory affairs in the United States, for example, there's the Regulatory Affairs Professional Society. General industry organizations include the Biotechnology Industry Organization and the Pharmaceutical Research and Manufacturers of America, covering biotech and pharma jobs. Regulatory-affairs professionals are also in demand in the expanding contract-research field, so a visit to the Association of Clinical Research Organizations might prove fruitful.

If one has a regional preference that meshes with regulatory affairs for, say, Massachusetts, there's the Massachusetts Biotechnology Council. San Francisco and San Diego have robust biotechnology associations as well.

If pioneers are still worried, there's no need to fret. They can look to the success of institutions such as the Keck Graduate Institute in California, which combines science and business training — including regulatory affairs — in a masters degree (see page 582). Almost all the graduates from that course got jobs in the life-sciences industry within six months. Being a pioneer does pay off.

Paul Smaglik, *Naturejobs* editor

CONTACTS

Editor: Paul Smaglik

Assistant Editor: Gene Russo

European Head Office, London

The Macmillan Building,
4 Crinan Street,
London N1 9XW, UK
Tel: +44 (0) 20 7843 4961
Fax: +44 (0) 20 7843 4996
e-mail: naturejobs@nature.com

European Sales Manager:

Andy Douglas (4975)
e-mail: a.douglas@nature.com

Business Development Manager:

Amelie Pequignot (4974)
e-mail: a.pequignot@nature.com

Natureevents:

Claudia Paulsen Young
(+44 (0) 20 7014 4015)
e-mail: c.paulsenyoung@nature.com

France/Switzerland/Belgium:

Muriel Lestringuez (4994)

UK/Ireland/Italy/RoW:

Nils Moeller (4953)

Scandinavia/Spain/Portugal:

Evelina Rubio-Morgan (4973)

Germany/Austria/The Netherlands:

Reya Silao (4970)

Online Job Postings:

Matthew Ward (+44 (0) 20 7014 4059)

Advertising Production Manager:

Stephen Russell
To send materials use London
address above.

Tel: +44 (0) 20 7843 4816

Fax: +44 (0) 20 7843 4996

e-mail: naturejobs@nature.com

Naturejobs web development:

Tom Hancock

Naturejobs online production:

Catherine Alexander

US Head Office, New York

75 Varick Street,
9th Floor,
New York,
NY 10013-1917
Tel: +1 800 989 7718
Fax: +1 800 989 7103
e-mail: naturejobs@natureny.com

US Sales Manager:

Peter Bless

Japan Head Office, Tokyo

Chiyoda Building,
2-37 Ichigayatamachi,
Shinjuku-ku,
Tokyo 162-0843
Tel: +81 3 3267 8751
Fax: +81 3 3267 8746

Asia-Pacific Sales Manager:

Ayako Watanabe
e-mail: a.watanabe@natureasia.com

ALTERNATIVES IN COLORADO



In his 2006 State of the Union address, President George W. Bush famously announced that “America is addicted to oil” and pledged a 22% increase in clean-energy investments. Soon afterwards, the National Renewable Energy Laboratory (NREL) in Golden, Colorado, fell victim to a bungled budget cut, resulting in the elimination of 32 staff positions, including eight researchers. On the eve of Bush’s visit to the labs to promote his energy plan, the Department of Energy hastily moved funds around to reinstate the jobs. The president blamed a mix-up in funding allocation.

Such mixed signals are indicative of the predicament faced by many researchers in Colorado. A handful of prestigious national labs and universities clustered along the foot of the Rockies between Denver and Fort Collins are leading the way in atmospheric research, geosciences and sustainable-energy research and development. And recent initiatives to pool resources and build strong links between the various institutes are promising to create new jobs and produce intellectual ferment.

But much of the region’s science and technology depends on federal dollars. And although the US political climate has swung decidedly in favour of weaning the nation from its dependence on fossil fuels, Congressional haggling over federal spending has resulted in flat budgets and funding cuts to the very institutes that are fuelling the progress.

“It’s a roller coaster, and it has been for the whole time that I’ve been here,” says a senior research scientist who’s been at the NREL for more than 15 years, and who prefers not to be named. “We’ve been almost

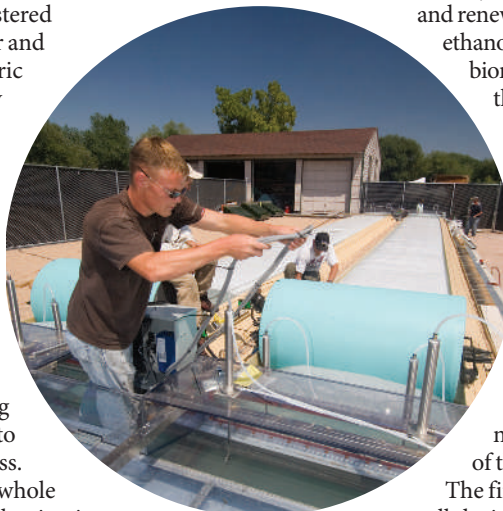
Despite tight government budgets, Colorado is brimming with alternative-energy jobs potential.
Amanda Haag reports.

zeroed out and then had budgets put back in.” Yet because of the NREL’s commitment to the mission of energy independence, he says, many scientists who went there “would forgo larger salaries elsewhere and come to jobs that were less stable and more subject to the vagaries of change”.

The NREL, home to the nation’s only large-scale pilot plant for the production of ethanol from biomass, is now experiencing a swell in the number of job openings, particularly in the areas of biomass and photovoltaic research. The lab currently employs some 900 engineers and scientists in R&D on biomass, wind, solar, hydrogen and other alternative-energy technologies. Its growth is directly attributable to the president’s energy initiatives and renewable-fuels standard alongside the current ethanol boom, says Andy Aden, an engineer in the biomass group. Research and engineering jobs at the NREL range from entry level with a bachelor’s degree up to a PhD requirement with at least 10 years’ experience. But although the biomass group’s funding has gone up, the overall budget took a 3% cut. “That means other programmes here are decreasing, which is sad,” Aden says.

Under the resolution for the 2007 budget, \$300 million is to be appropriated to energy-efficiency and renewable-energy programmes within the Department of Energy. The NREL has been promised \$107 million when the funds get divvied up, on top of the \$200 million it was already set to receive.

The first priority will be scaling up the pilot cellulosic ethanol biofuels refinery. Currently, the lab can handle about 1 tonne of biomass per day, which translates to production of some 265 litres (70 gallons)



CSU and Solix research on a photo-bioreactor.

of ethanol a day. The new building would allow for increased storage capacity and would enable testing of new processing technologies.

Uncertain budgets seem to be the norm for the Boulder laboratories run by the National Oceanic and Atmospheric Administration (NOAA) as well. During the past 18 months, federal funding in NOAA's Earth System Research Laboratory has been reduced by some 10%. In mid-January, the chemical-sciences division effectively lost more than 10% of its budget when its \$2.6-million participation in a long-term air-quality study was dropped. As a result, the jobs of 16 researchers are in jeopardy, and their fate and the agency's funding remain undetermined. NOAA officials say the money was put back in NOAA's hands. It remains to be seen how it will be allocated. Steven Brown, a NOAA atmospheric scientist who works in the division where the layoffs could occur, says that the budgetary fluctuations are taking a toll on morale. "It really clouds the outlook for the future in terms of not just 'will I have a job or not next year', but 'what will I be able to do careerwise or scientifically if the resources are going to be far more limited,'" Brown says. Projects that involve expensive field work, for example, could be put on hold.

Still, Brown and others are optimistic that the surge in public awareness regarding climate change and sustainable energy will have positive effects on budget priorities. Tom Hamill, a meteorologist in NOAA's Earth System Research Laboratory, notes that although "there's a fair amount of nervousness", the returns on investment are significant. For instance, upfront investment in weather-prediction capabilities pay off tenfold when it comes to forecasting hurricanes and other events affecting commerce and daily life, says Hamill. "I think and hope that we have a good cause to make, and that regardless of what administration we have we'll be able to justify our existence," Hamill says. Bush's 2008 budget could make possible new initiatives, including a drought-information system and sending unmanned aircraft into hurricanes.

Collaboratory colleagues

Although some of the region's R&D seems contingent on the whims of Congress, there are other collaborative opportunities springing up among various institutes. The University of Colorado (CU) at Boulder, Colorado School of Mines and Colorado State University (CSU) have just partnered with the NREL in what's dubbed a 'collaboratory'. Launched this month, it aims to harness the strengths of each institute in order to position Colorado as the nation's leader in renewable and sustainable energy innovation. "It is allowing us to compete for much bigger projects than we could do individually," says Susan Avery, graduate-school dean and vice chancellor for research at CU, Boulder.

The collaboratory is vying for a \$21.8-million grant from the Department of Energy to establish a centre for 'revolutionary photoconversion' and to invest in research geared towards solar-cell efficiency. Another project just unveiled this month is a large-scale programme in new biofuels and biorefining. Initially, most of the jobs will go to existing faculty. But many opportunities will arise as technologies are developed and deployed a few years down the road, Avery says.

An exciting collaboration on the horizon for CU is a \$60-million supercomputing data centre to be built in Cheyenne, Wyoming. A joint venture by CU, the



"The Collaboratory project is allowing us to compete for much bigger projects than we could do individually."

— Susan Avery



Maura Hagan: foresees strong opportunities for collaboration.

National Center for Atmospheric Research (NCAR) in Boulder, the University of Wyoming and the state of Wyoming, this is expected to generate a host of unique opportunities for collaboration with other parts of the research community. Simulations produced on the supercomputers will enable extensive studies in global and regional climate, weather, space physics, oceanography, Earth-system processes and related geosciences. Due to open by early 2011, the centre will need 40–50 employees, including some new hires.

Colorado competed with Wyoming to house the facility but lost the bid, as the state of Wyoming offered greater financial support. Although some Boulder-area jobs are likely to be relocated to Wyoming to run the centre, most people see it as an intellectual boon for both research communities. "In terms of local Boulder jobs, there may be some disappointment," says Maura Hagan, director of the Advanced Study Program at NCAR. "But in terms of opportunities for collaboration with the universities and NCAR, that's still very strong and joint appointments are viable."

Top dollar for atmosphere funding

Research at NCAR is going strong, with more buildings and staff than ever before. NCAR and its managing organization, the University Corporation for Atmospheric Research, employ some 225 scientists and 170 engineers, with an annual budget of around \$222 million. The centre, whose primary funding sponsor is the National Science Foundation (NSF), brings a steady flow of atmospheric-sciences funding into the region. Between 2003 and 2006, Colorado led the nation in atmospheric-research dollars from NSF, receiving \$463 million, with California trailing behind at \$110 million. Funding to NCAR accounts for the disparity. Each year, NCAR offers between four and six scientist I/research I positions and 10 postdoctoral appointments in its Advanced Studies Program. "We would not shut down our hires even in the most difficult of times," Hagan says. "What we would do is make fewer appointments."

Private firms also promise to energize the region with job growth and technical innovation in coming years. A garage-based start-up called Solix Biofuels is teaming with CSU and the 'green' microbrewery New Belgium to convert algal scum into biodiesel, diverting heat-trapping carbon dioxide in the process. In addition, a New York-based firm, Prism Solar, recently announced its hope of planting a 9,000-square-metre manufacturing facility for photovoltaic technology in Pueblo, about two hours' drive south of Denver. The company forecasts that it could bring 300 permanent jobs to the region. And in December, SkyFuel, a New York-based start-up company, announced plans to construct a \$2-billion solar-energy park — the world's largest — in Colorado's San Luis Valley. The project, with construction due to begin in 2010, would power 300,000 homes and businesses.

Where the government fails to come up with funds, perhaps private enterprise will increasingly step into the breach. Endowed with some 300 days of sunshine per year and enough wind potential to power about eight states its own size, Colorado continues to at least have the potential to become the nation's boomtown of renewable-energy and geosciences innovation.

Amanda Haag is a freelance science writer based in Denver, Colorado.

L. HARWOOD/UNIV. COLORADO, BOULDER

K. BARNEY

MOVERS

Sally Benson, executive director, Global Climate and Energy Project, Stanford University, California



1980–2007: Staff scientist (director 1993–1997), Earth Sciences Division, Lawrence Berkeley National Laboratory, Berkeley, California

2001–2004: Deputy director for operations, Lawrence Berkeley National Laboratory

1997–2001: Associate laboratory director, Energy Sciences, Lawrence Berkeley National Laboratory

As an undergraduate at Barnard College, New York, Sally Benson loved both physics and natural history. A geology course at nearby Columbia University showed her a way to combine those interests. Designed to lure those with strong quantitative backgrounds away from physics and chemistry, it put Benson on track for a geology degree. “I imagined working on the geophysical properties of the mantle–core boundary of the planet,” she says.

A summer job at the Department of Energy’s Lawrence Berkeley National Laboratory (LBNL) set Benson on a long-term path as a geothermal-energy researcher and environmental problem solver. Her PhD dissertation topic — remediation of toxic selenium from the soils and water of Kesterson reservoir, a marsh in California — was one of the first studies to use the natural biogeochemistry as a remediation strategy for inorganic contaminants. She demonstrated that microbes played a key role in converting selenium to an immobile, non-toxic form. “This project led me to believe science could play an immediate role in environmental problem solving,” she says.

Her ability to communicate science effectively swept her into administration, when she became director of the Earth sciences division at the LBNL. Certain that the team could provide solutions to major challenges, notably climate change, she kept an eye on emerging issues to develop the LBNL’s portfolio of research in regional climate modelling, carbon-flux monitoring, carbon sequestration and geological storage of carbon dioxide. After a few years, she also became the associate laboratory director for the energy sciences. In 2004, she left management to focus on her interest in testing geological storage of carbon dioxide as a method of mitigating climate change.

On 1 March, however, Benson’s experiences and interests coalesced when she became executive director of Stanford University’s Global Climate and Energy Project (GCEP). She says it was the breadth of the endeavour — covering all aspects of carbon dioxide and climate-related problems — that motivated her move.

“No one can guess how market forces and research will play out over the next 30–50 years,” says GCEP project director Franklin Orr. However, the LBNL’s acting director of earth sciences, Ernie Major, says Benson’s expertise lies in integrating all the research demands needed to find answers. And finding them is Benson’s new passion. “It’s a critical time to put solutions on the table,” she says. ■

Virginia Gewin

NETWORKS & SUPPORT

Opportunities in Poland

A young Polish scientist recently expressed concern in this column about the paucity of opportunities in Poland for young repatriates hoping to establish independent research groups (see *Nature* **445**, 792; 2007). We respectfully disagree.

Despite low science budgets and many old-fashioned procedures, there are institutes in Poland where postdocs can start independent careers. Several newly formed groups conduct research at a high level and attract funds from outside Poland. Most are headed by postdocs who have returned after successes abroad.

For example, in 2005, one of us, Marta Miaczynska, returned after 12 years abroad in which she completed a PhD and two postdocs in molecular cell biology. In 2003, she earned a position as a group leader at the International Institute of Molecular and Cell Biology in Warsaw (IIMCB).

Grants from the international programmes of the Howard Hughes Medical Institute (HHMI) and the Wellcome Trust helped her set up a new research group. Funding from the European Union, the Max Planck Society and the Polish Ministry of Science allowed her to build a nine-person research team and attract postdocs, including repatriates from abroad. We believe that such

opportunities are increasing steadily.

Miaczynska returned to Poland because she believed she would be able to develop quality, independent research, with sufficient funds, in a supportive environment. Two years on, she does not regret her decision.

We are convinced that top young researchers can find attractive options if they are ready to compete for positions and funds. True, such opportunities are not yet common in Poland; it is not as easy as in richer countries with a more advanced research infrastructure. But those who are successful can apply to several sources for extra funding, and can select the very best PhD students from a large number of graduates.

We agree that the system needs reforms, in particular more young people on faculty staffs. Despite some recent initiatives, by the Foundation for Polish Science, for example, more needs to be done to facilitate early independence of young scientists and to attract our compatriots back. After all, if Polish scientists stay in other countries, who will push for changes to Polish science?

Jacek Kuznicki is director of the IIMCB in Warsaw, Poland. Marta Miaczynska is an HHMI international scholar and a cell biologist at the IIMCB.

POSTDOC JOURNAL

Parent and mentor

Although I’ve mentored several undergraduate students in the past, I hadn’t realized what being a mentor was really about until I became a parent. Now I see that the similarities are uncanny.

When my student figures out something new or ‘gets it’, I feel proud and excited. When he shows up four hours late, I am disappointed that he didn’t warn me, and frankly, I feel that I should scold him (though I don’t). I find myself explaining, in great detail, simple things that I take for granted as routine or obvious. Other times, I find him plugging away at data analyses I hadn’t expressly told him to work on. Just like any parent, I take his successes, and failures, personally.

In my pre-parenting days, I had assumed that good students were born. But I now realize they are made, through careful and patient nurturing by scientists who are willing to devote their time.

My mentoring experience has taught me how to be a more patient teacher, a good listener and a better planner. Every student, successful or not, is unique and each can teach me something new and useful about myself. Of course, the best part of mentoring, for me, is watching their intellect and creativity shine as they progress in their projects, and watching their careers blossom when they leave the nest as they, perhaps, go on to nurture their own students.

Moir Sheehan is a postdoc in plant breeding and genetics at Cornell University.

The inside track from academia and industry

Translating science into business

The right kind of postgraduate training could help you to realize biotech's potential as well as your own.



Sheldon Schuster

Biosciences are revolutionizing our ability to understand and manipulate life. Yet the biotech sector has lost money over the past 25 years, while promised revolutions in the development of new drugs have not come to pass. The average cost of launching a new drug is now roughly the same for 'small' biotech and 'big' pharma: about \$1.2 billion. In 2005, the US Food and Drug Administration approved just 20 new drugs. Phase III trial failures have doubled in a decade to 40%.

One critical problem has been the lack of properly trained talent, although the number of promising scientific discoveries is greater than ever. The US Department of Labor estimates the biotech workforce is growing at 12% annually. By 2012, the demand for biological scientists and technicians is expected to grow by 19%.

"Because the industry is experiencing such rapid growth," a department report notes, "biotechnology firms often demand more skilled workers than are available and are projected to need more workers than are currently enrolled in training programs."

"Scientists trained in the traditional disciplines are not taught how to function in industry."

To turn this trend around, we must get better at translating basic scientific insights to commercial realities. In 1997, the Keck Graduate Institute of Applied Life Sciences (KGI) in Claremont, California, was established for this purpose. The institute is dedicated to a single mission: education and research translating the power and potential of the life sciences into practice for the benefit of society. It is the only US graduate school created exclusively to educate leaders for the life-sciences industry and offers a master of bioscience (MBS) degree, which combines business and science in

a team-based, project-focused curriculum. Students concentrate on five practical families of skills: biomedical devices and diagnostics; bio/pharmaceutical discovery and development; bioprocessing; the business of bioscience; and clinical and regulatory affairs.

We regularly consult leading scientists, managers and executives on trends in the industry. As a result, we've increased our offerings in regulatory and clinical affairs, intellectual property and licensing, and operations and manufacturing. It is not a coincidence that these are all areas with strong overlap between science and business.

The industry professionals on our advisory council have told us they have all the traditionally trained PhDs and MBAs they need. Instead, they are looking for people with solid, but broad, scientific training; strong backgrounds in business, finance and management, and an in-depth understanding of how the biosciences industry functions. Moreover, they want scientists who can work in teams to achieve integrated scientific and business goals, and can communicate these outcomes effectively.

"The KGI prepares students for what they will face in the industry," says Dennis Fenton, executive vice-president of operations at Amgen. "In the real world, you have to have business, people skills and science to get a product to market."

The success of KGI graduates proves the point: 97% are employed in the life-sciences industry within six months of graduation, as clinical scientists, research associates, business analysts and in regulatory affairs.

Scientists trained in traditional disciplines are simply not taught how to function in the bioscience industry under the pressure of deadlines, high-risk ventures and capital shortages. At the KGI, our students gain real experience in

businesses through mandatory, paid internships and corporate visits — and 35% of our students convert their internships into full-time posts. The capstone of the MBS is a year-long, industry-sponsored team project. With the help of an industry and a faculty mentor, groups of four or five students address business and scientific problems at the sponsoring company, signing confidentiality agreements and agreeing to strict timelines and budgets — as they will do throughout their careers. Last year, for example, one team helped Amylin Pharmaceuticals develop a line-extension strategy for its newly approved diabetes drug, Symlin. The team assessed drug-delivery options, regulatory requirements and business opportunities to present Amylin with a commercialization strategy. The project was so well received that two of the team members now work for Amylin.

Advances in the life sciences are occurring through the application of knowledge, tools and methods across traditional academic fields. Translating these advances into applications requires complex clinical and regulatory evaluations, market research and intellectual-property assessments. As the life-sciences industry looks to the future, it will need more scientists like the KGI's: technically savvy, commercially literate and adaptable.

As companies and research institutions think about preparing themselves for the decades ahead, they should consider adopting elements of the KGI model. Hybrid education, team-based learning, and project-centred curricula produce a flexible, mature and experienced workforce. That can improve decision-making throughout the chain of development, production and delivery.

Sheldon Schuster is president of the Keck Graduate Institute.

NATIONAL JEWISH

Medical and Research Center

Global Leader in Lung, Allergic
and Immune Diseases

FACULTY POSITION:

The Integrated Department of Immunology and Division of Mycobacterial and Respiratory Infections at National Jewish Medical and Research Center and the University of Colorado at Denver and Health Sciences Center invites applications for a faculty position at the Assistant or Associate Professor level.

The successful candidate will be expected to develop a competitive research program studying the host immune responses to pathogens. Candidates should have a Ph.D. and/or M.D. degree and at least three years of post-doctoral experience.

Please send your curriculum vitae and statement of research interests and arrange for three letters of reference to be sent to:

Dr. Philippa Marrack, Chair, Search Committee
National Jewish Medical and Research Center
1400 Jackson Street, 5th Floor, Goodman Building, Denver, Colorado 80206
marrackp@njc.org

The University of Colorado and National Jewish Medical and Research Center are Affirmative Action/Equal Opportunity employers.

 University of Colorado Health Sciences Center

SP99637R

POSTDOCTORAL POSITIONS – MOLECULAR MICROBIOLOGY AND PATHOGENESIS OF BACTERIAL AND VIRAL INFECTIONS.

NIH training grant-funded postdoctoral positions are available at the University of Colorado Health Sciences Center to study molecular mechanisms of bacterial infections (with Randall Holmes, Michael Schurr, Michael Vasil, Andres Vazquez-Torres or Martin Voskuil), molecular aspects of viral infections (with David Barton, Thomas Campbell, Robert Garcea, Donald Gilden, Kathryn Holmes, Jerome Schaack, Kenneth Tyler or Linda Van Dyk), molecular basis of innate immunity (with Charles Dinarello, Sonia Flores or Andres Vazquez-Torres) or structural biology of microbial pathogenesis (with Mair Churchill). See <http://www.uchsc.edu/sm/microbio/> for information about many of our research programs. Research facilities, grant funding and training environment are excellent. Applicants for these positions must be citizens or permanent residents of the United States. Candidates with Ph.D. or equivalent research degrees must have experience in microbiology, bacteriology, virology, immunology, molecular biology, genetics, biochemistry, cell biology, structural biology or a related field. Candidates with M.D., D.V.M or equivalent clinical degrees must have demonstrated competency for research related to our program. Individuals from under-represented groups are encouraged to apply. Compensation is determined by NIH policies.

Submit curriculum vitae, bibliography, and names of three professional references to **Training Program Director, UCHSC at Fitzsimons, Microbiology Department, Mail Stop 8333, P.O. Box 6511, Aurora, CO 80045. The University of Colorado Health Sciences Center is committed to Equal Opportunity and Affirmative Action.**

SP99729R



Change your
environment. Find
jobs where you'll
make a difference

naturejobs

NATIONAL JEWISH

Medical and Research Center

Global Leader in Lung, Allergic
and Immune Diseases

DIRECTOR OF BUSINESS DEVELOPMENT - CLINICAL LABS

As the Director of Business Development for the Clinical Reference Labs at National Jewish, you will be joining a rapidly growing entity with a bright line vision for future growth. The Clinical Labs are actively engaged in an initiative to accelerate growth over the next 5 years through effective develop of current clients, development of new, valued assays and services, as well as through strategic alliances with industry partners. The Business Development Manager will direct all phases of this business growth initiative project. Key traits for success in this position are self motivation, organizational skills, outstanding written and verbal skills & the ability to merge science & business strategies. Flexibility, high energy, a positive attitude, a sense of humor and a passion for integrity will make this position a fit for our team. BS/BA in Biomedical Sciences and/or Genetics, Molecular Biology or related field. MS/MA preferred. Ph.D. in Biomedical Sciences or related field desirable. 5+ years experience as a clinical scientist in a large scale R&D or commercial lab. 3+ years experience in project management, 2+ years business development in the healthcare, biomedical or biotechnology industries. National Jewish values diversity and we offer an excellent working environment & benefits package.

To apply, please go to www.njc.org.

AA/EO

SP99638R